Gypsum Deposits Associated with the Whitehill Formation (Ecca Group) in the Steytlerville-Jansenville Area, Southern Karoo, South Africa

By

Roberto Daniel Almanza

Submitted in fulfilment of the requirements for the degree of *Magister Scientiae* in the Faculty of Science at the Nelson Mandela University, Port Elizabeth

December 2017

Supervisor: Professor PWK Booth

DECLARATION

I, Roberto Daniel Almanza (student number 209029968), hereby declare that the dissertation for the qualification of *Magister Scientiae* (Geology) is my own work and that it has not previously been submitted for assessment or completion of any postgraduate qualification to another University or for another qualification.

Roberto Almanza

ACKNOWLEDGEMENTS

I wish to express my sincere gratitude towards the following people without whom this project would not have been possible:

- Professor Peter Booth (NMU), who supervised the project and provided invaluable input throughout the course of the study. His tireless dedication towards his students as well as his passion and enthusiasm for the subject has provided much encouragement and motivation. The completion of this dissertation would not have been possible without his continued guidance and exceptional knowledge of the study matter.
- Professor Maarten de Wit (AEON, NMU) for initiating the project and providing the necessary funding through Inkaba yeAfrika.
- The Department of Geoscience (NMU), whose staff is always willing to assist in a knowledgeable and friendly manner.
- Professor Mike Lee and Mr William Goosen (Centre for HRTEM, Department of Physics), for introducing me to and assisting with Scanning Electron Microscopy.
- My fellow students and colleagues, past and present, who gave up their valuable time to assist with various aspects of the project.
- Mrs Debbie Claasen (Council for Geoscience), for providing GIS data for the study area.
- Landowners and occupants within the Mount Stewart-Klipplaat area who provided access to their properties for fieldwork to take place, especially Mr Peter Cawood.
- Mr Jo van Heerden, who suggested, encouraged and contributed to the study via his vast general knowledge and wealth of mining and business experience.
- My parents, Andre and Anna Almanza, both of whom have worked tirelessly to provide me with the opportunities that I have had to further my studies. Thank you must also go to my close friends and relatives for their continued support.
- Miss Debbie Taylor, for her assistance with fieldwork, document formatting, proof-reading and general quality control. Not to mention her continued support, motivation, encouragement and love for which I am most grateful.

TABLE OF CONTENTS

LIST OF FIGURES

LIST OF TABLES

ABSTRACT

The Steyterville-Jansenville gypsum field is one of South Africa's smaller deposits, yet plays host to several gypsum mines, both past and present. This study aims to deconstruct the processes involved in the precipitation of various quantities and grades of gypsum in the lower Ecca Group of the Karoo Supergroup. The calcium and sulphate ions required to form the gypsum mineral ($CaSO_4 \bullet 2H_2O$) are derived from the mid- to lower-shale of the Whitehill Formation, which is carbonate- and pyrite-rich. Gypsum formation is dependent on the availability of pyrite as opposed to calcite, which is in abundance throughout the 30m thick, Early Ufimian (late Permian) Whitehill Formation.

Weathered shale, which has been folded and faulted, forms the host environment in which gypsum has precipitated. Folding of the shale occurs as a series of large- and medium-scale anticlines and synclines that strike east to west. These structures, which formed during the Cape Orogeny indicate that stresses were exerted from the south-southwest towards the north-northeast. Folded calcite veins surrounded by amorphous pyrite, observed in thin section suggest that pyrite and calcite were precipitated together prior to a deformation event. Oxidation of pyrite following these deformation events results in the concentration of sulphides within the hinge zones of the folds (weakest zone) and this is where the larger gypsum deposits are found at the surface.

Carbonate concretions in the Whitehill Formation up to 5m in length and 3m in width are common in the study area, and suggest a relationship with the deposition of the shale whereby calcium-rich nuclei grew in a concentric fashion during a non-depositional hiatus period. This period is also associated with a higher concentration of pyrite and could explain the occurrence of concretions together with adjacent gypsum-rich shale. Pyrite framboids observed under the Scanning Electron Microscope (SEM) provide evidence to suggest concentric growth of initially deposited microcrystals including nucleation and growth of nodules and concretions observed within the Whitehill Formation.

Prerequisites for gypsum formation also include restricted drainage such as a pan, a clay layer in the drainage area and an arid climate where evaporation exceeds

precipitation. The preferred surface conditions for gypsum formation would be low-lying areas which are surrounded by gently-sloping topography promoting the concentration of aqueous solutions in a calcite- and pyrite-rich area. Groundwater solution would initially dissolve the calcite and clay minerals, and pyrite and the quartz minerals would remain in the host rock. Areas with greater calcite and clay pores would accommodate more groundwater and thus promote a greater surface area for chemical reactions. This enhances the potential for the oxidation of pyrite to form sulphate ions, which can later combine with calcium ions to precipitate gypsum crystals. Alternatively, the oxidation of pyrite, which produces acidity, dissolves the carbonate host and the calcium- and sulphate-rich solution then precipitates gypsum.

The combination of the structural and geomorphological processes is key to the formation of economic gypsum deposits. The potential for extensive gypsum reserves within the Steytlerville-Jansenville field remains valid, provided the target is located over a predominantly weathered Whitehill Formation outcrop, preferably in an area which has undergone extensive deformation (such as a fold hinge zone), and is favourable for the concentration of ground and surface water within a low-lying area.

Keywords: Whitehill Formation; gypsum; Steytlerville; Jansenville; pyrite; calcite; carbonate; concretion; Cape Orogeny

1. INTRODUCTION

While relatively little importance is given to the gypsum commodity, it remains an essential component within the cement and agricultural industries. Gypsum, which requires semi-arid to arid conditions to form, is abundant in areas of northern Africa and Asia, but is also prominent in many regions of South Africa, especially within the Karoo Supergroup. Gypsum is an important natural resource as the demand for the commodity continues to increase with the continuous growth of the building and cement-making industries.

Gypsum in the Karoo Supergroup is generally associated with the sulphide-rich shale horizons of the Ecca or Dwyka Groups and occurs in gypsiferous layers which are between 1m and 23m in thickness and covered by compact red clayey soil. Other examples of gypsum occur in the Vanrhynsdorp area of the Western Cape, where the largest gypsum mine in South Africa is found, as well as in Ysterfontein along the West Coast and at the confluence of the Buffalo and Tugela rivers. These deposits occur in a wide range of environments from dried pans, to river terraces and in clayey soils (Lurie, 2004).

The Steytlerville-Jansenville gypsum field is one of South Africa's smaller deposits (**Figure 1.1**). It is covered by an average of 500mm of soil and has fine powdery gypsum bodies between 50 and 20 000 tons in size (Lurie, 2004). Its average thickness is 37cm, but these deposits are often duplicated due to thrust faults. The mineable deposits contain an average of 65% gypsum within the shale, and are thus considered to be medium grade deposits. The calcium and sulphate ions, essential to the precipitation process of gypsum, are derived from the Whitehill Formation (previously referred to as the 'white band' in older literature) (Oosterhuis, 1998).

The aim of this project is to determine the relationship between the physical and chemical properties of the Whitehill Formation in the Steyterville-Jansenville area and the potential for it to host several small, yet economically viable, gypsum deposits. The relative proportions of pyrite and calcite throughout the Whitehill Formation will be analysed to determine the extent of the influence that these minerals have on gypsum formation. Structural mapping of the project area will also take place to establish if there is a relationship between areas of structural

complexity and gypsum formation. In order to do this, various outcrops of the Whitehill Formation within this gypsum field will be mapped to determine folding, faulting and jointing patterns. The geomorphology will also be looked at as this is an integral component in the concentration of surface and groundwater which plays host to the chemical formation of gypsum minerals.

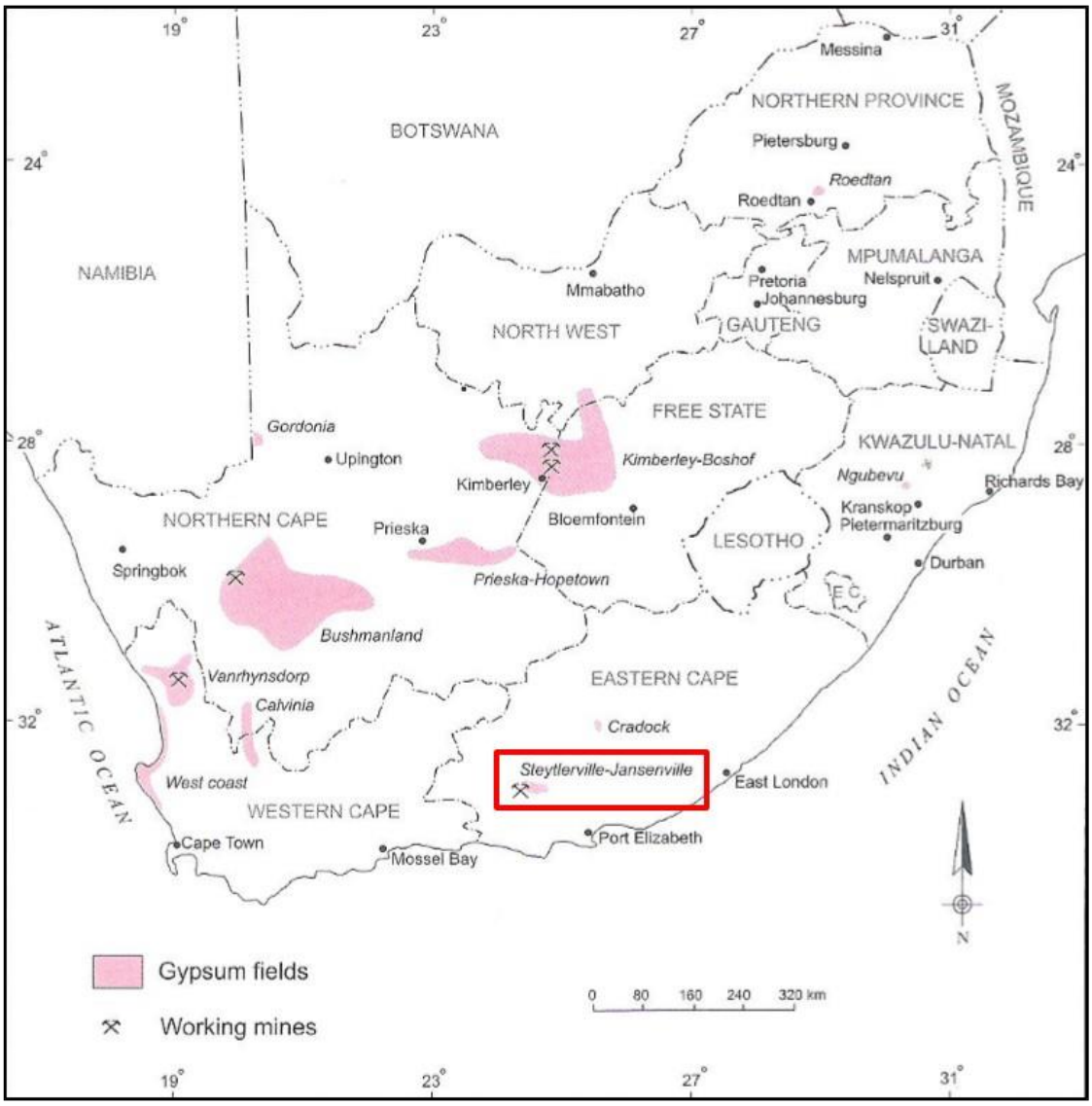

Figure 1.1: Gypsum fields in South Africa (from Oosterhuis, 1998).

In addition to this, the occurrence of dolomitic concretions of varying size, which are found at several of the study sites, will be examined. By looking at the combination of depositional environment and deformation, the project aims to determine how these concretions may have formed and to what extent they affect the occurrence of gypsum within the shale of the Whitehill Formation. The layering of the concretions could give an insight to chemical processes that were active

within this shale and provide evidence to suggest that oxidation of pyrite adjacent to the calcium-rich concretions resulted in precipitation of gypsum.

In summary, the objective of this project is to determine the relationship between the physical and chemical properties of the Whitehill Formation in the Steyterville-Jansenville area and the potential for it to host several small, yet economically viable, gypsum deposits. In order to achieve this, the research project will focus on the following aspects:

i. Mapping of geological structures to establish if there is a relationship between folding, faulting and jointing patterns that may account for the areal distribution of gypsum.
ii. An evaluation of pyrite and carbonate minerals in shales of the Whitehill Formation (these being the principal components required to form gypsum).
iii. Geomorphological development in the region, especially the confluence of drainage patterns which may have played a part in enhancing gypsum concentration at specific localities.
iv. The vertical and lateral occurrence and characteristics of dolomitic concretions throughout the Whitehill Formation (to test how these horizons control the spatial distribution of gypsum deposits in this formation).

2. LITERATURE REVIEW

The stratigraphic base of the Karoo Supergroup consists of the glacial deposits of the Dwyka Group which are overlain by marine shales of the Ecca Group (**Figure 2.1**). The Whitehill Formation, which is the subject of this study, is stratigraphically located in the lower Ecca Group. Johnson *et al.* (1996) and Catuneanu *et al.* (2005) provide a background to the "retro-arc foreland basin" in which the Karoo Supergroup sediments were deposited, including its lithostratigraphy, biostratigraphy, chronostratigraphy as well as a detailed tectonic setting. Johnson *et al.* (2006) and Kingsley (1981), provide a depositional history for the Karoo Supergroup and, more importantly, the shale of the Whitehill Formation within the lower Ecca Group, which is illustrated in Geel (2012).

Literature regarding the Whitehill Formation is presented by Visser (1992) which includes information pertaining to its distinct white-weathering colour, its approximate Early Ufimian (late Permian) age of approximately 265 million years as well as its thickness which is, on average, 30m. Also included are descriptions of the 'deep-water' and 'shallow-water' facies that make up the Whitehill Formation. This is explained in greater detail by Cole and Basson (1991). De Ville Wickens (1996) raises the subject of the correlations between the Whitehill Formation, Vryheid Formation and Tierberg Formation and provides insight into the higher carbon content of the Whitehill Formation compared to the underlying Collingham Formation and overlying Prince Albert Formation. This high carbon content, which is debated by Cole and Van Vuuren (1978) and Du Toit (1954), makes the Whitehill Formation an important target for naturally occurring shale gas (Geel *et al.*, 2013). This formation also has higher electrical conductivity making it a distinctly anomalous marker within the Karoo Supergroup (Branch *et al.*, 2007).

This particular study will focus on the gypsum which is precipitated at the surface sub-outcrop of the Whitehill Formation and its association with the higher calcium and pyrite content as mentioned in De Ville Wickens (1996). Other than Fockema *et al.* (1962) and Visser *et al*. (1963), there is limited literature regarding South African gypsum deposits.

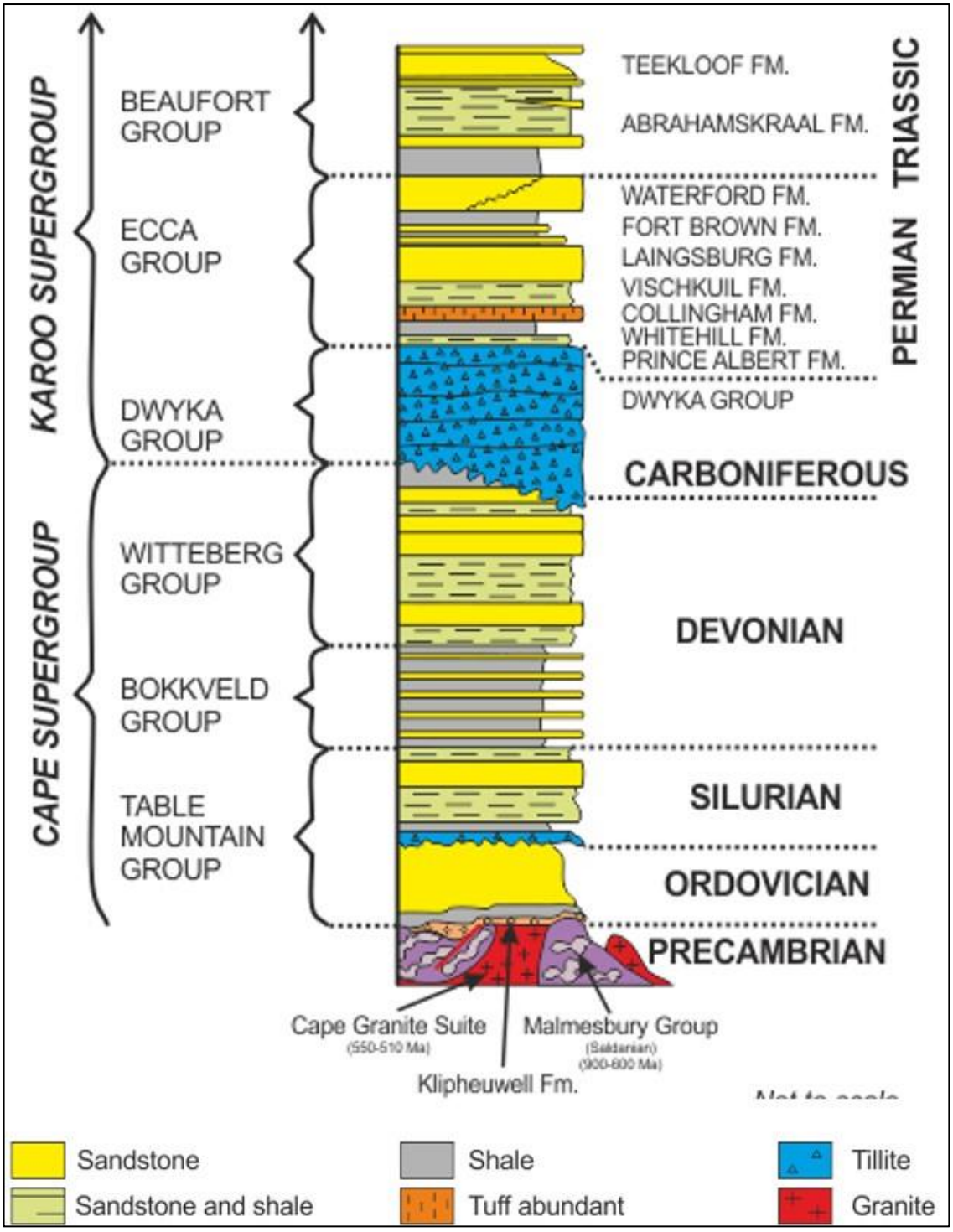

Figure 2.1: Generalised stratigraphic column for the Cape Supergroup and Karoo Supergroup (Flint *et al*, 2011).

Gypsum found in Namibia has been studied to determine the source of sulphur, and it was concluded that pyrite contained within the host rock would seem the most plausible origin for the Karoo gypsum deposits (Eckardt and Spiro, 1999). Lurie (2004) provides the basic properties of gypsum as a mineral and Oosterhuis

(1998) gives these properties meaning with regard to mineable quantities and qualities in South Africa. The latter also provides an understanding of the occurrences of gypsum. Brabers (1976) illustrates the prerequisites for gypsum to form as a mineable entity and these include the calcium and sulphate ions, a zone of weathering, restricted drainage, a clay layer and an arid climate. The geochemical process for the formation of gypsum, as well as the reactions thereof, are outlined by Pirelt *et* al. (2010) and Chermak and Schreiber (2014). Gypsum deposits located in the study area are denoted on the 1:250 000 geological map (Rogers *et al.*, 1991). Almond (2009) describes PPC's gypsum mine at Mount Stewart, which is at the centre of the study area, as "deeply-weathered mudrocks" which are located under "a thin cover of soil."

While Cole and Basson (1991), Visser (1992) and Geel *et al.* (2013) all make mention of the dolomitic concretions found within the Whitehill Formation, little detail is provided on the origin of these concretions. McBride *et al*. (2003) provide an understanding of several aspects regarding concretions including their size, spacing, structure and the chemical composition which considers the pyrite and iron traces. Abdel-Wahab and McBride (2001) provide more detail regarding the spatial patterns of the concretions and propose several theories for the nucleation and growth of these concretions. Whereas the previous two authors investigated concretions in sandstone, carbonate concretions within shale were studied by Lash and Blood (2004) and Mozley (1996), who support the notion that concentric layering of successive layers of cement nuclei is the conventional growth model for carbonate concretions.

3. STUDY AREA

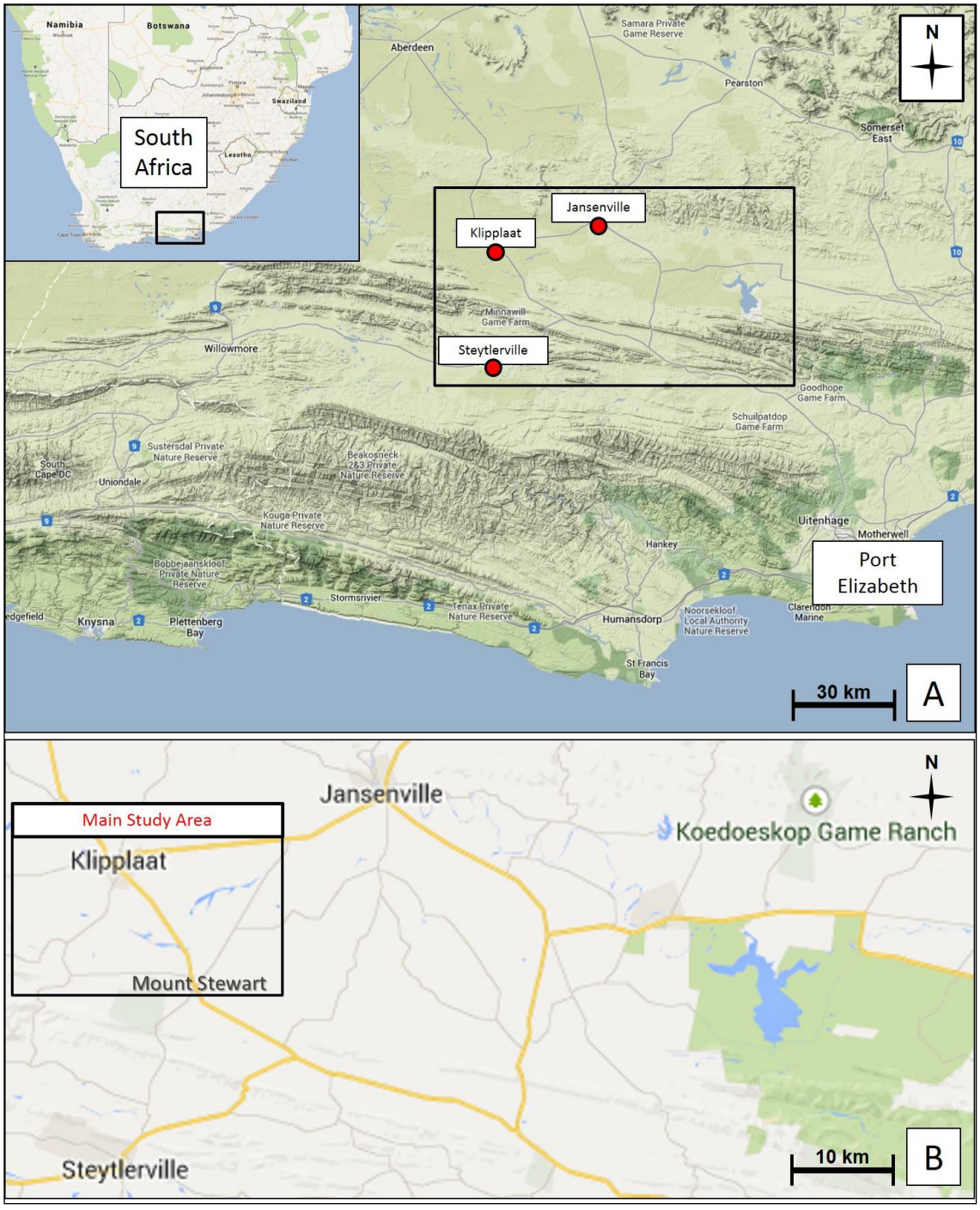

Figure 3.1: Location of the study area: A) Terrain map showing the Karoo towns of Steytlerville, Klipplaat and Jansenville in relation to Port Elizabeth; B) Main Study Area shown in relation to Steytlerville, Klipplaat and Jansenville.

The study area is located in the Eastern Cape province of South Africa, within a small portion of the Great Karoo, approximately 120km north-west of Port Elizabeth (**Figure 3.1**). Nearby towns include Steytlerville (located to the south of the study area), Klipplaat (just north of the study area) and Jansenville (north-east

of the study area). The study area extends approximately 50 km in an east-west direction and 15 km from north to south. It is located between the $33^0$00'S and $33^0$20'S lines of latitude, and between the $24^0$05'E and $24^0$55'E lines of longitude.

3.1 Climate

Located south of the Great Karoo are the escarpment mountain chains associated with the Cape Supergroup – commonly referred to as the Cape Mountains. These mountains prevent humid sea air from passing over to their leeward side and while rain falls in the south, very little reaches the north, leaving the Karoo notoriously dry (The Great Karoo, 2014). Only 5% of the minimal rain which falls over the Karoo reaches the rivers, meaning that almost all watercourses within the semi-arid to arid region are non-perennial (SA National Biodiversity Institute, 2015).

Historical data for Klipplaat, which is the nearest centre to the project area, reveals a climate which can be classified as a dry-cold Desert climate - category "BWk" according to the "Köppen climate system" (Strahler and Strahler, 2006). 'B' refers to a dry climate which has no permanent streams and has greater evaporation than precipitation throughout the year. 'W' refers to an arid climate with less than 400mm of annual rain (as opposed to 'S' which denotes a Semiarid or 'Steppe' climate). The letter 'k' refers to a 'dry-cold' climate where mean annual temperatures are below 18 °C, as is the case for Klipplaat which has a 17.8 °C mean annual temperature. The average rainfall of Klipplaat is between 158mm and 289mm according to different sources (**Table 3.1** and **Figure 3.2**). On average, the driest month is June which has 9mm of rain, while March is the wettest with 46mm. Mean midday temperatures range from 18.5°C in July to 31.4°C in January and the coldest average midnight temperature is 2.9°C in the month of July (SA Explorer, 2014 and Climate-Data.org, 2012).

Table 3.1: Klipplaat average monthly climate data (from Climate-Data.org, 2012).

month	1	2	3	4	5	6	7	8	9	10	11	12
mm	27	36	46	25	17	9	11	17	17	26	31	27
°C	23.2	23.2	21.3	18.2	14.5	11.8	11.3	13.2	15.5	17.8	19.9	21.9
°C (min)	15.6	15.8	14.5	11.3	7.6	4.6	4.1	5.7	8	10.3	12.4	13.8
°C (max)	30.9	30.6	28.2	25.1	21.4	19.1	18.5	20.8	23	25.3	27.4	30

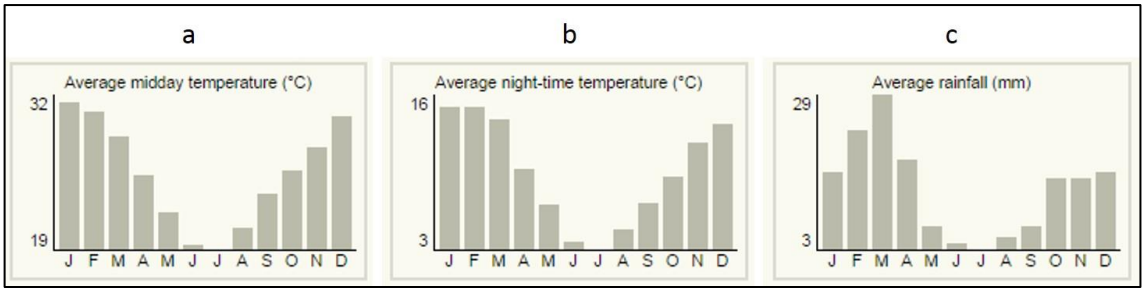

Figure 3.2: Klipplaat monthly climate data: a) Mean midday temperatures, b) Mean midnight temperatures, c) Mean rainfall (from SA Explorer, 2014).

3.2 Flora and Fauna

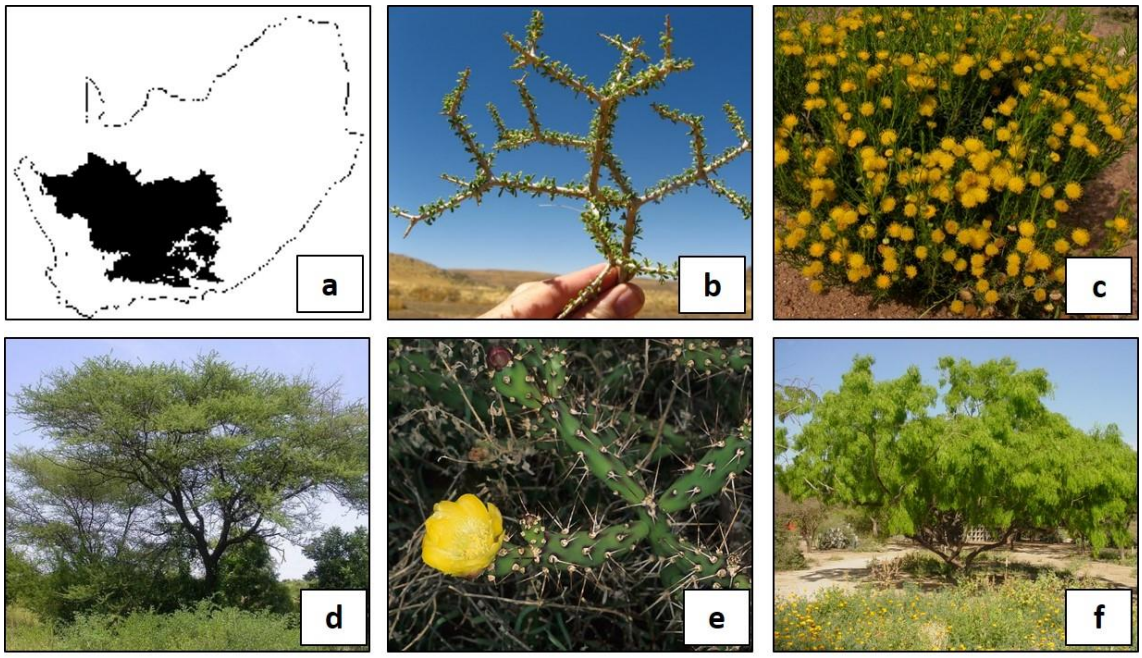

Figure 3.3: **a)** Extent of Nama Karoo biome in South Africa (from SA National Biodiversity Institute, 2015); **b)** Three-thorn *Rhigozum trichotomum* (from Kyffhäuser, 2014); **c)** Bitterbos *Chrysocoma ciliata* (from Fodden and Potter, 2005); **d)** Sweet Thorn *Acacia Karoo* (from Jacana, 2012); **e)** Prickly Pear *Opuntia aurantiaca* (from Robertson, 2011); **f)** *Mesquite Prosopis glandulosa* (from Arid Zone Trees, 2015).

The project area is located within the Nama Karoo Biome, which is the second largest biome in the country and is located between 500m and 2000m above sea-level over the central plateau. Rainfall is the primary factor determining the distribution of this biome and also determines the soil type which consists of over 80% lime-rich, weakly-developed soils which are easily eroded especially in areas of overgrazing. The sandy soils support the grassy vegetation especially in depressions within the biome, while on the clayey soils, grasses are less abundant. In livestock areas, grassland is often lost due to overgrazing and therefore the relative proportion of dwarf shrubland increases over the grasses.

Some areas of the Karoo are flourishing with indigenous species such as the Three-thorn *Rhigozum trichotomum*, the Bitterbos *Chrysocoma ciliata* and the Sweet Thorn *Acacia Karoo*. These particular species, which cope reasonably well with overgrazing, play a part in the reduced occurrence of grassland and other palatable species in the area. While invader species such as Prickly Pear *Opuntia aurantiaca* and *Mesquite Prosopis glandulosa* are common within the biome, there are very few rare or Red Data Book species associated with the Nama Karoo (**Figure 3.3**). Veld fires are rare as the fuel load contained within this vegetation is not sufficient to burn for long periods of time (SA National Biodiversity Institute, 2015).

Faunal species in the Karoo tend to be nomadic in their pursuit of areas where rainfall events have occurred. These isolated rainfall events are favourable to the Brown Locust and Karoo Caterpillar which are preyed on by a variety of birds and mammals. Today there are far fewer large herds of Springbok and other game as previously found in the Karoo. This is due to livestock farming becoming prevalent in the area resulting in land now being grazed by sheep and goats (SA National Biodiversity Institute, 2015). The Steytlerville area, located to the south of the project area, is the centre for wool and mohair in the south-eastern Great Karoo. Springbok and Kudu are still common to the area and are usually found on farms catering to the 'Ecotourism' market. The Kori Bustard, the largest flying bird, is also located in the Steytlerville district (**Figure 3.4**) (Baviaans Tourism, 2012).

Figure 3.4: Left: Herd of Kudu (from Baviaans Tourism, 2012); Right: Kori Bustard – largest flying bird (from Jacana, 2015).

3.3 Geological Setting

This study area has been chosen due to the exposed shale of the Whitehill Formation, accessible outcrops in road quarries and proximity to PPC Mt Stewart, a current supplier of gypsum to PPC Cement in Port Elizabeth. The outcropping geology within the study area consists entirely of Karoo Supergroup and younger rocks, but is surrounded by rocks of the Witteberg Group of the upper Cape Supergroup and as per (**Figure 2.1**). Outcrops of the Dwyka Group and Ecca Group are regularly encountered within the study area, the latter including the Prince Albert, Whitehill, Collingham and Ripon Formations. At the PPC Mount Stewart mine, the sediments of the Whitehill Formation, which host the various gypsum deposits, form part of a WNW-ESE synclinal fold structure (Almond, 2009). The 1:250 000 Port Elizabeth geological map combines the Prince Albert Formation, Whitehill Formation and Collingham Formation into one layer (light brown 'Pp' layer) and distinguishes these three from the overlying Ripon Formation (dark brown 'Pr' layer) as well as the underlying Dwyka Group (blue 'C-Pd' layer) (**Figure 3.5**). Several phases of deformation associated with the Cape Fold Belt (Cape Orogeny) resulted in large-scale structural controls on the geological setting of the study area. Forces from the south resulted in duplication and thickening of strata via numerous thrust faults occurring in four phases at approximately 277 Ma, 259 Ma, 246 Ma and 229 Ma (Halbich, 1983). This, together with the development of calcite and pyrite veins in the Cape Fold Belt source rocks, as described by Craddock *et al*. (2007), provide the original geological setting of the study area.

3.3.1 The Ecca Group, Lower Karoo Supergroup

The Karoo Supergroup covers approximately 300 000km^2 of South Africa and the deposition of its sediments occurred over a 100-million-year period, between 300 and 180 million years ago, beginning in a foreland trough during the subduction of the paleo-Pacific plate below the Gondwana Supercontinent. The depositional period continued until the break-up of Gondwana in the Mid Jurassic Period. Within the Karoo Supergroup, glacial deposits of the Dwyka Group underlie the marine deposited shale of the Ecca Group. The Beaufort Group, which is not part of this study, overlies the Ecca Group and the volcanic activity, which resulted in

the emplacement of the Drakensburg Group, marked the end of the deposition of the Karoo Supergroup (Geel *et al.*, 2013).

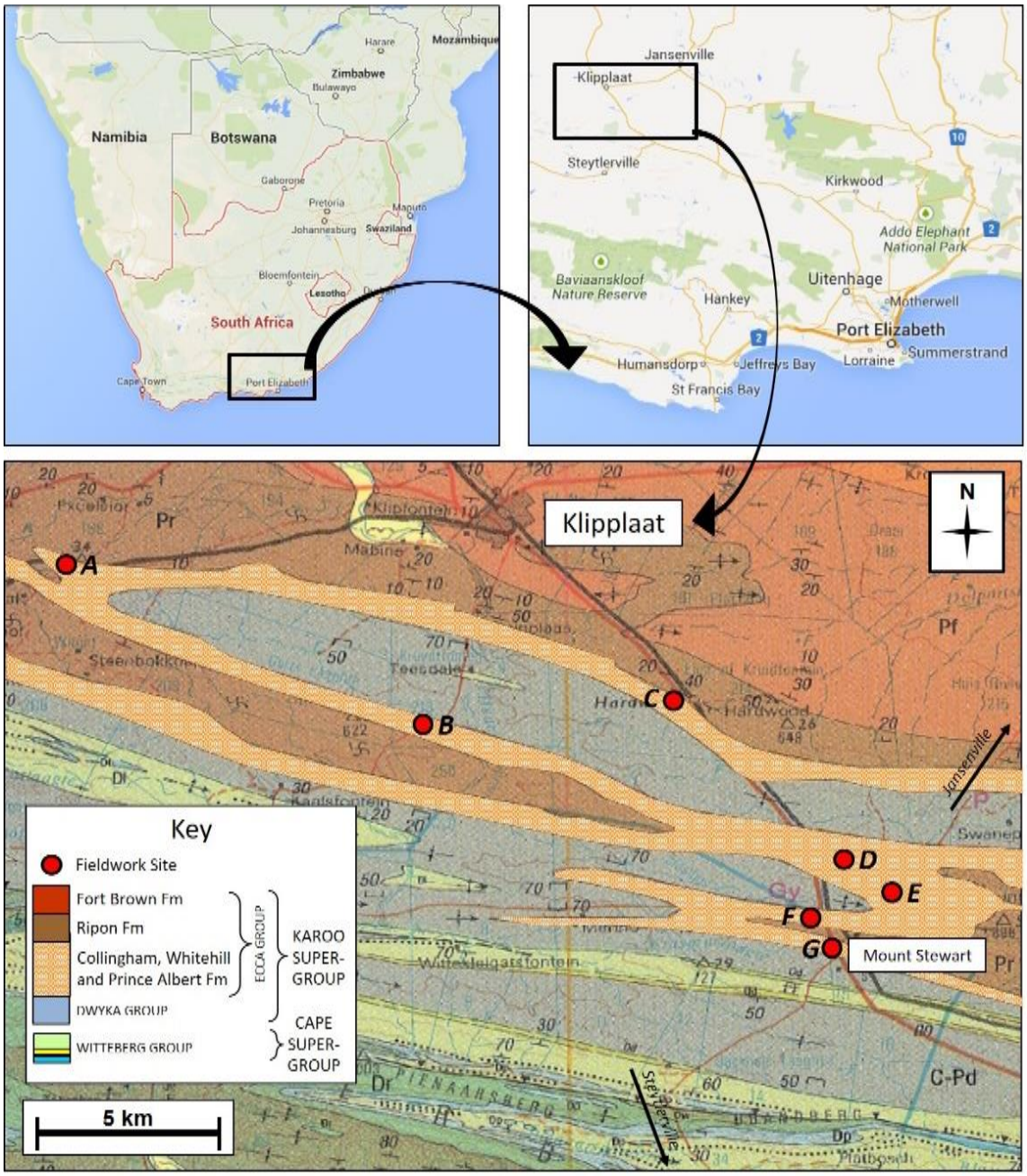

Figure 3.5: Geology of the study area as per the 1:250 000 Port Elizabeth geological map (from Rogers *et al.*, 1991).

The pre-erosion thickness of the Karoo Supergroup is 10km and this includes a range of depositional environments from glacial to deep marine, shallow marine, deltaic, fluvial, lacustrine as well as aeolian. This period of deposition also contained the transition phase from reptile to mammal organisms (Johnson *et al*., 1996). While most authors suggest that the Karoo Basin was closed, some suggest that it was open to the sea (e.g. Ryan, 1967). There is also debate as to

the characteristics of the source rocks, where De Villiers & Wardough (1962) suggest a source of greenschist metamorphic origin, Theron (1973) describe a granite source rock. The general consensus is that the sediment was derived from a landmass situated to the south and south-east of the basin (Kingsley, 1981). Bordy & Catuneanu (2002) provide petrographic analyses suggesting multiple source areas together with the reworking of the Basal Unit below. The granite and gneiss complex basement is the probable source area feeding the Ecca Group in the Central Kalahari Sub-basin (Nxumalo, 2001).

The Ecca Group consists of mudstone, siltstone, sandstone with minor conglomerate and coal in a clastic sequence. It covers most of the Permian Period (298.9 ± 0.2 to 252.2 ± 0.5 million years ago) and its maximum thickness is 3000m. The mode of origin for the sediment is that of deep-water and shallow-water marine turbidites as well as submarine fan deposits. It also includes volcanic ash deposits within the Collingham Formation that have been altered to Potassium-Bentonite. Coal mining within the Ecca sandstones and mudstones of the northern Karoo Basin, make it an important economic resource as some of the coal seams are up to 80m in thickness (Catuneanu *et al*., 2005).

The Ecca Sea was a shallow basin which contained brackish to fresh water (Almond, 2009). The Ecca Group deposition, within the Karoo Supergroup, included a series of river deltas which prograded from the south and south-east and deposited sediment on top of other material on the basin floor which was already present due to suspension and gravity settling (**Figure 3.6**). This basin floor mud later lithified into what is currently defined as the lower Ecca Group. Uplifting, due to Cape Orogeny (Permo-Triassic), gave rise to the source area towards the south. The sediment is likely to derive from low grade greenschist metamorphic rocks proven in the studies carried out by Nel (1962) and Theron (1967). Occurrences of quartzite, chert, quartz-mica schist and garnet provide more evidence to suggest a greenschist metamorphic origin from a homogeneous source area which was most likely a part of the Cape Supergroup. The deltaic sediments also overly turbidites which were initiated by slumping of the sediment at the delta fronts. At the end of the deposition of the sediments of the Ecca Group, the sea-level dropped and the delta front advanced to begin the deposition of the Beaufort Group (Kingsley, 1981). Within the lower Ecca Group, the Whitehill

Formation is underlain by the darker shale of the Prince Albert Formation and overlain by the alternating layers of shale and tuffaceous sediment of the Collingham Formation (**Table 3.2** and **Figure 3.7**).

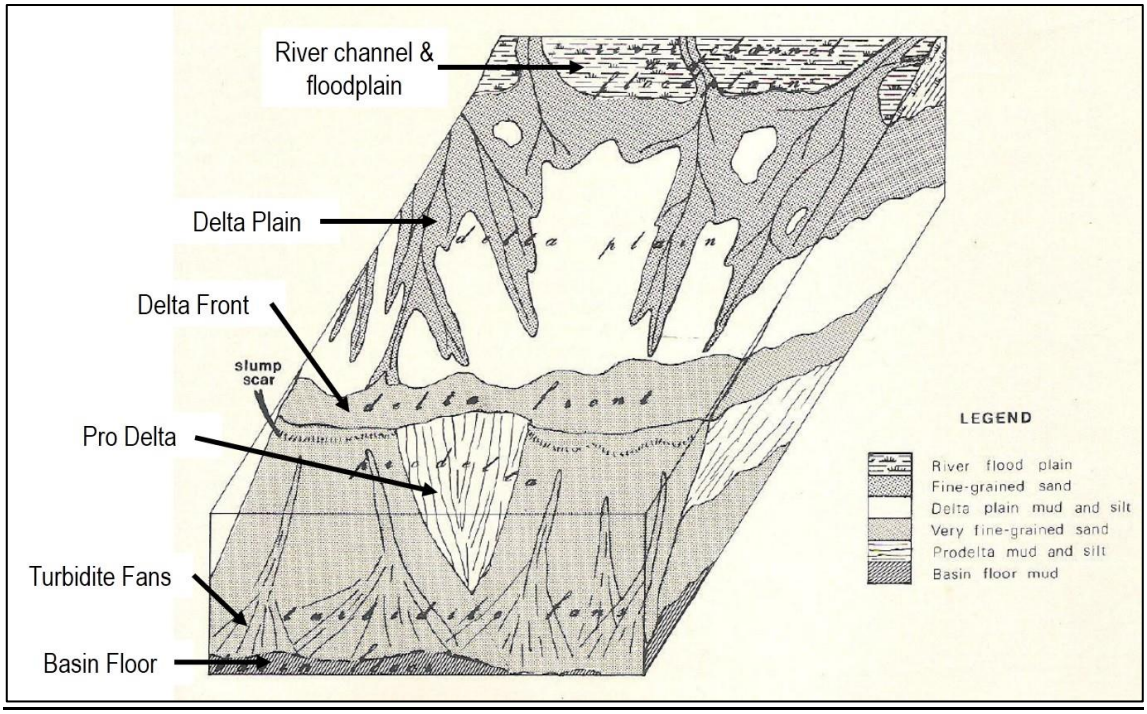

Figure 3.6: Sedimentation Model for the Ecca Group and Beaufort Group of the Karoo Supergroup (from Kingsley, 1981).

Table 3.2: Stratigraphy of the Lower Karoo Supergroup (from Geel, 2012).

Group	Formation	Lithology	Characteristics	Age
Ecca	Fort Brown	Sandstone, Shale	Rhythmites	≈258-262 Ma
	Ripon	Sandstone, Shale	Wave ripples, Glossopteris plant fossils, Rhythmites	≈262-270 Ma
	Collingham	Shale, Tuff, Chert, Siltstone, Sandstone	Thin beds of yellow tuff, Glossopteris plant fossils, Trace fossils	≈270-274 Ma
	Whitehill	***Shale, Dolomite***	***Weathers white, Pyritic, Surface gypsum, Dolomite Concretions***	***≈274-275 Ma***
	Prince Albert	Shale, Siltstone	Pyritic, Foraminifera Fossils	≈275-280 Ma
Dwyka		Diamictite, Shale, Sandstone	Fine grained, Small clasts	≈288-302 Ma

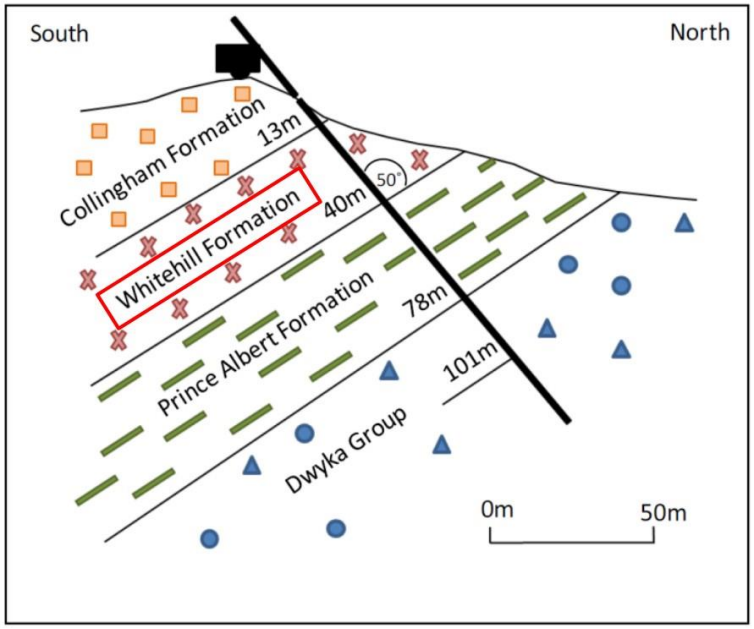

Figure 3.7: Drill hole SFT1 section showing the thicknesses of the Lower Ecca Group including the Whitehill Formation which is 27m thick (from Geel, 2012).

3.3.2 Whitehill Formation

Outcrops of the Whitehill Formation are present throughout most of the Karoo Basin and are characterised by the fact that the shale weathers to a white colour at the surface. The Whitehill Formation correlates with the Vryheid Formation in the Free State – both mid-Ecca in age although the Vryheid Formation contains minor coal-bearing seams. There is also a correlation with the Irati Formation in Namibia which extends into the Paraná Basin of South America. The age of the Whitehill Formation is Early Ufimian (late Permian), i.e. approximately 265 million years old (Visser, 1992). While the formation has no official member names, there exists a clear colour difference at a 76m outcrop in Loeriesfontein in the Northern Cape, as well as ferruginous concretions and a limestone marker (Cole and Basson, 1991).

In general, the thickness of the Whitehill Formation ranges from 10m to 80m (Cole and Basson, 1991). It is approximately 30m thick on average, but this is unreliable in areas where folding associated with the Cape Fold Belt has disturbed the strata. The deposition of the Whitehill Formation muds represents a change in the boundary conditions at a specific part of the basin. The lithology is split into 'deep-water' facies and 'shallow-water' facies. The former consists of chert and carbonate concretions while the latter has silty horizons, carbonate beds, but no chert. There are primary gypsum crystals, in the form of lenticles, associated with

the carbonate beds, but these have been replaced by dolomitic material in some places. The overlying Collingham Formation contains the 'Matjiesfontein chert', a dark grey, white-weathering chert layer which acts as a useful marker bed layered 10m above the contact with the Whitehill Formation (Visser, 1992).

A holostratotype of the Whitehill Formation, showing a 53m section of the shale, is documented at a railway siding near Laingsburg in the Western Cape (**Figure 3.8**). The lithology is divided into mudrock (which makes up approximately 80%) and rhythmite (up to 20%), but the latter mainly occurs north of Boshof in the Free State. The mudrock is carbonaceous, pyritic and ferruginous and includes dolomitic concretions which can be up to 1m in thickness. It also includes tuffaceous layers which are usually less than 10cm thick. The rhythmite contains fine-grained, grey sandstone as well as cherty beds less than 10cm thick which are only found in the southern Karoo. In general, the strata were formed from suspension settling of mud in the Karoo Basin which were sufficiently oxygenated and played host to free-swimming and benthic fauna. Within the deposited sediment however, anoxic conditions prevailed as is inferred by the rarity of bioturbation and the presence of pyrite and carbon. The upper boundary separating the Whitehill Formation from the Collingham Formation is sharp and conformable with a distinct decrease in organic material above. The boundary with the Prince Albert Formation below is gradual, but towards Kimberley and Welkom, the Whitehill Formation and Prince Albert Formation shales are indistinguishable from one another (Cole and Basson, 1991).

The shale of the Whitehill Formation, which is 21m thick at the Ecca Pass road-cutting (Kingsley, 1981), are thinly laminated, black, carbonaceous and pyrite-bearing with a maximum of 17% organic carbon. They were deposited in a young, under-filled foreland basin by means of suspension settling and incurred anoxic conditions at the bottom of the basin. Less anoxic conditions were found in the shallower marginal areas of the basin (Johnson *et al.*, 2006). Sediments of the Whitehill Formation are believed to have been deposited on an unstable marine slope, where slumping would have taken place. Décollement folding and associated faulting are a common feature of the Whitehill Formation (Kingsley, 1981).

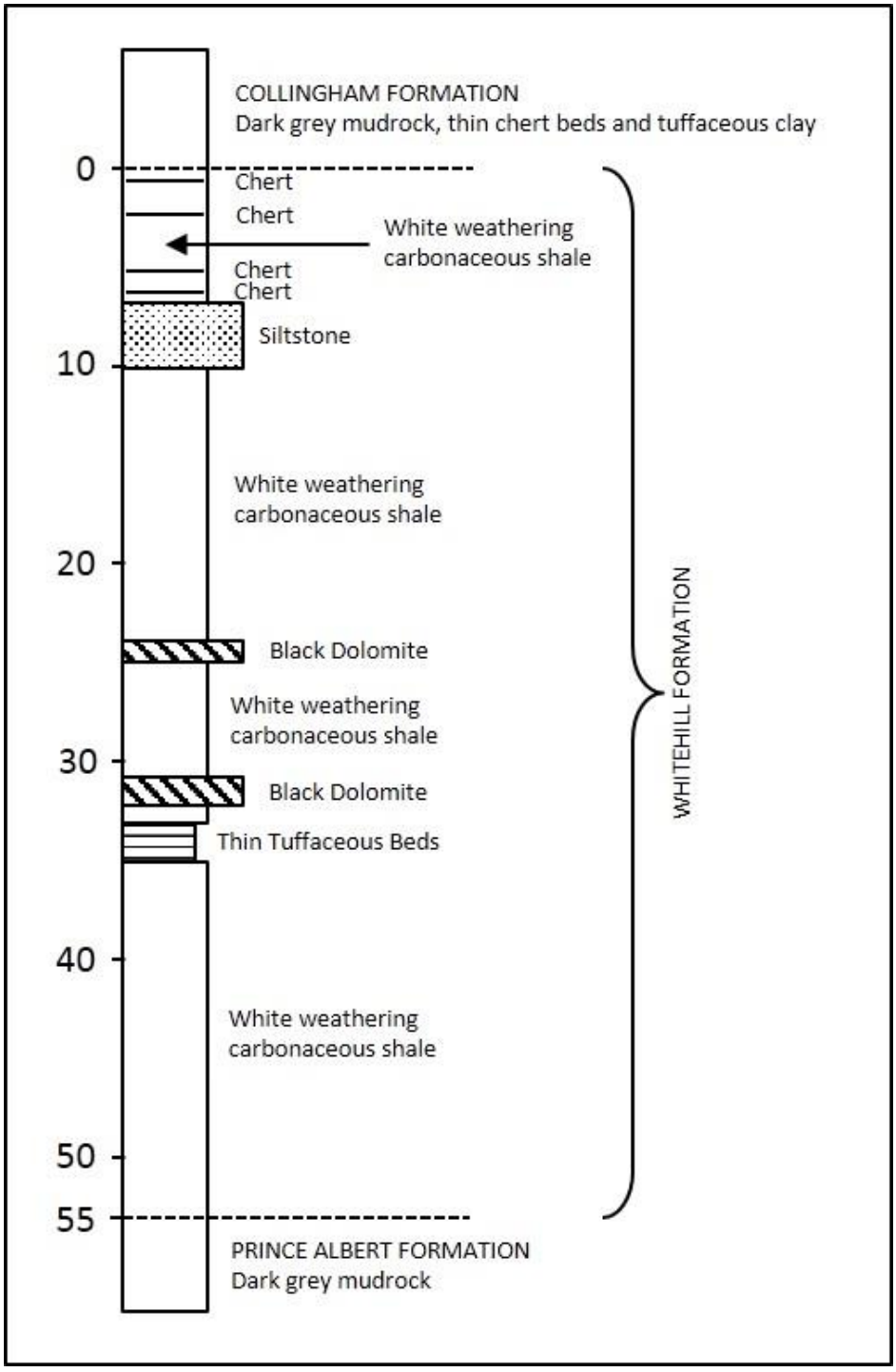

Figure 3.8: Holostratotype of the Whitehill Formation located near Laingsburg in the Western Cape (after Cole and Basson, 1991).

The Whitehill Formation is conformably overlain by the Tierberg Formation in the Ceres and Tanqua Karoo areas. In subsurface, it can be differentiated from the overlying and underlying strata by its dark black colour (compared to dark grey of the Prince Albert and the Collingham formations) and by its higher carbon and pyrite content (Cole and Basson, 1991). The upper strata of the Whitehill Formation are rich in pyrite and there are chert layers and chert lenses located at

irregular intervals throughout the formation. Du Toit (1954) noted that the carbon content ranges between 12% and 14%, but Cole and Van Vuuren (1978) calculated it to be 3.3% ± 2.1 and Geel *et al.* (2013) mention 4.5% total organic carbon (TOC) of shale within the Whitehill Formation in the area near Wolwefontein in the Eastern Cape. The shale of the Whitehill Formation also has the lowest quartz/mica ratio within the Ecca Group, as well as the highest sulphur weight percentage measured in terms of pyrite and oxidized forms such as gypsum, barite and organic sulphur (Geel *et al.*, 2013).

The fossil *Mesosaurus tenuidens* (**Figure 3.9**) is found within the shale of the Whitehill Formation (De Ville Wickens, 1996). These and other reptile, fish and crustacean remains are preserved in the upper strata of the formation, while insect wings, leaves and wood are preserved in the central part of the Whitehill Formation. This suggests that climatic conditions during the initial deposition period of the succession were cold whilst the existence of fossils in the later depositional period suggest a warmer climate (Cole and Basson, 1991). This formation also contains potential shale gas reserves between 32 and 485 trillion cubic feet (Decker and Marot, 2012). The shale of the Whitehill Formation has been intruded by dolerite sills and dykes in the northern part of the Karoo Basin (Cole and Basson, 1991).

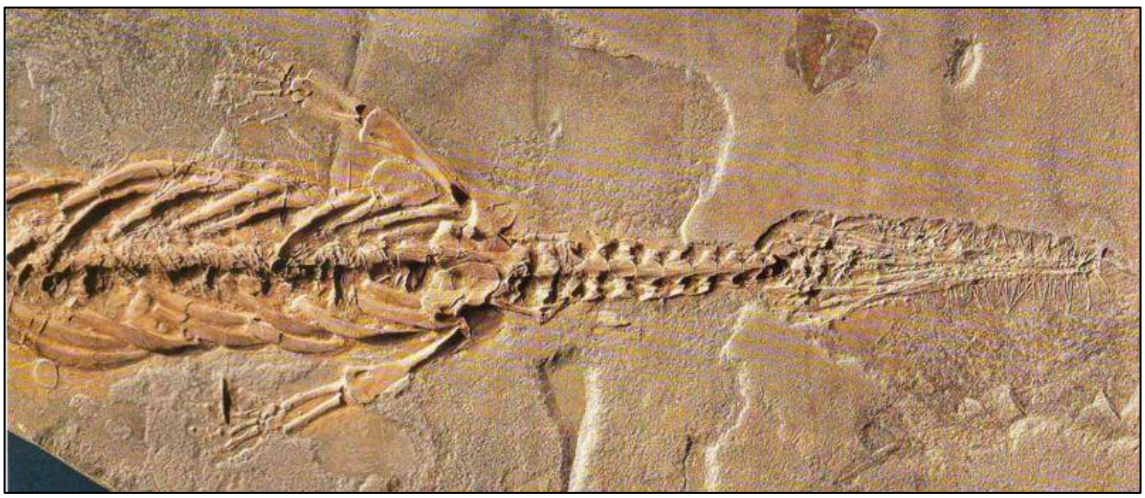

Figure 3.9: Fossil of *Mesosaurus tenuidens* within the shale of the Whitehill Formation near Kimberley (from MacRae, 1999).

3.3.3 Gypsum, $CaSO_4 \cdot 2H_2O$

Gypsum is a hydrated calcium sulphate with a monoclinic crystal system and precipitates as tabular, massive or granular crystals. It exhibits various colours due to impurities, but is naturally colourless with a white streak and a pearly lustre. It has perfect cleavage parallel to its 001 Miller's Index plane (similar to mica), referred to as 'pinacoidal' cleavage, and often forms swallowtail twins and rosettes (desert roses). Gypsum-rich evaporite commonly forms in salt deposits and is therefore classified as a 'chemically-formed' sedimentary rock (Lurie, 2004). It also has a biaxial positive optical sign and two cleavage planes (Visser *et al.*, 1963).

Cement manufacture, 'plaster of Paris' and gypsum board used in construction constitute the main uses of gypsum. In South Africa, gypsum is used as a retarder to stabilize the settling time of cement (Oosterhuis, 1998). While gypsum is generally unsuitable for outdoor use due to its solubility in water, it is still used in a variety of sectors (**Table 3.3**). The global production of gypsum has more than doubled since 1994, with an increase from approximately 101 million tonnes in to 261 million tonnes in 2015, China is the leading miner of gypsum accounting for almost half of the total gypsum mine production in 2015 (130 million tonnes). Other far lesser, yet significant, producers are Iran (16 million tonnes), United States (15.2 million tonnes), Turkey (12.6 million tonnes) and Thailand (11.2 million tonnes). The production of gypsum in South Arica has levelled out since 2005 which an average of 556 000 tonnes between 2005 and 2013 (U.S. Geological Survey, 2017).

The global demand for gypsum is largely dependent on the economic strength of the construction industry within each country and only 20% of all gypsum is exported on the global market (U.S. Geological Survey, 2017). A number of countries rely on the manufacture of synthetic and recycled gypsum in order to meet their domestic demands (Crangle, 2017). Synthetic gypsum production is a developing industry in South Africa, especially with the demand for gypsum increasing due to the proliferation of a number housing development projects (Oosterhuis, 1998).

Table 3.3: Main uses of Gypsum (after Oosterhuis, 1998).

Application of Gypsum	Description
Cement	Retarder in Portland cement.
Plaster Board	Provides dry linings to masonary walls, ceilings, partitions, fire protection as well as noise and sound insulation.
Medicinal	'Plaster of Paris' bandages for splinting of bone fractures, rest splints and body support casts. Also used for dental moulds and casts.
Fertiliser	Low-grade gypsum dissolves quicker than agricultural lime, both of which are used to neutralise acidic soils.
Paint	High-grade gypsum used as a base in cold-water paints.
Paper	Used as a filler in certain writing paper and boards.
Other	Insecticides, pesticides, textiles, food and beverage ingredient, lighting-matches and chalks

There is a surplus of information regarding the industrial function of gypsum, but the literature referring to its deposition and occurrence is limited, especially that of South African gypsum deposits. Geel *et al.* (2013) refer to the gypsum as originating from the oxidation of subaerial pyrite which results in the distinct white-weathering of the otherwise black shale of the Whitehill Formation. Almond (2009) states that the pyrite was precipitated within the oxygen-poor muds within the Ecca Sea.

Gypsum is flexible, but not elastic, has a hardness of 2 on the Mohr's scale (meaning it can be scratched with a fingernail) and has a specific gravity of 2.3. It is slightly soluble in water (1 part in 495), soluble in hydrochloric acid and insoluble in sulphuric acid (Visser, 1963). Its varieties include alabaster, desert rose, gypsite, rock gypsum, satin spar and selenite. Hemihydrate, $2CaSO_4 \cdot H_2O$, is formed from gypsum when three-quarters of its water content is removed during heating up to 160^0C. All of gypsum's water is removed between 480^0C and 700^0C producing anhydrite, $CaSO_4$, also referred to as 'insoluble anhydrite' or 'dead-burned gypsum' (Oosterhuis, 1998). A minimum of 70% $CaSO_4 \cdot 2H_2O$ is needed to classify a material as gypsum (Brabers, 1976). The theoretical content of gypsum is 32.6% calcium oxide (CaO), 45.5% sulphur trioxide (SO_3) and 20.9% water (H_2O) with very little variations (Visser *et al.*, 1963).

While gypsum is commonly known to form as a chemical precipitate from highly saline marine water, in South Africa it predominantly forms near the surface in clay, in veins or as powders in discontinuous horizontal geological layers located several hundred kilometres from any marine area. Prerequisites for gypsum formation include the supply of calcium and sulphate to a zone of weathering, restricted drainage such as a pan, a clay layer within the drainage area and an

arid climate where evaporation exceeds precipitation (Brabers, 1976). Gypsum commonly occurs within 10m of the surface in 'gypsum crusts' which contain between 15% and 95% gypsum and are approximately 5m thick. There are three types of crust: horizontally bedded crusts, surface crusts and non-bedded surface crusts. The latter occurs when surface deposits become consolidated by meteoric water which contains the necessary gypsum-forming ions (Ca^{2+} and SO_4^{2-}). The process of gypsum crystallization is affected by the salinity, temperature, pH and organic matter of the host water (Oosterhuis, 1998).

The mineralogy and geochemistry of carbon-rich shale is highly susceptible to weathering. This takes place via the oxidation of pyrite and the dissolution of carbonate (Chermak and Schreiber, 2014).

$$2FeS_{2\,(s)}\ (\text{pyrite}) + 7O_{2\,(g)} + 2H_2O_{(l)} \rightarrow 2Fe^{2+}_{(aq)}\ 4SO_4^{2-}_{(aq)} + 4H^+_{(aq)} \quad (1)$$

$$CaCO_{3\,(s)}\ (\text{calcite}) + H^+_{(aq)} \rightarrow Ca^{2+}_{(aq)} + HCO_3^-{}_{(aq)} \quad (2)$$

The oxidation of pyrite results in a pH drop and produces an acidic aqueous solution (1) which will neutralize alkaline minerals such as calcite resulting in dissolution of carbonate (2). In order for the solution to be neutralized, 400g (4 mol) of calcite is required per 119.85g (1 mole) of pyrite (Chermak and Schreiber, 2014). The carbonate dissolution results in increased porosity in the sediments providing a suitable host for the formation of authigenic gypsum in the presence of meteoric water (Pirlet *et al*., 2010).

$$SO_4^{2-}_{(aq)} + 2Ca^{2+}_{(aq)} + 4H_2O_{(l)} \rightarrow 2CaSO_4{\bullet}2H_2O_{(s)} \quad (3)$$

A solution which becomes oversaturated with calcium and sulphate in the presence of water will result in the precipitation of gypsum crystals (3). Gypsum crystals are often seen on the surface of carbonaceous shale drill core as a result of the drying of pore water (Pirlet *et al*., 2010). The calcium component in gypsum within the study area is likely to be derived from the limestone and dolomite strata. Pyrite is common in the Whitehill Formation as well as the lower half of the Collingham Formation and thus provides the necessary sulphur content within the study area (Geel *et al.*, 2013).

In South Africa, gypsum has been exploited since 1913 where 121 tons was mined in the Northern Cape Province. There is an estimated total reserve of 94 million

tonnes of gypsum in the country with all deposits closely associated with the Whitehill Formation except for negligible alluvial deposits along the western coastline. The gypsum located in the Steytlerville-Jansenville gypsum field is of medium grade at an average deposit thickness of 37cm consisting of powdery $CaSO_4 \bullet 2H_2O$ at an average of 65% (Fockema *et al.*, 1962). Many mines in this area have been abandoned due to transportation costs and varying gypsum grades. Gypsum prospecting had taken place at Baroe station since 1923, but large-scale production only began in 1952. At the time, the largest deposit was 44,000 tons with a total estimated reserve of 85,300 tons. It is associated with the isoclinal folding of the shale horizons within the Whitehill Formation, but good grades generally occur in flat areas where it is overlain by a thin soil overburden (Visser *et al.*, 1963).

3.3.4 Dolomitic Concretions

Shale of the Whitehill Formation contains dolomite, especially near the base of the formation. While the shale particles are tightly packed, the dolomite shows greater porosity under a scanning electron microscope (SEM). The porosity of the dolomite units is 2.9%, while the shale is 1.57% (Geel *et al.*, 2013). This ‘boudinage’ structuring is often observed as large dolomitic concretions. McBride *et al*. (2003) provide an understanding of several aspects regarding concretions including their size, spacing, structure and chemical composition, which shows decreasing carbonaceous material from the edge to the centre of the concretion. The term “septarian” structure is used to describe the cracked nature of the surface of the concretions and “intergranular volume” (IGV) is used to determine stages of cementation of the concretion. Concentric layering can help determine growth rates of concretions (McBride *et al.*, 2003).

Abdel-Wahab and McBride (2001) provide detailed descriptions of calcite-cemented concretions found in the sandstones of Egypt with interpretations relating to their dimensions, distribution and interactions. The concretions can be orientated in an oblate or prolate direction, with the latter being uncommon. Most of the concretions are solitary, but there are also cases where two or more separate concretions have coalesced (**Figure 3.10**). Marine carbonate shells are the likely source of concretionary cement.

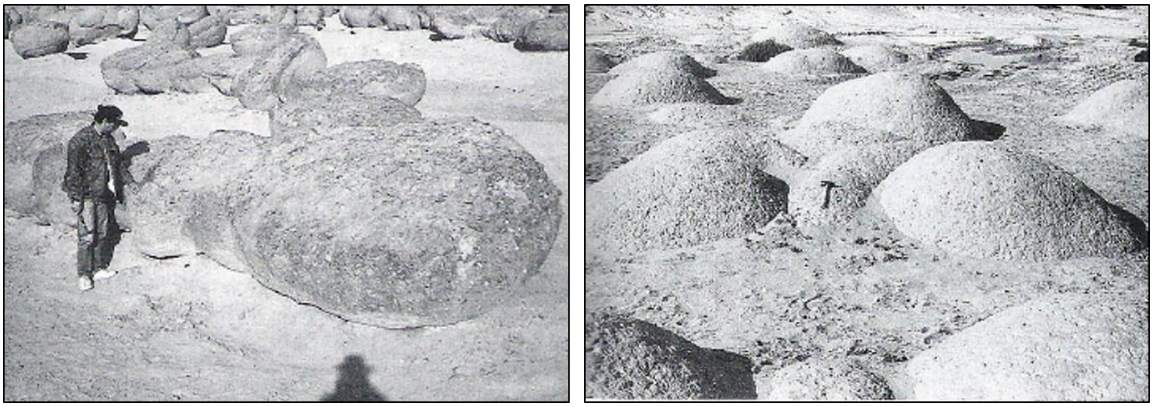

Figure 3.10: Coalesced concretions of the Temple Member, Qasr El Sagha Formation, Egypt (from Abdel-Wahab and McBride, 2001).

Concretionary growth occurs at a shallow depth mixed with meteoric water ranging from 10°C to 20°C. Separate spheroidal concretions are formed when carbonate shells are uniformly deposited at widely distributed nucleation sites and the occurrence of concretions at a uniform depth within a stratigraphic unit is due to the concentration of marine shells on a particular bedding plane. Large concretions can be formed in less than 20 million years due to large concentrations of carbonate shells, widely spread nucleation growth sites as well as a stable hydrological cycle. A concretion with an aspect ratio of less than 1.5:1.0 is described as ‘equant or circular’ and is ‘elongate’ at greater than 2.5:1.0. Concretions are ‘subequant or subcircular’ when the aspect ratio is between 1.5:1.0 and 2.5:1.0 (**Figure 3.11**). Carbon and oxygen isotopes within the concretion generally become more depleted towards the edge of the concretions. Iron oxide is formed by the replacement of sulphide in pyrite.

The conventional concentric model for concretionary growth is adopted by many authors, but it may not hold true for all concretions, especially those found in mudrock deposits. Many of these concretions are complexly zoned and exhibit cement from late-stage precipitation not only on the outer concretion, but also throughout the concretion, in and amongst the early-stage precipitated cements. This occurred due to the incompletion of early-stage cementation which left behind a porous and permeable inner concretion that could be filled with late-stage precipitated cement (Mozley, 1996). The presence of tilted concretions in the Rhinestreet black shale, western New York State, suggests that there was early diagenetic growth within unconsolidated sediment. This is also supported by differential compaction of the host sediment which surrounds the concretions.

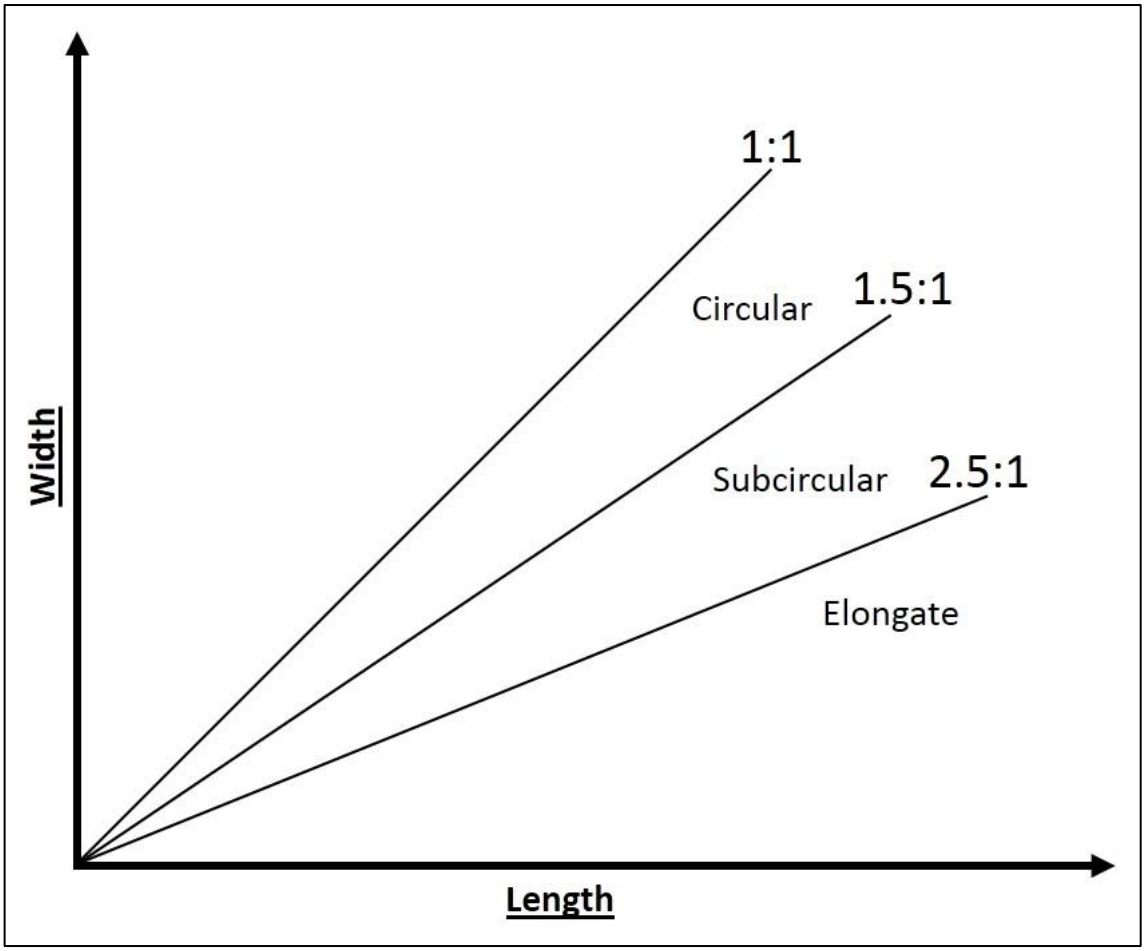

Figure 3.11: Cross-plots or 'aspect ratio' diagrams of concretion dimensions (from Abdel-Wahab and McBride, 2001).

The 'cardhouse' clay fabric is preserved around the concretion, suggesting rapid growth within a metre of the sea floor. For concretionary growth to continue, a pause in deposition is required to allow the precipitation of carbonate at this shallow depth. Once sedimentation is resumed, burial and compaction causes concretionary growth to cease. The two Rhinestreet concretionary horizons vary in thickness and concretion size and this is due to differences in the periods of non-sedimentation as well as difference in reduction of the rate of sedimentation. There are distinct similarities between the Rhinestreet Shale and the shale of the Whitehill Formation, such as the dark-grey to black colour, the 60-80m thickness, the presence of pyrite and concretions and the fact that they are overlain and underlain by grey shale of lesser total organic carbon (**Figure 3.12**). Septarian fractures extend outward from the centre of the concretions and pyrite content is highest at the rim of the concretion as well as within these fractures. Anaerobic bacterial reduction of organic matter is partially responsible for the origin of the

concretionary carbonate, as is suggested by the depleted carbon isotopes towards the edges of the concretions (Lash and Blood, 2004).

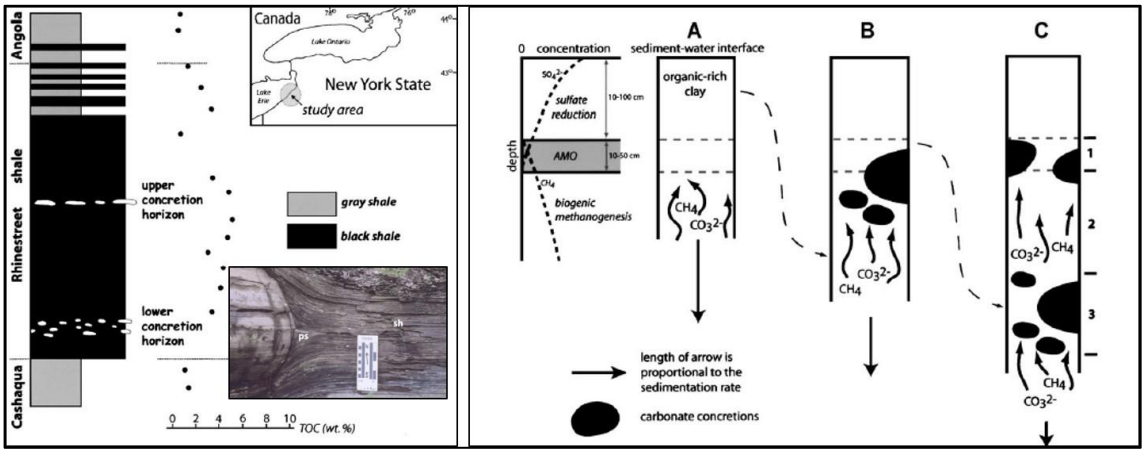

Figure 3.12: The Rhinestreet shale, New York State, USA: Left: Stratigraphy of Rhinestreet shale and surrounding lithology; Insert: 'Cardhouse' clay fabric surrounding a concretion; Right: Concretionary growth supported by anaerobic methane oxidation (AMO) within a specific zone when sedimentation is slow enough as in column B and C (from Lash and Blood, 2004).

4. METHODS AND MATERIALS

The methods and materials used in this dissertation focus mainly on techniques applied in fieldwork (mapping and data collection), and the laboratory (map compilation, characterising lithological and geomorphic features, structural data processing, thin-section descriptions, and XRF and SEM analyses).

4.1 Fieldwork

Due to the extensive nature of the Whitehill Formation throughout South Africa, the project area needed to be confined to an area which would satisfy the requirements of the study. Restrictions were therefore placed on the number of shale outcrops that could be analysed with regard to structural orientation. The quality of the outcrops within the project area are generally poor due to the weathered nature of the Whitehill Formation. This had a limiting effect on the structural data obtained from the Whitehill Formation rock outcrops. However, the 'Matjiesfontein chert' of the Collingham Formation not only served as a good marker horizon to locate the Whitehill Formation, but also proved to be useful for obtaining compass readings as it is not prone to erosion and thus can be accessed for geological compass readings. The chert layer is also relatively continuous and, in most cases, provides the necessary representation of the general strike and dip of the large-scale fold systems located within the project area. Bedding orientation readings were obtained using a Geosurveyor Compass Clinometer (Geology Superstore, 2012). The readings were taken on the chert as well as any shale layer which exhibited a distinct bedding plane. The azimuth and dip values (in degrees) were recorded manually for each of the bedding readings. In addition to bedding planes, orientation readings pertaining to faults, joints and lineations were also collected. All compass readings were corrected for magnetic declination, which is 26° west for the study area.

4.2 Data Management

On completion of the manual recording of bedding, fault, joint and lineation readings, the data was captured into a Microsoft Excel spreadsheet and arranged according to the localities visited within the project area (refer to **Appendix C**). Filters were applied to the data in order for it to be summarized per the

requirements of the location, bedding orientation (north-dipping or south-dipping), fold class (macro-scale fold or meso-scale fold) or fold type (e.g. anticline or syncline). For example, a filter could be inserted over the data so that it shows only the structural data pertaining to the macro-scale folds. This is important with regard to classifying the fold systems into separate domains. The data was later exported as a text file to be used in the chosen stereonet programme.

4.3 Stereoplots

The “Stereonet 8” software was used to produce stereoplots for this study. This programme served as a useful and more accurate alternative to manually drawing stereoplots using a stereonet and tracing paper. The software allowed for the text file (.txt) saved from Microsoft Excel to be imported and saved as a stereonet file (.stnt). The programme allows the user the option of displaying the data as planes using the dip direction (azimuth) and dip values assigned from the database. Once the bedding planes are displayed on the stereonet, the “points to a plane” option can be selected. The points are then contoured using the “1% Area” setting which enables the user to view the area of the graph where most the points to the bedding plane have accumulated. The middle of the ‘highest’ contour is therefore used as the average point to plane for that set of bedding orientation data.

The stereonet programme was often used to represent a fold, generally resulting in two ‘high points’ represented by the contoured poles to plane. This represents the average azimuth and dip of the two limbs of that particular fold. In order to obtain values for the orientation of the axial plane of the fold, the “Calculations” option is selected, followed by the “Axial Plane Finder” option. This opens a new window into which the user can insert the trend and plunge of the two ‘high points’ by clicking and selecting them from the contoured stereoplot. The Stereonet 8 program then calculates the trend and plunge of the fold axis, the strike and dip of the axial plane as well as the interlimb angle between the two folds.

The program automatically displays the axial plane on the stereoplot. In this project, the axial plane on the stereoplot always intersected the two high points of the contour plot – as would be expected when dealing with symmetrical folds. To display the fold axis on the stereoplot, a “New Data Set” in the form of a “Point” was selected from the programme menu. The trend and plunge obtained during

the axial plane calculation can then be typed manually into this dataset. The fold axis is then displayed as a point on the stereoplot and, as expected, it is located along the axial plane. The 1% Area contour is then unselected and the remaining points to plane, axial plane and fold axis line (represented as a point) can then be exported as a JPEG image. These images were then labelled using Microsoft PowerPoint.

In order to compare different folds, a separate stereonet was compiled to display the axial planes and fold axes of the folds as one stereoplot. This was achieved by importing a dataset from Microsoft Excel which consisted of only the axial plane and fold axis data from the original stereoplots. The same methods were then used to display this data and allowed for closer comparison of the various folds in the project area.

4.4 Analysis of core from the Whitehill Formation

The SFT2 borehole, which was core-rock drilled in 2011 between Wolwefontein and Jansenville in the Karoo, intersects the entire lower Ecca Group sequence including the Whitehill Formation. The borehole, which was sited as part of the 2012 shale gas venture, is located approximately 45m east of the study area, It is situated along the strike of the Whitehill Formation where minor surface gypsum deposits were identified, and is therefore relevant to this study. It is the only source of unweathered rock readily available for analysis which provides a meaningful representation of the complete sequence of the Whitehill Formation in the regional area. The Whitehill Formation is located approximately between 190m and 220m below the collar position of the SFT2 borehole and therefore consists of reasonably unweathered shale rock which can be used for the analysis of pyrite and calcite components relevant to the project. The Whitehill Formation, as well as its upper and lower contacts with the Prince Albert and Collingham Formation respectively, were logged in detail. Sampling positions were then chosen within the section that was logged.

4.4.1 Core Logging

Logging of the SFT2 core was carried out initially to determine lithological changes within the sequence and to outline the relative increases or decreases in carbonate material as well as pyrite mineralisation. A tape measure, Munsell

Colour chart, streak tile and 5% dilute hydrochloric acid (HCl) were the main materials required. The marker blocks provided by the drillers were used as reference for determining the depth within the borehole. Any core losses measured were assigned to areas where distinct drilling loss could be observed or otherwise to an area of broken or weathered material. All distinct colour changes were noted throughout as well as any changes in streak colour. Any contacts (sharp or gradual) were assigned to areas of relatively greater or lesser hydrochloric acid (HCl) effervescence as well as noticeable changes in pyrite content on a mesoscopic scale. A borehole log was then drawn up as a database to display the recorded changes (refer to **Appendix A**). Any changes in lithology were logged together with changes in colour, texture and weathering. More importantly, however, the changes in visible calcium carbonate and pyrite were logged and were assigned an approximate percentage of the total visible shale. Any noticeable folding or faulting was logged separately as well as areas which may have contained nodules, volcanic tuff or thick pyrite, calcite or quartz veins. Photographs were taken of core which exhibited distinct folding, faulting, jointing as well as calcite veining, pyrite-rich zones as well as other notable features. Photographs were also taken of each core box both of the dry core as well as the wet core.

4.4.2 Core Sampling

Samples were initially designated at 5m intervals throughout the Whitehill Formation. However, it was later found that the pyrite and carbonate distribution would not be reflected by a relatively small sample over a 5m depth. To accommodate for this discrepancy, samples were then taken at specific areas within the drill core where distinct changes in carbonate and pyrite content could be interpolated at the mesoscopic scale. Samples were also taken on other distinguishable features – the cherty shale layer identified as the ‘Matjiesfontein chert’ is one such example. A total of 21 samples were assigned numbers according to their depth within the borehole. The prefix “SFT2“was used for the sample numbers in order to refer to the SFT2 drill core. The samples were therefore given numbers (from 1 to 21) with SFT2-1 being the shallowest sample taken from the borehole (at 189.95m) and SFT2-21 being the sample taken at the deepest point (228.51m).

4.5 Petrographic Light Microscopy

In order to better understand the mineralogy associated with the shale of the Whitehill Formation within the study area, thin section analysis was required. This would allow, to some extent, the determination of minerals included in the samples, but more importantly, would provide a better understanding of the textural relationships between the rock forming minerals, especially those concerning pyrite and calcite, which are the main minerals required to form gypsum. To display the minerals and textures on a microscopic scale, thin slices of rock were cut and reduced to 1mm thickness, polished and mounted as thin-sections on a 3mm glass base. Resin had to be used to consolidate many of the samples due to their fractured nature and tendency to break apart. A Leica DM EP polarising microscope was used for the analysis and a digital camera (Canon PowerShot S40) was connected via an adapter (Leica Dc 150) in order to obtain photographs of the thin sections under the optical microscope.

4.6 SEM Analysis of SFT2 Core Samples

Samples from the SFT2 borehole core were selected for Scanning Electron Microscope (SEM) analysis to obtain elemental data regarding the shale of the Whitehill Formation by means of EDS (Energy Dispersive Spectroscopy). The SEM would also provide an idea of the textural relationships between the gypsum-forming minerals (pyrite and calcite) as well as textural relationships between these and other minerals contained in the lithology of the Whitehill Formation at a microscopic scale.

Samples were prepared by cutting rectangular blocks (approximately 10cm by 10cm by 5cm) from the core samples. In general, the same specimens which were used in the slides for thin-section analysis were also used for the SEM samples. The 8 blocks which were cut were then sent for preparation at the NMU Centre for High Resolution Transmission Electron Microscopy (CHRTEM) where they were placed in a resin compatible with the SEM. Samples selected for SEM analysis included Sample 2, 6, 9, 14, 15, 19 and 21. Sample 14 was divided into two SEM samples (namely 14a and 14b) to allow for an analysis on a pyrite rich and pyrite poor sample from the same position within the Whitehill Formation lithology.

Samples were then analysed under the SEM and, using the EDS, mineral identification was conducted through the recognition of elements. Several views were chosen using the SEM for EDS analysis to be conducted. Due to the high carbon content of the samples as well as in the resin used to prepare the samples, elemental carbon could not be analysed quantitatively.

4.7 XRF Analysis of gypsum-rich shale

In order to analyse the quality of the gypsum deposits within the project area, X-Ray Fluorescence (XRF) analysis, made available by PPC Cement, was included in this study. In most cases the best method for comparing gypsum quality within a project area would be to set up a grid and have all samples located within the separate blocks of the grid tested. However, due to budget restrictions as well as the specific locality of gypsum deposits, the PPC Cement and/or SA Lime Eastern Cape sampling was used to supplement this section. Samples are therefore randomly selected from areas which are visibly gypsum-rich. These samples were sent to the laboratories listed below who analysed, amongst others, the CaO and SO_3 content of the sample. Most laboratories provided a calculated $CaSO_4$ value.

The laboratories used to undertake the XFR analyses included NviroTek Labs, Nitrophoska (Edms) and PPC Cement laboratories. The results of the XRF analyses were displayed in a different format depending on the preference of each laboratory. For example, NviroTek Labs and Nitrophoska (Edms) would provide the calcium (Ca), magnesium (Mg) and sulphur (S) elemental percentage, while PPC Cement laboratories would provide the proportions of calcium oxide (CaO), magnesium oxide (MgO) and sulphates (SO_3). In order to standardise the results, the elemental percentages (e.g. Ca, Mg and S) were converted to their respective oxide states. This was done by means of conversion factors set out in the 1983 Farm Chemicals Handbook which uses International Atomic Weights, based on Carbon-12, for converting the elemental percentages. In a few analyses, the lab report did not provide a percentage of gypsum contained in the sample. To obtain this value, the elemental sulphur percentage (% S) was converted to gypsum (% $CaSO_4 \bullet 2H_2O$) using the multiplication factor of 5.3696 as provided by the Farm Chemicals Handbook (1983).

4.8 Concretions

The size and spacing of the concretions can provide clues as to the geological setting in which they were formed. For the concretions that were fully exposed in old road quarries, the length, width and height dimensions could be measured. Most of the *in-situ* concretions, however, could only be measured along two dimensions. The method used to measure concretion spacing is from centre to centre (McBride *et al*., 2003). Concretion dimensions are important as well as petrographic features which can be determined by SEM, XRD, optical, stable isotope and trace element analysis. For this project, only concretion dimension data and SEM data were analysed. 'Aspect ratio' and 'distance to centre' graphs are used to describe the concretion dimensions, while rosette diagrams are used to show the concretion orientations (Abdel-Wahab and McBride, 2001).

5. RESULTS

In this chapter the results of borehole core analysis, fieldwork and laboratory studies are presented. The includes a detailed log of the SFT2 borehole which was drilled approximately 45km east of the project area as well as the petrographic and Scanning Electron Microscope (SEM) analyses which were conducted on samples obtained from the drill core rock. Additional X-Ray Fluorescence data from the study area is included in this chapter to provide additional insight into the characteristics of the gypsum deposits within the study area. This chapter will also describe all structural orientation data collected from the seven sites (Site A to Site G) located within the study area, representing bedding plane data, joint orientation data as well as folding and faulting structures. Gypsum and concretion occurrences from each site will be described and analysed in detail.

5.1 Study Sites, Lithological Descriptions and Gypsum Deposits

Fieldwork was undertaken at seven different locations within a 12km radius of the town of Klipplaat. The sites have been labelled A to G with the associated farm names and numbers (**Figure 5.1**). Gypsum deposits have been identified at all of these fieldwork sites, but have a wide variety of occurrences, from small gypsum veins, to massive mineable gypsum reserves in highly weathered shale. Each site was useful to the study for various reasons. While some study sites were used as locations for structural analysis due to the presence of unweathered outcrops with measurable orientation planes, others were used for lithological descriptions and to better understand the occurrence of gypsum. In general, the study sites with abundant gypsum were not suitable for structural analysis and sampling as the shale was weathered and did not exhibit any measurable bedding planes.

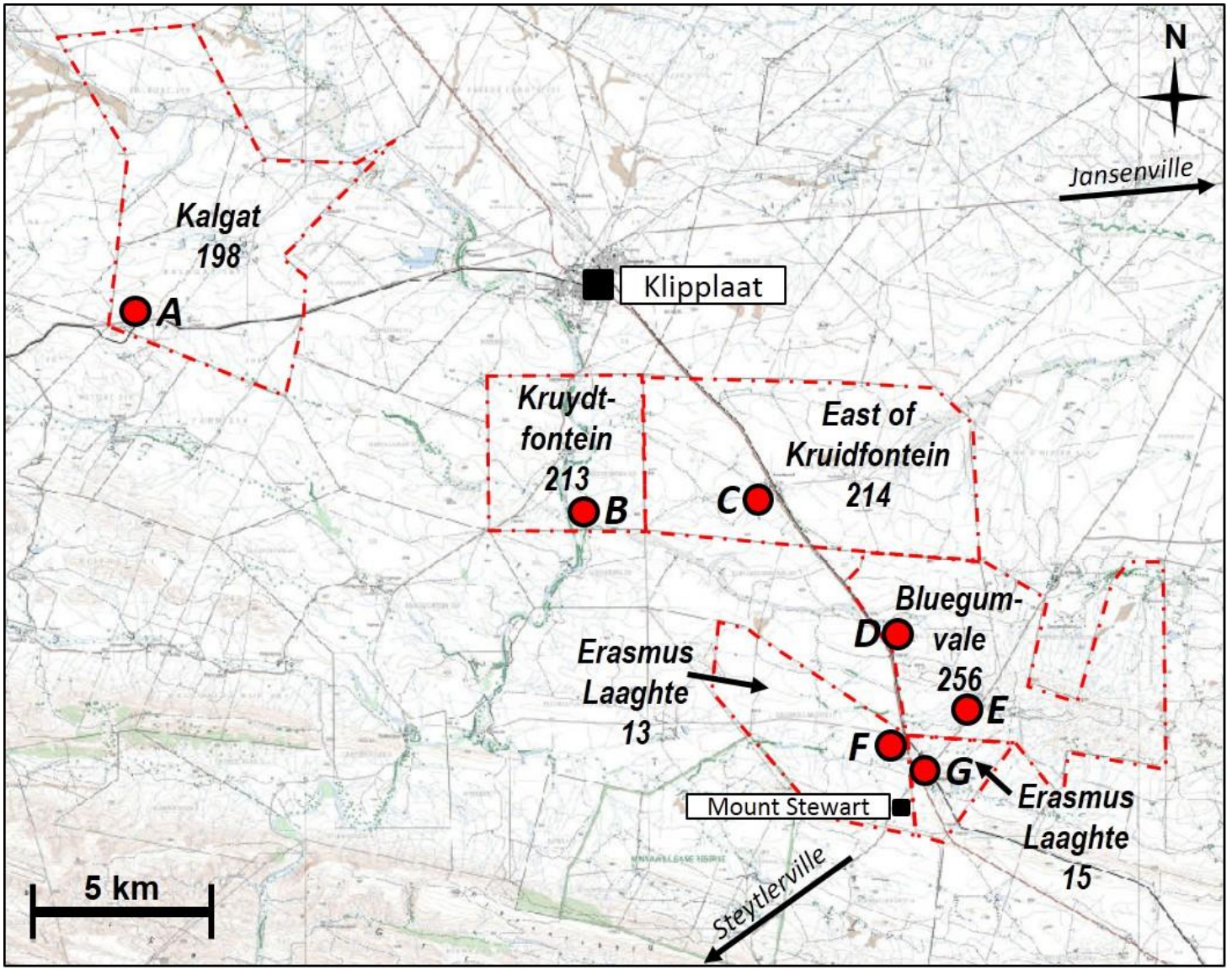

Figure 5.1: Map showing location of fieldwork sites A to G within the various farms in relation to Klipplaat and Mount Stewart.

5.1.1 Site A

5.1.1.1 Kalgat Farm 198 – West of Klipplaat

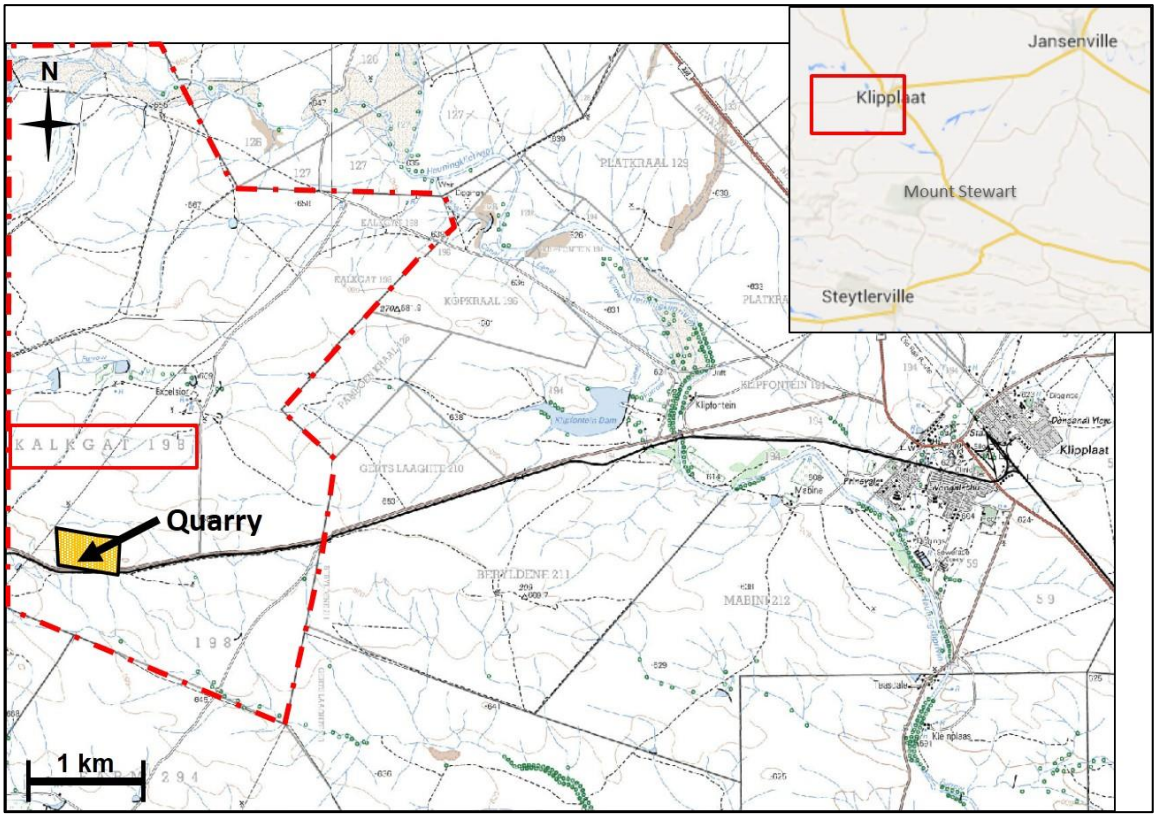

Figure 5.2: Location of the quarry on Kalgat Farm 198 along the road west of Klipplaat.

Along the road heading west from Klipplaat, which eventually joins the National Highway Route Nine (N9) at approximately 50km, there is a large quarry with shale outcrops of the Whitehill Formation (**Figure 5.2**). This quarry exhibits an array of gypsum deposits and contains evidence of the large carbonate concretions which are noted throughout the study area. Sectional studies which were conducted along the northern wall of the quarry provide the most geological detail within this study site (**Figure 5.3**).

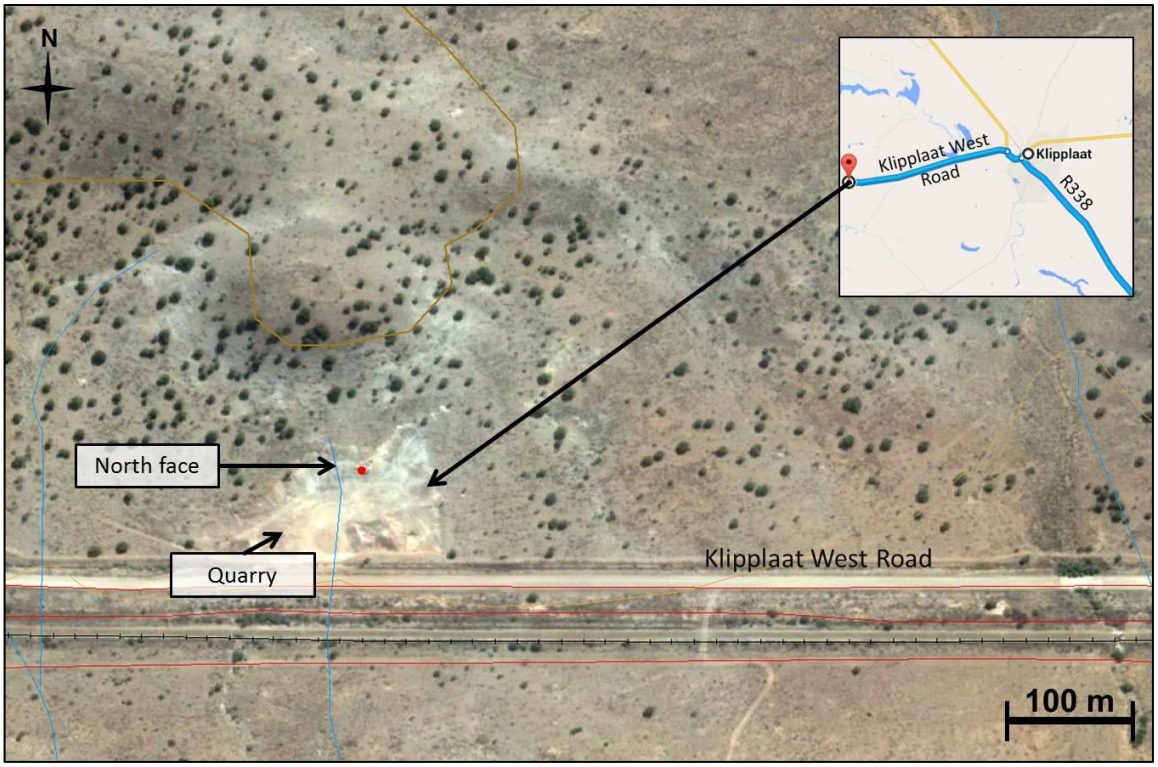

Figure 5.3: Location of quarry on Kalgat Farm 198 showing the northern wall where cross-sections were drawn.

5.1.1.2 170cm Vertical Section of Weathered Shale

The highly-weathered shale of the Whitehill Formation, which is exposed in cross-section on the northern wall of this quarry, exhibits a great deal of variation regarding colour, texture, gypsum content and structural characteristics. A lithological section was compiled from approximately half way up the northern wall of the quarry, down to the quarry floor (**Figure 5.4**).

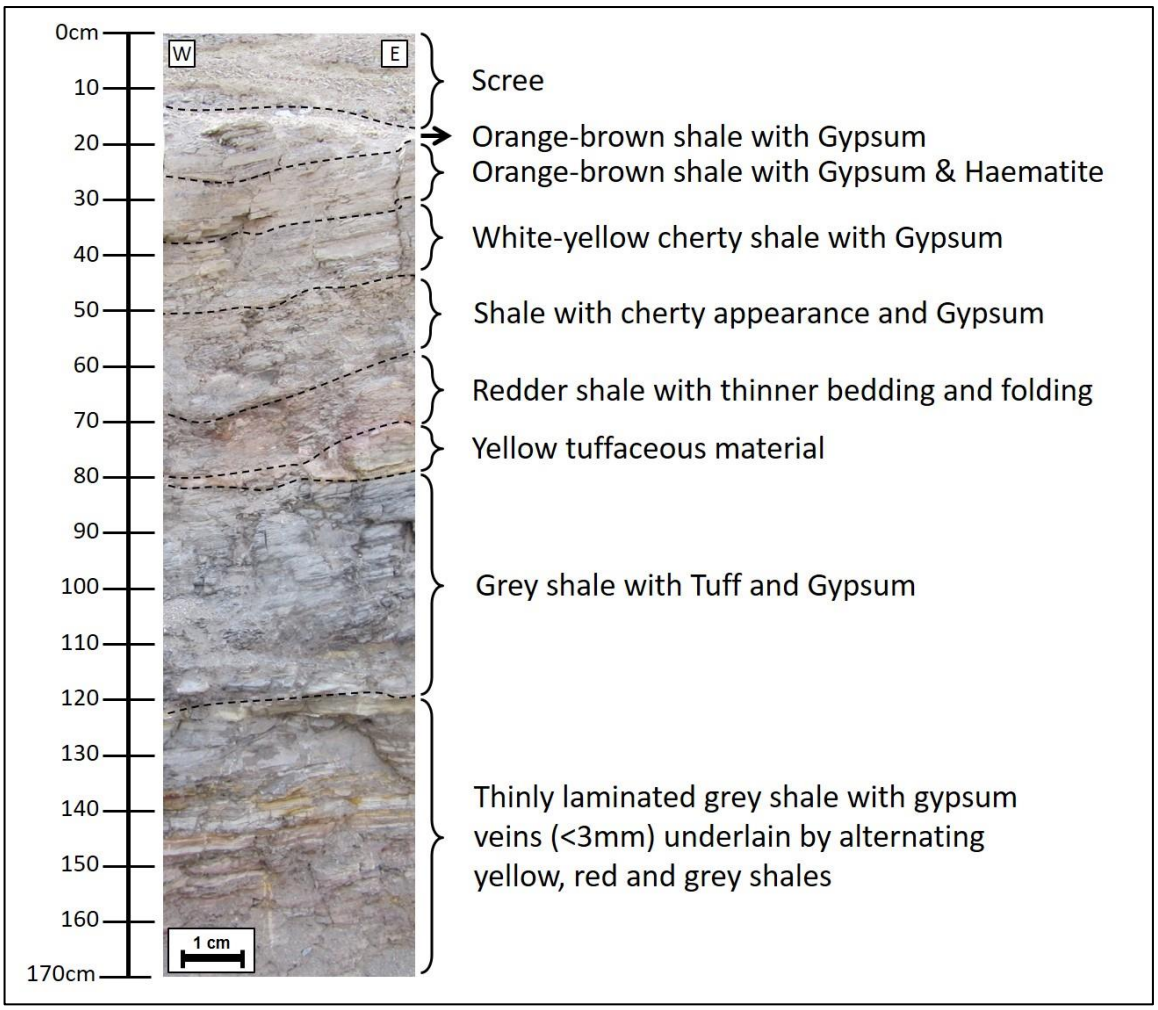

Figure 5.4: Cross-section from west to east through the shale of the Whitehill Formation exposed on the northern wall of the quarry located on Kalgat Farm 198.

The highest part of this section begins with a 10cm layer of scree material which has settled on the quarry bench located approximately half-way down the northern quarry wall. The scree material consists of broken and powdered shale which has collected on the bench since the quarry was abandoned over 30 years ago. The following 10cm towards the quarry floor consists of fine-grained orange-brown shale with a thin gypsum vein (<6mm). The shale has a precipitated or 'cherty' appearance and seems to have been vertically disturbed (compacted) by the gypsum veins (**Figure 5.5**).

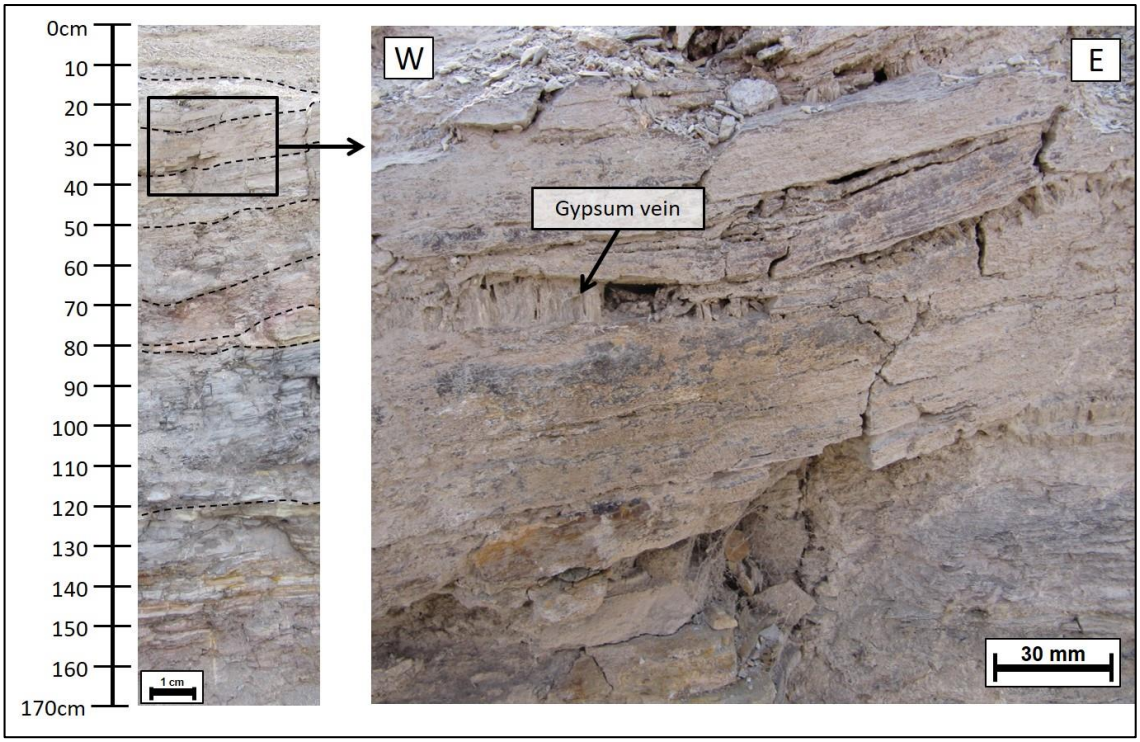

Figure 5.5: Gypsum vein located in between the orange-brown shale of the cross section shown in **Figure 5.4**. Note how the vertical crystal growth of the gypsum has caused apparent folding of the shale.

From 20cm to 35cm working down the section, similar shale is observed with a thinner, approximately 1cm thick, gypsum vein, with the strata exhibiting small folds and faults as well as small quantities of haematite which is overlain by a small lens of gypsum.

From 35cm to 50cm, a 6mm gypsum vein is overlain by unweathered shale beds of a white and yellow colour exhibiting a cherty or precipitated appearance and underlain by a white-grey mudstone shale. From 50cm to 70cm, the shale exhibits a precipitated appearance, along with a variety of colour changes. From top to bottom, red followed by orange and finally yellow shale, with a gypsum vein approximately 6mm thick, is observed. This is underlain by a greyer, less cherty-looking shale with a larger (2cm thick) gypsum vein. From 70cm to 80cm, the shale exhibits a cherty appearance, is more red in colour, has thinner bedding planes and is separated by a gypsum vein less than 2mm thick. The shale horizons in this portion appear to be slightly folded.

From the 80cm to 90cm portion, a 3.5cm yellow, soft, powdery material is overlain by redder shale and underlain by grey shale. Below this, there is a grey shale with some yellow strata and a few small gypsum veins less than 4mm thick. This shale

appears to be highly jointed and continues down to 120cm in this section. Continuing to the quarry floor at 170cm, a thinly laminated grey shale with laminated gypsum less than 3mm thick is underlain by alternating yellow, red and grey shale.

5.1.1.3 Bedding and Jointing of the Whitehill Formation

Approximately 4m further towards the north-east of the location of the cross-section described in Section 5.1.1.2, bedding and joint readings were taken on a harder, less weathered shale outcrop. Stratigraphically, this outcrop is approximately 3m above the succession of shale presented in the previous section. The average bedding dip of the shale is 21º towards the north and strikes approximately east to west at 79º. The joint readings show that there are two distinct jointing planes. Joint plane 1 (J_1) dips at an average of 86º to the east and therefore strikes north to south (at 171º). Joint plane 2 (J_2) dips at an average of 62º to the south and therefore strikes east to west (at 101º). The dip direction of J_1 is almost negligible due to the vertical nature of the joint plane. Some readings on J_1 dip towards the west, but the strike direction remains the same (north to south). Because J_1 and J_2 are at approximately perpendicular angles to one another, this produces orthogonal blocks within the shale outcrop (**Figure 5.6**).

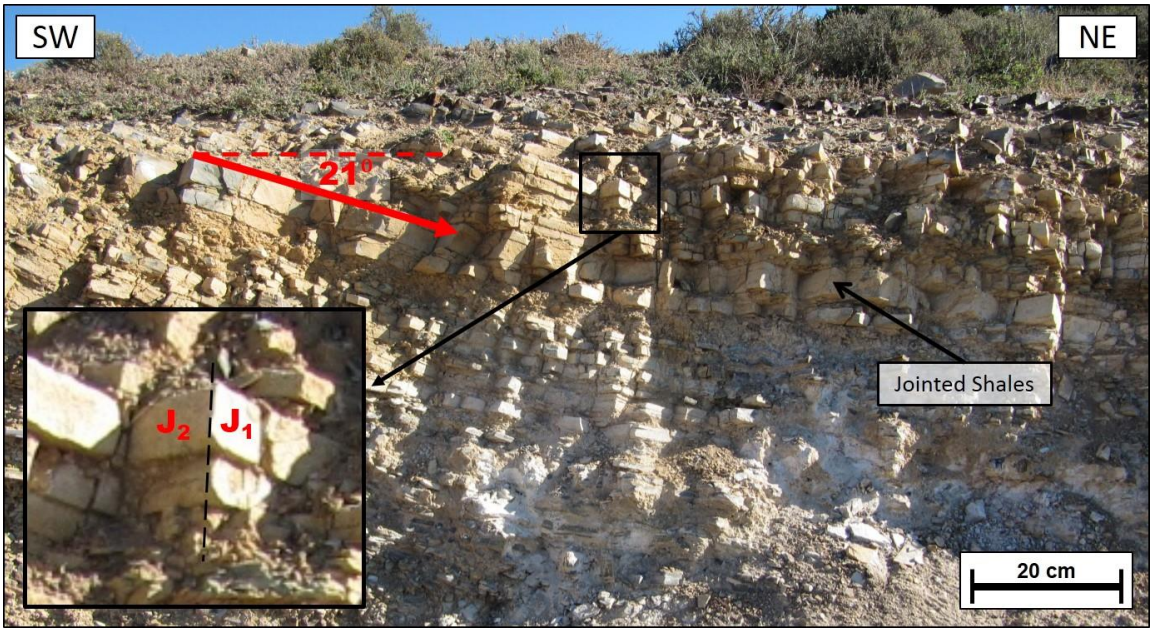

Figure 5.6: Jointed shale in the upper section of the northern wall of the quarry located on Kalgat Farm 198.

5.1.1.4 Broken Concretion in Quarry

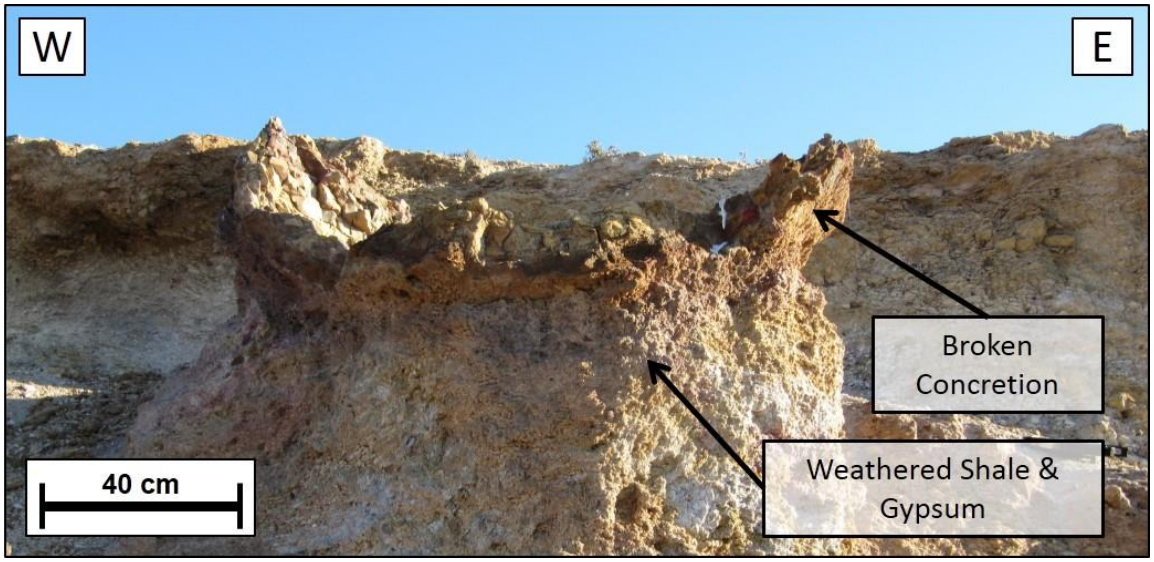

Figure 5.7: Broken Concretion located *in situ* above the weathered shale with massive gypsum located on the northern wall of the quarry of Kalgat Farm 198.

Concretions were observed in this quarry as well as in the area surrounding the quarry where they have most likely been transported by miners who removed them during quarrying. The oblate concretion observed in this quarry is still located *in situ* and can therefore be studied in relation to the surrounding shale of the Whitehill Formation as well as the gypsum deposits which are prevalent in this area (**Figure 5.7**).

Below this concretion there are several layers of weathered shale containing non-bedded surface gypsum crusts. There are also joints which are filled with laminated gypsum. The initial area below the concretion consists of shale, underlain by white-grey weathered shale with some gypsum crystals which exhibit no particular crystal growth orientation, similar to the enterolithic gypsum deposits described in Abdel-Wahab and McBride (2001). Below this there is larger, yellow-orange, weathered shale rich in gypsum, with no particular crystal growth direction and non-bedded in nature. This is underlain by white-grey, thicker, less weathered shale, however, the weathered areas do contain non-bedded surface crusts of gypsum as well as gypsum rosettes. The white-grey area contains a small portion of purple folded shale underlain by orange-yellow shale with a limited amount of gypsum. At the base of this section, there are alternating layers of grey and orange-yellow shale with minor gypsum which has no particular crystal growth orientation (**Figure 5.8**).

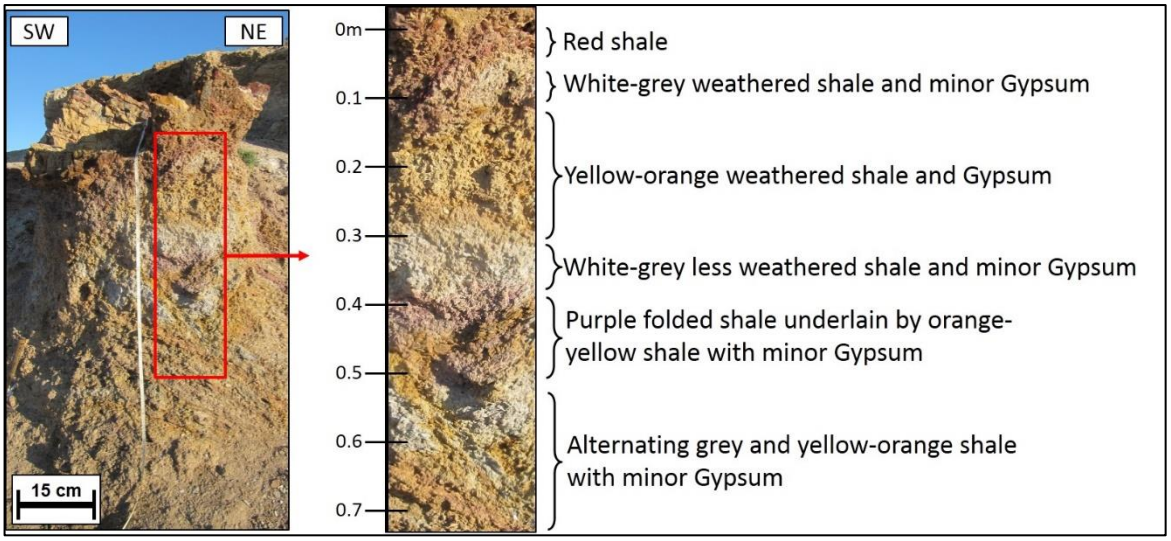

Figure 5.8: Cross-section from south-west to north-east through the Whitehill Formation observed on the northern wall of the quarry located on Kalgat Farm 198. Section is located directly beneath the *in situ* broken concretion.

A small, 20cm, section of the 'shell' of this concretion has been studied more closely. This section is reported from the inside of the concretion shell working towards the outside of the shell (**Figure 5.9**). From the inside of the shell up to 8cm working outwards, there is yellow, weathered shale with indistinct layering which is jointed and, in some cases, filled with black (smoky) quartz. From 8cm to 11cm, there is a gradual change from a yellow to a brown coloured shale, exhibiting a layered appearance with few noticeable joints. At 11cm, there is a small gypsum vein, which pinches out and acts as a contact between strata. From 11cm to 15cm, a hard, red-brown, weathered shale occurs with noticeable layering and some jointing, outlined by a redder, precipitate-looking shale layer approximately 2mm in thickness. From 15cm to 16cm, there is a cluster of white gypsum veins with crystals that are generally horizontal, but also bent in certain areas. Finally, from 16cm to 20cm, there is a weathered area containing a large zone of non-bedded gypsum which exhibits no particular crystal growth direction. The gypsum is also black in some places.

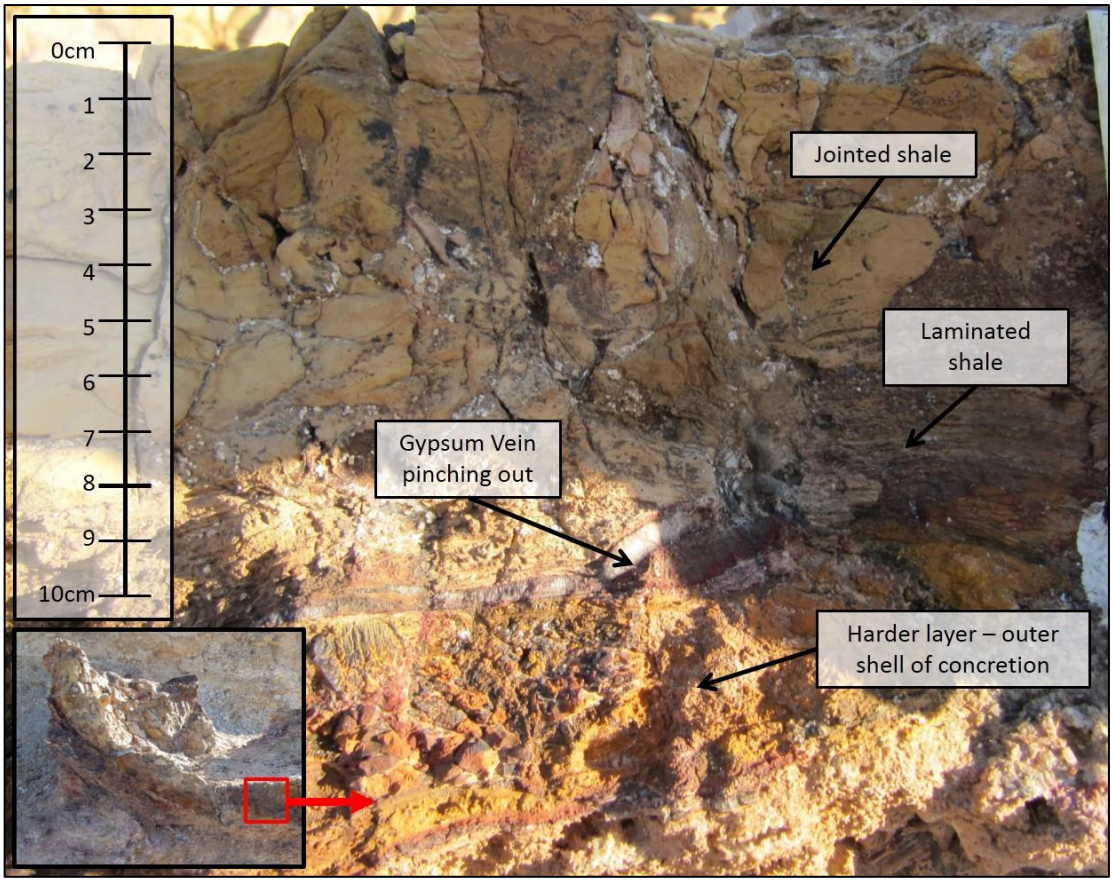

Figure 5.9: Section through the shell of a concretion (inside at the top of the picture).

5.1.1.5 14m Horizontal Section from West to East along the Northern Wall of the Quarry

This is a lateral cross-section which is located directly above the cross-section described in section 5.1.1.2 as well as above the broken concretion described in section 5.1.1.4. This area is highly weathered, making it difficult to distinguish any bedding features. A simple drawing of the cross-section can therefore not contain every specific detail, but the one used here displays the most noticeable features which were observed in the section. Working from west to east, the first 1m consists of gentle folds in highly weathered, white shale which exhibits a yellow-orange colour at the base. From 1m to 1.5m from the western edge of the section, gypsum is located directly to the left (to the west) of a possible fault system. One particular layer of shale pinches out between the distances of 1.5m and 2.0m. From 2.0m to 3.0m, the shale has a red colouring and is folded. Several strata appear to pinch out towards the top of the section. From 3.0m to 5.0m, there is a distinct pinching-out of the lower, yellower layers and a fault is noticeable where the white and yellow shale meet. Non-bedded surface gypsum crusts, exhibiting

no particular direction of crystal growth, are found at the distances of 5.0m to 6.0m from the western edge of the section and are related to what appears to be a duplex structure located at this point. From 6.0m to 7.0m, the pinching out of the lower, yellow layer is less distinct and there is a fold noted directly after the 6.0m mark a fault appears (**Figure 5.10**).

At the 7.1m point of this section, the angle of view is changed from a west to east cross-section, to a southwest to northeast cross-section. This is simply due to the orientation in which the quarry wall had been mined. The latter angle of view gives rise to a distinct bedding orientation as well as relatively unweathered shale. From this point, there appears to be little or no gypsum within the cross-section. This could be due the fact that the gypsum is predominantly located below these horizons within the stratigraphic sequence or could simply be due to the lack of sufficiently weathered surfaces.

From 7.0m to 8.0m, there are two distinctly thicker grey shale layers towards the top of the cross-section. The folding gives rise to a water escape structure, and there is also faulting related to these structures. From 8.0m to 10.0m, the shale is folded and results in duplex structures as well as water-escape structures within the shale. There is no gypsum, but there is some red colouring of the weathered shale. Finally, from 10.0m to 14.0m, there is highly jointed shale, with no visible folding or fault structures, separated by weathered ‘weak zones’ between the strong shale (**Figure 5.11**).

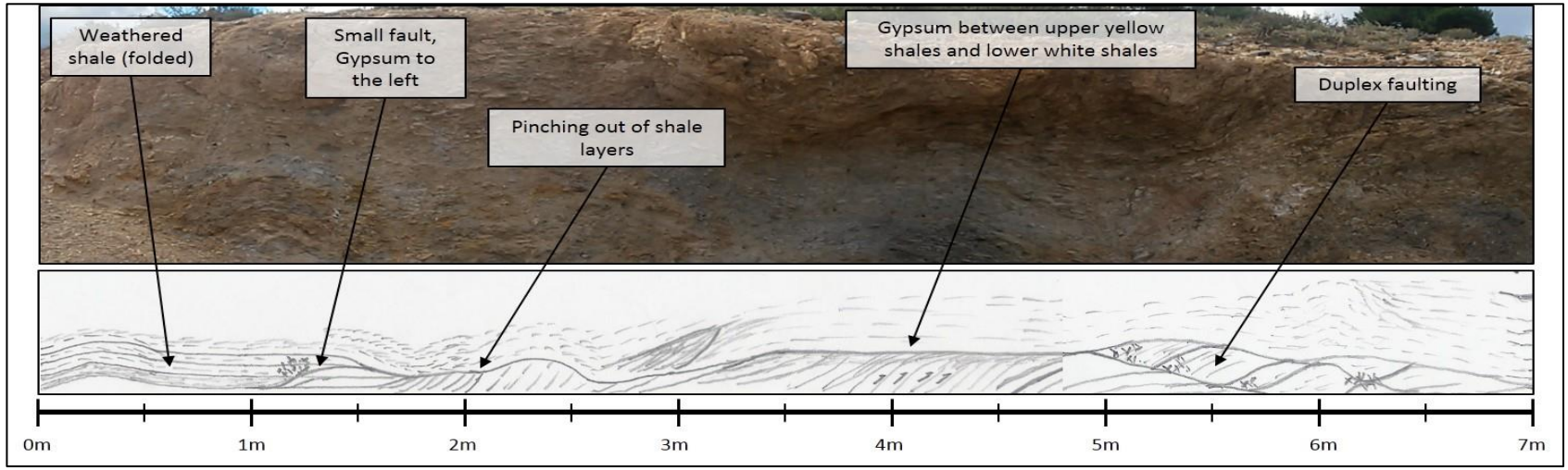

Figure 5.10: West to east cross-section through the shale of the Whitehill Formation observed on the northern wall of the quarry located on Kalgat Farm 198. Section is located directly above the *in situ* broken concretion.

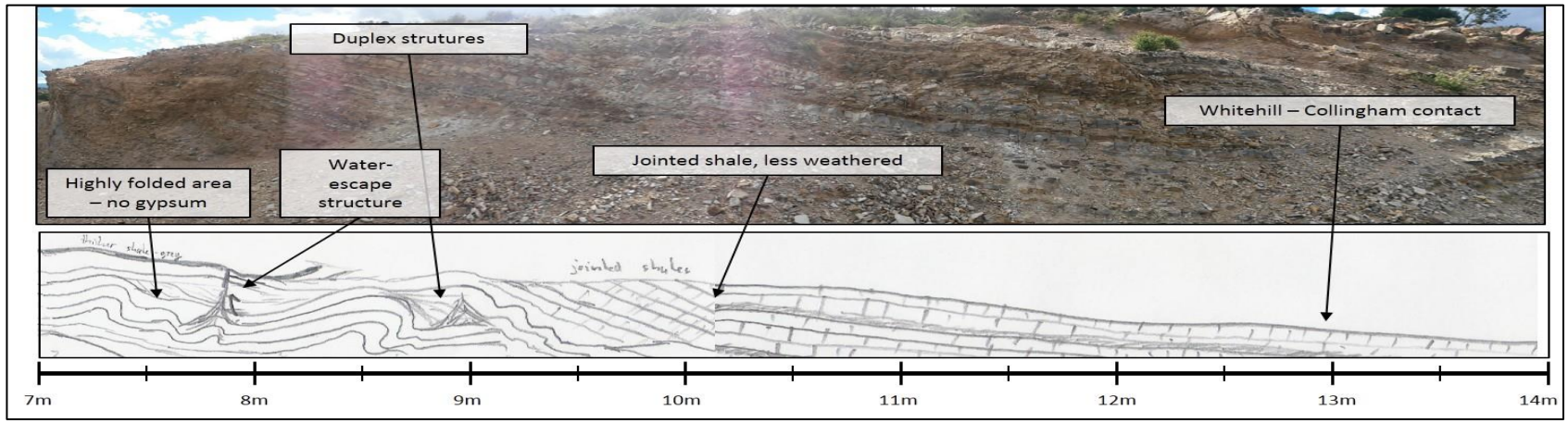

Figure 5.11: Southwest to northeast cross-section through the shale of the Whitehill Formation observed on the northern wall of the quarry located on Kalgat Farm 198 (continuation of previous section). Section is located directly above the *in situ* broken concretion.

5.1.1.6 Concretion Removed from Quarry

A loose oblate concretion was found outside of the quarry. It has a red outer shell with black (smoky) quartz veins, gypsum in places (often dark in colour) and a dolomitic appearance. The red outer layer was removed and a yellow, silty inner layer was found. There appeared to be a narrow hollow between the outer layer and the inner layer (**Figure 5.12**).

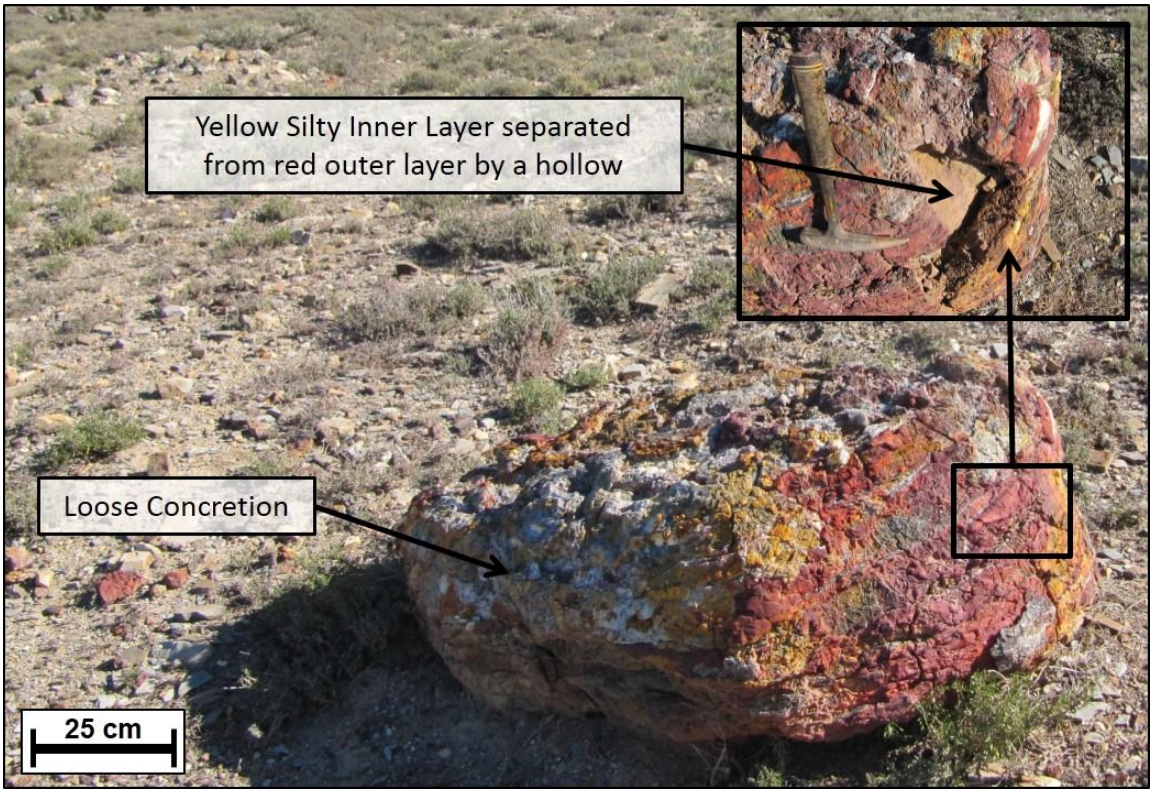

Figure 5.12: Loose concretion found outside the quarry on Kalgat Farm 198. The concretion exhibits a red outer layer which is separated from the yellow inner layer by a hollow.

5.1.1.7 Cherty Shale Outcrop

The harder, less erodible 'Matjiesfontein chert', a dark grey, white-weathering chert layer which is located in several areas throughout the project area, acts as a helpful marker bed near the contact between the Collingham Formation and the Whitehill Formation (Visser, 1992). The cherty shale outcrops north of the quarry on Kalgat 198. The shale does not exhibit the distinct dip in a particular direction as observed in other areas, but this is likely due to its location near the hinge zone of a macro-scale fold. On average, the outcrop strikes east to west (187º) and dip 17º to the south.

5.1.1.8 Whitehill Formation Road Cutting

Approximately 700m east of the quarry, there is a shallow exposure of the Whitehill Formation on the northern side of the road (**Figure 5.13**). The shale is jointed and weathered and appears to be folded in a gentle monocline. It is also intersected by a green-grey tuffaceous material that has a distinctly different fracture pattern to the remaining shale (**Figure 5.14**). The shale dips at 17° towards the north and strikes in an east to west direction (at 100°). Walking in a westerly direction along the road cutting, one can follow the various shale horizons although some horizons pinch out due to faulting while others are intersected by concretions of varying sizes. Some of the smaller concretions are surrounded by gypsum veins as well as randomly orientated gypsum crystals (**Figure 5.15**). The larger, more consolidated concretions seem to be surrounded by less weathered shale with little to no gypsum precipitation present.

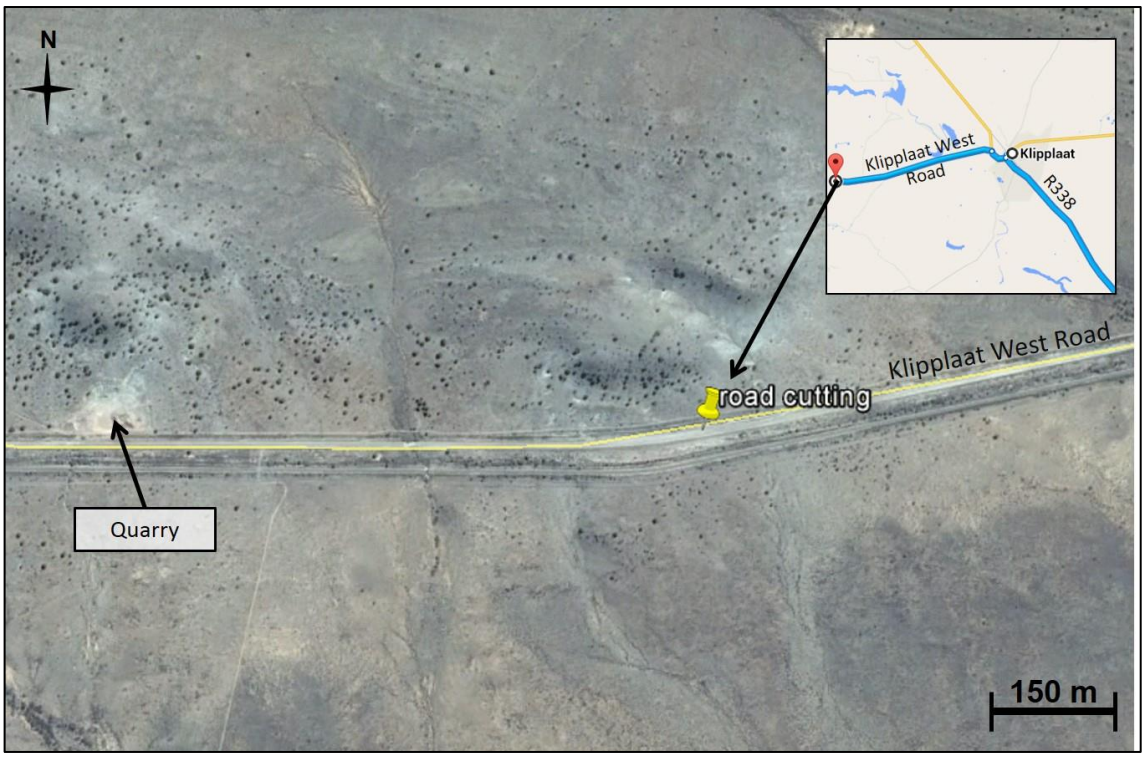

Figure 5.13: Location of Whitehill Formation road cutting along the road west of Klipplaat (approximately 700m east of the quarry).

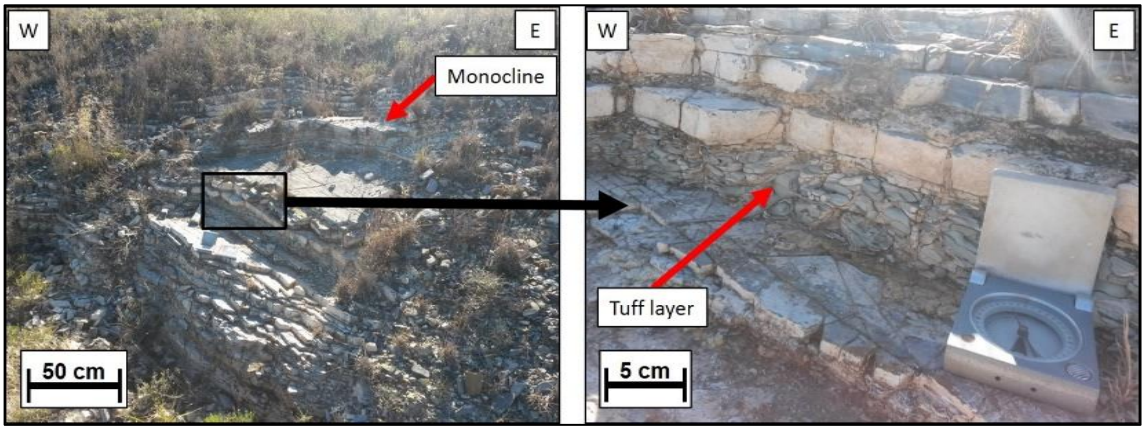

Figure 5.14: Whitehill Formation outcrop exhibiting white-weathered, jointed shale interbedded with green-grey fractured tuff.

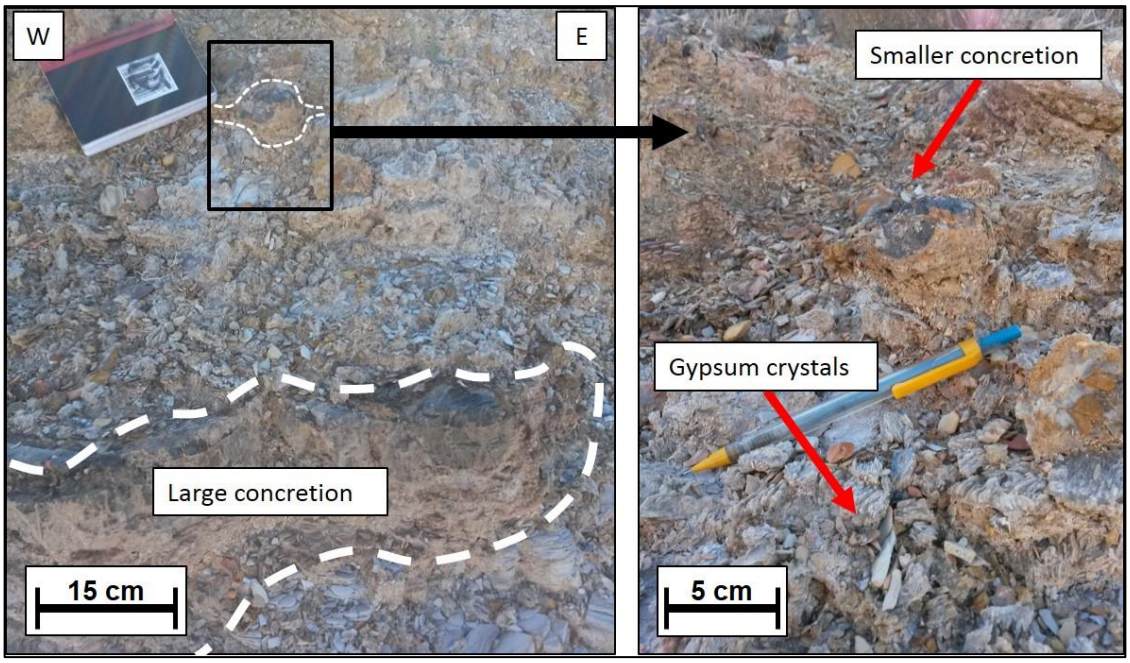

Figure 5.15: Highly weathered shale of the Whitehill Formation exhibiting concretions of variable size as well as gypsum crystals which are randomly orientated.

There were only two noticeably large concretions in this road cutting and it was apparent that they are not located along the same shale horizon (**Figure 5.16**).

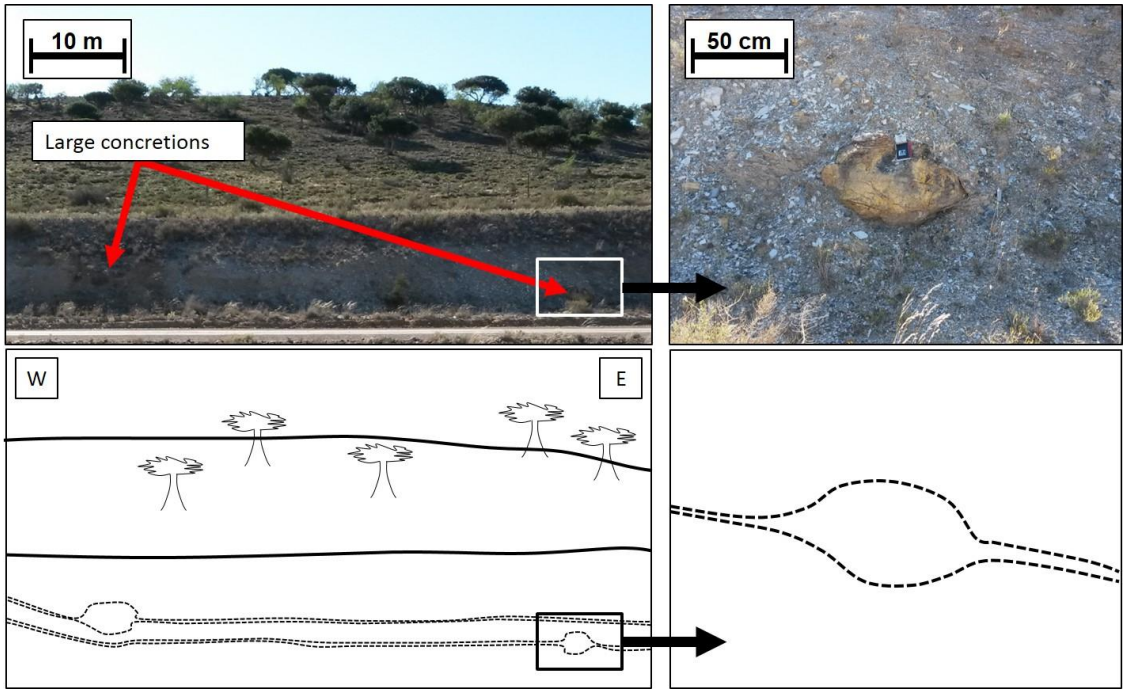

Figure 5.16: Exposed road cutting showing orientation of concretions – note that the two large concretions are not situated along the same shale horizon.

5.1.2 Site B

5.1.2.1 Kruydtfontein Farm 213 – South of Klipplaat

This farm is located to the south of Klipplaat and contains an old road quarry which is conveniently situated on an outcrop of the Whitehill Formation. The quarry is situated approximately 13km west of the PPC Mt Stewart Gypsum Mine, but is located along the same south-dipping northern limb of the synclinal fold which traverses this area (**Figure 5.17**).

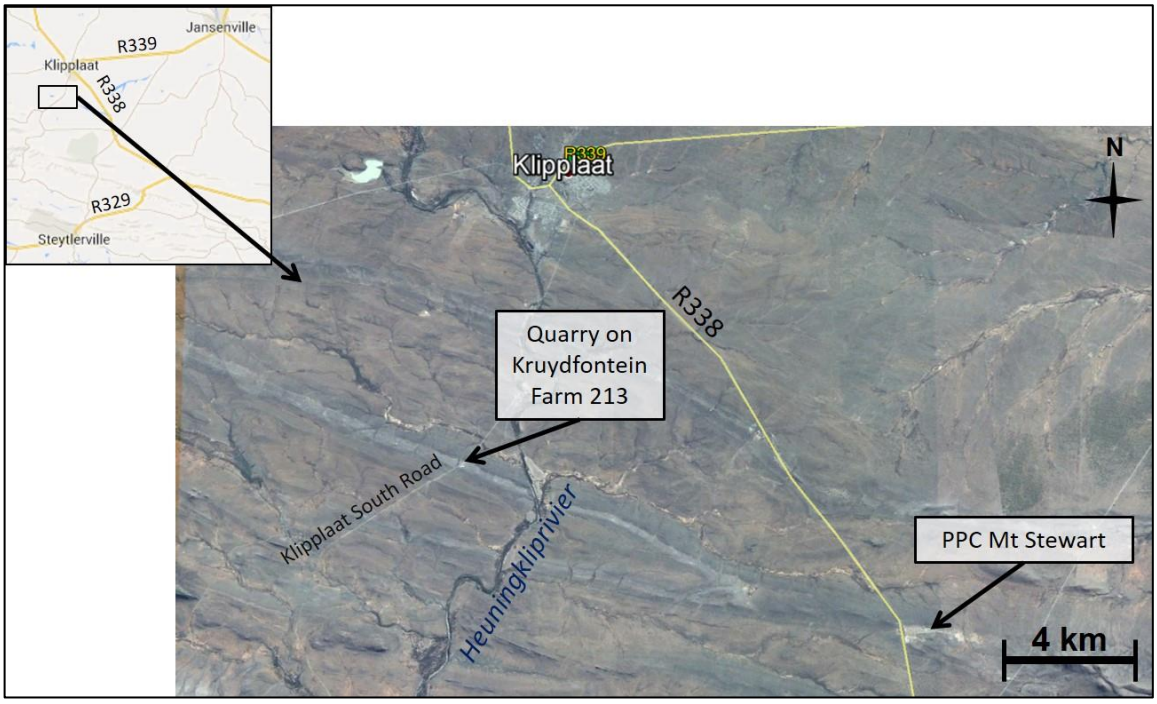

Figure 5.17: Location of the Kruydtfontein Farm 213 quarry on the road south of Klipplaat. Note the 'white-band' of the Whitehill Formation and the location of the quarry which occurs on the same south-dipping northern limb of the same syncline as that of the mine at PPC Mt Stewart.

An extensive shale outcrop was observed on the western and southern walls of this quarry. The western wall exhibits a 4m vertical section which exposes the contact between the Whitehill Formation and the Collingham Formation. The shale of the Collingham Formation is a brown to grey colour and contains manganese dendrites precipitated along the shale bedding planes. The shale is also interbedded with yellow tuffaceous sediments as well as some light-coloured cherty strata. The shale is very jointed and some of the joints are filled with quartz veins. The contact with the Whitehill Formation occurs where the shale becomes greyer in colour. The underlying Whitehill Formation exhibits thinner bedding, whiter shale and fewer yellow tuffaceous horizons (**Figure 5.18**). The shale exposed here is, on average, dips 12º towards the south-southwest (SSW) and strikes 103º in an east-southeast to west-northwest (ESE to WNW) direction.

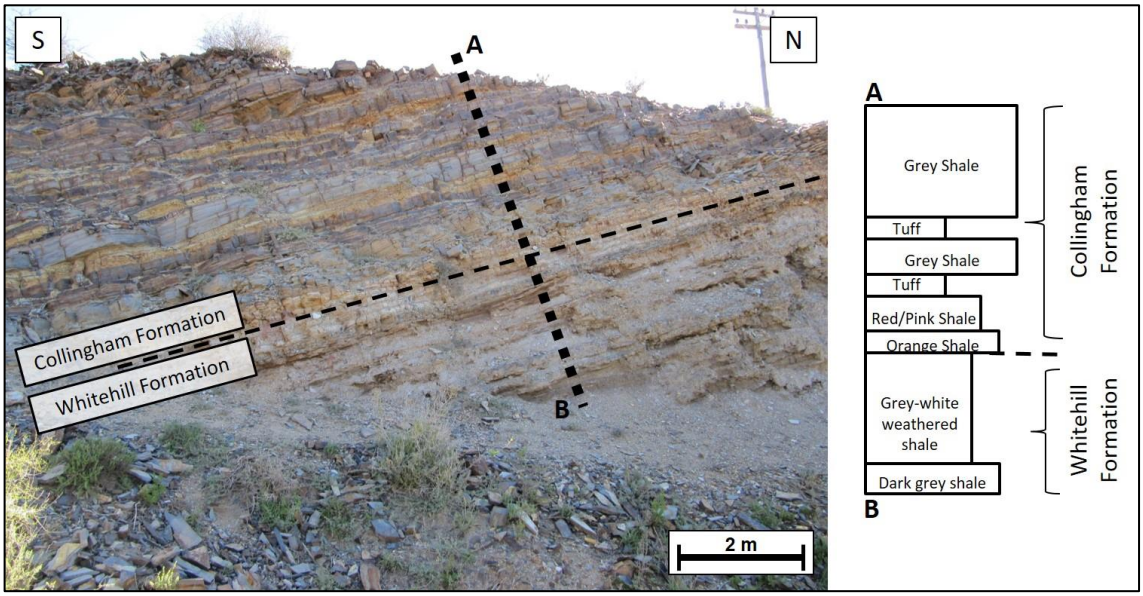

Figure 5.18: Section from south to north through shale exposed in the Junction View Farm 213 quarry on the road south of Klipplaat. Note the contact between the Whitehill Formation and Collingham Formation.

An additional section, exposing the shale in a north-east to south-west direction, was observed near the road adjacent to this quarry. The Collingham-Whitehill contact, together with some small concretions that cause minor folding of the shale, are also exhibited in this section (**Figure 5.19**). The grey shale is highly weathered throughout this section, similar to the sections examined at Site A, however there are no abundant gypsum deposits located at Site B. In this section, the bedding plane strikes west-northwest to east-southeast (114º) and dip 16º in a south-southeast direction.

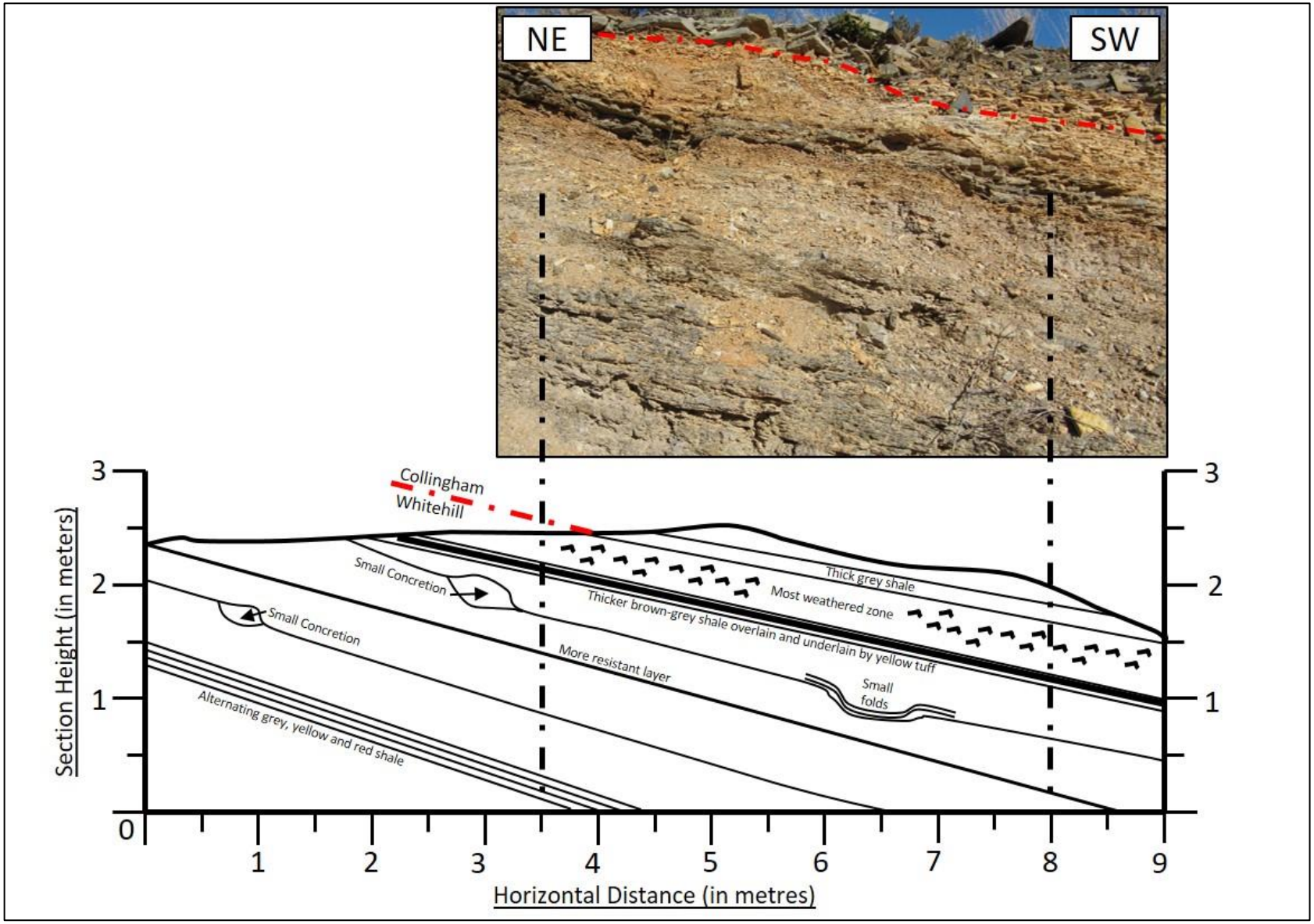

Figure 5.19: Section from northeast to southwest through shale exposed in the Junction View 213 quarry. The Whitehill Formation - Collingham Formation contact is observed at the top of this section.

Along the southern wall of the quarry, only the Whitehill Formation is exposed and exhibits less weathered, white-grey shale with a distinct oblate concretion located *in situ* approximately half way up the quarry wall. The concretion is approximately 50cm long and 20cm in height and is a distinctly yellower colour than the surrounding shale (**Figure 5.20**). Unlike the rich gypsum deposits associated with the concretion studied at Site A, there are no noticeable gypsum precipitates located along this section.

Figure 5.20: East-west section in Junction View Farm 213 quarry showing *in situ* concretion.

5.1.3 Site C

5.1.3.1 East of Kruidfontein Farm 214 – Hardwood Quarries on R338

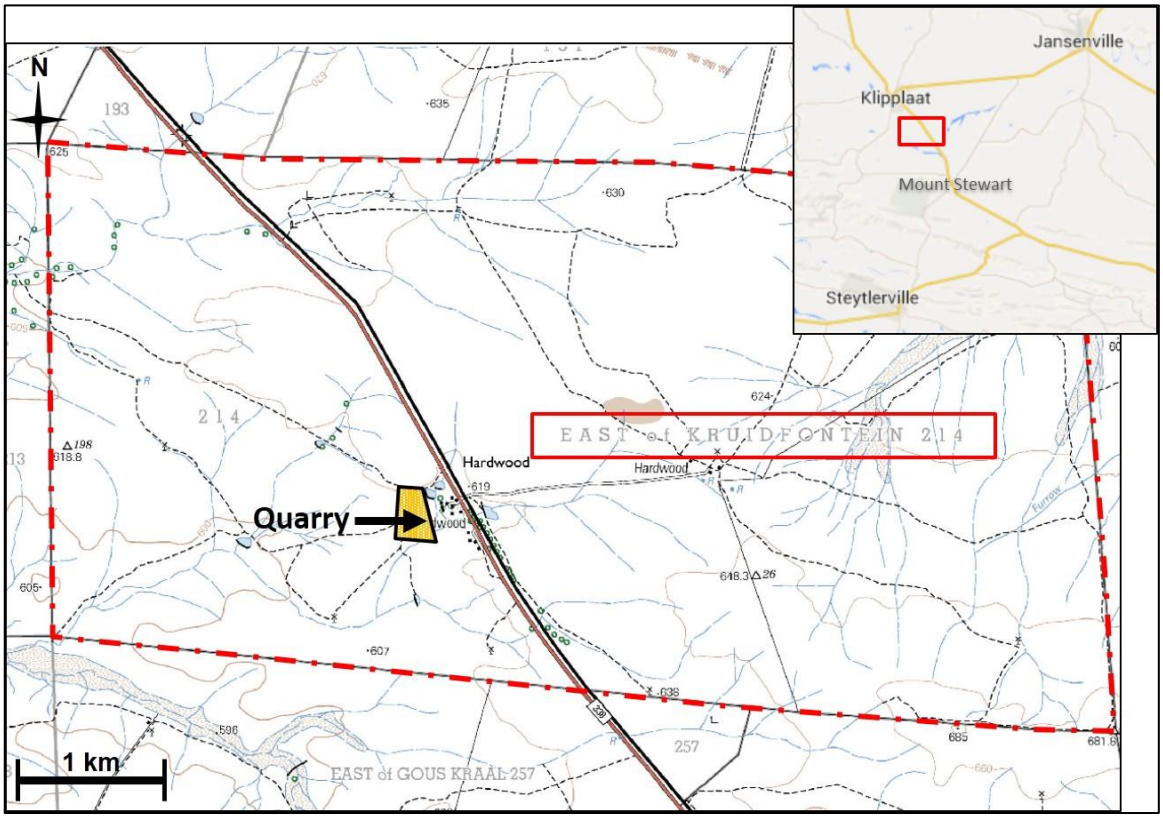

Figure 5.21: Location of the East of Kruidfontein Farm 214 on the R338 south of Klipplaat.

This farm is located along the R338 district road approximately 7km southeast of Klipplaat and 6km northwest of the PPC Mount Stewart Gypsum Mine (**Figure 5.21**). The farm consists of two previously-excavated road quarries which display a number of Whitehill Formation outcrops (**Figure 5.22**). One particular outcrop exhibits vertically-dipping strata, which also exposes the concretion structures in a sectional view (**Figure 5.23**). There are seven oblate concretions of varying size located along the same horizontal strata. An additional three oblate concretions are located along a different position within the shale succession. The largest concretion observed in the quarry is 3.9m in length and 1.4m in width, while the smallest is 1.2m in length and 0.5m in width (**Table 5.1**). The two closest concretions are 1.9m apart and the average distance between any two concretions is 6.1m (**Table 5.2**).

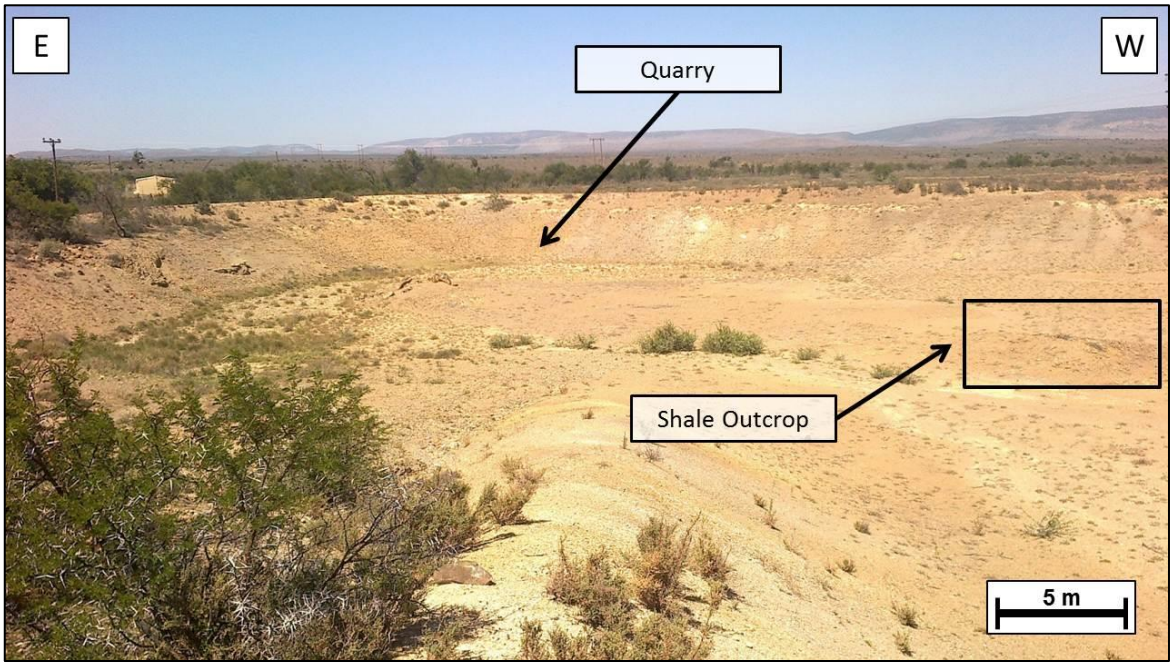

Figure 5.22: One of two quarries located on East of Kruidfontein Farm 214 located next to the R338. The blocked area is the outcrop which is shown in **Figure 5.23**.

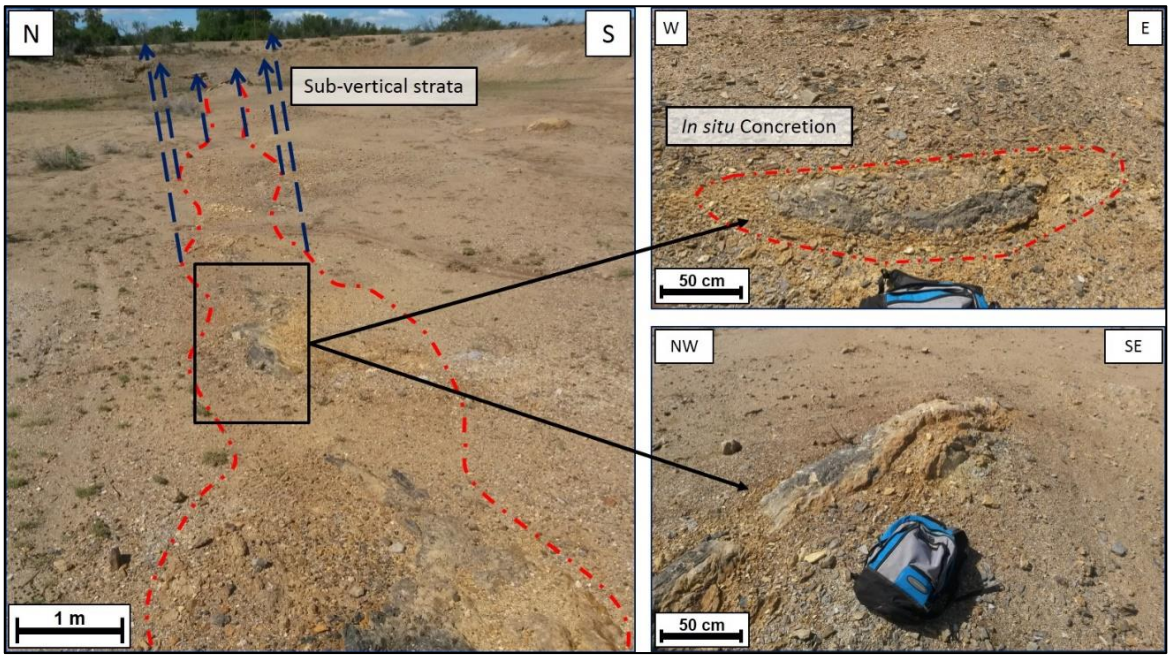

Figure 5.23: Outcrop within a quarry on East of Kruidfontein Farm 214 along the R338. Sub-vertical dipping strata and exposed concretions on the quarry floor.

Table 5.1: Two-dimensional concretion dimensions - Site C.

	Length (m)	Width (m)
Concretion 1	2.6	1
Concretion 2	2.6	0.9
Concretion 3	1.2	0.5
Concretion 4	1.6	0.5
Concretion 5	1.7	0.7
Concretion 6	1.6	1.3
Concretion 7	1.1	0.7
Concretion 8	2.7	0.9
Concretion 9	3.9	1.4
Concretion 10	2.4	0.8
Concretion 11	2.1	0.9
Average	**2.1**	**0.9**

Table 5.2: Distance between concretion centres - Site C.

Distance between Concretions (m)	
1 to 2	4.1
2 to 3	2.5
3 to 4	7.2
4 to 5	1.9
5 to 6	9.8
6 to 9	2.3
7 to 8	7.4
7 to 9	8.1
5 to 7	11.8
Average	**6.1**

5.1.4 Site D

5.1.4.1 Bluegumvale Farm 256 - PPC Mount Stewart East of R338

This area is located 3km north of Mount Stewart along the R338 and is the location of Pretoria Portland Cement's (PPC) gypsum mining operation (**Figure 5.24**). While PPC's mining area includes outcrops of the Whitehill Formation of both the northern and southern limbs of this syncline, they have only conducted mining activity along the northern (south-dipping) limb as well as within the area of the fold hinge zone further to the west (directly adjacent to the road) (**Figure 5.25**).

An area consisting of cherty-shale, representative of the other cherty-shale horizons located throughout the study area (related to the 'Matjiesfontein chert'), is found at the summit of a small hill which is located between the northern and southern limbs of the syncline. The cherty horizons are located at the hinge zone of the syncline and there are both north-dipping and south-dipping outcrops of the chert within this area. There are two distinct north-dipping and south-dipping outcrops of the cherty-shale located between the macro-scale limbs of the syncline. Slickensides are exhibited along the exposed planes of these cherty-shale outcrops (**Figure 5.26**).

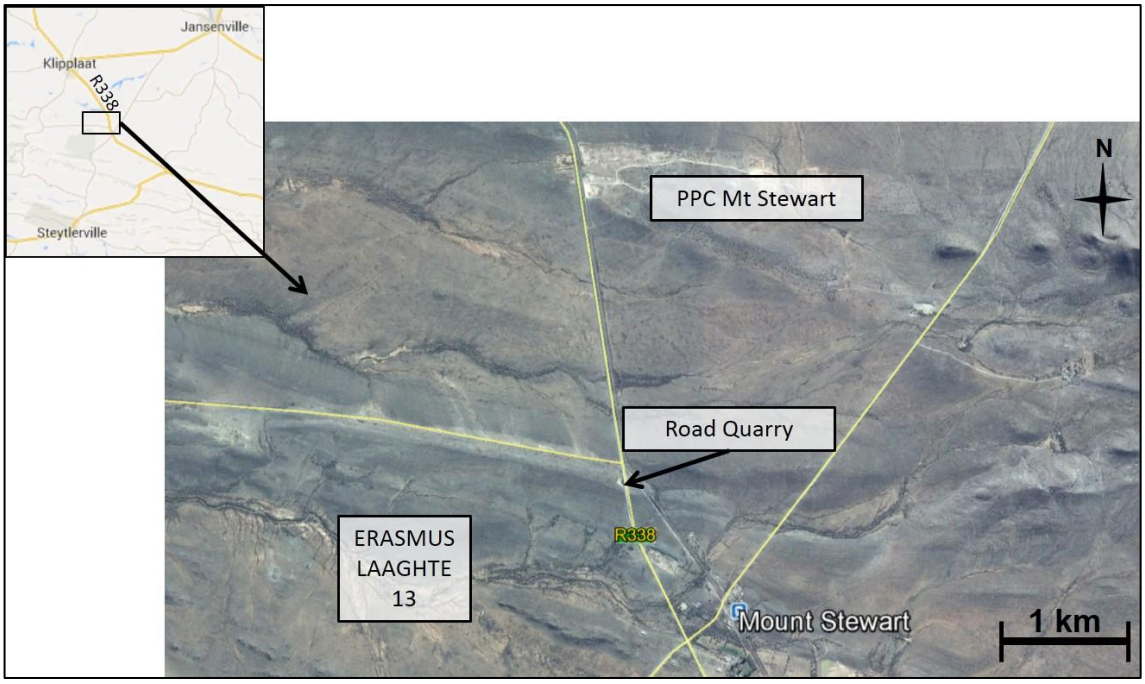

Figure 5.24: Location of PPC Mount Stewart mine site along the R338 in relation to the Erasmus Laaghte Farm 13 and Mount Stewart.

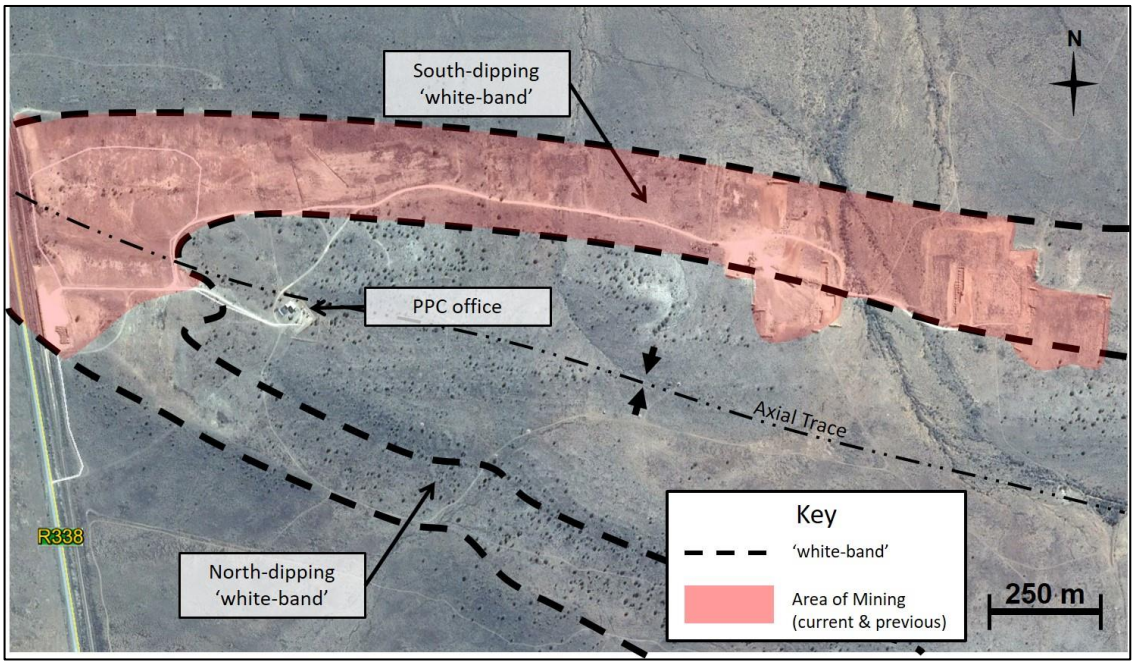

Figure 5.25: Google Earth image showing the 'white-band' associated with the weathered shale of the Whitehill Formation as well as the area currently and previously mined by PPC.

Figure 5.26: Slickensides exhibited on the cherty-shale outcrop which is located at the hinge zone of the Bluegumvale Farm 256 syncline.

The four distinct outcrops of the cherty-shale have been recorded within a lateral distance of 100m in a northwest to southeast traverse. The outcrop located farthest towards the northwest is a south-dipping cherty-shale. The outcrops located to the southeast alternate between north-dipping and south-dipping strata. All four outcrops exhibit an east to west strike. The outcrop farthest to the northwest dips 50º to the south (with a strike of 86º). The second outcrop towards the southeast dips 40º to the north (with a strike of 98º). The third dips 46º to the south (with a strike of 93º) and the outcrop located farthest to the southeast dips 45º to the north (with a strike of 95º) (**Figure 5.27** and **Figure 5.28**).

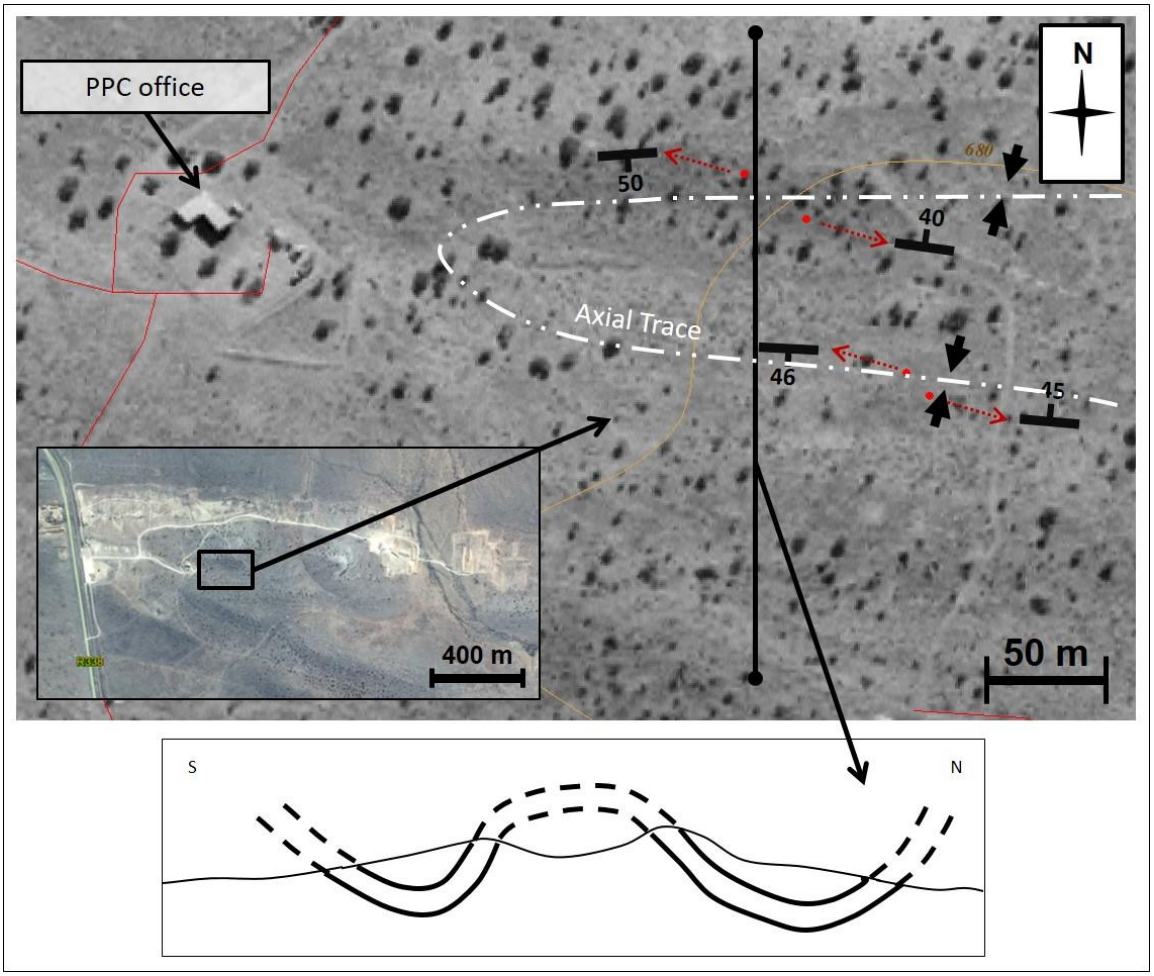

Figure 5.27: Macroscale syncline at Bluegumvale Farm 256 with mesoscale anticline located within the hinge zone of the syncline.

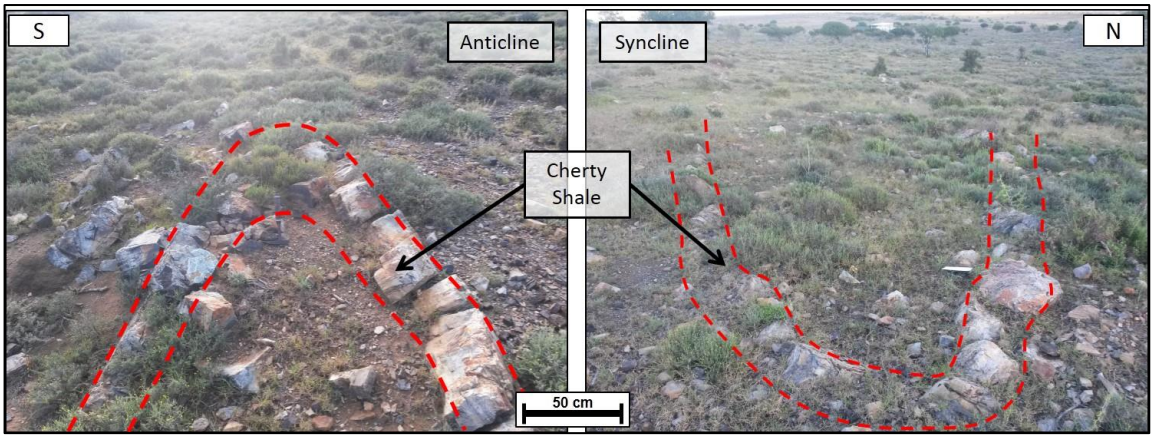

Figure 5.28: Mesoscale folds of the cherty shale located at Bluegumvale Farm 256 and located within the fold hinge zone of a macroscale syncline.

5.1.5 Site E

5.1.5.1 Bluegumvale Farm 256 – Jansenville Road Quarry

There is a large quarry located on the southwest-northeast road which joins Mount Stewart and Jansenville (**Figure 5.29**). There are several areas within the quarry which are rich in gypsum and this is generally associated with weathered areas where gully erosion has taken place (**Figure 5.30**). A cherty-shale outcrop ('Matjiesfontein chert') is located approximately 50m northwest of the quarry. This outcrop dips 36º towards the east-northeast and strikes in a south-southwest to north-northeast direction, almost perpendicular to the macroscale strike of the strata. The cherty-shale outcrop is underlain by weathered shale strata which is separated by minor dolomite layers which are exposed due to their hard and less erodible nature (**Figure 5.31**).

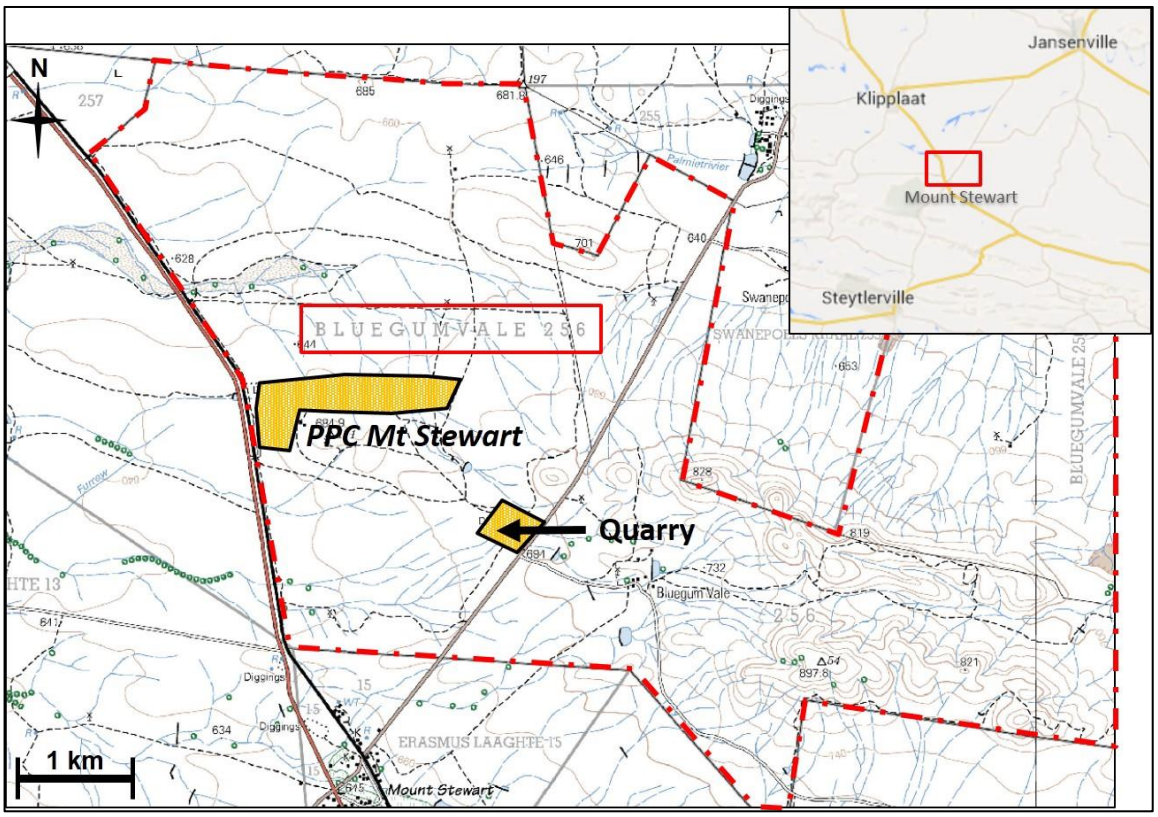

Figure 5.29: Location of the quarry on Bluegumvale Farm 256 along the Mount Stewart-Jansenville road. The quarry is situated along the same north-dipping limb as PPC Mt Stewart.

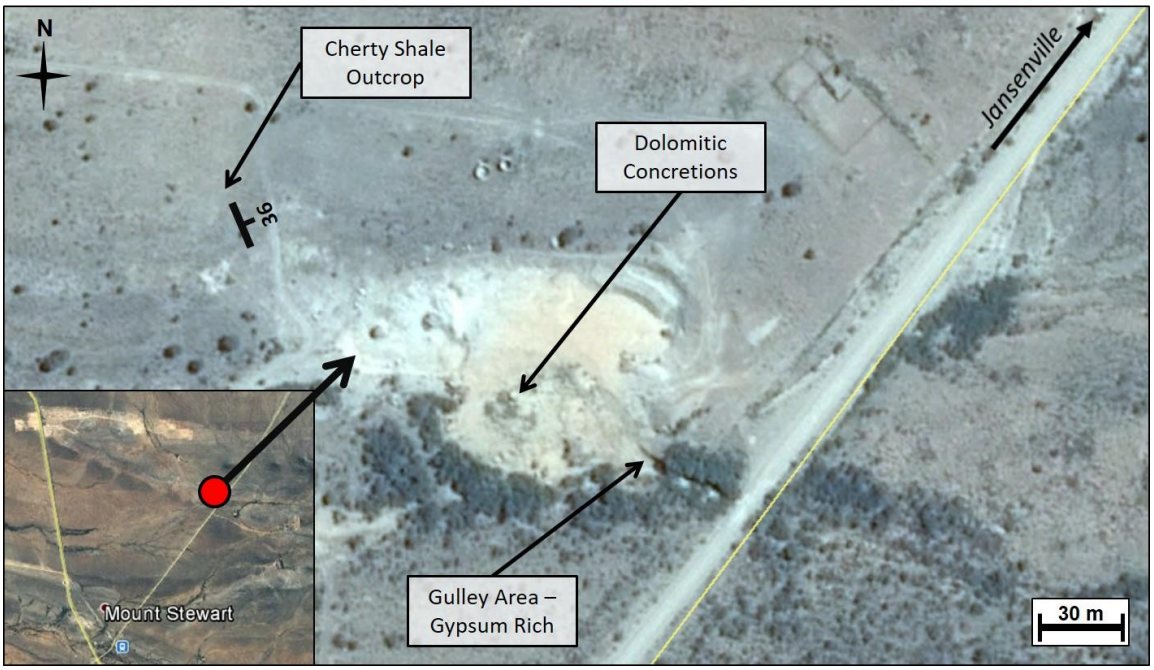

Figure 5.30: Zoomed-in aerial map of the quarry showing the location of cherty-shale outcrops, dolomitic concretions and the gypsum-rich gully area.

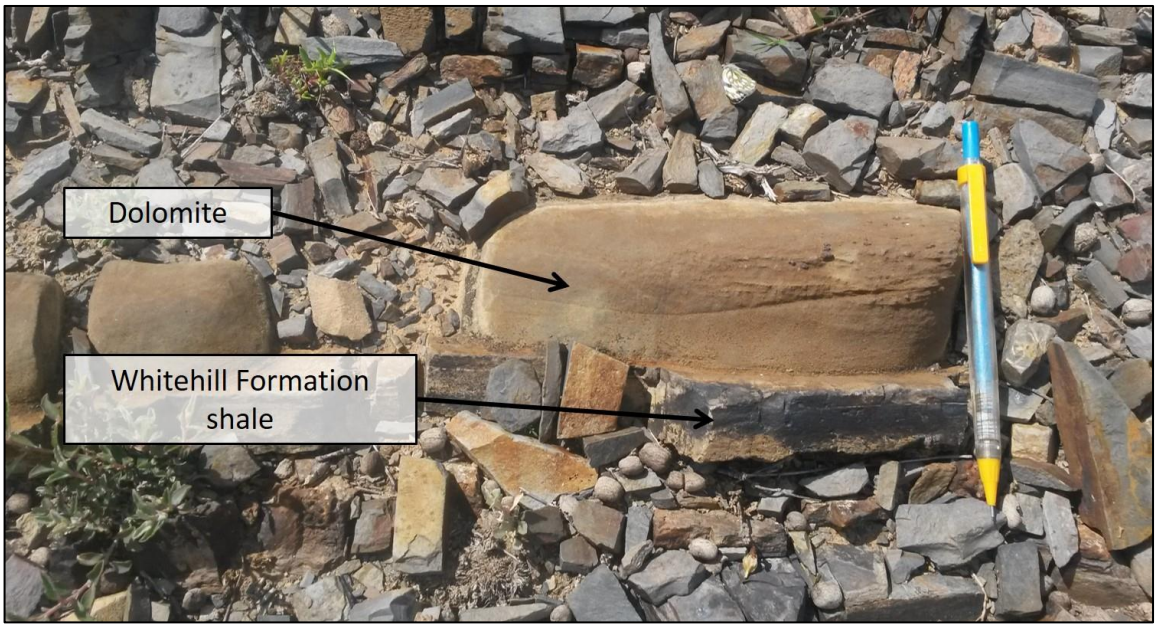

Figure 5.31: Shale of the Whitehill Formation interbedded with less erodible dolomitic successions as observed directly adjacent to the Jansenville Road quarry on Bluegumvale Farm 256.

The northern limb of the macroscale syncline is intercepted approximately 1km north of the quarry along the Mount Stewart – Jansenville road. Although no Whitehill Formation outcrops are exposed in this area, a shale outcrop of the Collingham Formation was observed directly adjacent to the road. This shale strikes east to west (101°) and dips at an average of 7° towards the south. The

shale consists of brown, fairly unweathered material with distinct jointing fractures surrounded by liesegang iron discolouration (**Figure 5.32**). There are three distinct joint planes which are noted. Namely J_1, J_2 and J_3 where J_3 is orientated parallel to the bedding plane. The sub-perpendicular intersection of J_1, J_2 and J_3 creates orthogonal blocks within the shale. The joint plane J_1 dips at an average of 83° towards the west (with a north to south strike of 354°) while the J_2 plane has an average dip of 86° towards the south-southeast and therefore strikes ENE to WSW (at 75°). Boudinage structures are located along the bedding planes within these strata and several trace fossils are noted on the surface of these planes (**Figure 5.33**).

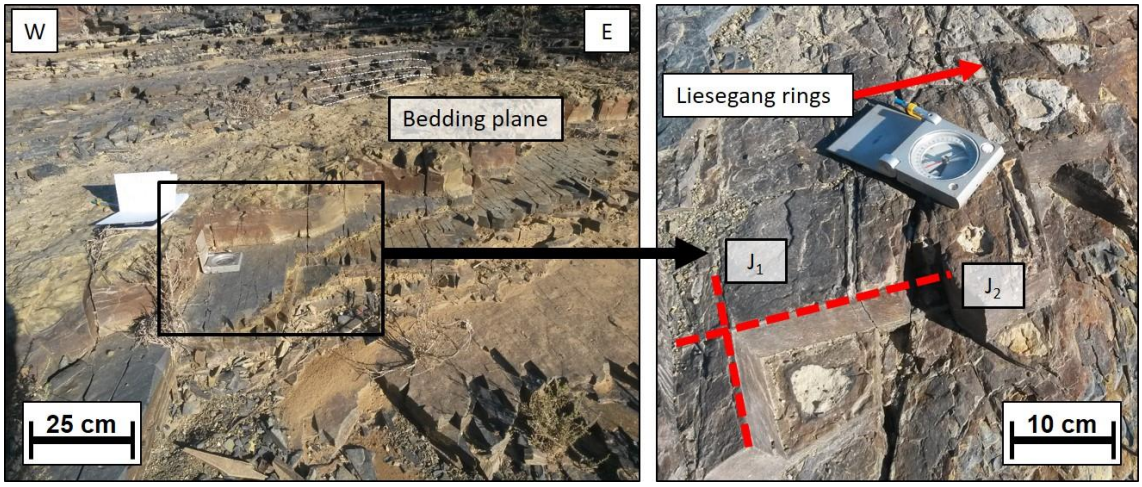

Figure 5.32: Collingham Formation outcrop along the Mount Stewart - Jansenville road exhibiting jointing planes which intersect at 90° to form orthogonal blocks with mineralisation in the form of Liesegang rings.

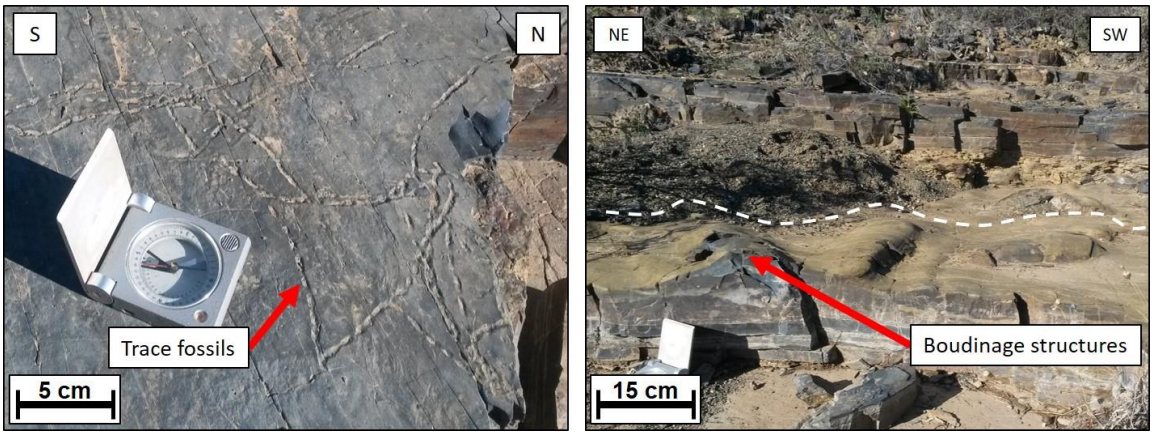

Figure 5.33: Collingham Formation outcrop along the Mount Stewart - Jansenville road: Left: Trace fossils observed on the surface of the shale; Right: Boudinage structures along the bedding surface.

5.1.5.2 Concretions Observed in the Jansenville Road Quarry

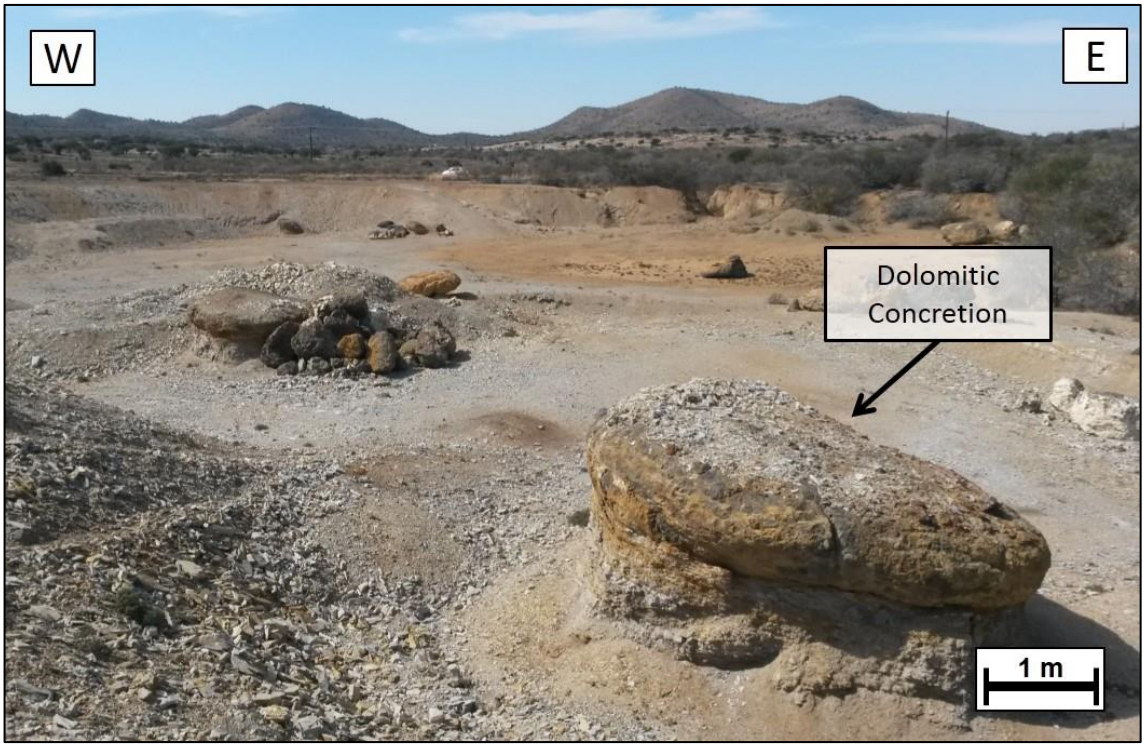

Figure 5.34: Dolomitic concretions observed in the Jansenville Road quarry within Site E.

A number of concretions are exposed within the Jansenville Road quarry, some of which remain *in situ* providing a good representation of the position of the concretions within the Whitehill Formation. The concretions exhibit a variety of colour changes but are all generally yellow-brown to dark-grey in colour. Their surfaces are made up of hard dolomitic material which exhibits septarian fractures throughout. The majority of the concretions are scattered about the quarry floor in positions likely chosen by the miners who had excavated the softer material from the quarry for use on the adjacent gravel road (**Figure 5.34**). This allows for measurements to be obtained along the x, y and x axes of the concretions. The concretions have an average horizontal length of 3.1m, an average width of 2.0m and an average vertical height of 0.8m (**Table 5.3**).

Table 5.3: Three-dimensional concretion dimensions - Site E

	Length (m)	Width (m)	Height (m)	Area (m^2)
Concretion 1	2.1	1.5	0.7	2.2
Concretion 2	3.5	2.2	1.0	7.7
Concretion 3	6.6	2.1	1.6	22.2
Concretion 4	3.0	1.7	0.9	4.6
Concretion 5	1.8	1.3	0.5	1.2
Concretion 6	1.0	0.7	0.4	0.3
Concretion 7	4.3	3.0	0.7	9.0
Concretion 8	3.2	2.1	0.8	5.4
Concretion 9	2.0	0.8	0.8	1.3
Concretion 10	3.4	2.4	0.8	6.5
Concretion 11	2.0	1.7	1.0	3.4
Concretion 12	2.2	1.1	0.5	1.2
Concretion 13	2.0	0.9	0.5	0.9
Concretion 14	3.9	2.3	0.8	7.2
Concretion 15	2.4	1.3	0.7	2.2
Concretion 16	1.8	1.1	0.6	1.2
Concretion 17	3.4	1.8	1.4	8.6
Concretion 18	4.8	2.0	1.2	11.5
Concretion 19	3.2	3.1	0.6	6.0
Concretion 20	4.6	3.3	0.7	10.6
Concretion 21	4.4	3.1	1.1	15.0
Concretion 22	1.1	1.0	0.4	0.4
Concretion 23	3.3	2.6	0.9	7.7
Concretion 24	4.0	3.0	1.1	13.2
Concretion 25	4.2	3.2	0.8	10.8
Average	**3.1**	**2.0**	**0.8**	**5.1**

The largest concretion observed throughout the study area is located within this quarry and is 6.6m by 2.1m by 1.6m with an approximate volume of 22.2m^3. The *in-situ* concretions which remain in the quarry are underlain by a thin, black gypsum vein which extends around many the concretions. Below the gypsum vein are alternating layers of grey-white weathered shale and minor yellow-brown tuffaceous material. Some shale located below the *in-situ* concretions also exhibits non-bedded minor gypsum deposits as well as minor haematite identified as red-brown 'rust-like' crustal strata. The shale layers underlying the concretions are generally horizontal however they do exhibit evidence of folding in certain places (**Figure 5.35**).

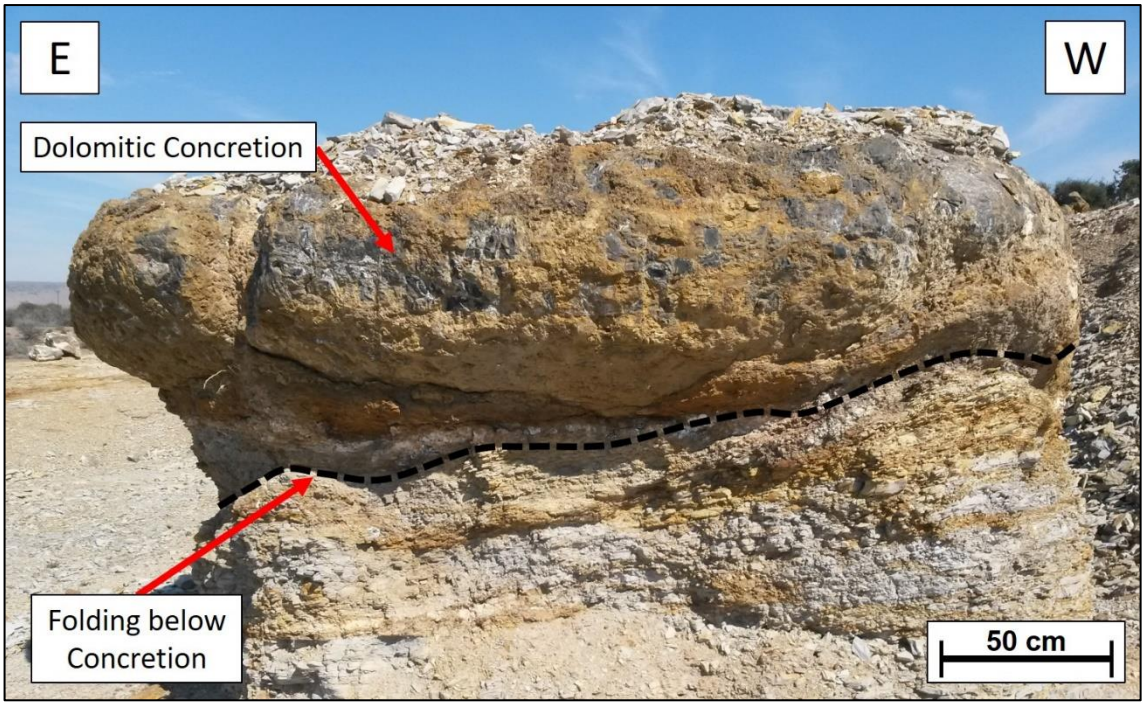

Figure 5.35: Concretion within the Jansenville Road quarry underlain by folded shale layers.

5.1.6 Site F

5.1.6.1 Erasmus Laaghte Farm 13 – West of R338

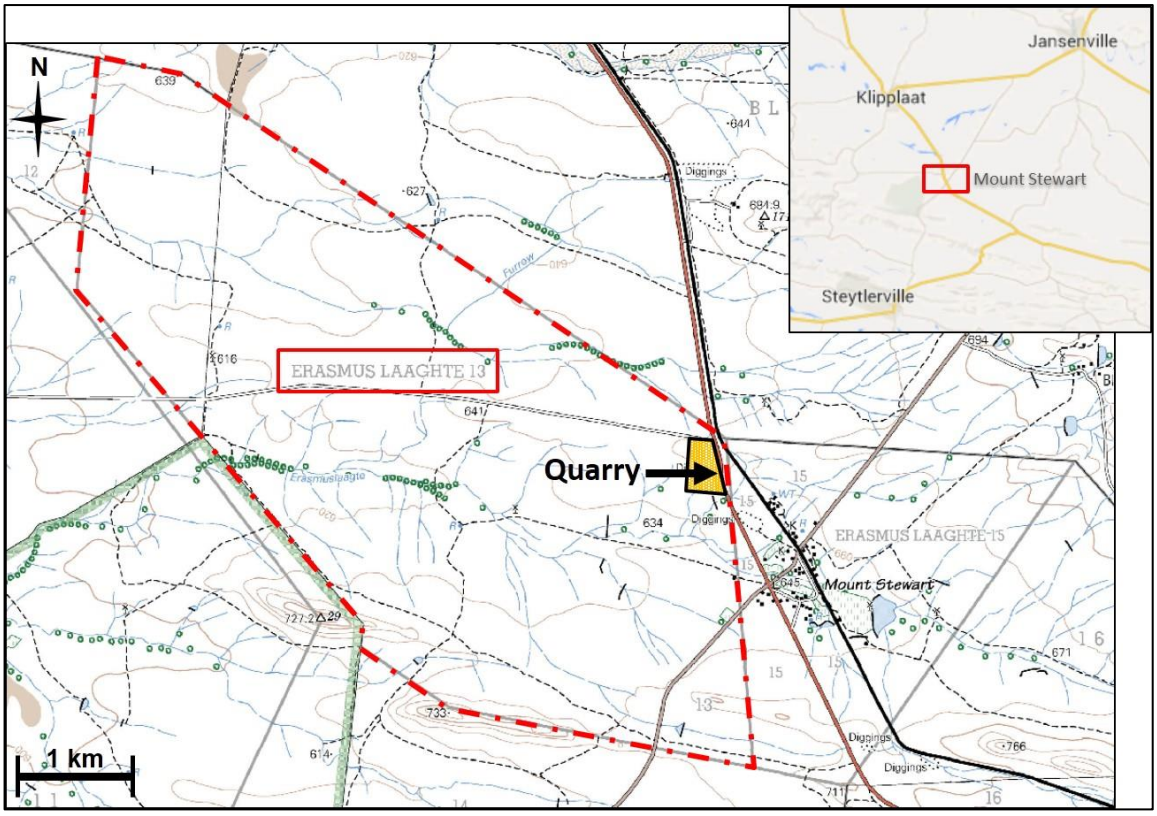

Figure 5.36: Location of Erasmus Laaghte Farm 13 west of the R338 in the Mount Stewart area.

There is an old road quarry situated in the northeast corner of this farm which is located 600m west of Mount Stewart and 2.5km south of the Mt Stewart PPC Gypsum Mine (**Figure 5.36**). Grey-white shale, interbedded with white or yellow tuffaceous sediment as well as white to translucent gypsum veins, are common within this quarry. Mudstone, in the form of mud flasers are also present (**Figure 5.37**). The western wall of the quarry exhibits a relatively large gypsum deposit which has a variation of colours including grey, white, yellow, orange and red gypsum crystals (**Figure 5.38**). The surface area where the gypsum is found is covered by the succulent shrub "*Euphorbia Esculenta*" which farmers in the region refer to as "vingerpol" (**Figure 5.39**).

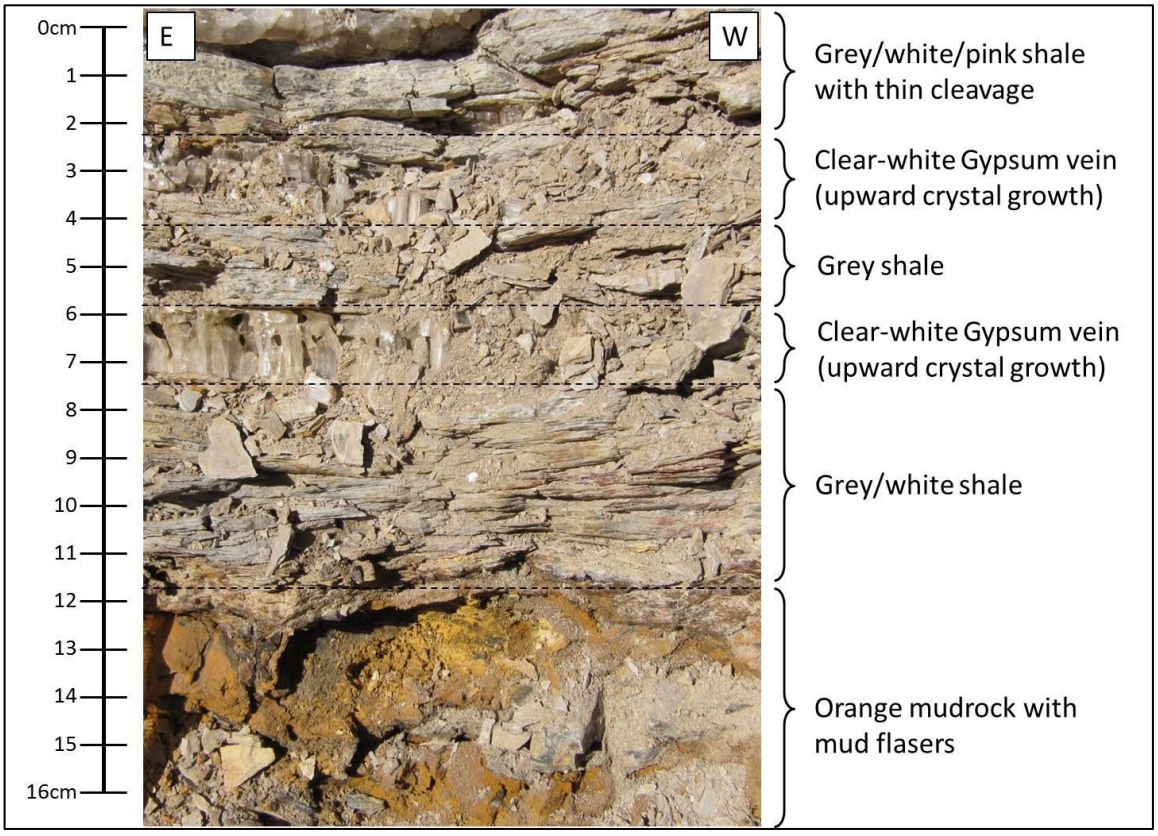

Figure 5.37: Cross section from east to west through shale of the Whitehill Formation located within the road quarry on Erasmus Laaghte Farm 13 next to the R338.

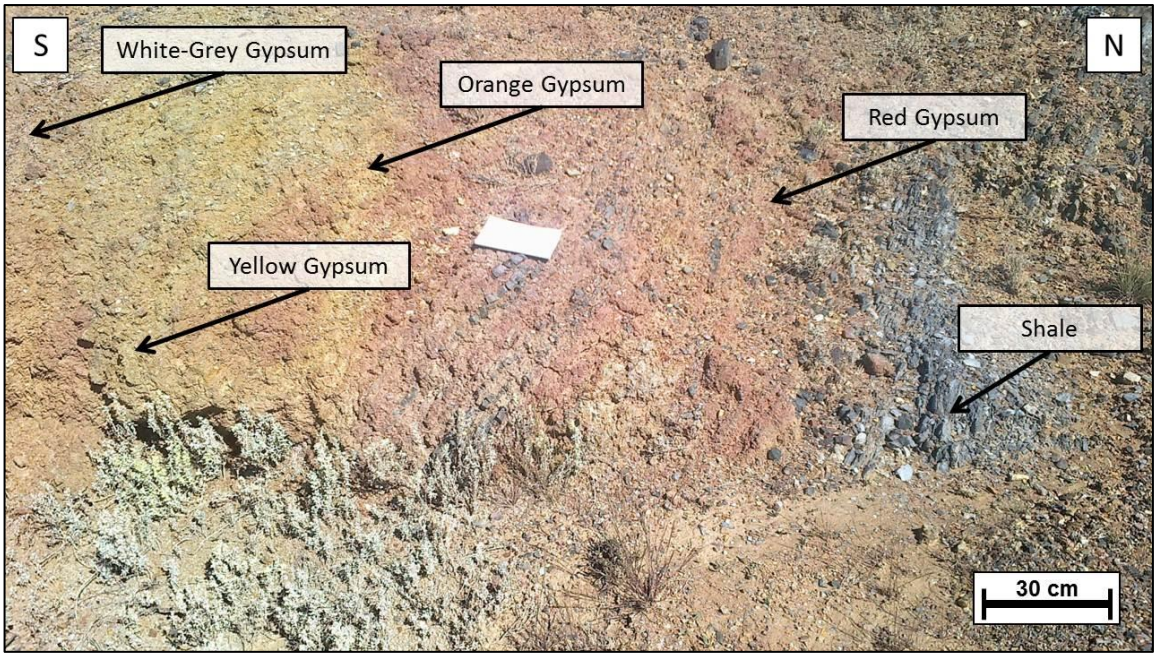

Figure 5.38: Cross section from south to north through a large gypsum deposit within the road quarry on Erasmus Laaghte Farm 13. Notice the variation of colours exhibited by the gypsum crystals.

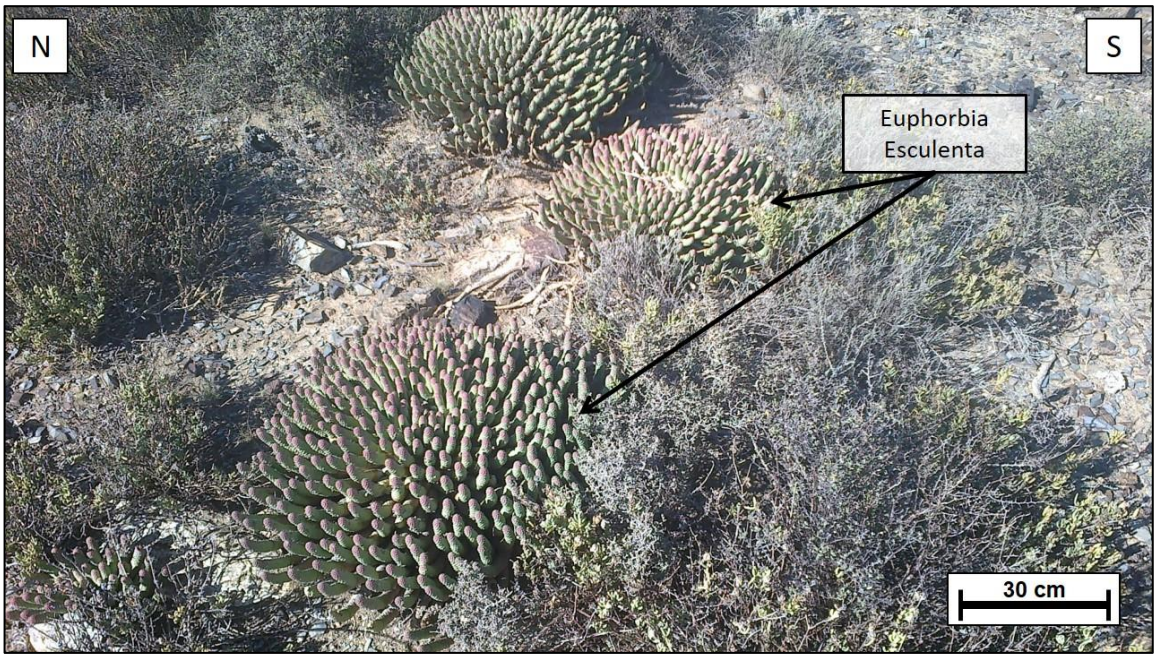

Figure 5.39: *Euphorbia Esculenta* located on Erasmus Laaghte Farm 13.

5.1.6.2 Traverse from South to North through Erasmus Laaghte 13 Quarry

The geology of the western wall of the quarry was mapped along a 40 metre traverse (**Figure 5.40**). The quarry wall consists mostly of grey shale which weathers to a light-grey or white colour. The shale is interbedded with yellow

tuffaceous sediment which also weathers to a lighter colour. Non-bedded gypsum surface crusts are found as both massive deposits of varying crystal colours and sizes as well as gypsum veins which precipitate vertically between the shale strata (**Figure 5.37**).

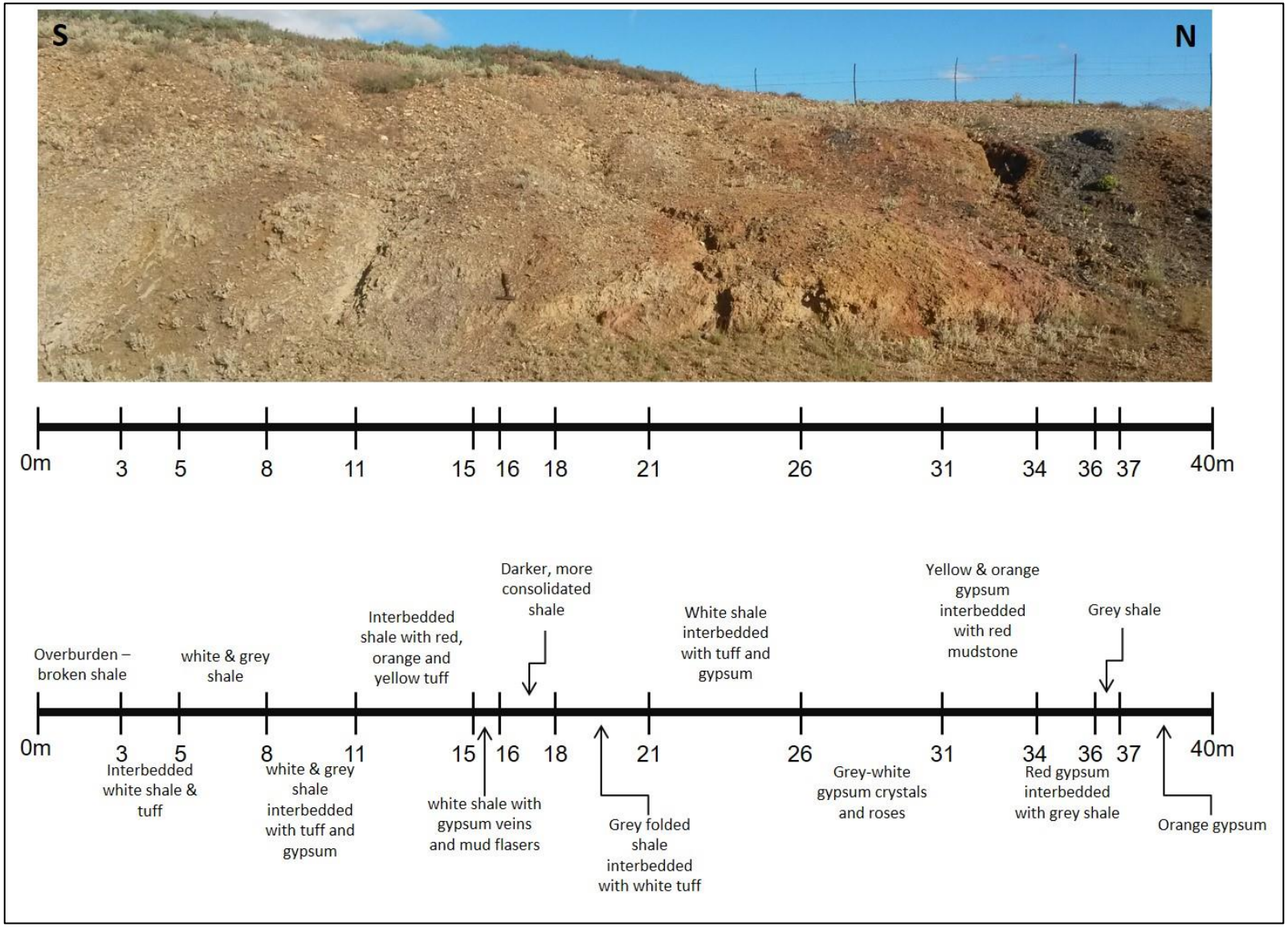

Figure 5.40: South-north traverse along quarry on Erasmus Laaghte Farm 13 next to R338. The scale represents changes in lithology over a 40m traverse where both sectional and plan view lithologies were noted.

There is a distinct change in the degree of weathering of the shale at a specific point within the succession (**Figure 5.41**). Towards the south, the shale is weathered and plays host to a larger quantity of gypsum. Towards the north however, the shale is harder, less weathered and contains little to no gypsum. The harder shale is brown in colour, has a rough texture and exhibits iron oxide encrustations at the surface. The harder shale is jointed at perpendicular angles to the bedding plane which results in small orthogonal blocks of shale. The layers of tuff remain interbedded within the shale.

Another portion of the quarry exhibits a small monocline fold where, at the point of weakness, a small gully has formed (**Figure 5.42**). North of this monocline, large gypsum deposits consisting of multi-coloured crystals have been precipitated.

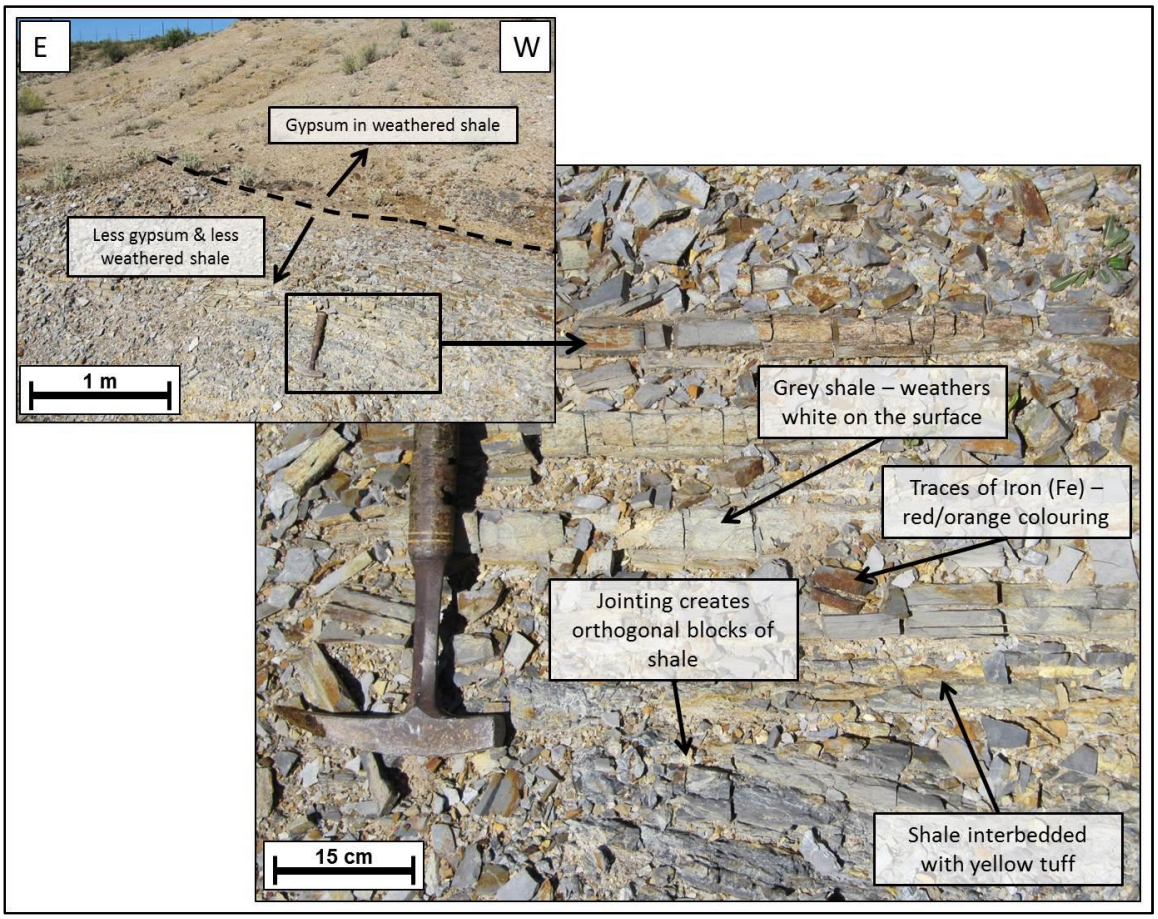

Figure 5.41: Shale of the Whitehill Formation observed in the quarry on Erasmus Laaghte Farm 13 adjacent to the R338 district road. Note the change in the weathered nature of the shale in the north, compared to those in the south.

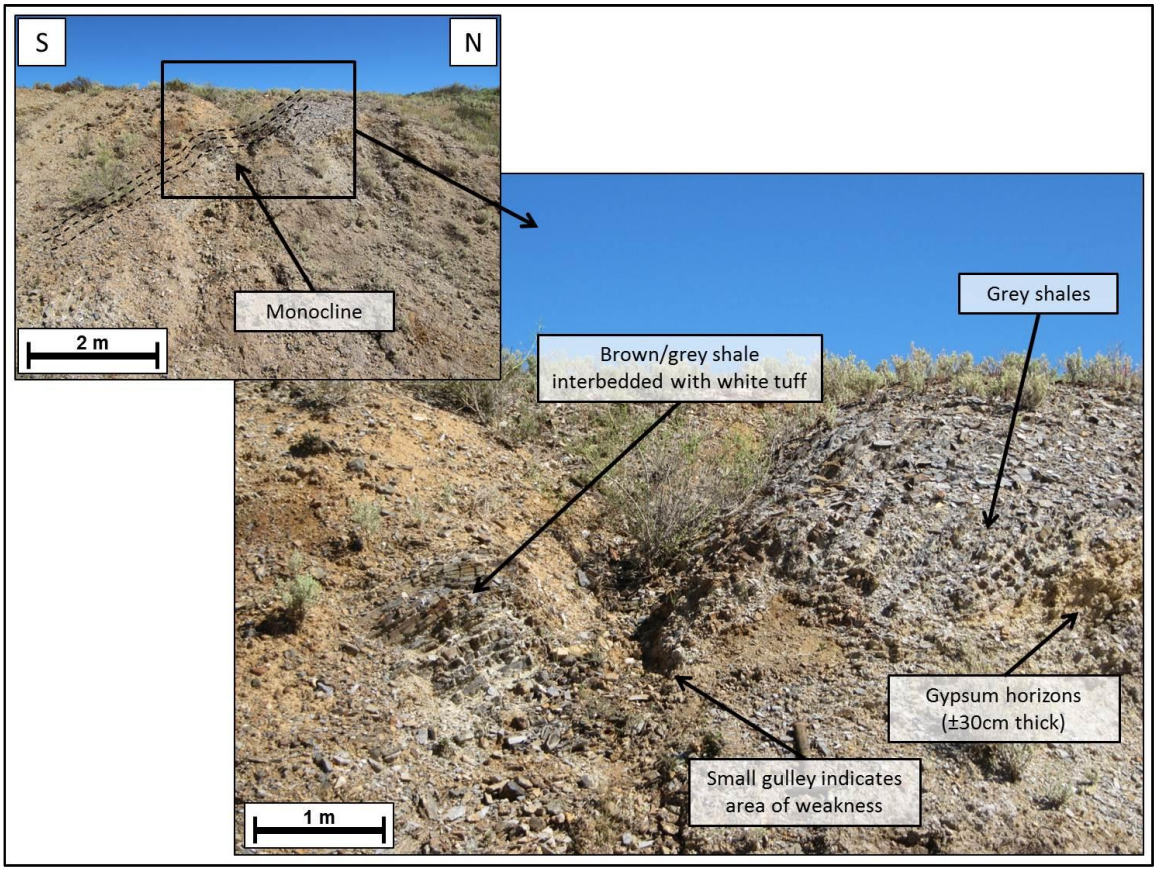

Figure 5.42: Monocline observed in the shale exposed along the western wall of the quarry on Erasmus Laaghte Farm 13 next to the R338. Note the gully that has formed in line with the monocline as well as the gypsum deposits to the north of the fold.

5.1.6.3 Strike and Dip Readings Taken along Cherty-Shale Outcrop

Bedding orientation data was obtained along two outcrops of cherty-shale (Matjiesfontein chert) located south of the quarry within Erasmus Laaghte 13. Azimuth and dip readings were taken along a 2.5km extent of the northern and southern limb of a macroscale syncline. The south-dipping northern limb of the chert is, on average, dips 47º to the south-southwest and strikes at 108º ESE to WNW. The north-dipping southern limb of the syncline also strikes ESE to WNW (at 114°) and dips at an average of 54° towards in a north-northeast direction. The orientation of mesoscale folds was also recorded within the area where the macroscale fold hinge zone is exposed at the surface. The north-dipping limbs of the mesoscale fold dips, on average, 64° towards the south-southwest, while the south-dipping limbs have an average dip of 63° towards the north-northeast. The average strike of the respective limbs is 109° and 106° and therefore both strike in an east-southeast to west-northwest direction (**Figure 5.43**).

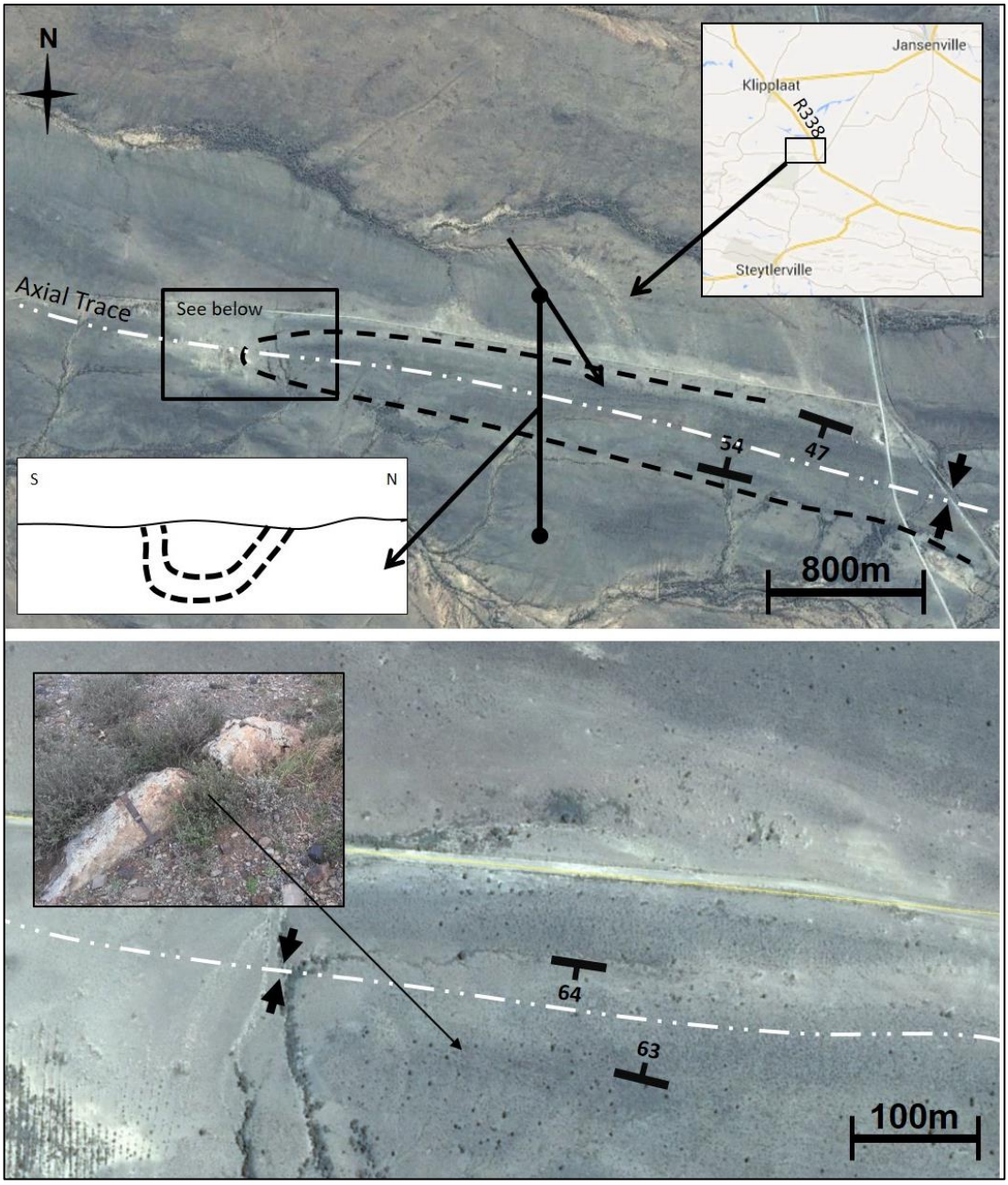

Figure 5.43: Syncline on Erasmus Laaghte Farm 13 west of the R338.

5.1.7 Site G

5.1.7.1 Erasmus Laaghte Farm 15 – East of R338

Another road quarry is located on a section of Erasmus Laaghte Farm 15, this one being on the east side of the R338 district road, directly adjacent to the Mount Stewart settlement (**Figure 5.44**). Shale of the Whitehill Formation is exposed on the northern wall of the quarry and the Matjiesfontein cherty-shale layer is outcropping approximately 80m north of the quarry. In the southeast corner of the quarry, a dry river bed with a rich deposit of gypsum is exhibited. The quarry is

located on the north-dipping, southern limb of the same fold which was studied on Erasmus Laaghte Farm 13 west of the R338 (**Figure 5.46**).

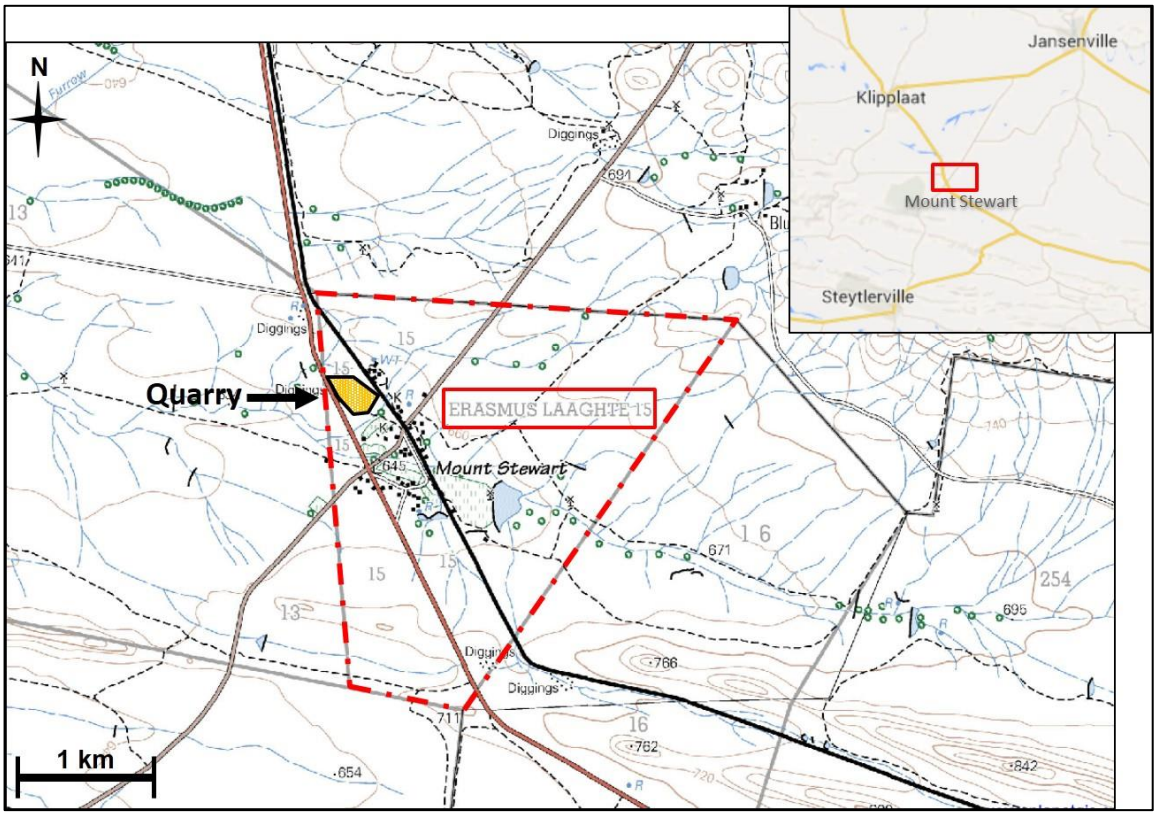

Figure 5.44: Location of road quarry on Erasmus Laaghte Farm 15 east of the R338 with relation to Mount Stewart.

On average, the bedding planes dip 60º to the north-northeast and strike east-southeast to west-northwest (at 109º). The contact between Whitehill Formation and Collingham Formation is observed on the northern wall of the quarry showing the distinct change from grey-white, thinly bedded shale of the Whitehill Formation to the brown, thicker shale beds of the Collingham Formation strata. The shale of the Whitehill Formation has also precipitated a fine-grained white powder at the surface (**Figure 5.45**). The *in-situ* gypsum deposits located in the dry river bed occur as wavy, horizontally bedded, highly-weathered crusts and the gypsum crystals show no particular direction of crystal growth (**Figure 5.47**). The cherty-shale outcrop, to the north of the quarry (within the Collingham Formation), dips 61º to the north-northeast and it strikes east-southeast to west-northwest (at 113º) (**Figure 5.46**).

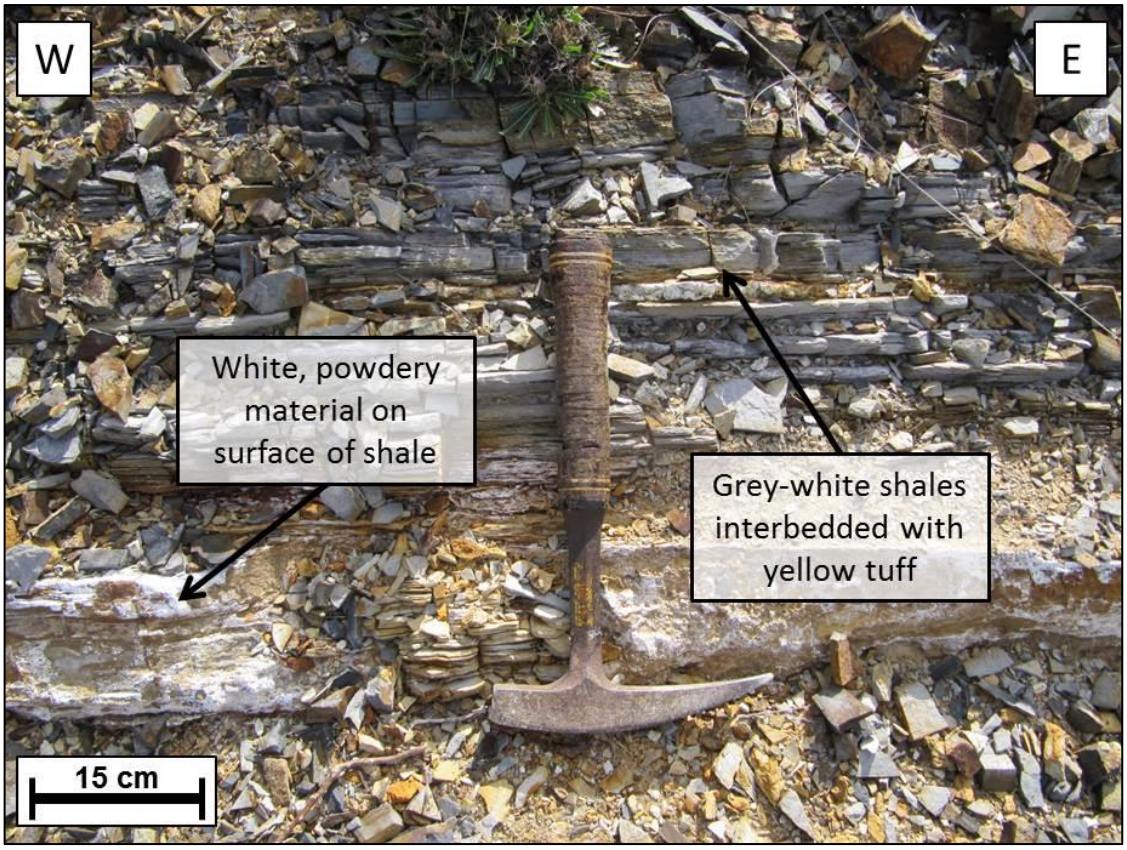

Figure 5.45: Shale of the Whitehill Formation observed on the northern wall of the quarry on Erasmus Laaghte Farm 15 east of the R338. Note the interbedded tuffs as well as the powdery material on the surface of the shale. This shale dips to the north as part of the southern limb of a syncline.

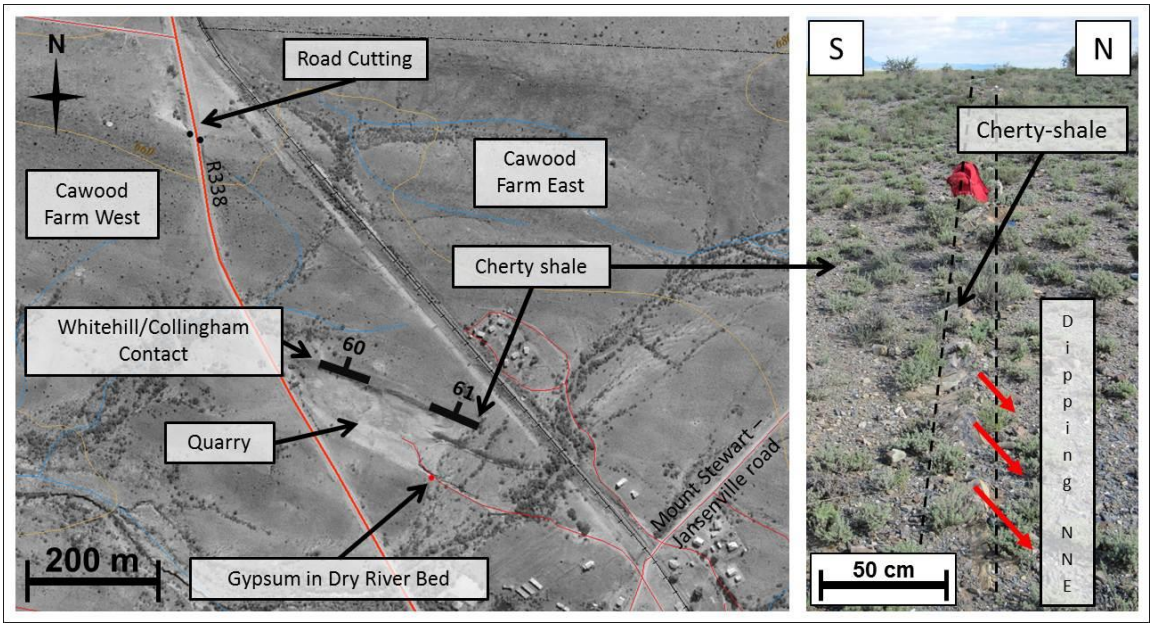

Figure 5.46: Left: Area of Erasmus Laaghte Farm 15 with the road quarry on the east side of the road. Whitehill Formation-Collingham Formation contact is shown along with the outcrop of the cherty-shale and the gypsum deposit in a dry river bed. Right: Cherty-shale outcrop north of the quarry.

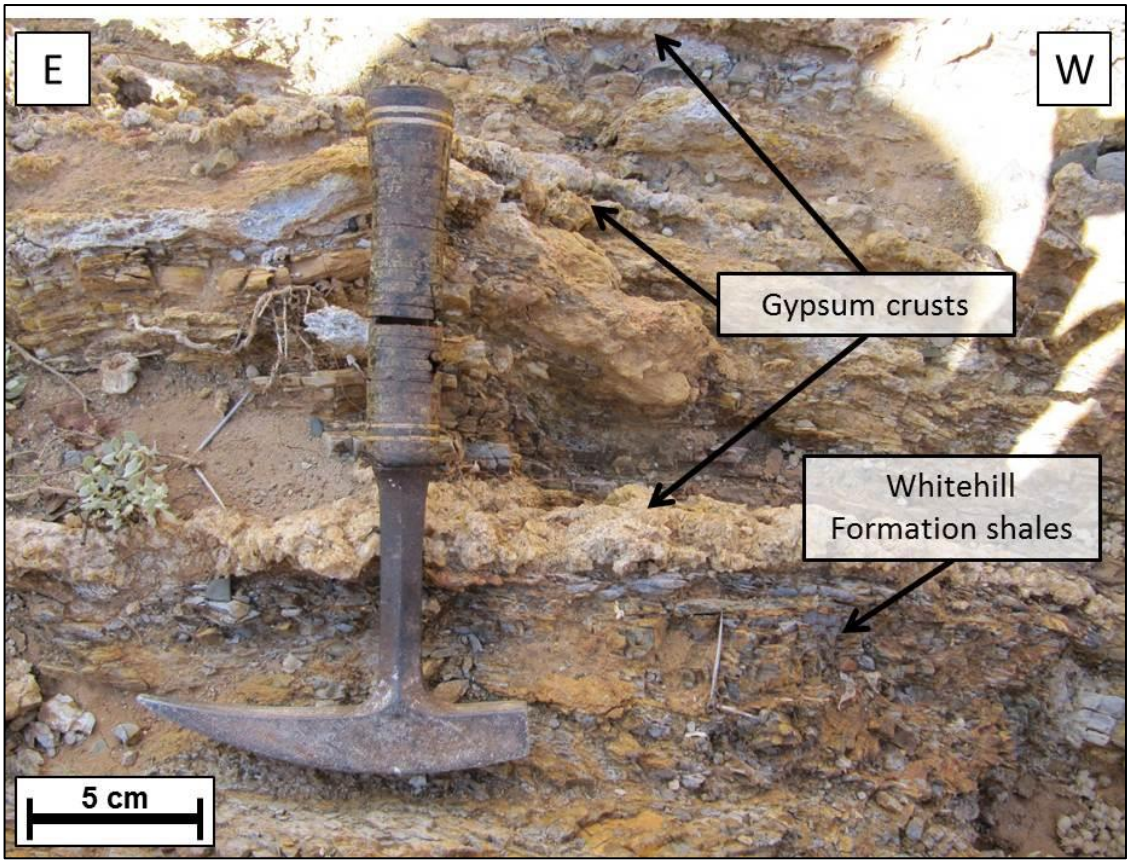

Figure 5.47: Gypsum crusts observed on the southern wall of the quarry located on Erasmus Laaghte Farm 15 east of the R338 (see **Figure 5.46**). These deposits occur in a dry river bed and exhibit no particular crystal growth direction.

5.2 Structural Analysis

The project area is characterised by intensely folded strata consisting of meso- and macro-folds occurring on different scales. Macro-scale folds can only be seen from satellite imagery and their north-dipping and south-dipping limbs are outcropping, on average, approximately 3km apart. Smaller folds are observed in the field outcropping at the hinge zones of the larger folds. The limbs of these folds are separated by between 2m and 20m depending on the position relative to the fold axis. Much smaller folds (no more than 10cm between limbs) have also been observed on certain outcrops including areas where gypsum has precipitated. In addition to this, folding is apparent on a microscopic scale as observed during thin section analysis.

Four macro-scale folds occur in the project area – one anticline and three synclines (**Figure 5.48**). Fold 'A' is a simple syncline with its hinge zone 'a' outcropping in the east. The fold hinge zone 'b' of syncline 'B' outcrops west of the fold limbs and forms part of a bigger syncline, Fold 'C.' The fold hinge zone 'c'

outcrops west of the fold limbs and is also at the location of PPC Mount Stewart as well as well SA Lime Eastern Cape located directly across the R338 road. Fold 'D' is the only measurable macro-scale anticline in the project area and the outcropping hinge zone 'd' is located towards the west of the fold limbs.

430 bedding readings have been recorded in the project area. 150 are from south-dipping fold limbs and 111 from north-dipping fold limbs. The other 169 readings have been recorded from outcrops at the fold hinge zones (**Figure 5.49**).

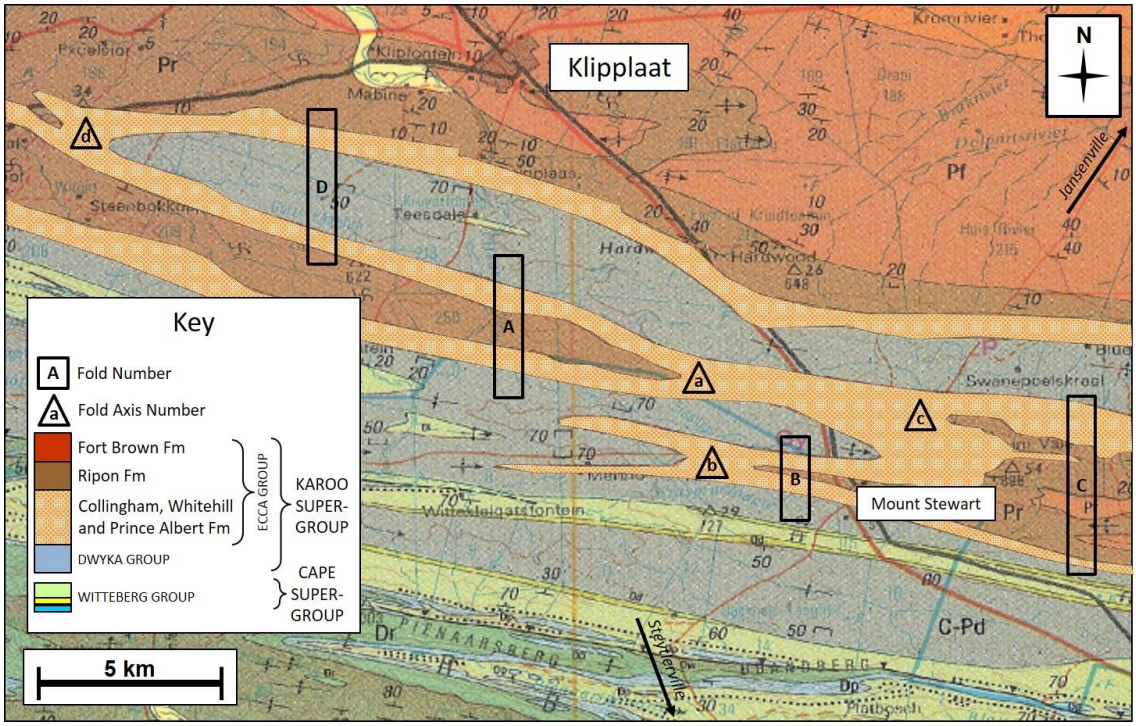

Figure 5.48: Geology of the project area showing Folds A, B, C and D as well as the outcropping fold hinge zone (a, b, c and d) as described in the text. Note that A, B and C are synclines while D is an anticline.

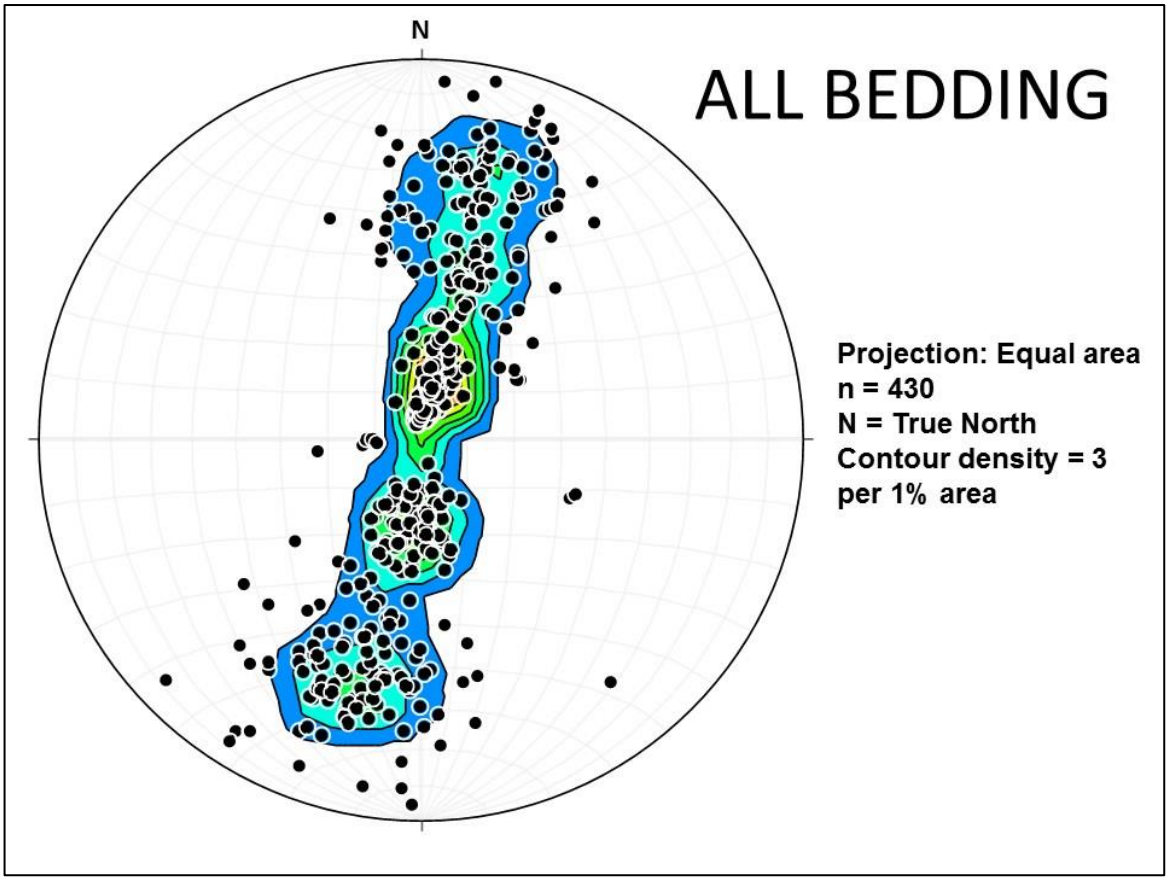

Figure 5.49: Stereoplot of all 430 bedding readings obtained in the project area. Points represent poles to bedding planes and have been contoured to 3 per 1% area.

5.2.1 Macro-Scale Folds and Meso-Scale Folds

The macro-scale folds, namely Fold A, B, C and D were illustrated on a stereoplot as points to a bedding plane and were then contoured by the 1% Area setting. The contoured poles to bedding plane provide an understanding of the most common orientation for the folds which are observed from satellite imagery. While the degree of dip varies considerably, the azimuth of the macro-scale folds all dip in either a north or south direction (**Figure 5.50**). The readings obtained at the hinge zones of the macro-scale folds have also been represented on a stereoplot (**Figure 5.51**). While the orientation of these readings appears to be randomly distributed, the overall direction of dip continues in either a north or south direction. Because these plots represent data from different locations within the project area, it does not allow for direct comparison between the limbs of a macro-scale fold and the smaller folds at its hinge zone.

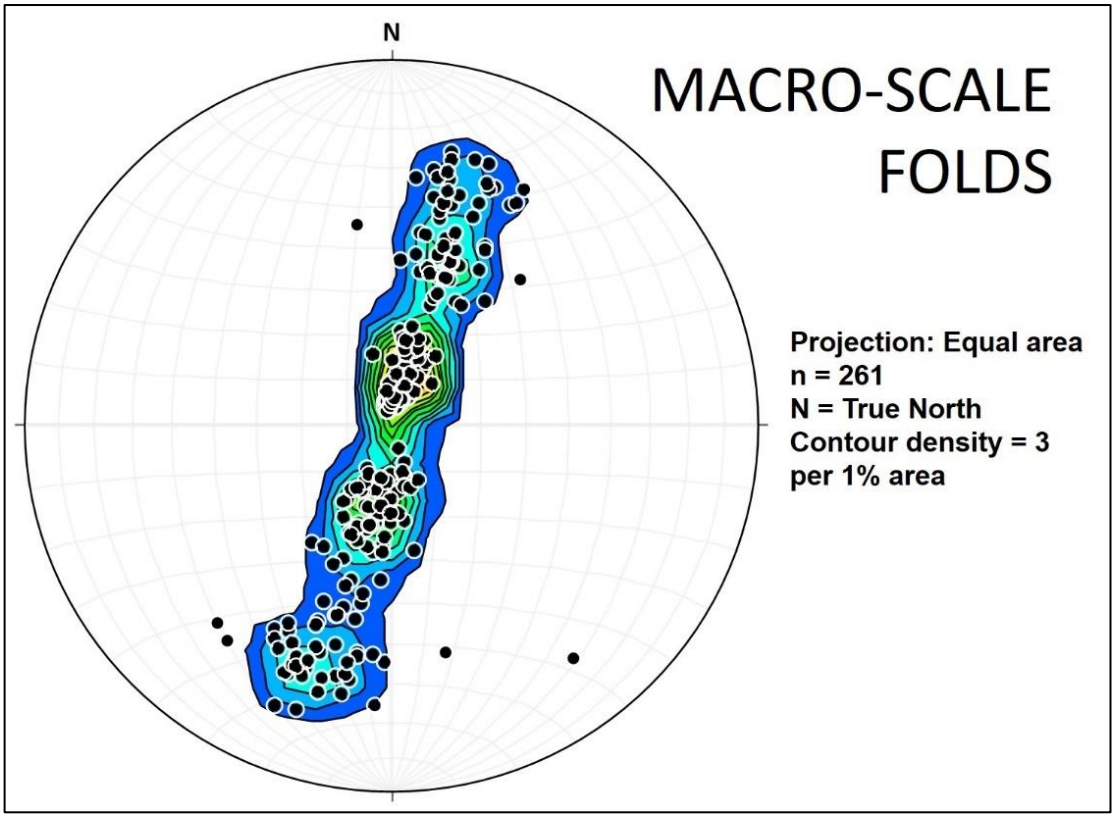

Figure 5.50: Stereoplot of 261 bedding readings obtained on macro-scale fold limbs. Points represent poles to bedding planes and have been contoured to 3 per 1% area.

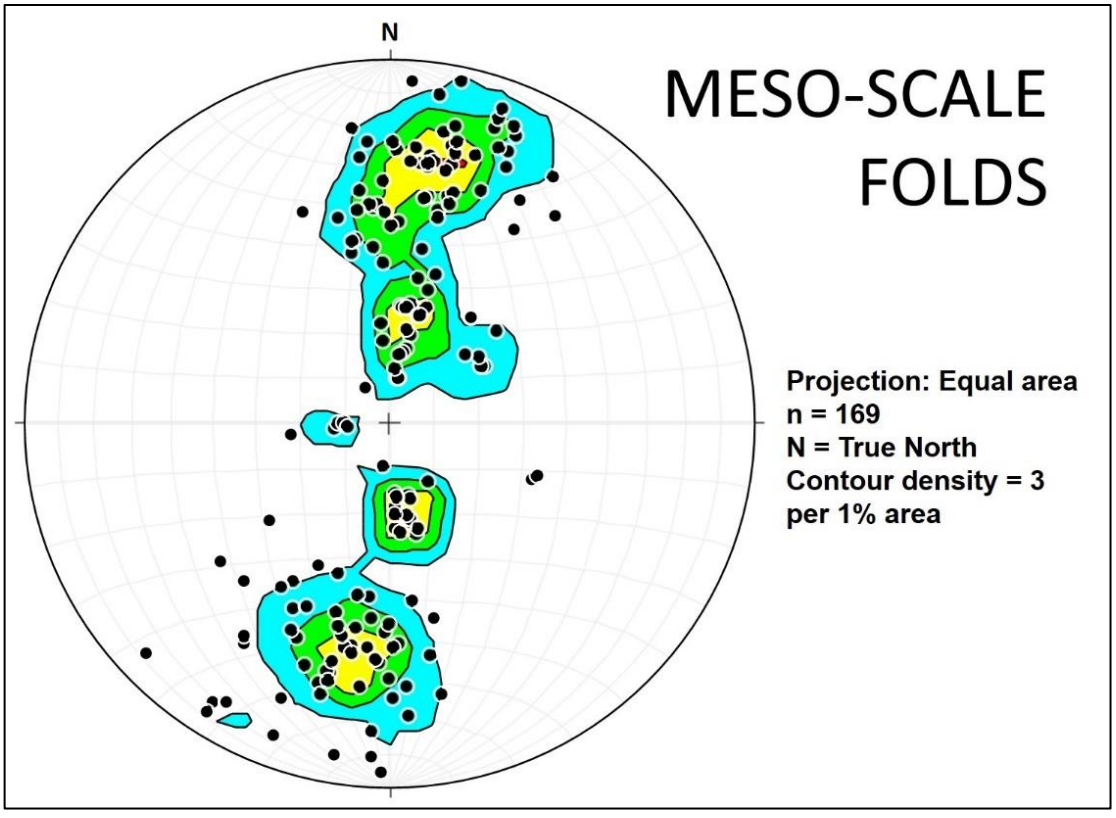

Figure 5.51: Stereoplot of 169 bedding readings obtained on smaller folds at the hinge zones of macro-scale folds. Points represent poles to bedding planes and have been contoured to 3 per 1% area.

5.2.1.1 Fold A

This syncline is located in the centre of the project area and extends in a westerly direction with its fold hinge zone outcropping in the east on the farms Erasmus Laaghte 13/2, East of Gouskraal 257/4 and East of Gouskraal 257/1. 50 bedding readings were taken on both fold limbs and 51 readings were taken at the outcrop of the fold hinge zone. The axial plane of Fold A strikes WNW to ESE (at 282°) and dips at 89° in a south-southwest direction (**Figure 5.52**). The interlimb angle is 146° and the fold axis trends in a west-northwest direction (282°) plunging at 2°. The meso-scale folds at the hinge zone of Fold A have an average axial plane which strikes ESE to WNW (at 104°) and dips 83° towards the north-northeast (**Figure 5.53**). The average interlimb angle is 62° while the fold axis trends in an east-southeast direction (104°) plunging at 4°. The classification of Fold A on a macro-scale, as well as the classification of meso-scale folding at the hinge zone, is presented in **Table 5.4**.

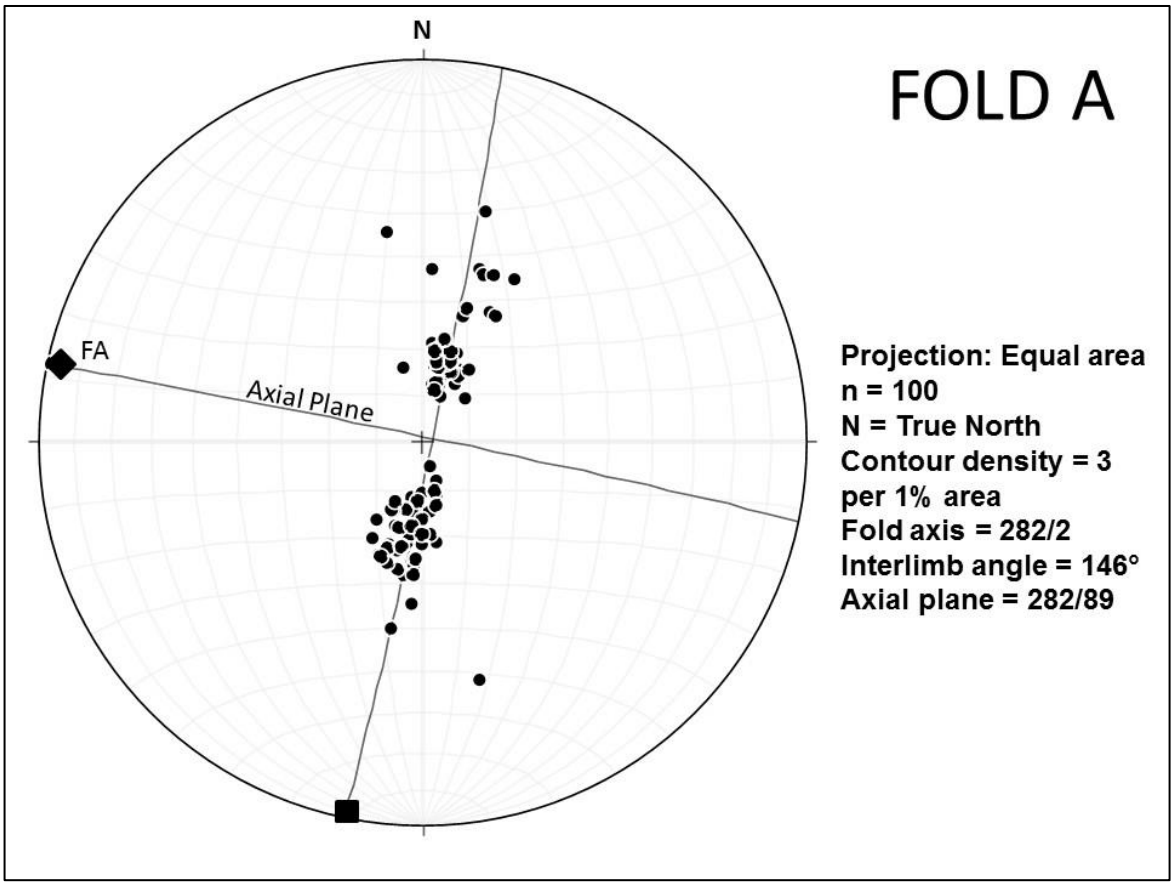

Figure 5.52: Stereoplot of 100 bedding readings obtained on the limbs of Fold A. Points represent poles to bedding planes. The axial plane and fold axis (FA) are also displayed.

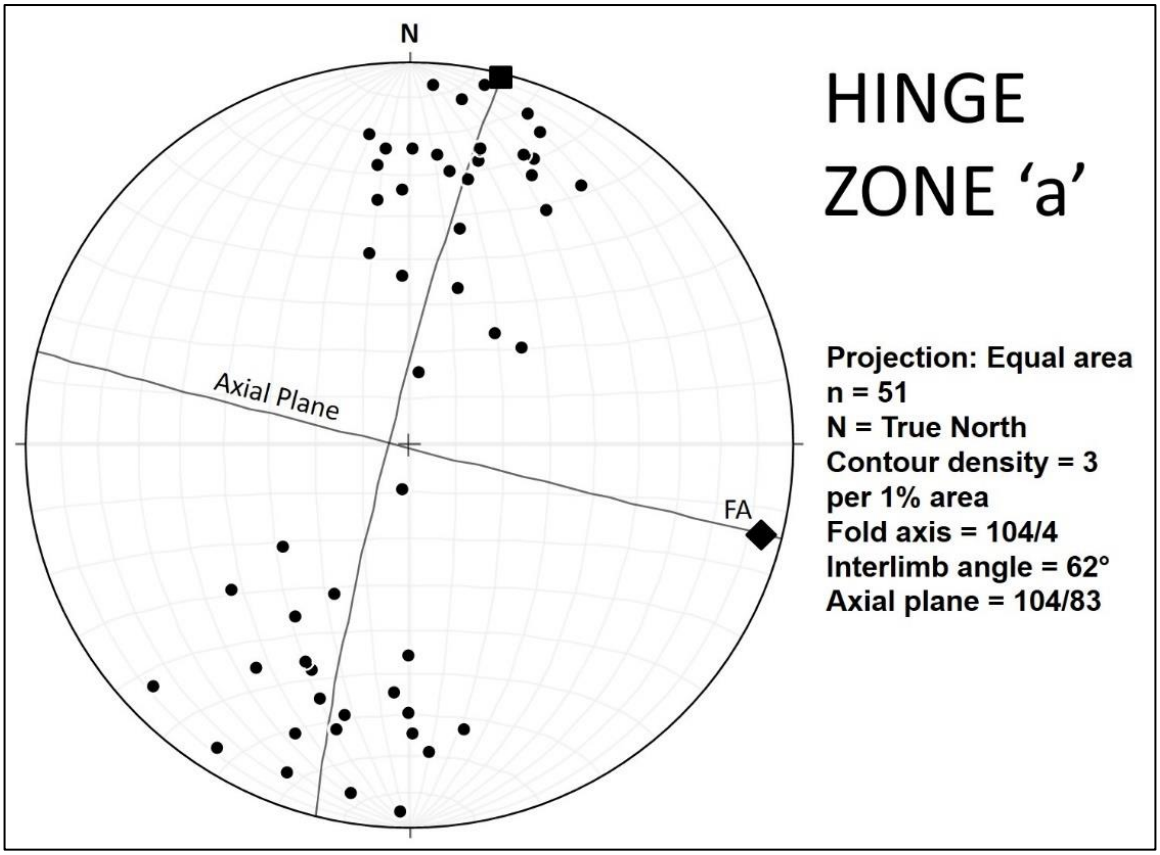

Figure 5.53: Stereoplot of 50 bedding readings obtained at the outcrop of the hinge zone of Fold A. Points represent poles to bedding planes. The average axial plane and fold axis (FA) are also displayed.

Table 5.4: Properties of Fold A (macro-scale fold) and Fold A Hinge Zone (meso-scale folds).

Fold Property	Fold A (Macro-scale)	Fold A Hinge Zone (Meso-scale)
Type	Syncline	Anticlines & Synclines
Shape	Cuspate	Cuspate
Tightness	Gentle (146°)	Close (62°)
Symmetry	Symmetrical	Symmetrical
Deformation Style	Similar	Similar

5.2.1.2 Fold B

Located in the south-east of the project area, this smaller syncline extends in an easterly direction with its fold hinge zone outcropping in the west on the farm Erasmus Laaghte 13/RE. Fold B shares a north-dipping limb with Fold C and is essentially a 'meso-scale' fold within Fold C. 50 bedding readings were taken on the south-dipping limb and 51 on the north-dipping limb whilst only 19 bedding readings were recorded at the outcrop of the fold hinge zone. The axial plane of Fold B strikes ESE to WNW (at 108°) and dips at 80° in a north-northeast direction

(**Figure 5.54**). The interlimb angle is 76° and the fold axis trends in a west-northwest direction (282°) plunging extremely gently at 1°. The meso-scale folds at the hinge zone of Fold B have an average axial plane which strikes WNW to ESE (at 287°) and dips at 81° towards the south-southwest (**Figure 5.55**). The average interlimb angle is 60° while the fold axis trends in a west-northwest direction (288°) plunging at 4°. The classification of Fold B on a macro-scale, as well as the classification of meso-scale folding at the hinge zone, is presented in **Table 5.5**.

Table 5.5: Properties of Fold B (macro-scale fold) and Fold B Hinge Zone (meso-scale folds).

Fold Property	Fold B (Macro-scale)	Fold B Hinge Zone (Meso-scale)
Type	Syncline	Anticlines & Synclines
Shape	Cuspate	Cuspate
Tightness	Open (76°)	Close (60°)
Symmetry	Symmetrical	Symmetrical
Deformation Style	Similar	Similar

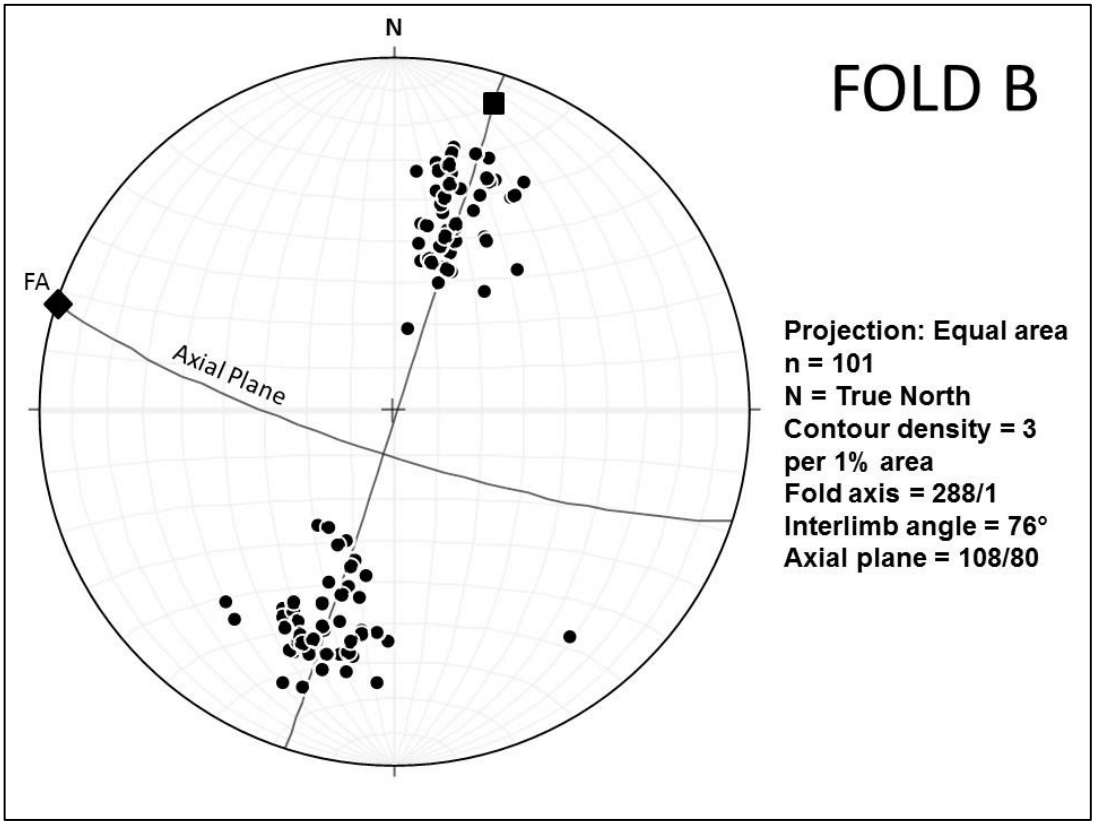

Figure 5.54: Stereoplot of 101 bedding readings obtained on the limbs of Fold B. Points represent poles to bedding planes. The axial plane and fold axis (FA) are also displayed.

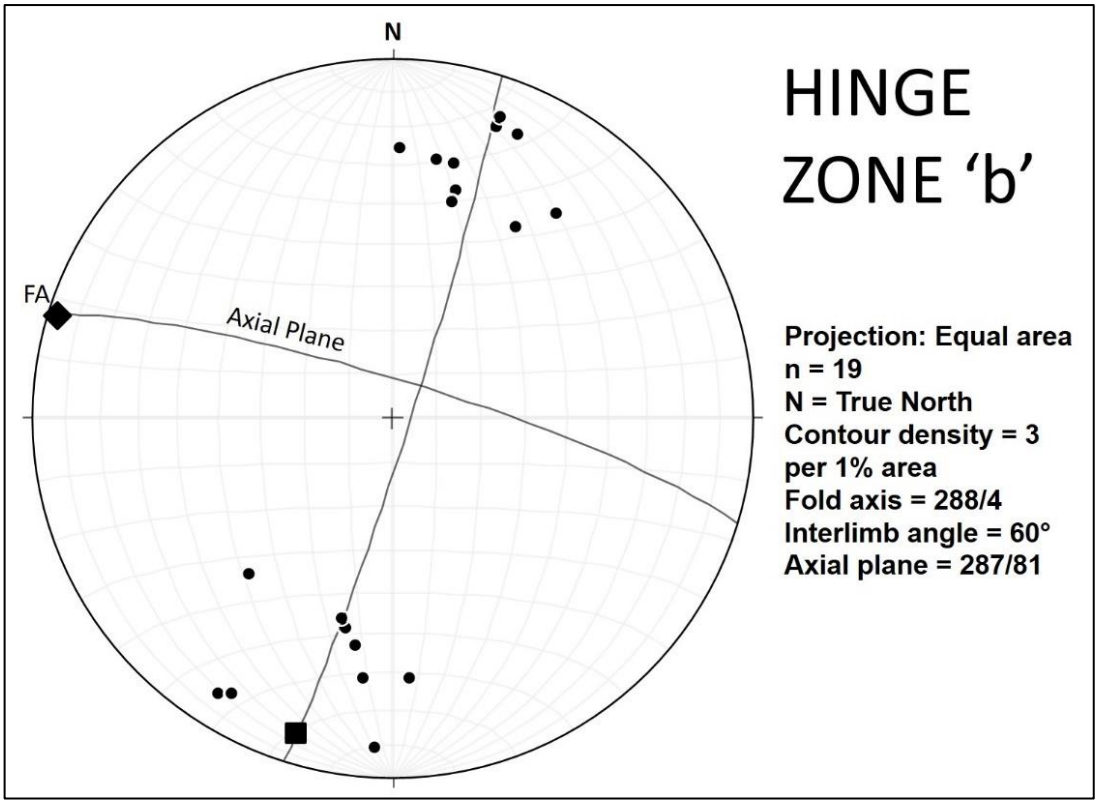

Figure 5.55: Stereoplot of 19 bedding readings obtained at the outcrop of the hinge zone of Fold B. Points represent poles to bedding planes. The average axial plane and fold axis (FA) are also displayed.

5.2.1.3 Fold C

This syncline, Fold C, is located in the east of the project area and extends in an easterly direction with its fold hinge zone outcropping in the west on the farms Bluegumvale 256/RE and East of Gouskraal 257/1. This fold is complex as it shares the same north-dipping limb as Fold B and therefore has a fold hinge zone which consists of macro-scale folds (e.g. Fold B) as well as small folds. 51, 50 and 64 readings were taken on the north-dipping limb, south-dipping limb and hinge zone folds respectively. The axial plane of Fold C strikes ESE to WNW (at 107°) and dips at 63° in a south-southwest direction (**Figure 5.56**). The interlimb angle is 109° and the fold axis trends in an east-southeast direction (107°) plunging at 1°. The meso-scale folds at the hinge zone of Fold C have an average axial plane which strikes ESE to WNW (at 97°) and dips at 89° towards the north-northeast (**Figure 5.57**). The average interlimb angle is 80° while the fold axis trends in an east-southeast direction (97°) and is horizontal (plunge of 0°). The classification of Fold C on a macro-scale, as well as the classification of meso-scale folding at the hinge zone, is presented in **Table 5.6**.

Table 5.6: Properties of Fold C (macro-scale fold) and Fold C Hinge Zone (meso-scale folds).

Fold Property	Fold C (Macro-scale)	Fold C Hinge Zone (Meso-scale)
Type	Syncline	Anticlines & Synclines
Shape	Cuspate	Cuspate
Tightness	Open (109°)	Open (80°)
Symmetry	Asymmetrical	Symmetrical
Deformation Style	Similar	Similar

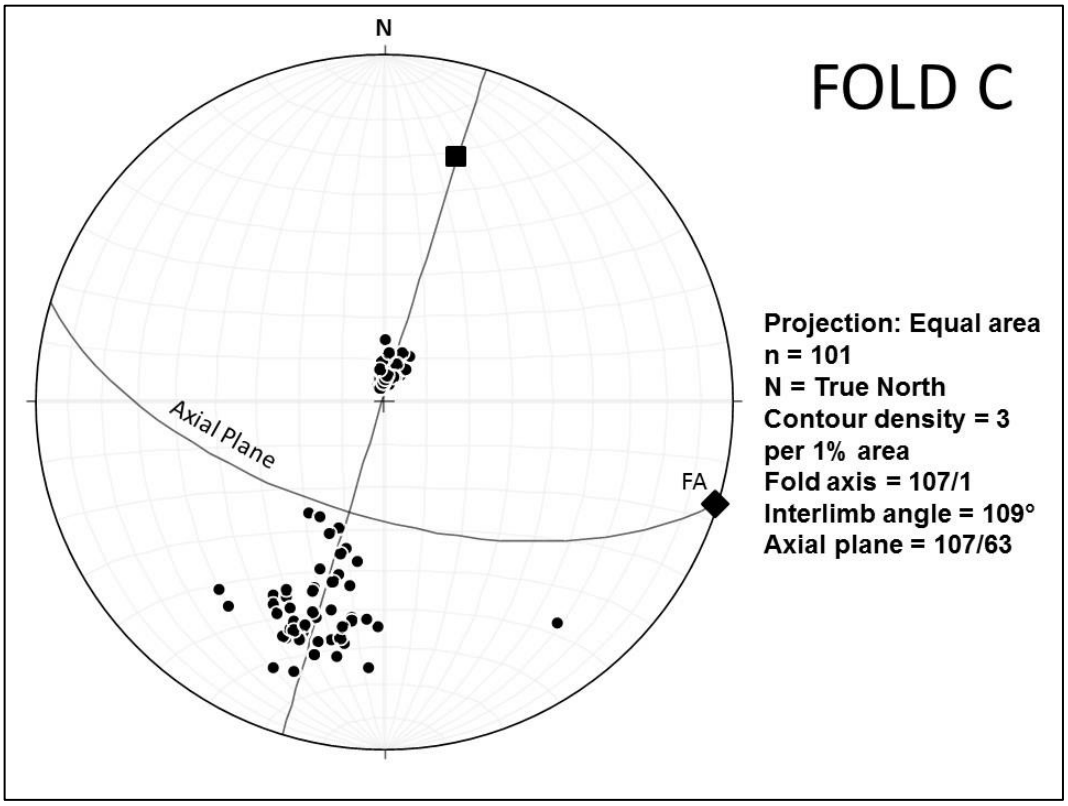

Figure 5.56: Stereoplot of 101 bedding readings obtained on the limbs of Fold C. Points represent poles to bedding planes. The axial plane and fold axis (FA) are also displayed.

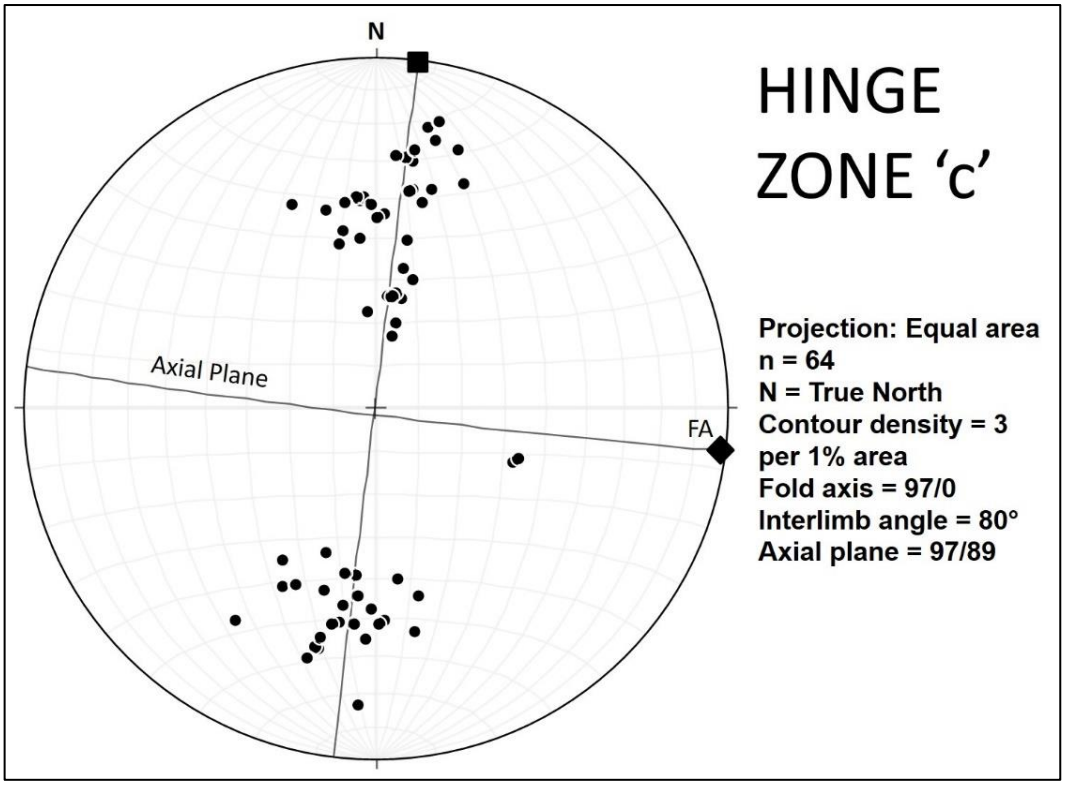

Figure 5.57: Stereoplot of 64 bedding readings obtained at the outcrop of the hinge zone of Fold C. Points represent poles to bedding planes. The average axial plane and fold axis (FA) are also displayed.

5.2.1.4 Fold D

This is the only macro-scale anticlinal fold of the Whitehill Formation which outcrops in the project area. It extends from the northwest towards the northeast of the project area with its hinge zone outcropping in the northwest on the farm Damplaats 198. 50 bedding readings were taken on the south-dipping limb and 10 on the north-dipping limb whilst only 35 bedding readings were recorded at the outcrop of the fold hinge zone. The axial plane of Fold D strikes WNW to ESE (at 284°) and dips at 89° in a south-southwest direction (**Figure 5.58**). The interlimb angle is 147° and the fold axis trends in a west-northwest direction (284°) plunging at 1°. The meso-scale folds at the hinge zone of Fold D have an average axial plane which strikes west to east (at 279°) with a perpendicularly dip of 90° (**Figure 5.59**). The average interlimb angle is 145° while the fold axis trends in a westerly direction (279°) plunging at 4°. The classification of Fold D on a macro-scale, as well as the classification of meso-scale folding at the hinge zone, is presented in **Table 5.7**.

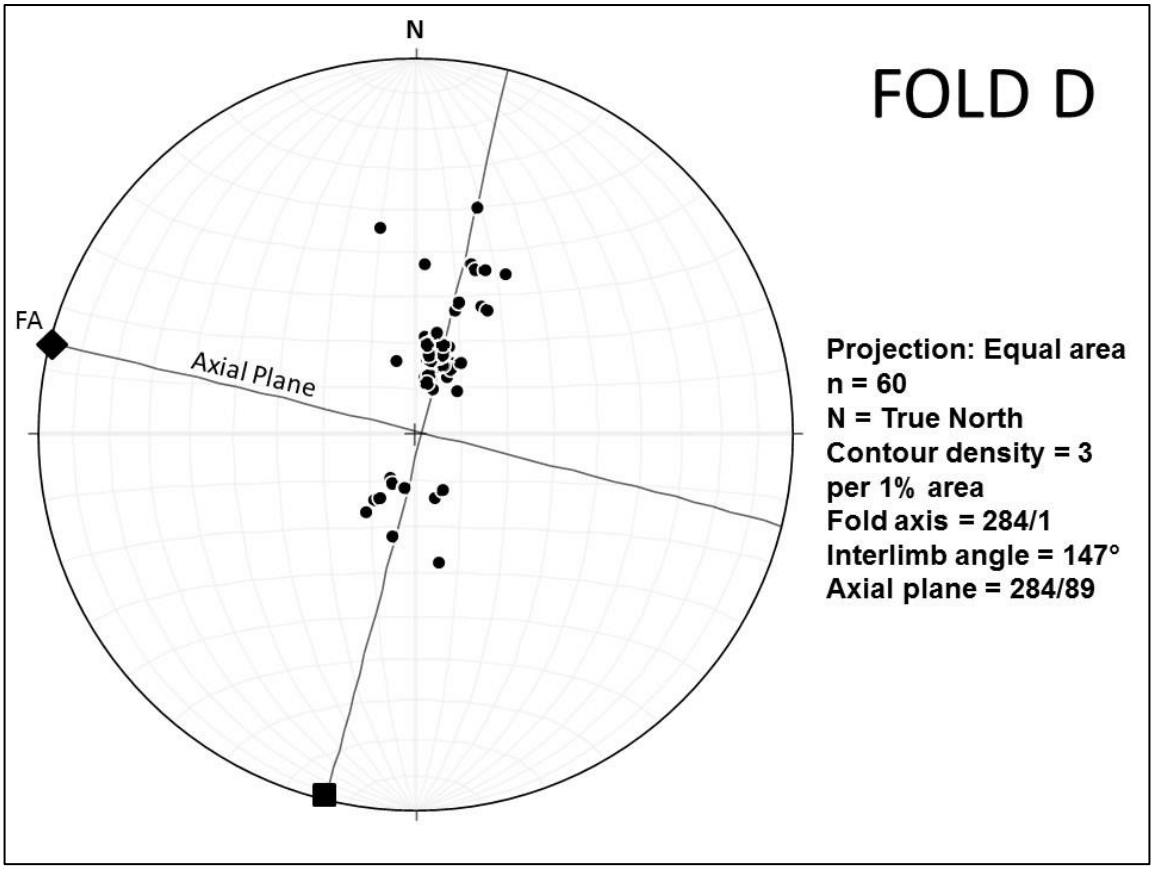

Figure 5.58: Stereoplot of 60 bedding readings obtained on the limbs of Fold D. Points represent poles to bedding planes. The axial plane and fold axis (FA) are also displayed.

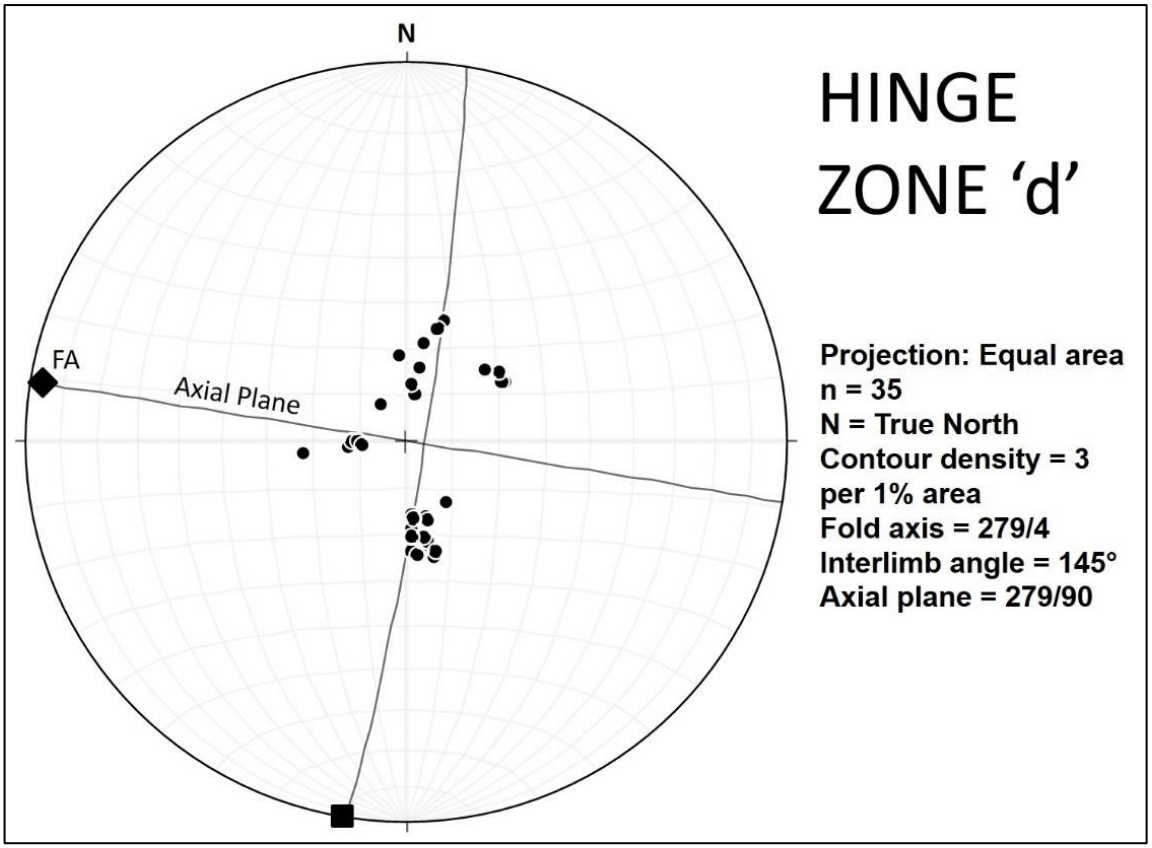

Figure 5.59: Stereoplot of 35 bedding readings obtained at the outcrop of the hinge zone of Fold D. Points represent poles to bedding planes. The average axial plane and fold axis (FA) are also displayed.

Table 5.7: Properties of Fold D (macro-scale fold) and Fold D Hinge Zone (meso-scale folds).

Fold Property	Fold D (Macro-scale)	Fold D Hinge Zone (Meso-scale)
Type	Anticline	Anticlines & Synclines
Shape	Cuspate	Cuspate
Tightness	Gentle (147°)	Gentle (145°)
Symmetry	Symmetrical	Symmetrical
Deformation Style	Similar	Similar

5.3 Analysis of the SFT2 Core

In 2011, the Nelson Mandela University (NMU) commissioned a drilling team to drill a 300m deep borehole through the lower strata of the Ecca Group. The borehole was collared in the Ripon Formation in an area approximately 45km east of this project's study area (**Figure 5.60**). The core drilling method was used to recover representative samples of the Ripon, Collingham, Whitehill and Prince Albert formations as well as to intersect the Dwyka Group tillites located at the base of the sequence. The core samples are currently stored at NMU South Campus and have been used in this study to better understand the properties of

the Whitehill Formation which are responsible for the proliferation on gypsum in this part of the Karoo Basin.

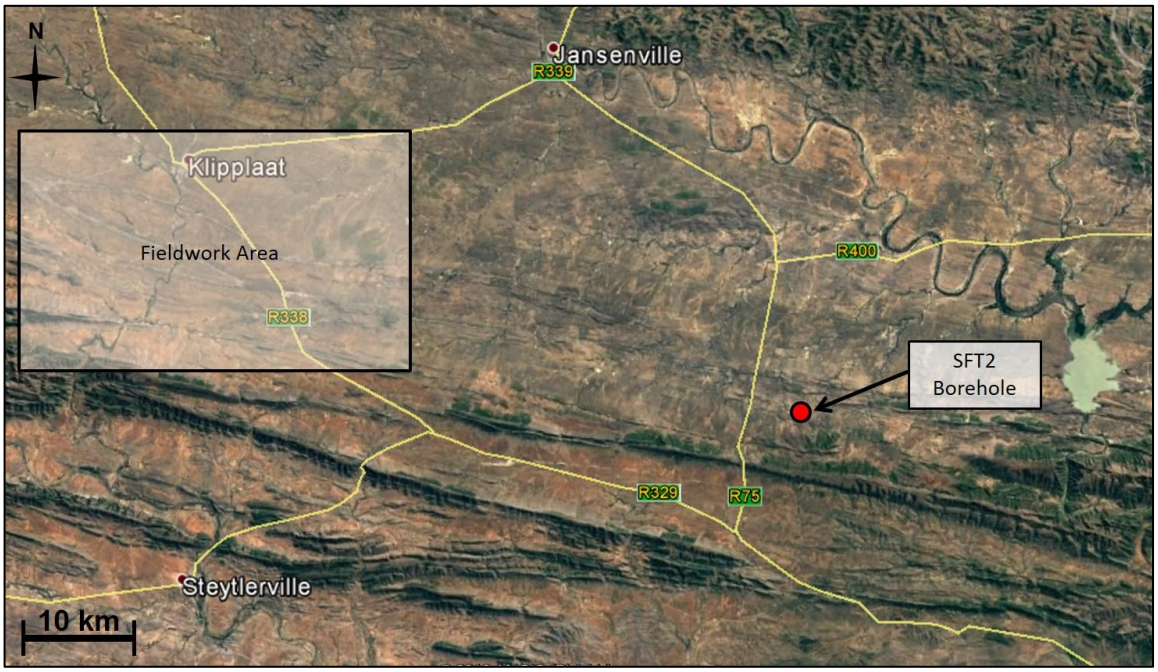

Figure 5.60: Location of the SFT2 Borehole in relation to the fieldwork area for this study.

For the purposes of this study, the geological log is described from a depth of 189.95m below hthe collar position of the SFT2 borehole and ends at 230.80m. This range was chosen to include the entire Whitehill Formation as well as shale from the Collingham Formation and Prince Albert Formation which includes the upper and lower contacts respectively. The borehole core log is included as **Appendix A** and the dry and wet core rock photos as **Appendix C**.

5.3.1 Collingham Formation

The logging of borehole SFT2 began at 189.95m below the collar position. The lithology here consists of an 11cm thick medium- to dark-grey siltstone which has a distinctly coarser grain size in comparison with the overlying and underlying shale. It also has a somewhat cherty texture and has a very weak reaction in dilute hydrochloric acid (HCl). Below this is the greyish-black shale interbedded with yellow-brown tuff typical of the Collingham Formation. This continues until 195.15m and has, in certain places, a very weak reaction with dilute HCl. A 16cm layer of light-grey chert occurs at 195.15m and has a distinctly smaller grain size as well as a much duller lustre in comparison with the shale. The cherty layer is also much harder (silica rich) and less weathered (**Figure 5.61**). This is likely to

be what is known as the ‘Matjiesfontein chert’ horizon as it portrays the characteristics described by Visser (1992) and is located in a similar position within the lower Ecca stratigraphy.

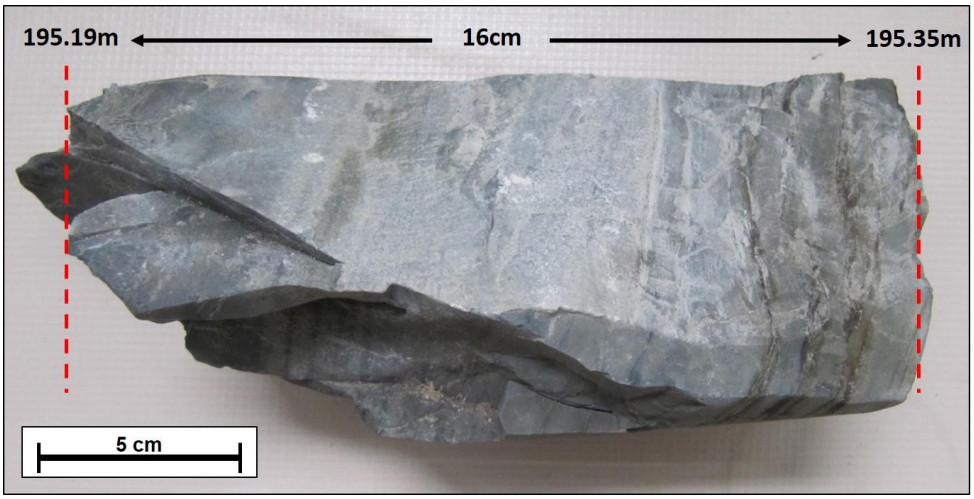

Figure 5.61: Cherty layer at 195.19m – a possible correlation to the 'Matjiesfontein chert’ as described by Visser (1992).

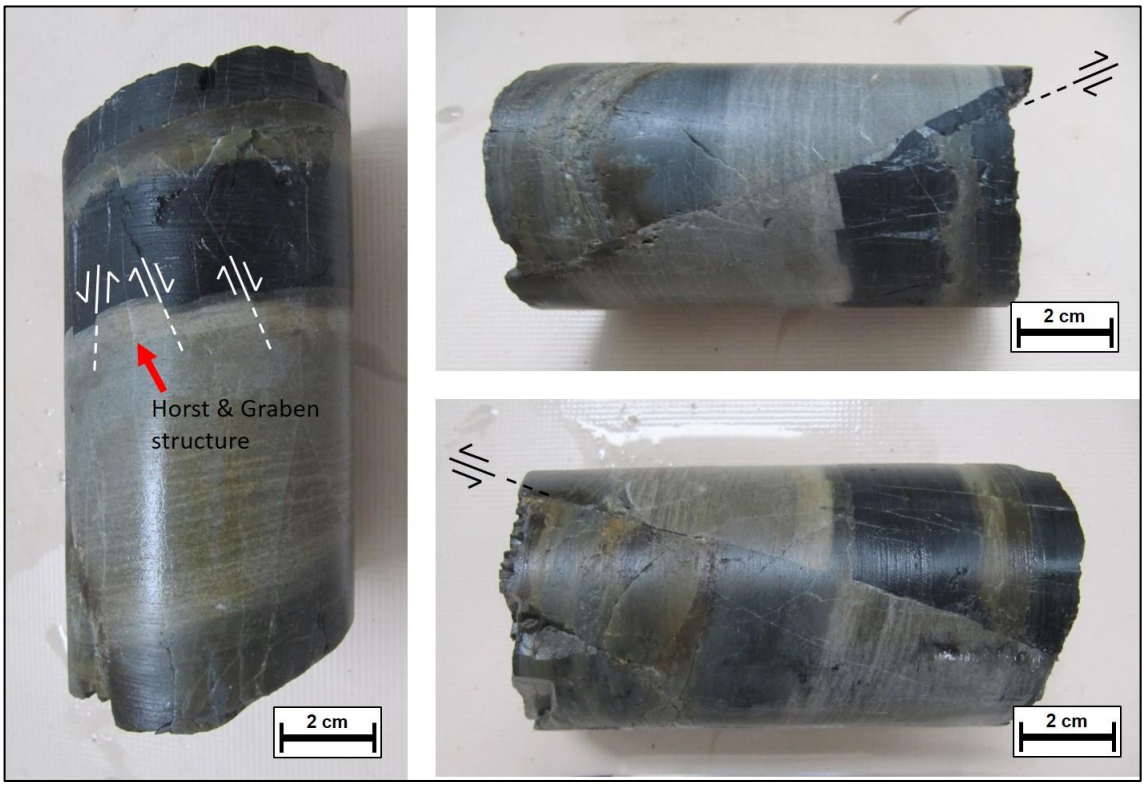

Figure 5.62: Normal faulting of a siltstone layer with horst and graben structures.

Below the chert is another 18cm thick siltstone horizon resembling similar properties to the one located at 189.95. However, here there is no reaction in dilute HCl. From 195.53m down to 197.66m, the alternating shale and tuff predominates

with very weak to no reaction in dilute HCl except along the occasional calcite vein which is located at irregular intervals and is orientated perpendicular to bedding. There is also another 26cm layer of silica-rich, coarse-grained rock located at 196.39 interbedded in the shale. Normal faulting with 'horst and graben' type movement is noted at 197.66m within a thicker (62cm) siltstone horizon (**Figure 5.62**). Below the faulting, at approximately 198.04m, there is a fluvial escape structure exhibited by dark material penetrating the lighter-coloured siltstone (**Figure 5.63**).

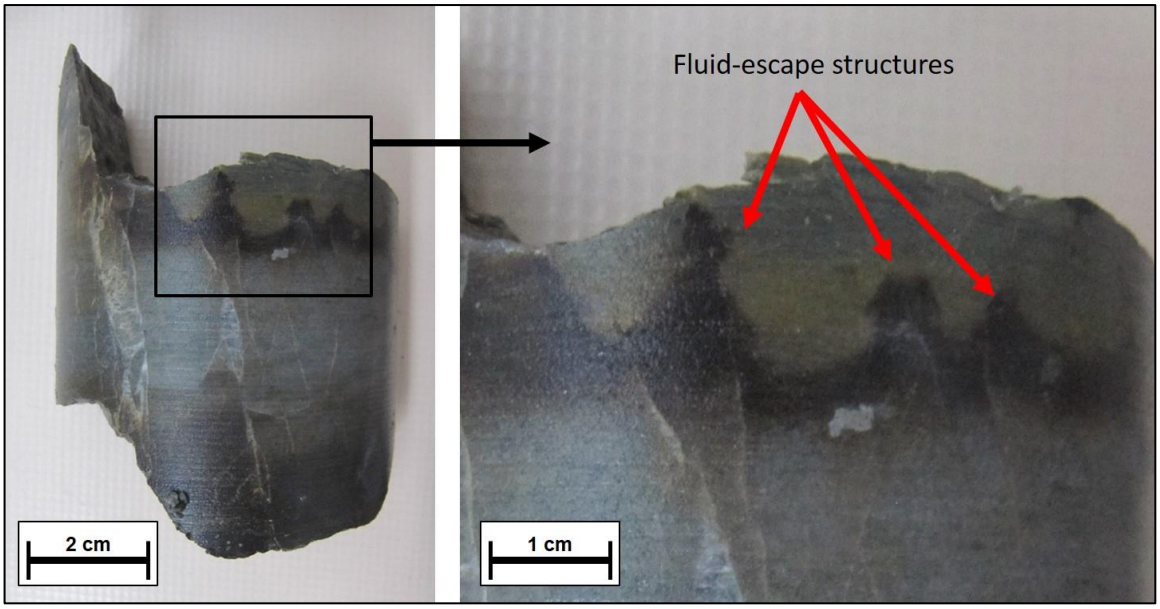

Figure 5.63: Fluid-escape structures within the dark siltstone.

5.3.2 Collingham-Whitehill Contact

The contact between the Collingham Formation and the Whitehill Formation has been assigned as a sharp contact at 198.28m where the siltstone horizon overlies a black, fine-grained shale. The volcanic tuff, which was previously regularly interbedded within the shale, is no longer present below this point. The shale located below the contact also exhibits a homogeneous texture and is more carbon-rich than the shale in the Collingham Formation, which becomes more apparent when the core is wetted down. The occasional siltstone which is present in the Collingham Formation is absent below 198.28m.

5.3.3 Whitehill Formation

Beginning at 198.28m below the collar position of SFT2, the Whitehill Formation is dominated by carbon-rich, black shale with varying proportions of calcite and

pyrite veins in places. From the Collingham-Whitehill contact to 202.58m there is a homogenous black shale which is distinctly carbon-rich, exhibits a pearly lustre in places, and has no noticeable pyrite. It also exhibits no reaction in dilute HCl except along the very minor calcite lenses observed at 199.34m as well as the calcite veins at 200.66m which are parallel to bedding. The shale appears to have a distinct bedding cleavage, however, this could be a fault cleavage as slickensides are located on the surface of a number of the planes. At 202.58m to 202.66m, the first pyrite mineralisation is noted and appears to be associated with small calcite veins surrounding lenses of pyrite mineralisation (**Figure 5.64**). The homogeneous black shale continues thereafter until 205.88m with only minor calcite veins and no distinguishable pyrite (**Figure 5.65**).

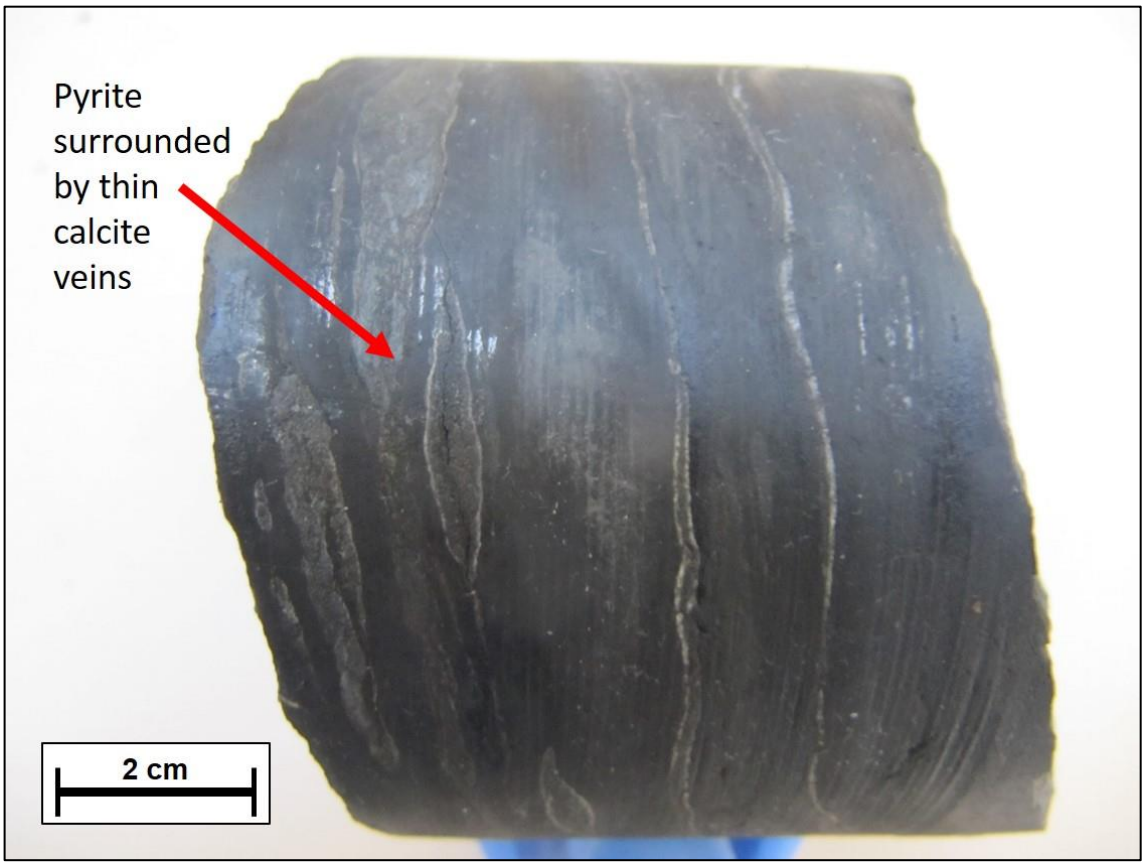

Figure 5.64: Black shale with pyrite lenses which are surrounded by thin calcite veins.

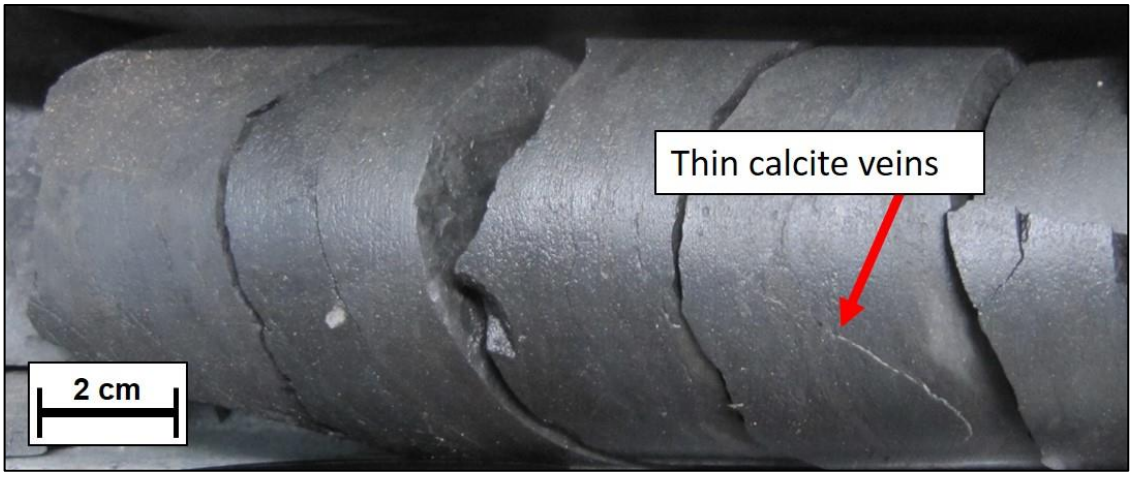

Figure 5.65: Homogeneous black shale with thin calcite vein.

The calcite content increases at 205.88m below the collar position, with randomly-orientated calcite veins present in places as well as calcite veins which are parallel to bedding as well as the odd calcite vein which is perpendicular to bedding. Pyrite is only visible again at 212.33m where normal faulting is also observed. The fault here appears to have caused folding of the pyrite and calcite lenses on either side of the fault plane. The black shale is separated by small lenses of pyrite which are surrounded by calcite veins that are generally parallel with the orientation of the bedding plane (**Figure 5.66**).

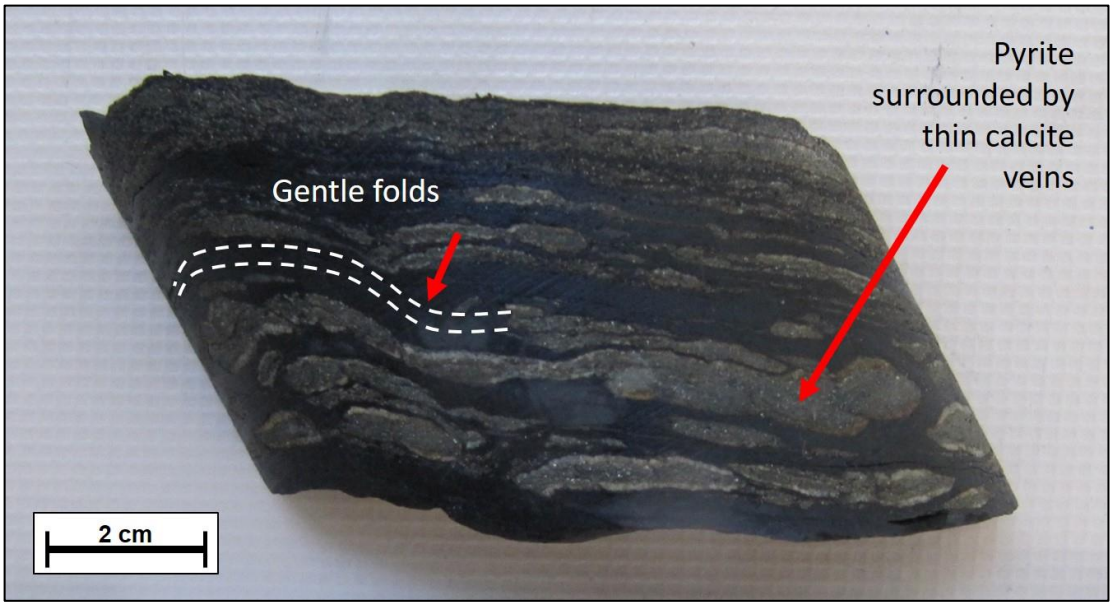

Figure 5.66: Black shale separated by lenses of pyrite surrounded by thin calcite veins. Gentle folds distort the bedding orientation.

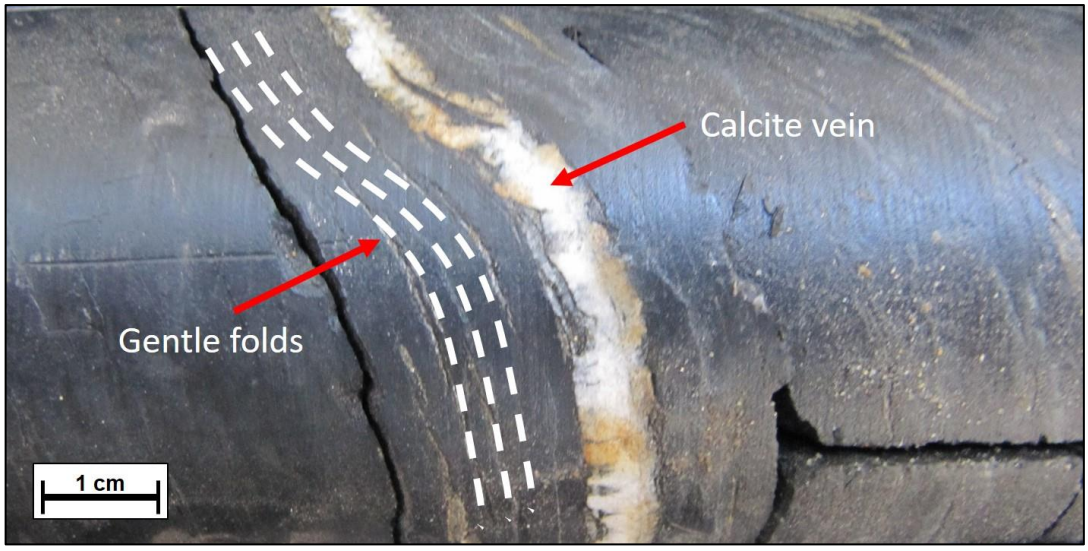

Figure 5.67: Thick calcite vein parallel to the bedding plane disturbed by a gentle fold within the black shale.

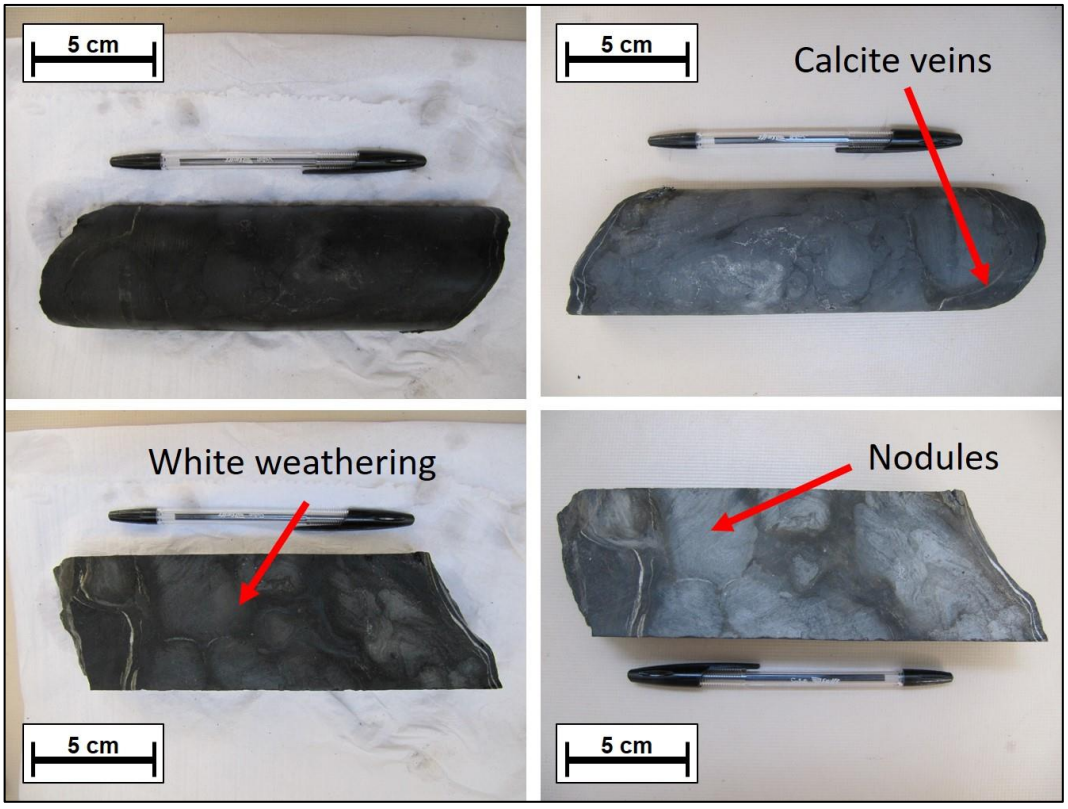

Figure 5.68: Black shale which has weathered to a medium grey colour in places. Weathered areas resemble small nodules which are enclosed by very thin calcite veins.

These lenses and veins are disturbed by gentle folds in places (**Figure 5.67**). There are also secondary, randomly-orientated calcite veins which are not associated with any pyrite. At 213.95m, the black shale shows weathering to a white colour and exhibits nodular features (**Figure 5.68**). Very minor calcite mineralization occurs along the outer edges of these nodules. This is visible until

214.12m, after which the shale returns to its distinct black colour except for the randomly-orientated swarms of calcite veins and pyrite lenses which occur throughout. Another nodular concretion, which is approximately 4cm in diameter, is located at 214.82m and consists of black shale surrounded by calcite veins and pyrite lenses continuing to 215.00m (**Figure 5.69**).

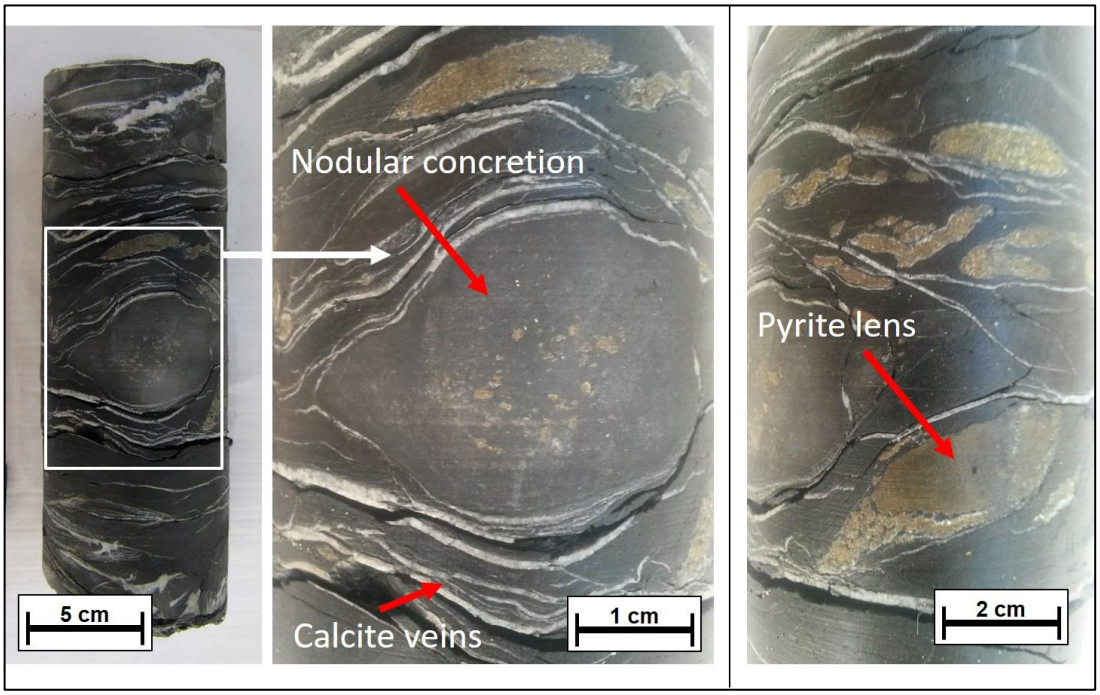

Figure 5.69: Nodular concretion within black shale surrounded by calcite veins and thick pyrite lenses. Small lenses of pyrite are also observed in the centre of the concretion.

Below this point, there is calcite veining which is parallel to bedding with minor pyrite lenses appearing from 215.14m. Thin flakes of calcite appear to have recrystallized along the distinct cleavage planes of the black shale. Movement associated with faulting along these cleavage planes has given the shale a pearly lustre in places. At 215.22m, another normal fault is observed together with folding of calcite and pyrite veins on either side of the fault plane (**Figure 5.70 A**). The black shale continues from 215.29m to 215.73m and contains randomly distributed calcite veins with smaller and fewer pyrite lenses as well as another nodule (5cm diameter) at 215.67m. A reverse fault is visible at 215.73m where it distorts a calcite vein and causes folding adjacent to the fault plane. The calcite vein exhibits brown discolouration especially directly adjacent to the fault (**Figure 5.70 B**).

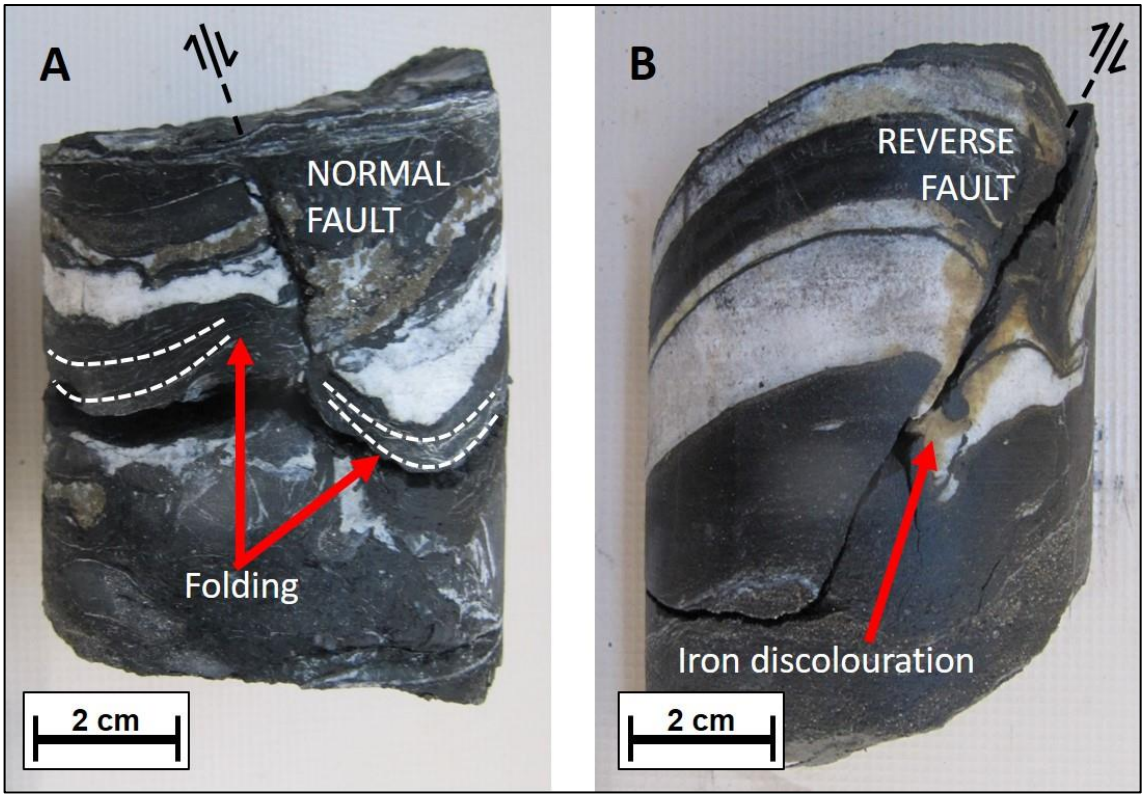

Figure 5.70: Faulting in SFT2: **A**: Normal fault distorting a calcite vein and associated pyrite lens and resulting in folding adjacent to the fault plane; **B**: Reverse fault distorting a thick calcite vein which has been discoloured by iron oxide.

The reasonably calcite-rich black shale continues to 216.95m and is intersected by a number of large calcite veins at 215.97m that are perpendicular to the bedding orientation, as well as swarms of randomly-orientated calcite veins with minor pyrite nodules at 216.63m (**Figure 5.71**). From 216.95m to 219.08m, the pyrite content reaches its maximum and occurs in the form of large veins associated with calcite that are orientated parallel to the bedding plane. These mineralization features are interbedded with the homogenous black shale and are separated by sharp contacts which may represent a thrust faulted area of the lithology (**Figure 5.72**).

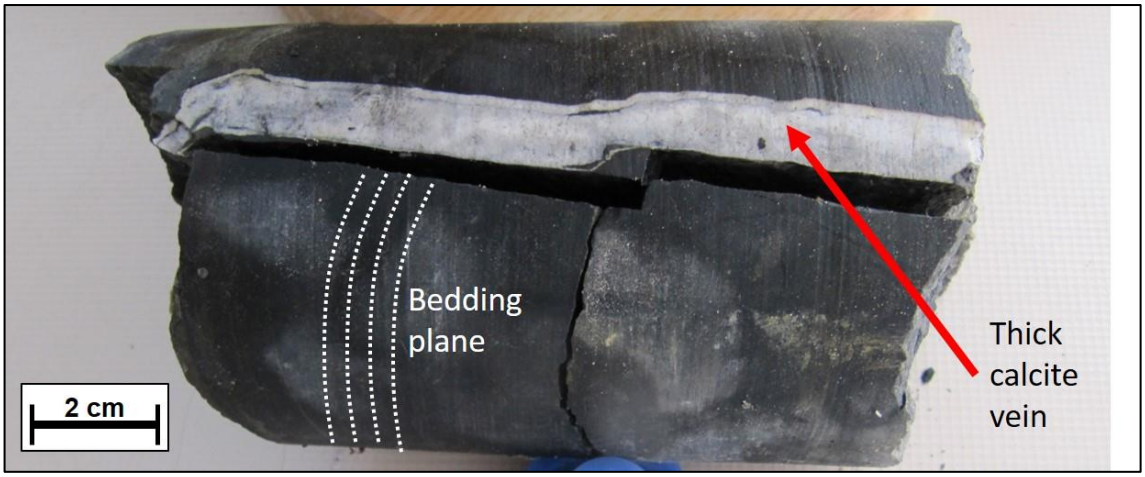

Figure 5.71: Thick calcite vein perpendicular to the bedding plane.

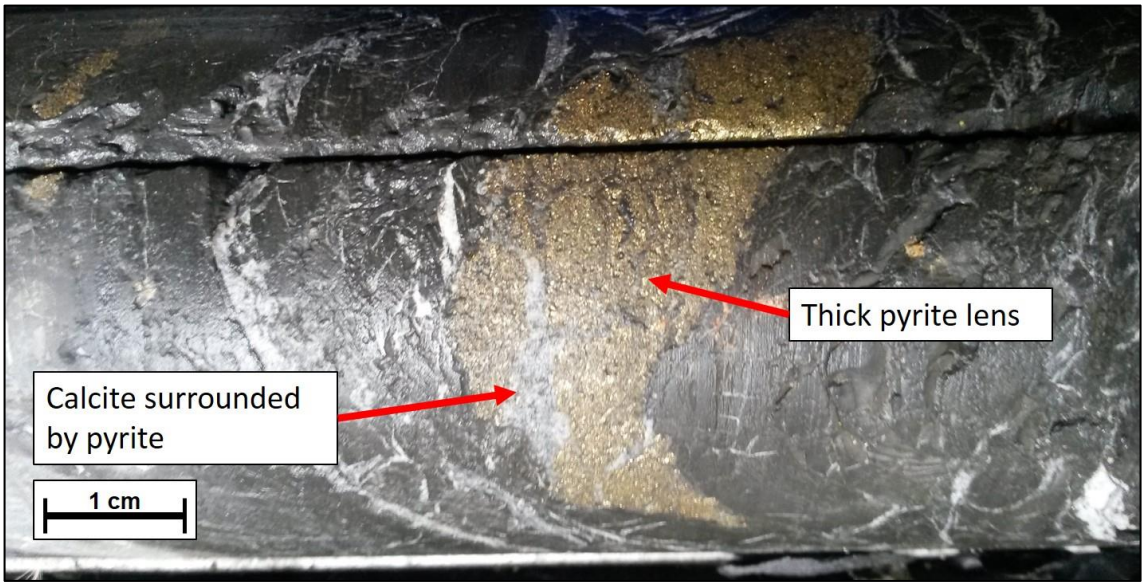

Figure 5.72: Thick pyrite lenses associated with randomly orientated calcite veins. Contacts between the areas rich in calcite and pyrite seem to be represented by thrust faults which separate them from the homogeneous black shale.

Gentle folding of the veins is noted at 218.22m while open symmetrical folds are visible at 218.72m (**Figure 5.73**). A 6cm thick limestone or dolomite layer intersects the shale at 219.08m and is differentiated by its coarser texture, lighter colour and extreme effervescence reaction in dilute HCl, not only along the randomly-orientated calcite veins within it, but also on the matrix material (**Figure 5.74**).

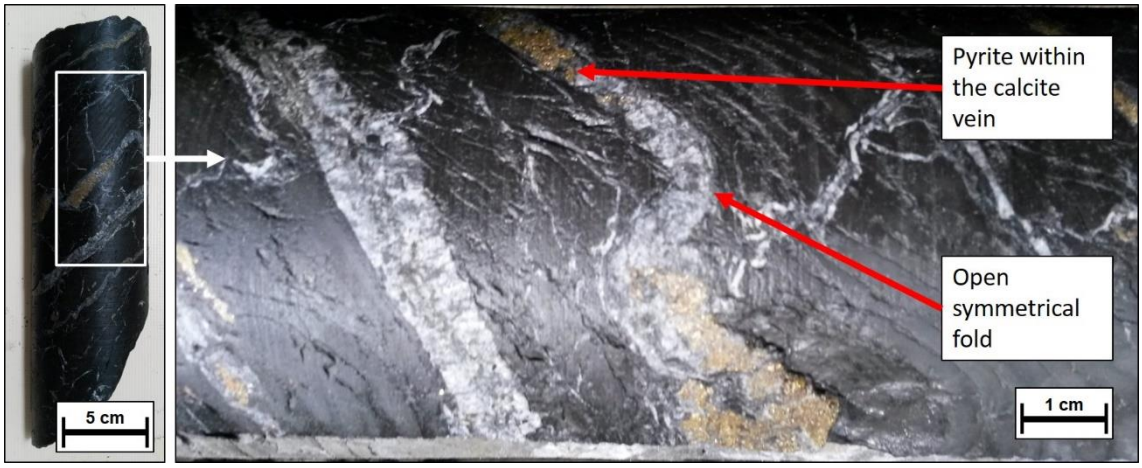

Figure 5.73: Pyrite and calcite veins intersecting the black shale and then distorted by a symmetrical open fold.

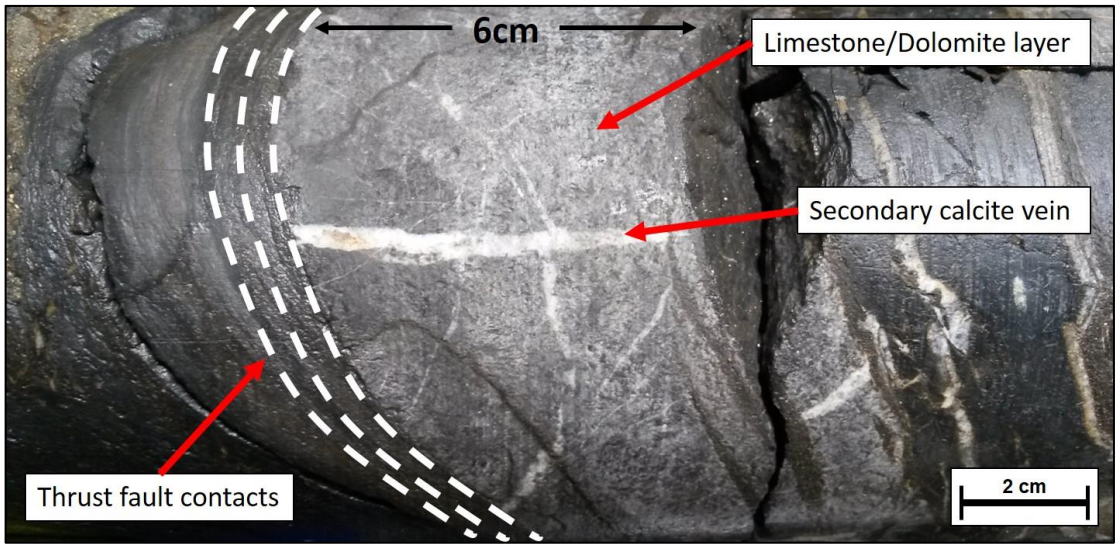

Figure 5.74: Limestone or dolomite layer interbedded in the black shale and intersected by a secondary calcite vein. The contact between the carbonate and the shale is likely to represent a thrust fault plane.

Below the carbonate layer the shale continues, but is now depleted of calcite and pyrite, with only very minor reactions in dilute HCl, as well as very minor pyrite cubes noticed throughout. There is, however, a distinct discolouration of the shale down to 222.41m and is likely to be caused by the oxidation of pyrite which no longer displays as a shiny gold colour, but instead as a rusty yellow-brown colour surrounded by calcite veins (**Figure 5.75**).

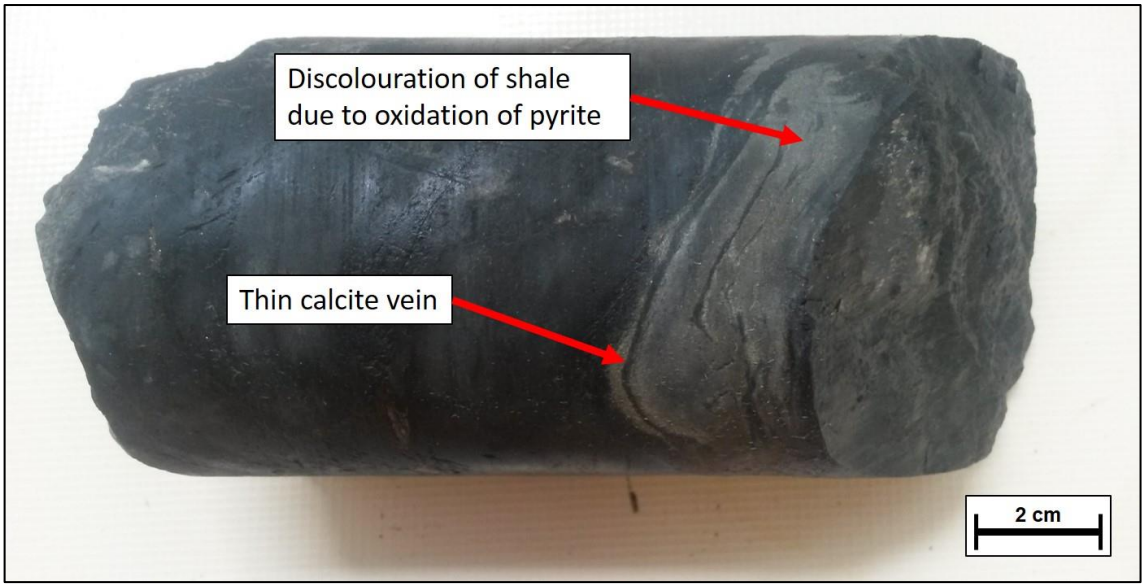

Figure 5.75: Weathering of black shale due to the oxidation of pyrite. This forms nodule-type features which are surrounded by thin calcite veins.

At 222.41m the calcite and pyrite content increases in the form of randomly-orientated swarms of calcite with medium to large lenses of pyrite (**Figure 5.76**). The pyrite content then decreases and no more visible pyrite is noted below 223.96m. At 223.10m a normal fault with a perpendicular fault plane offsets several calcite veins (**Figure 5.77**). Below this, the shale once again exhibits rust-like discolouration and, at 223.96m, a 15cm layering is observed within the strata (**Figure 5.78**). This 'concretion,' which also exhibits swelling of the shale, is underlain and overlain by relatively thick discoloured calcite veins. The discolouration continues down to 226.87m and is interbedded with brown calcite and white quartz veins with nodular features at 224.23m and 225.95m (**Figure 5.79**).

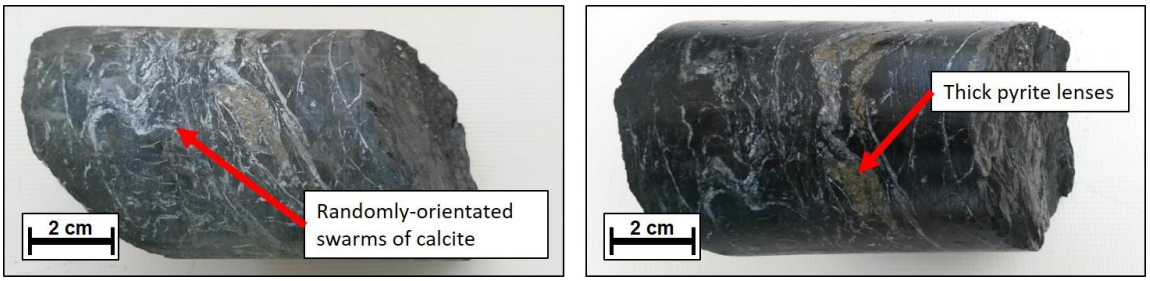

Figure 5.76: Swarms of randomly orientated calcite veins intersected by thick pyrite lenses.

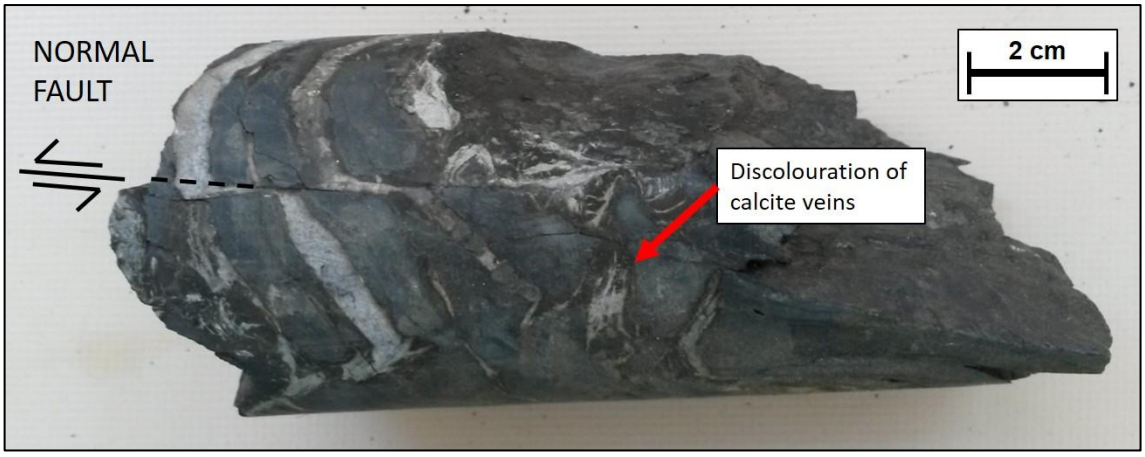

Figure 5.77: Calcite veins discoloured by iron oxide are offset by a normal fault orientated perpendicular to bedding.

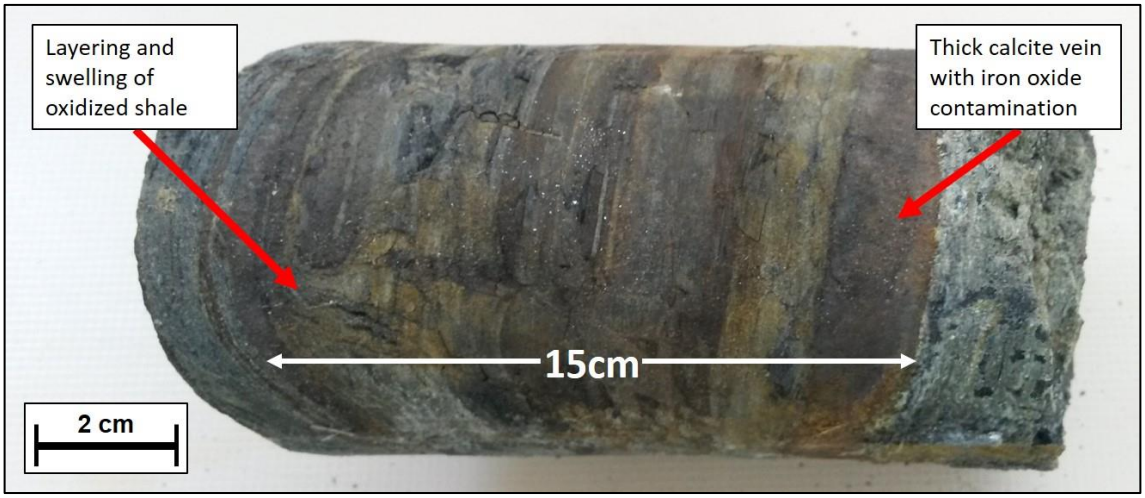

Figure 5.78: Discolouration and swelling of shale caused by oxidation of pyrite. The outer layers are calcite veins which have been contaminated by iron oxide.

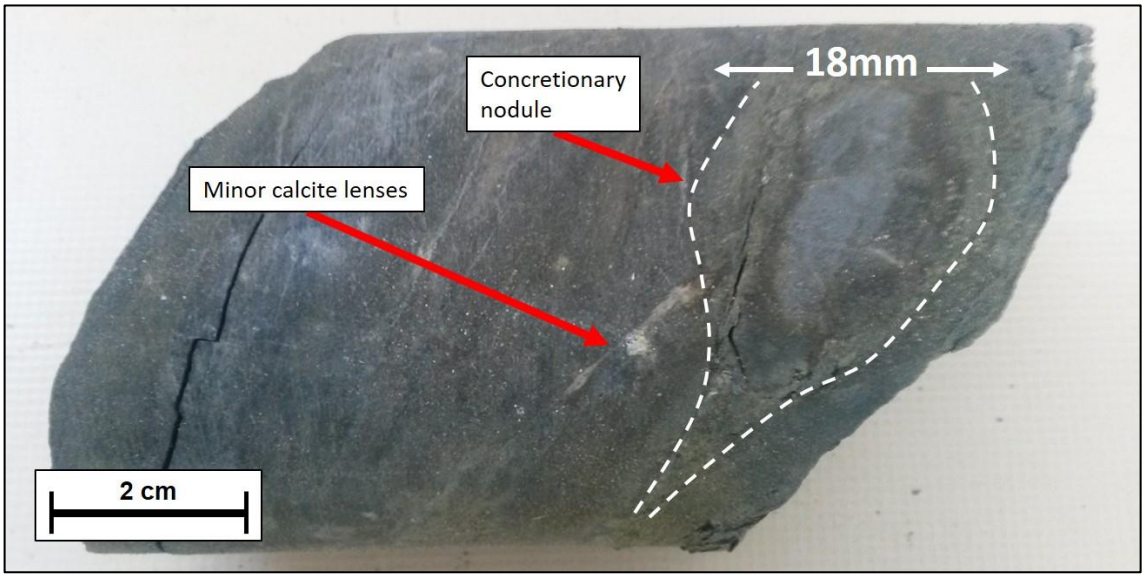

Figure 5.79: Nodule surrounded by thin calcite veins.

From 225.95m to 228.85m, the black shale contains no pyrite, but calcite and quartz veins are common with swarms of calcite and quartz observed from 225.95m to 228.37m. The shale has also precipitated a white powder upon its weathered surface (**Figure 5.80**). The layering appears to be in the form of small thrust zones which are most noticeable at 226.93m and 228.51m (**Figure 5.81**).

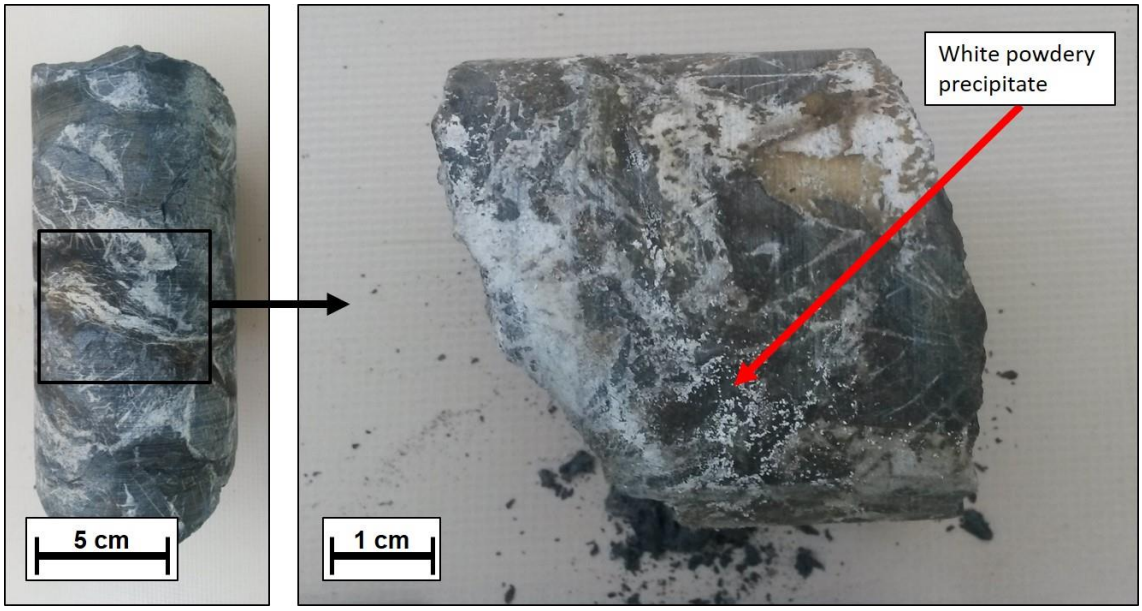

Figure 5.80: Precipitation of fine white powder on the surface of a calcite-rich shale.

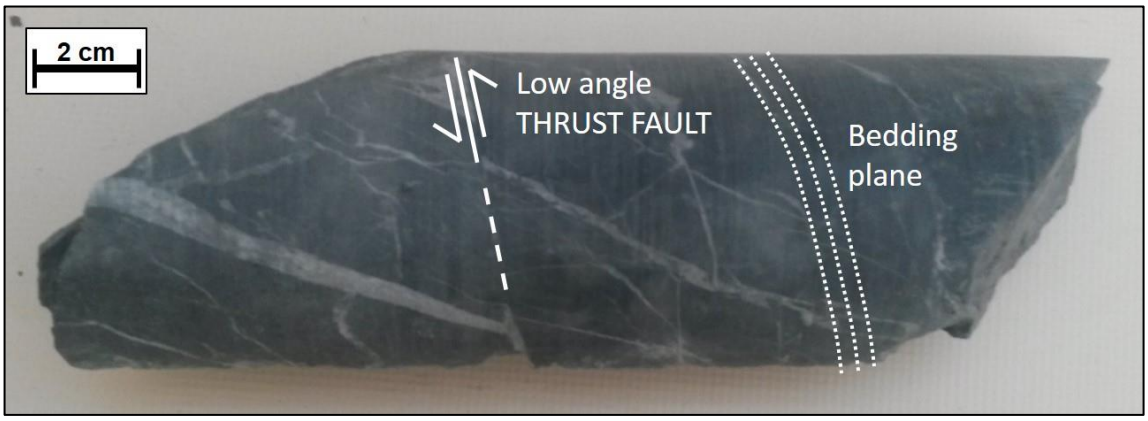

Figure 5.81: Black shale intersected by randomly orientated calcite veins which are offset by low-angle thrust faults.

5.3.4 Whitehill-Prince Albert Contact

The contact between the Whitehill Formation and the underlying Prince Albert Formation is not distinctly recognised and cannot be assigned to a particular point within the SFT2 succession. Instead, it is a gradual contact beginning at 226.93m (beneath the discoloured shale which has also precipitated the white powder) and continuing down to 230.80m where the shale is a distinctly browner colour and is

slightly coarser grained. The shale therefore becomes lighter in colour from 226.93 and is coarsening downwards in the succession. Its reaction with dilute HCl also decreases gradually moving downwards through the succession and the quartz to calcite proportion seems to increase into the Prince Albert Formation strata. The same distinct bedding cleavage prevails throughout most of the shale and manganese dendrites are visible on many of these cleavage planes (**Figure 5.82**).

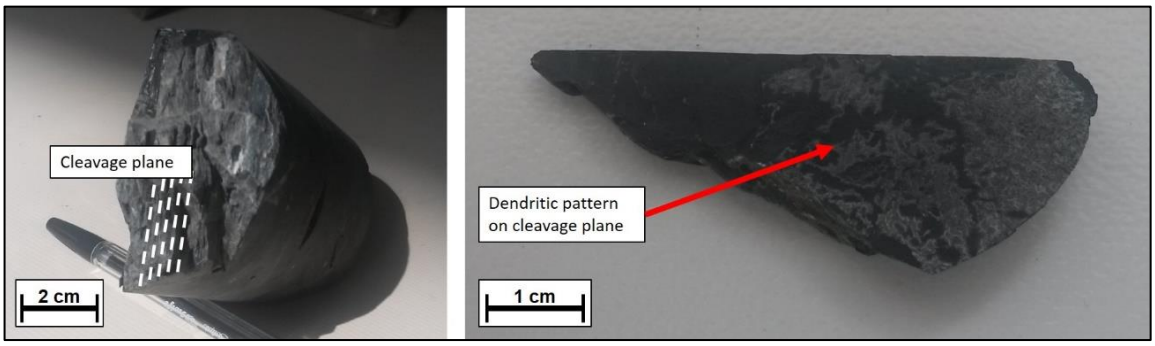

Figure 5.82: Homogeneous black shale with a distinct cleavage plane usually orientated parallel to bedding. Dendritic patterns are observed on many of the cleavage plane surfaces.

5.3.5 Prince Albert Formation

From 230.08m downwards, the shale remains slightly coarser grained than the black shale of the Whitehill Formation. It is now a yellow-grey colour with larger quartz veins that are more evenly distributed. The veins do react weakly to dilute HCl which could suggest that there is some calcite present within them. However, the shale matrix does not produce any effervescence in dilute HCl, unlike the shale matrix within the Whitehill Formation. There is also no visible pyrite below 223.96m and the shale from 230.80m downwards within the SFT2 core appears to be well consolidated (likely due to the increased silica proportion) and shows no distinct weathering, oxidation, nodules or swelling features as was noticed within the Whitehill Formation.

5.4 Thin Section Analysis

In order to assess the mineralogy and textural characteristics of the Whitehill Formation, thin sections were cut from specific samples and mounted on glass to produce a 3mm thick glass slide. This thin section can then be studied under an optical microscope to identify minerals, observe the textural relationships between crystals as well as to compare the rock forming mineral proportions, especially those of calcium and pyrite, for different samples.

5.4.1 SFT2 Borehole Samples

Samples have been cut from the SFT2 core at specifically chosen horizons within the borehole log (**Table 5.8**). Thin sections were cut from four samples - SFT2/1, SFT2/9, SFT2/12 and SFT2/14 (**Figure 5.83**). The thin section for each sample, represents an area which is approximately 2cm by 2cm. Additional thin section samples were cut, but were not included in this study as they did not add any value due to the opaque nature of the shale minerals in question.

Table 5.8: List of samples chosen from the SFT2 borehole core.

Sample No.	Depth	Formation	Description
SFT2/1	189.95	Collingham	Sandy, cherty siltstone
SFT2/2	195.19	Collingham	Matjiesfontein' chert bed
SFT2/3	195.35	Collingham	Sandy, cherty siltstone
SFT2/4	196.39	Collingham	Black shale with calcite veins
SFT2/5	197.66	Collingham	Siltstone intersected by normal, horst and graben-type faults
SFT2/6	202.58	Whitehill	Black shale with calcite veins and weathered pyrite lenses
SFT2/7	213.48	Whitehill	Black shale with lenses of pyrite surrounded by calcite
SFT2/8	213.95	Whitehill	Black shale with nodular weathering pattern and pyrite
SFT2/9	214.51	Whitehill	Black shale with calcite veins
SFT2/10	214.82	Whitehill	Black shale with nodule surrounded by calcite veins and pyrite lenses
SFT2/11	215.78	Whitehill	Black shale separated by tuffaceous horizons and a shiny lustre on the cleavage planes
SFT2/12	216.95	Whitehill	Black shale separated from limestone/dolomitic layers by thrust faulting
SFT2/13	218.20	Whitehill	Black shale with lenses of pyrite surrounded by calcite
SFT2/14	218.72	Whitehill	Black shale separated by thick calcite veins and pyrite lenses
SFT2/15	219.08	Whitehill	Limestone/dolomite cross-cut by calcite veins
SFT2/16	219.71	Whitehill	Weathered shale with nodules, iron discolouration and quartz veins
SFT2/17	221.15	Whitehill	Shale with oxidized pyrite mineralisation
SFT2/18	222.95	Whitehill	Black shale with lenses of pyrite and calcite veins
SFT2/19	223.10	Whitehill	Shale with white and brown calcite veins intersected by normal fault
SFT2/20	225.95	Whitehill	Weathered shale with nodules, iron discolouration and minor calcite
SFT2/21	228.51	Prince Albert	Dark brown - black shale with calcite veins

Figure 5.83: Samples sent for thin section cutting – SFT2/1, SFT2/8, SFT2/9, SFT2/12 and SFT2/14. Note that SFT2/8 could not be cut into thin section due to its weathered nature.

5.4.1.1 SFT2/1

This sample is distinctly coarser grained than the shale in many of the samples. The mineral grains are approximately 200 micrometres (µm) in diameter which is characteristic of medium grained sand particles. There is a distinct layering which is observed in hand sample and can also be seen under the microscope (**Figure 5.84 a**). The larger crystals, usually plagioclase feldspar (distinguished by the polysynthetic twins, low relief, weak birefringence and a biaxial 2V angle), are aligned sub-horizontally along the same plane (**Figure 5.84 b**). The mineralogy is matrix supported and consists of minor quartz crystals which are characterised by its colourless appearance under plane polarised light, its second order birefringence under crossed polars and its positive uniaxial 2V angle (**Figure 5.84 c**). Much of the sample is composed of calcite, identified by its polysynthetic twinning, uniaxial negative sign and distinct 'twinkling' (**Figure 5.84 d**). The most interesting characteristic of this sample is the presence of silicified ooliths. They are scarce throughout the sample, but when found, tend to accumulate together (**Figure 5.84 e**). There is also a brown mineral within the sample identified as goethite due to its yellow-brown pleochroic colour, its isotropic 2V angel and its anomalous birefringence (**Figure 5.84 f**).

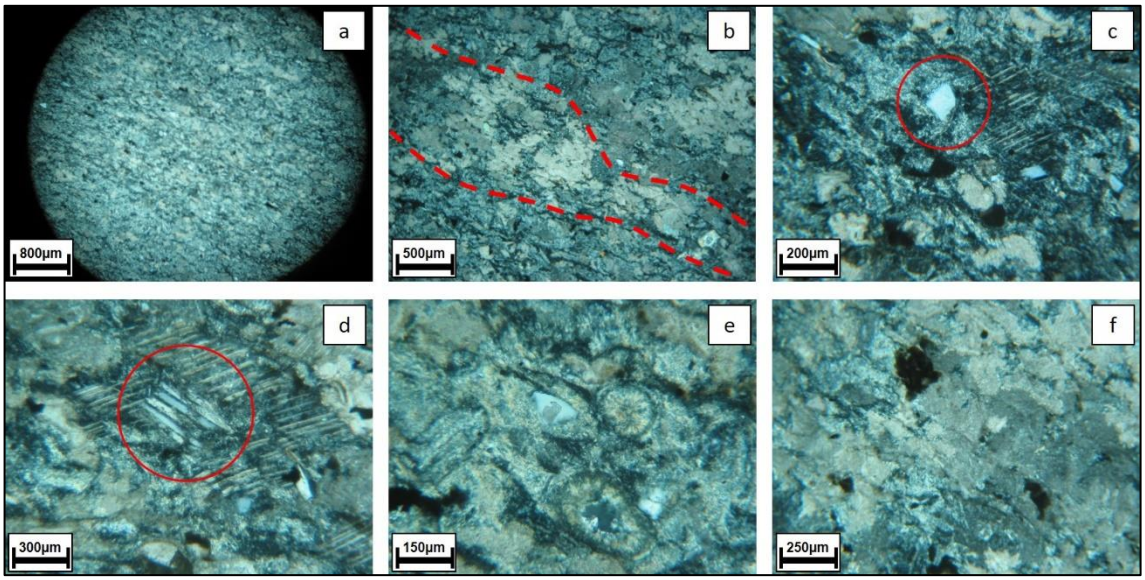

Figure 5.84: SFT2/1 under the petrographic microscope: **a)** The distinct layering can be seen throughout the sample; **b)** Larger mineral grains, such as plagioclase feldspar, tend to accumulate along the same horizon; **c)** Quartz is dispersed throughout the sample and makes up the majority of the mineralogy; **d)** Calcite is dominant throughout the sample; **e)** Silicified ooliths are present in certain parts of the sample and are approximately 150µm in diameter; **f)** Dark brown goethite minerals occur throughout the sample.

5.4.1.2 SFT2/9

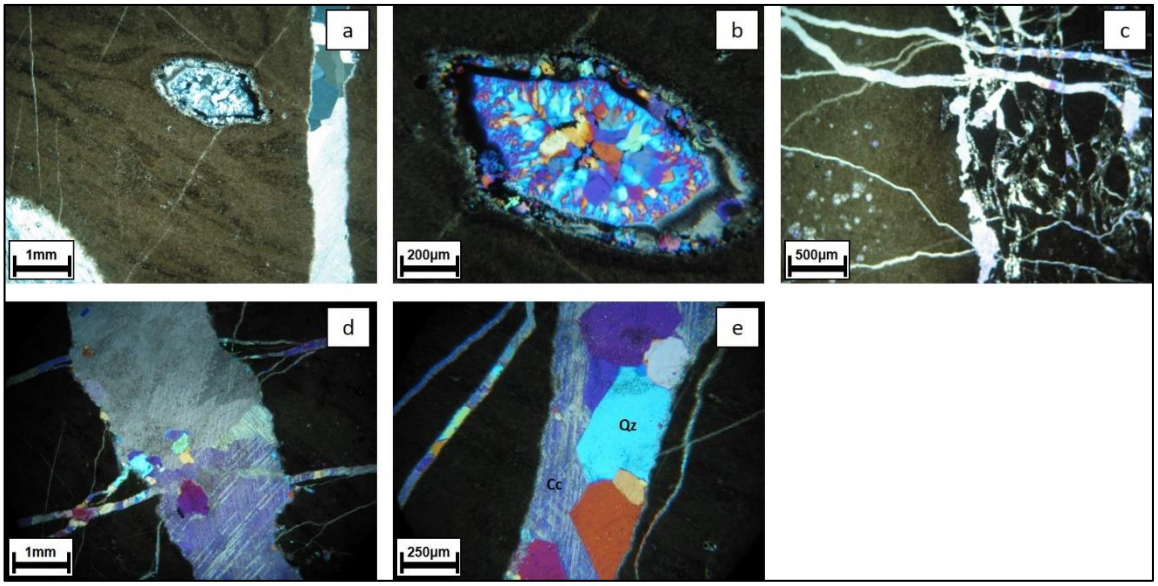

Figure 5.85: SFT/9 under the petrographic microscope **a)** Brown-black clay particles exhibiting folding and intersected by a hexagonal nodule; **b)** The hexagonal nodule under cross polars exhibiting quartz crystals of varying size extending from its boundary; **c)** The shale appears darker in areas which have extensive calcite and quartz veins; **d)** A large calcite-rich vein with 'branches' of smaller veins extending outwards; **e)** A smaller vein exhibiting alternating quartz (Qz) and calcite (Cc) grains.

Sample SFT2/9 exhibits the characteristics of a typical shale from the Whitehill Formation which contains quartz and calcite veins. The brown-black clay matrix makes up the majority of the sample and these clay particles are layered in places (**Figure 5.85 a**). The clay particles are less than 10µm in diameter and are thus defined as fine grained silt particles (Schaetzl and Anderson, 2005). The layering shows no particular orientation, but micro-folds and micro-unconformities are observed in places.

The opaque minerals that are interbedded with the shale is likely to be pyrite due to its cubic crystallographic system and brassy yellow colour under reflected light. The anomalous feature of this sample is the deformed hexagonally shaped crystal which resembles the characteristics of a micro-amethyst (**Figure 5.85 b**). In certain places, the shale is much darker and this is usually in areas where the shale is disturbed by a high concentration of veins – the randomly orientated swarms of veins tend to be associated with the darker shale (**Figure 5.85 c**).

The veins in this sample occur in varying sizes and the minerals which make up the larger veins are identified as calcite and, to a lesser extent, quartz. The

average crystal size of the larger mineral grains in the prominent veins is greater than 2mm, but this varies greatly (**Figure 5.85 d**). While the larger veins are predominantly made up of calcite with minor quartz, the smaller veins tend to have an equal ratio of calcite to quartz. The crystals located in the smaller veins are, on average, greater than 700µm in diameter, however, some are much smaller (**Figure 5.85 e**).

5.4.1.3 SFT2/12

The sample consists of a relatively large proportion of pyrite and calcite interbedded with the shale. The clay minerals are fine grained, layered and deformed by the pyrite and calcite grains in the sample. The layering is evident from the different colours exhibited in the shale particles. In some cases, the colour changes exhibit nodular features within the shale (**Figure 5.86 a**). Small opaque minerals are also noted amongst the brown shale, likely to be pyrite.

The large opaque pyrite grains, distinguished by their cubic habit, are generally surrounded by calcite veins (**Figure 5.86 b**). The calcite veins are common throughout the sample and appear to be surrounding the amorphous opaque minerals (**Figure 5.86 c**). The pyrite grains, surrounded by calcite as well as quartz veins, cause distinct distortion of the shale in several places (**Figure 5.86 d**). Quartz grains surround several cubic pyrite crystals in a radial texture (**Figure 5.86 e**). These quartz-enclosed pyrite cubes appear to result in a great deal of deformation of the shale in the form of microscopic foliations (**Figure 5.86 f**).

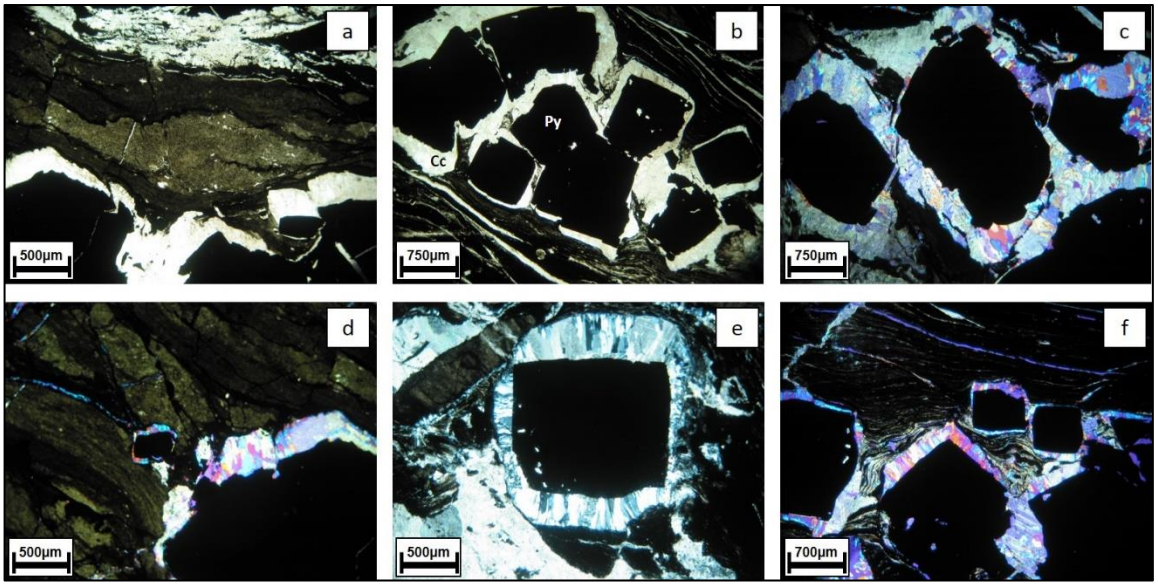

Figure 5.86: SFT2/12 under the petrographic microscope: **a)** Alternating dark-brown and light-brown shale layers deformed by pyrite mineralisation which has been surrounded by calcite veins; **b)** Pyrite cubes surrounded by calcite veins; **c)** Distorted pyrite cubes surrounded by calcite-rich and quartz-rich veins which form nodular features; **d)** The pyrite occurs on different scales, but has a distinct deformation effect on the shale; **e)** An undistorted pyrite cube surrounded by a quartz-rich vein in which the mineral grains are arranged radiating away from the pyrite; **f)** The shale can be greatly distorted by the pyrite cubes which are surrounded by the calcite- and quartz-rich veins.

5.4.1.4 SFT2/14

This sample consists of a much darker black shale and thus the layering of the particles is not as clear as in the other samples. The shale is often intersected by thin (less than 25µm) subparallel veins of calcite and quartz (**Figure 5.87 a**). While this sample also consists of large amount of pyrite, it is far less than SFT2/12. The pyrite is generally separated by calcite veins and there is noticeably more calcite and less quartz in this particular sample (**Figure 5.87 b** and **Figure 5.87 c**) as opposed to the other samples. Mineral grains located in the veins of this sample are randomly orientated and the size of the pyrite cubes varies greatly (from less than 150µm in to greater than 2mm in diameter). The sample also exhibits a great deal of undistorted pyrite cubes, but, unlike the previous samples, these do not exhibit separate vein structures surrounding them (**Figure 5.87 d**). In some areas, the interaction between calcite and pyrite appears random and the pyrite crystals appear amorphous in shape (**Figure 5.87 e**). There are also calcite veins surrounding amorphous pyrite which exhibit distinct folding deformation features (**Figure 5.87 f**).

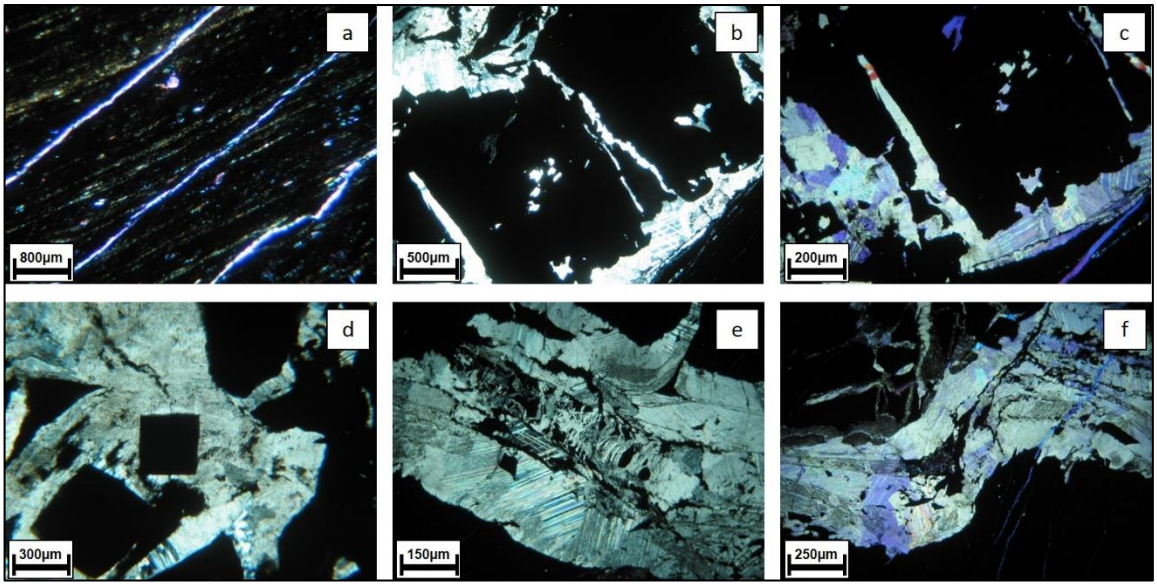

Figure 5.87:SFT2/14 under the petrographic microscope: **a)** Black shale exhibiting some layering and intersected by thin sub-parallel calcite veins; b) Pyrite cubes surrounded by calcite veins under normal light; **c)** The same pyrite cube under polarised light clearly exhibiting the calcite twinkling of the surrounding veins; **d)** Undistorted pyrite cubes in a calcite- and quartz-rich matrix; **e)** Amorphous pyrite enclosed by larger calcite grains; **f)** Folded calcite vein in polarised light exhibiting deformed pyrite within.

5.5 SEM Analyses

Samples analysed using energy dispersive spectroscopy (EDS), via the scanning electron microscope (SEM), provided a comprehensive mineralogical representation of the lithology of the selected samples in the Whitehill Formation. Eight samples were selected from the SFT/2 borehole core rock, as described in Section 4.6, and several notable minerals, as well as mineral textures, were observed using the SEM. The samples are described as per the particular section which was observed under the SEM microscope and therefore does not necessarily represent a true reflection of the mineralogy of the entire sample. The chemical composition of the minerals identified in these samples is represented with oxygen removed and normalised to a percentage of the total mineral composition. These compositions are summarized in **Appendix D**.

5.5.1 SFT/2 Sample 2

This sample consists of a quartz (SiO_2) and albite ($NaAlSi_3O_8$) matrix with minor apatite ($Ca_5(PO_4)_3(F, Cl, OH)$), relatively minor clay minerals (smectite and illite) and several trace minerals such as zircon ($ZrSIO_4$) and rutile (TiO_2) (**Figure 5.88 a**). There is also minor pyrite (FeS_2) in the sample which exhibits a framboidal

texture and occurs with no particular crystal orientation (**Figure 5.88 b**). The sample reveals a semi-oblate pyrite grain located within the quartz-rich matrix (**Figure 5.88 c**). This sample is rich in albite feldspar, but quartz remains the dominant mineral throughout, as is displayed by a facet in the sample where quartz crystals have precipitated within a vein (**Figure 5.88 d**). The trace zircon and rutile grains exhibit zonation in places.

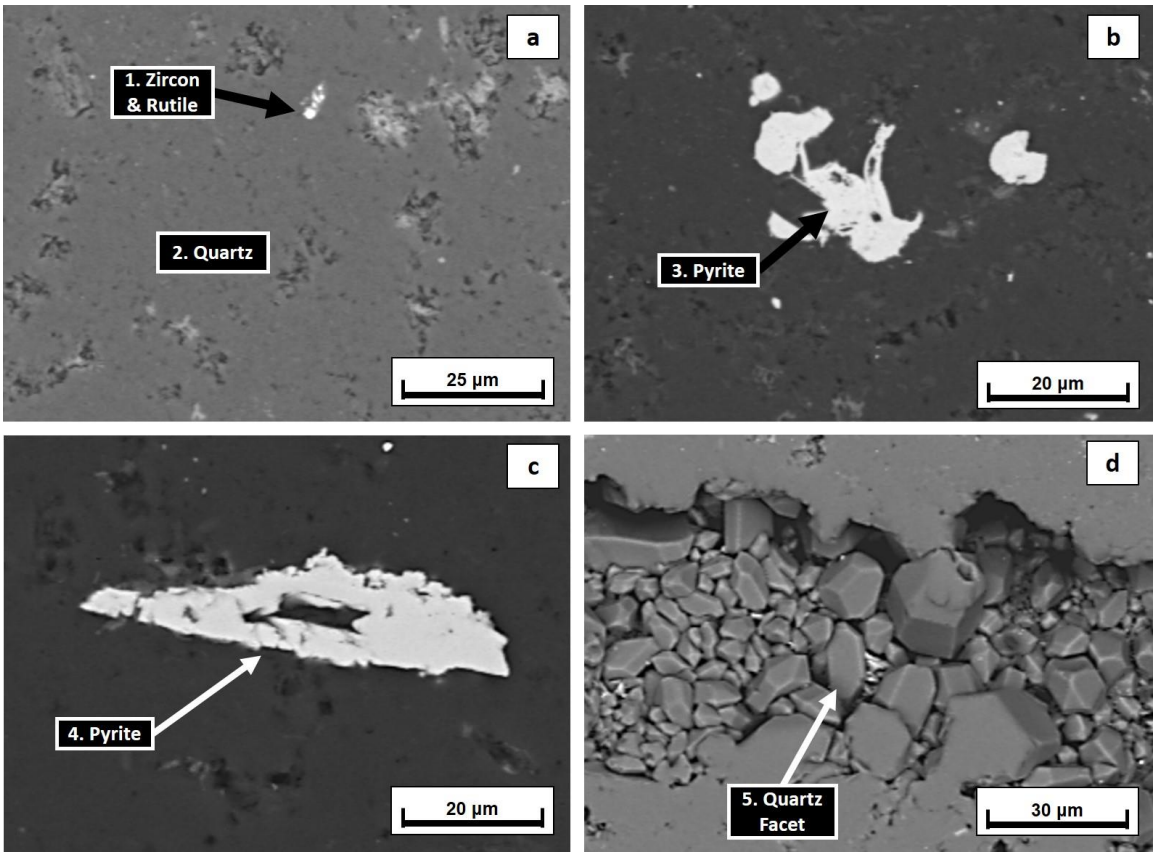

Figure 5.88: SFT2/2 under the Scanning Electron Microscope (SEM) exhibiting **a)** zircon and rutile grains within a quartz matrix; **b)** framboidal pyrite; **c)** semi-oblate pyrite; **d)** a quartz-rich facet within a hollow vein.

5.5.2 SFT/2 Sample 6

This sample consists of a dolomite ($CaMg(CO_3)_2$) matrix penetrated by a calcite ($CaCO_3$) vein that, in certain places, is separated from the dolomite by the occurrence of quartz. Barite ($BaSO_4$) nodules are observed within the calcite vein and there is evidence to support the occurrence of strontianite ($SrCO_3$), which appears to be located within the cleavage plane of the calcite (**Figure 5.89 a**). The sample exhibits an oddly-shaped apatite crystal which is relatively rich in fluorine, a variety of apatite known as fluorapatite ($Ca_5(PO_4)_3F$). The apatite is located in the dolomite matrix which also consists of irregularly-shaped quartz mineralization

(**Figure 5.89 b**). Small pyrite grains are located in the dolomitic shale. Certain veins within the dolomite matrix are separated into calcite and quartz domains which appear to be separated by distinct boundaries (**Figure 5.89 c**).

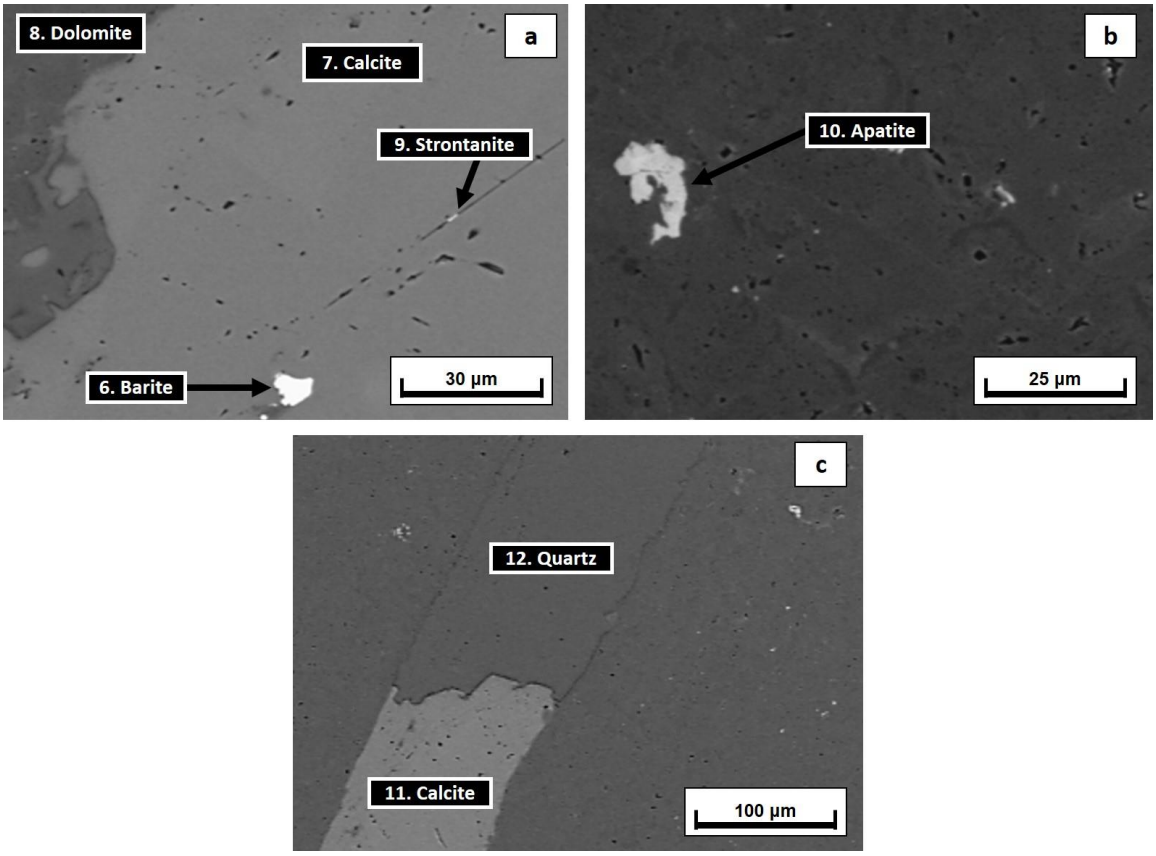

Figure 5.89: SFT2/6 under the SEM exhibiting **a)** a large calcite vein within a dolomite matrix. The calcite vein exhibits a distinct cleavage pattern within which minor barite and strontianite was identified; **b)** an irregularly-shaped apatite grain; **c)** a calcite- and

5.5.3 SFT/2 Sample 9

The sample exhibits distinct layering features where quartz, pyrite and clay minerals (mostly illite and smectite) are arranged together in separate areas of the sample. The pyrite observed in the layered portions of the sample exhibit a sub-rectangular shape as the edges of the mineral grains are somewhat rounded, especially those located along the outside of the pyrite layer (**Figure 5.90 a**).The quartz- and calcite- rich portions of the sample also exhibit minor feldspars, including albite and orthoclase ($KAlSi_3O_8$), as well as minor muscovite ($KAl_2(AlSi_3O_{10})(F,OH)_2$) in places. The EDS detected small traces of Manganese (Mn) associated with minerals such as pyrolusite (MnO_2), rhodochrosite ($MnCO_3$) and manganite (MnO[OH]) (**Figure 5.90 b**). In a different location within the same

sample, where layering is less distinct, pyrite cubes are observed within a calcite-rich matrix (**Figure 5.90 c**).

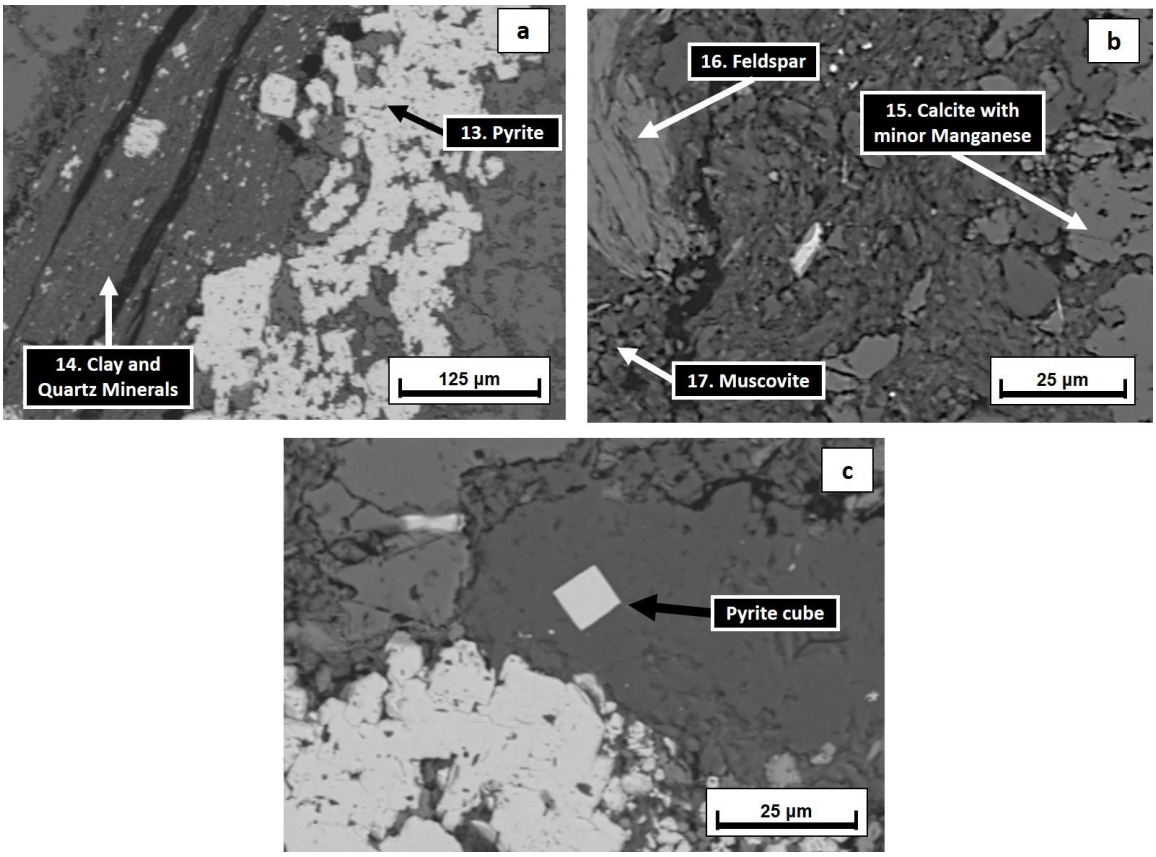

Figure 5.90: SFT2/9 under the SEM showing **a)** layering of calcite separated by pyrite in a quartz and clay matrix; **b)** layering of a variety of mineral grains (feldspar, quartz, muscovite) within a calcite matrix; and **c)** a pyrite cube within a calcite matrix.

5.5.4 SFT/2 Sample 14b

In this sample, the sharp contact between the calcite-rich shale and the iron-rich pyrite lens is clearly observed. There is a very thin, fine-grained layer of broken calcite grains along the contact exhibiting some form of deformation associated with the formation of pyrite within the shale. While calcite grains generally surround the pyrite, there are certain areas where it is surrounded by quartz. The pyrite also contains smaller quartz grains as well as several sphalerite (ZnS) grains which exhibit a zoned texture (**Figure 5.91 a**).

5.5.5 SFT/2 Sample 15

This sample consists of a calcite-rich matrix with minor apatite, traces of dolomite and rutile, and several pyrite nodules surrounded by fine-grained clay, quartz and

calcite. The pyrite exhibits a wavy (possibly folded) texture along the outer border of the nodules (**Figure 5.91 b**).

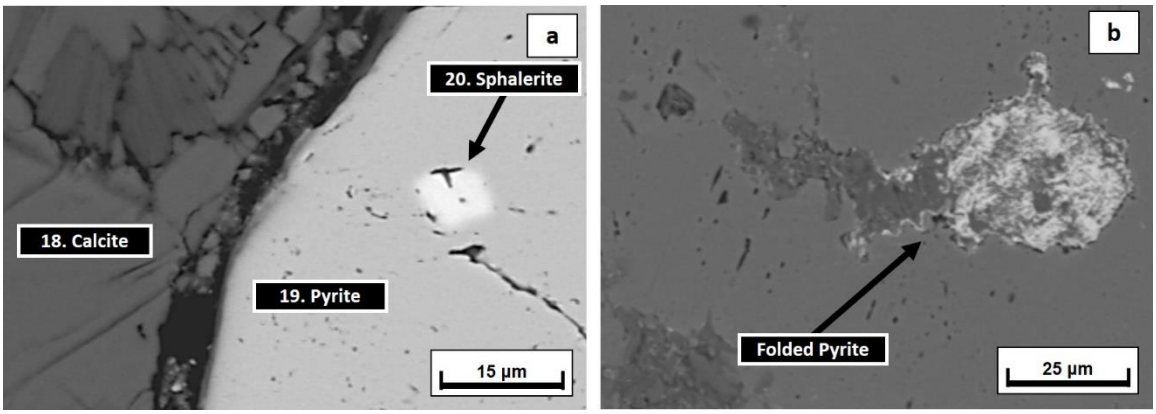

Figure 5.91: **a)** SFT2/14b under the SEM showing the intersection between the pyrite and the calcite with interlocking muscovite. Note the deformation of the calcite grains along the contact as well as the sphalerite zonation within the pyrite; **b)** SFT2/15 under the S

5.5.6 SFT/2 Sample 21

In Sample 21, nodular textures are observed throughout the quartz- and clay-rich matrix with certain nodules exhibiting a calcite nucleus (**Figure 5.92 a**). The sample contains trace rutile, sphalerite and chalcocite (CuS_2) (**Figure 5.92 b**).

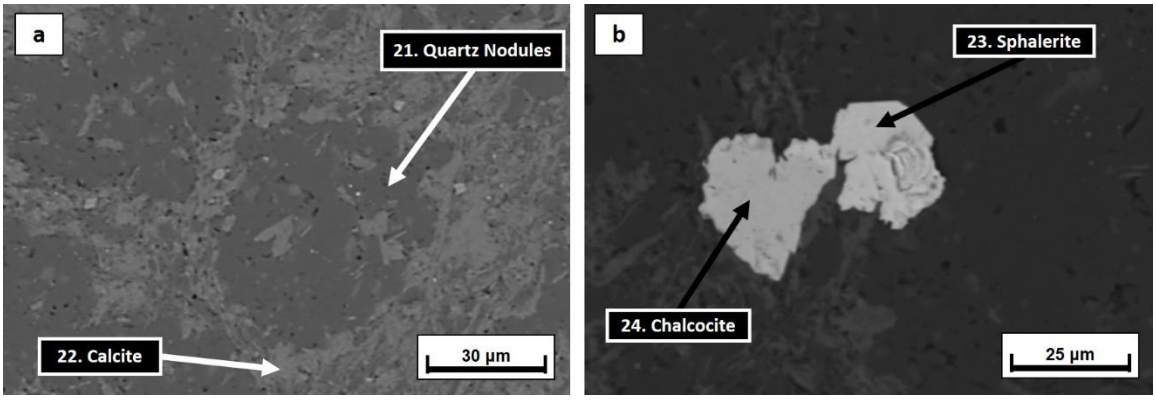

Figure 5.92: SFT2/21 under the SEM showing **a)** quartz nodules surrounded by a calcite- and clay-rich matrix; **b)** chalcocite and sphalerite within a quartz-rich matrix.

5.6 XRF Analyses

PPC Cement and SA Lime Eastern Cape obtained samples from certain areas within the project area to determine the quality of the gypsum which was found within their mining licence area. These samples supplemented the need of PPC Cement to determine what quality of gypsum they would be adding to their cement mix and met SA Lime Eastern Cape's need to understand the gypsum quality used in agricultural soil. The samples therefore all originated from areas where gypsum

was being mined at the time. In most cases, the samples were crushed and screened in order to represent the sample that would be added to the cement mix and/or the agricultural land.

5.6.1 Samples Specifically Tested for Gypsum Content (% $CaSO_4 \cdot 2H_20$)

Sample KA1661 and KA1662 were both obtained from Site F (**Figure 5.36**) and were tested for gypsum percentage (% $CaSO_4 \cdot H_2O$) on 22 October 2014. KA1661 was an unscreened sample and therefore represents the gypsum sample selected from the field prior to any attempt regarding upgrading via screening processes. KA1662 represents a sample which has undergone a screening process whereby only the portion of the sample which has passed through a <0.106mm screen (61.98% of the total sample) has been tested (**Table 5.9**).

Table 5.9: XRF analysis on Samples KA1661 and KA1662 from Site F.

Sample No.	Site	CaO	MgO	SO_3	<0.106mm	$CaSO_4 \cdot 2H_2O$
KA1661	F	20.47	1.758	21.62	NA	**77.88**
KA1662	F	18.43	1.36	20.9	61.98	**82.19**

Sample KA1925, also obtained from Site D and not screened, was tested on 30 June 2015 to determine its gypsum content. This sample has a CaO of 14.01 % (more than 6% less than KA1661) and an SO_3 of 18.65 (approximately 3% less than KA1661). This results in the $CaSO_4 \cdot 2H_2O$ of the KA1925 sample being 35% less than in KA1661 (**Table 5.10**).

Table 5.10: XRF analysis on Sample KA1925 from Site F.

Sample No.	Site	CaO	MgO	SO_3	$CaSO_4 \cdot 2H_2O$
KA1925	F	14.01	0.199	18.65	**41.62**

Only two samples were tested from Site D (**Figure 5.24**), namely Sample 4290/99R and Sample 4291/99R. These samples were tested for the main purpose of determining the gypsum quality at the PPC Mount Stewart mine, but also to compare fine-grained and medium-grained gypsum deposits. Their analysis also included MgO, Na_2O, Cl (in parts per million), K_2O and P_2O_5 elemental composition, but focused mainly on determining the CaO and SO_3 which contribute towards the gypsum. The two samples resulted in very similar gypsum quality with the fine-grained sample (4290/99R) producing a gypsum

grade only 0.48% higher than that of the medium-grained sample (4291/99R). While the CaO of the finer gypsum is higher, the SO_3 is relatively lower, with an overall higher gypsum content observed in the coarser sample (**Table 5.11**).

Table 5.11: XRF analysis on Sample 4290/99R and 4291/99R from Site D.

Sample No.	Site	CaO	MgO	Na_2O	SO_3	Cl (ppm)	K_2O	P_2O_5	$CaSO_4•2H_2O$
4290/99R	D	28.07	0.265	1.281	30.06	1.98	0.6384	0.0458	64.65
4291/99R	D	28.52	0.282	1.577	29.84	2.02	0.6143	0.0458	64.17

5.6.2 Samples with a Full Elemental Analysis

Sample GMTS14 and GMTS15 were obtained from Site D and underwent a full XRF analysis. The gypsum quality was determined from the XRF data and it was found that GMTS014 had a $CaSO_4•2H_2O$ percentage of 68.39% while GMTS15 had a $CaSO_4•2H_2O$ percentage of 59.14% (**Table 5.12**). The Silica in both samples was above 17% and Aluminium and Iron were also notable in both samples. Magnesium was the only other element which was found to be higher than 1% in abundance. The two samples, which were taken in a gypsum mining trench at Site D, were approximately 20m apart from one another *in situ*, however, there is a notable difference in the SO_3 content with GMTS15 being greater than 4% richer in sulphur trioxide. The calcium oxide proportion of the two samples is, however, fairly similar.

Table 5.12: XRF analysis on Sample GMTS14 and GMTS15 from Site D.

Sample No.	Site	SiO_2	Al_2O_3	Fe_2O_3	Mn_2O_3	TiO_2	CaO	MgO	P_2O_5	Cl (ppm)	SO_3	K_2O	Na_2O	CaSO4•2H2O
GMTS14	D	17.2	4.76	5.94	0.066	0.20	23.8	1.34	0.14	103.2	27	0.7	0.18	**59.06**
GMTS15	D	17.9	5.29	5.21	0.122	0.23	24.7	1.12	0.12	42.52	31	0.7	0.16	**68.37**

Samples GPPC/01 and GPPC/02 were obtained at Site D in the old prospecting trenches which are located on the property. The samples were obtained from the same trench and were approximately 20m apart along strike. Both samples were then screened and the minus 20mm portion was analysed in both cases. The results show that the two samples are very similar in gypsum quality – 57.5% for GPPC/01 and 54.0% for GPPC/02 (**Table 5.13**). In general, however, the GPPC/01 sample is a higher quality gypsum as it has higher CaO and SO_3 values and lower Silica, Aluminium and Iron. Once again, Magnesium is the only other element which is found to be greater than 1% in abundance. The Chlorine is notably lower in this sample as opposed to the samples which were tested from

Site A. In general, the two samples here are of slightly poorer quality in comparison to the samples GMTS14 and GMTS15.

Table 5.13: XRF analysis on Sample GPPC/01and GPPC/02 from Site A.

Sample No.	Site	SiO_2	Al_2O_3	Fe_2O_3	Mn_2O_3	TiO_2	CaO	MgO	P_2O_5	Cl (ppm)	SO_3	K_2O	Na_2O	CO_2	$CaSO_4 \cdot 2H_2O$
GPPC/01	A	16.0	3.31	2.75	0.13	0.17	25.3	1.46	0.10	0.10	32.2	0.52	0.21	21.5	57.50
GPPC/02	A	21.2	4.47	4.90	0.08	0.21	21.8	1.35	0.15	0.15	27.6	0.72	0.28	18.6	54.00

6. INTERPRETATION OF RESULTS

This chapter focuses on the interpretation of the results presented in Chapter 5. Interpretations of the SFT2 core analysis are summarized to address the characteristics of the shale of the Whitehill Formation. Mineralogy and mineral textures observed during thin section and SEM analyses assist in uncovering the chemical systems which result in the formation of gypsum whereas XRF analyses, which were conducted by PPC Cement and SA Lime, will supplement interpretations relating to gypsum deposits within the study area. The fieldwork observations will be correlated to the occurrence of gypsum within the study area. Fold analysis data are related to deformation events associated with the Cape Fold Belt on a variety of different scales.

6.1 Interpretation from Fieldwork

Gypsum occurrences associated with weathered shale are a common theme throughout the study area. In areas where shale is fairly unweathered and bedding planes could easily be identified, gypsum mineralisation was rare or non-existent. In areas where shale was highly weathered, gypsum of various forms was generally found. The occurrence of gypsum throughout the study area is mostly in the form of impure crystals and crusts (**Figure 5.37** and **Figure 5.47**) however, there is also evidence of minor gypsum powder in places (**Figure 5.45**). There is evidence to suggest that *Euphorbia Esculenta* favours soils or weathered shales with a high gypsum content, as observed at Site F (**Figure 5.39**), and therefore can be used as an initial indication for potential gypsum deposits.

The chemical reactions (1 to 3) involving the calcite- and pyrite-rich portions within the shale of the Whitehill Formation are likely to have occurred within the project area. Iron (II) sulphide combined with calcium carbonate, produces Calcium Sulphate (gypsum) and is oxidized to Iron (III) oxide (ferric hydroxides) through the series of chemical reactions outlined by Pirlet *et al*. (2010) and Chermak and Schreiber (2014). As a result, gypsum and the haematite minerals are located together at Site A (**Figure 5.4** and **Figure 5.5**) as well as at Site F (**Figure 5.35**). In addition to this, the various colours of the shale and gypsum, such as those observed at Site A (**Figure 5.4** and **Figure 5.8**) and Site F (**Figure 5.38**), are likely

associated with a chemical sequence which results in the precipitation of gypsum (white colour), iron-rich minerals (red and yellow colour) and sulphur-rich minerals (yellow colour). The yellow colour shale observed in several areas throughout the project area is also related to the tuffaceous horizons which are commonly interbedded with the shale. The white to grey colour of the Whitehill Formation compared to the yellow to brown shale of the Collingham Formation observed at Site B (**Figure 5.18**) is a result of increased calcium content within the former as well as greater proportion of tuffaceous horizons within the latter. The tuff layers identified between shale throughout the project area provide evidence of a volcanic eruption which expelled sulphur-rich minerals such as sulphur dioxide (SO_2) and hydrogen sulphide (H_2S). These sulphur-rich strata may undergo dissolution and allow sulphur-ions to become available for gypsum formation, but further study would be required to prove this.

Cherty shale horizons, such as those observed in the section studied at Site A (**Figure 5.4**) preserve the original Whitehill Formation sequence as these were deposited in a deep marine setting associated with the Karoo Basin. The silica-rich chert does not weather as easily as the surrounding calcium-rich shale. Dolomite strata, such as the example observed at Site E (**Figure 5.31**) are generally not found in areas where gypsum mineralisation has occurred. Dolomite, $CaMg(CO_3)_2$, is less likely to weather due to the relatively compact crystal structure associated with magnesium, in comparison to shale which contains pure calcite ($CaCO_3$). The dolomite strata throughout the study area are mostly unweathered and therefore do not provide a suitable host rock for the precipitation of gypsum.

The grey-white shale observed at Site B (**Figure 5.18**) is highly weathered and should therefore be suitable for the formation of gypsum, similar to the sections examined at Site A (**Figure 5.10** and **Figure 5.11**). However, there are no abundant gypsum deposits located at Site B. While Site B is located along an exposed south-dipping limb of a syncline, Site A is located at an exposed fold axis, which is potentially more favourable for gypsum formation due to the likely concentration of pyrite and calcite mineralisation as a result of deformation associated with the fold hinge zone. The series of alternating south- and north-dipping cherty shale outcrops located at Site D (**Figure 5.27** and **Figure 5.28**)

indicates that there is a mesoscale anticline located within the hinge zone of the larger macroscale syncline (Fold B). The mesoscale folding of hard, less ductile chert horizons within the hinge zone suggests that this area underwent a great deal of deformation, thus weakening the shale and making it more susceptible to weathering processes in comparison to areas located away from the hinge zone of the macro fold. Another example of gypsum mineralisation associated with shale deformation is observed at Site F (**Figure 5.42**) where a monocline fold and its resultant weakening of the shale has led to the formation of a small gully located directly adjacent to a large gypsum deposit.

Slickensides identified along the exposed planes of cherty-shale outcrops suggest associate faulting of strata within the hinge zone of the macro-scale fold. The faulting is likely a result of tight folds formed by compressional forces acting upon the strata. The faults also provide a weakened surface in which gypsum-forming aqueous solutions in meteoric water, can penetrate the shale and later precipitate into a rich gypsum deposit. Areas with higher gypsum proportions are usually associated with thinner shale horizons. Thinner shale horizons are generally weaker and more susceptible to compressive forces which result in folding or faulting of the strata. The deformed and weaker shale resulting from folding and faulting was observed at Site A (**Figure 5.4** and **Figure 5.5**).

Figure 5.10 and **Figure 5.11**) as well as at Site F (**Figure 5.42**) provides a more penetrable area in which gypsum is able to precipitate. The gypsum observed at Site G (**Figure 5.47**) is likely a result of faulting in the area which provided a weakness in the shale allowing a river channel to form. No gypsum is observed in areas more than 10m from the river channel, suggesting that the formation of the gypsum crusts is associated with the present geomorphological characteristics of the study area.

The orthogonal blocks observed at Site A and Site E (**Figure 5.6** and **Figure 5.32**) suggest that the shale underwent expansion due to pressure release as it became exposed at the surface. The boudinage structures observed within the Collingham Formation shale at Site E (**Figure 5.33**) also suggest that the strata were extended laterally. Expansion decompression contributed further to deformation of the shale thus making it susceptible to weathering. Ground or surface water would likely

traverse the gaps (joint planes) between orthogonal blocks and enter the strata below to dissolve calcite and pyrite minerals to subsequently precipitate gypsum.

Even with an abundance of calcium and sulphate, the formation of mineable quantities of gypsum in the study area requires the correct surface conditions. Evaporitic gypsum deposits of any economic thickness require a surface layer of soft weathered material preferably with a relatively recent overlying clay deposit. A supply of groundwater is also necessary, but the movement of this water should be restricted so that the gypsum can precipitate slowly and form relatively large crystal structures. Although this does not necessarily translate to larger gypsum deposits, it is likely to increase the quality of gypsum mined *en masse* in a particular area. The gypsum veins observed throughout the study area vary greatly in size and texture and are likely dependent on the cooling temperatures and flow rates of the solutions which carried the calcium- and sulphate-rich ions. Larger veins with similarly orientated crystals are associated with slower cooling (**Figure 5.37**), more stagnant solutions while smaller veins with crystals having no particular orientation (**Figure 5.38**) are associated with faster cooling, flowing solutions.

Therefore, the ultimate surface conditions would be an area which is low-lying compared to its immediate surroundings, but where there is no extreme topography allowing water to move away at any significant rate. At Site D, the Whitehill Formation is overlain by a thick (approximately 2m) weathered surface. This is possibly due to water movement from the higher topographic area down into a hollow, forming large weathered areas and depositing clay material at the surface. Groundwater within the weathered and clayey horizons then dissolves the required calcium and sulphate from the underlying Whitehill Formation and forms the gypsum which is found there today. Although no mining has been conducted along the north-dipping southern limb of the syncline at Site D (**Figure 5.25**), there have been exploration boreholes drilled in this area which, according to the mine manager, intersected some minor gypsum. The north-dipping southern limb also extends to Site E (**Figure 5.29**) where gypsum deposits have been identified. Therefore, although gypsum does occur within the shales of the north-dipping southern limb, it has not been mined due to the lack of abundant gypsum. A map of the topography and rivers of the area shows a small water course located

in the centre of the Whitehill at Site D (**Figure 6.1**). This water course could be the reason for the weathered surface in the area and there could also be an associated groundwater system in which the gypsum elements are concentrated. The drainage characteristics of this area, in contrast to the north-dipping limb, are more favourable for the formation of large, minable gypsum deposits because there are more interconnected channels in this part of the Whitehill Formation outcrop.

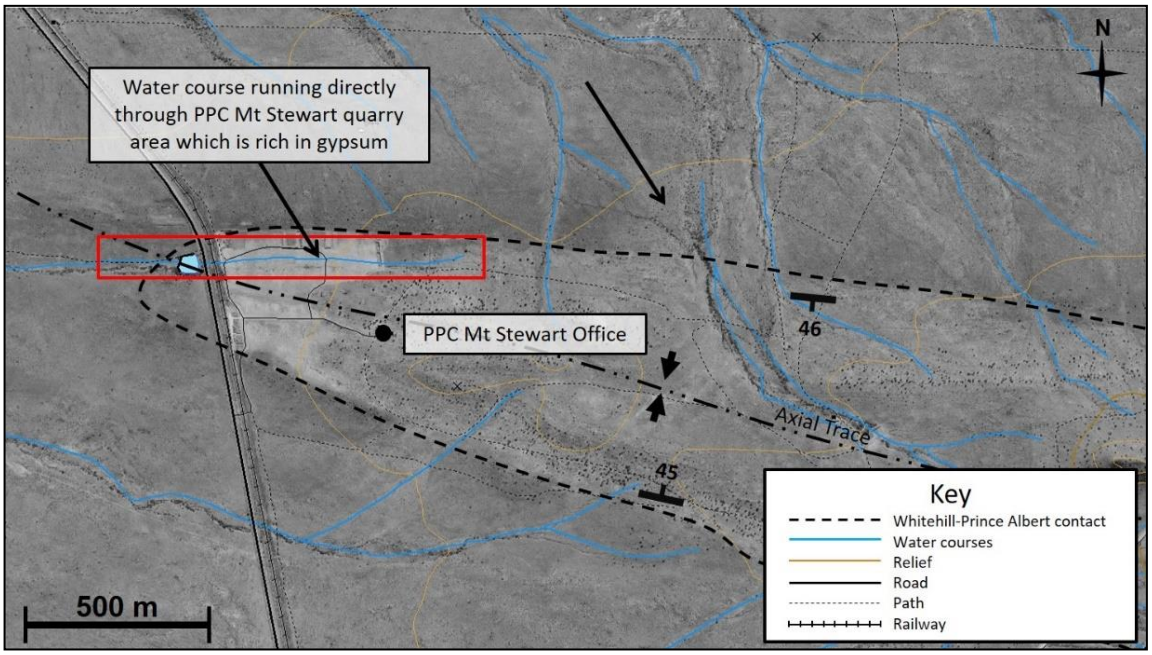

Figure 6.1: Topography and hydrology of Site D, the location of PPC Mt Stewart and a number of rich gypsum deposits.

The gully erosion, observed in the Jansenville Road Quarry located on at Site E (**Figure 5.30**), is likely a result of weaker strata where faulting may have occurred and thus provides the opportunity for erosion, movement of surface and/or groundwater and later, the precipitation of gypsum. The majority of the road quarries located throughout the project area display sections of the shale of the Whitehill Formation, such as those studied at Site A to Site E (**Figure 5.3**, **Figure 5.17**, **Figure 5.22**, **Figure 5.24** and **Figure 5.30**). These quarries were likely opened to supply road material for the secondary gravel roads located in and around the study area. The reason that the majority of the quarries were mined over Whitehill Formation is that the shale, due to its highly weathered nature, is easier to mine in comparison to the underlying Prince Albert Formation shale and the overlying Collingham Formation shale.

The large dolomitic concretions observed in the road quarry at Site E show evidence to support the concretionary growth model presented by Lash & Blood (2004). The shale directly below the concretion appears to be folded in the same orientation of the oblate structure, suggesting that as the concretion grew it caused the surrounding strata to deform. This deformation likely resulted in weaker shales directly below the concretions, thus providing a suitable host for gypsum precipitation (**Figure 5.7** and **Figure 5.35**). The joints which are filled with gypsum, such as those located below the *in-situ* concretion at Site A (**Figure 5.9**), are vastly different to those which produce the orthogonal blocks observed in the unweathered shale, and are likely to be associated with deformation as a result of concretionary growth.

The *in-situ* concretions observed at Site E (**Figure 5.35**) are immediately underlain by red shale meaning that iron oxide formation results from the chemical processes undergone during the growth of these concretions. The iron oxide is generally underlain by gypsum deposits again suggesting that concretionary growth plays a role in the formation of gypsum within the study area. The distinct yellow colour of concretions, such as the one observed at Site B (**Figure 5.20**), could suggest that the concretions are sulphur-rich, likely associated with the proliferation of pyrite during concretionary growth. Quartz mineralisation observed within the shell of the concretions at Site A (**Figure 5.9** and **Figure 5.12**) provides a hard exterior which prevents significant erosion or deformation of the concretion.

The average concretion size at Site C is 2.1m long by 0.9m wide and is classified as an elongate concretion according to Abdel-Wahab and McBride (2001) (**Figure 6.2**). The concretions located at Site E (**Figure 5.34**) have an average horizontal length of 3.1m, an average width of 2.0m and an average vertical height of 0.8m, classifying them as oblate subcircular concretions (**Figure 6.3**). Concretions throughout the study area are generally subcircular to elongate, while the lateral spacing between concretions is irregular. This suggests that the deposition of concretion-forming nuclei was random although the growth of concretions was generally uniform throughout the Whitehill Formation. Concretions of similar appearance and size are not necessarily located along the same stratigraphic horizons (**Figure 5.16**). This suggests that sediments of the Whitehill Formation

were deposited in several repetitive sequences resulting in the nucleation and growth of concretion-forming nodules at several horizons within the shale.

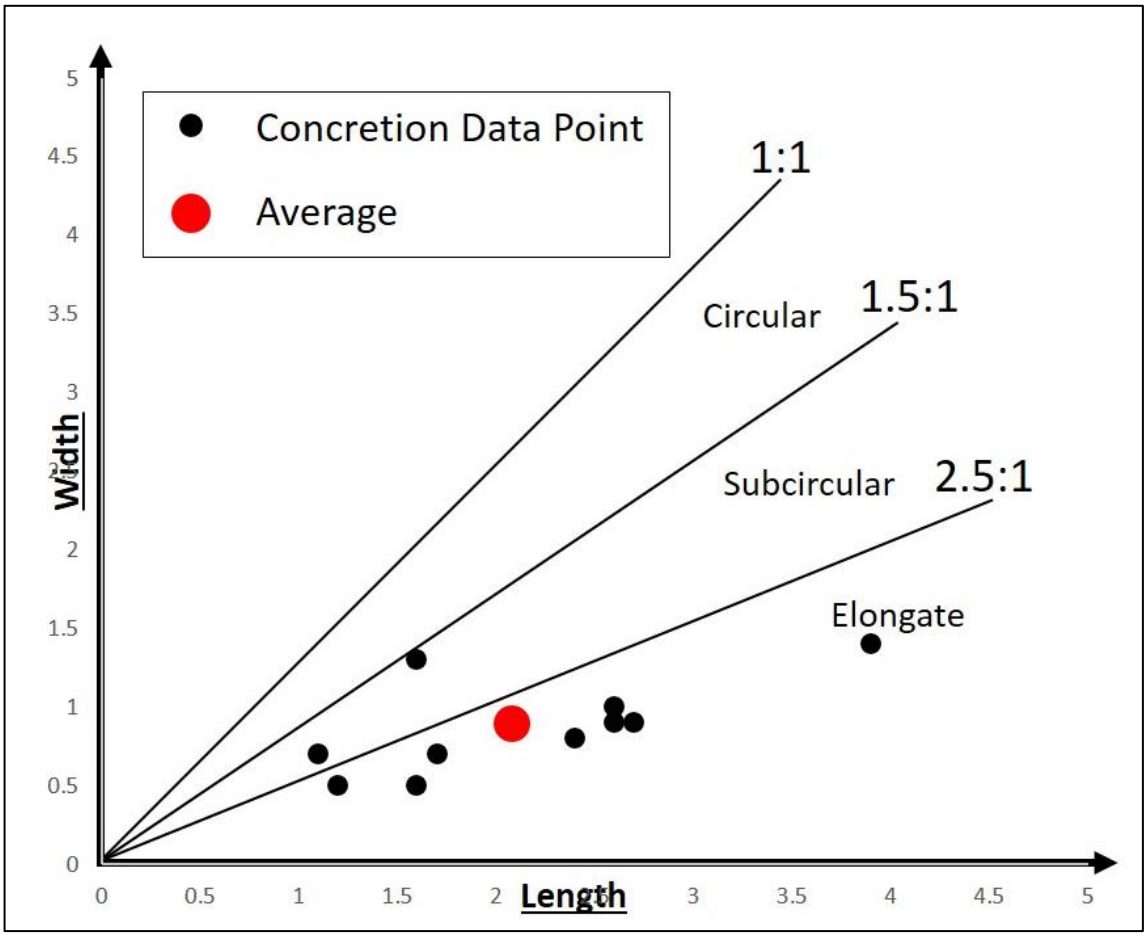

Figure 6.2: Aspect Ratio graph for the ten oblate concretions (black points) located on the within a quarry on East of Kruidfontein Farm 214 along the R338. The average concretion is represented by the red point and is classified as an elongate concretion.

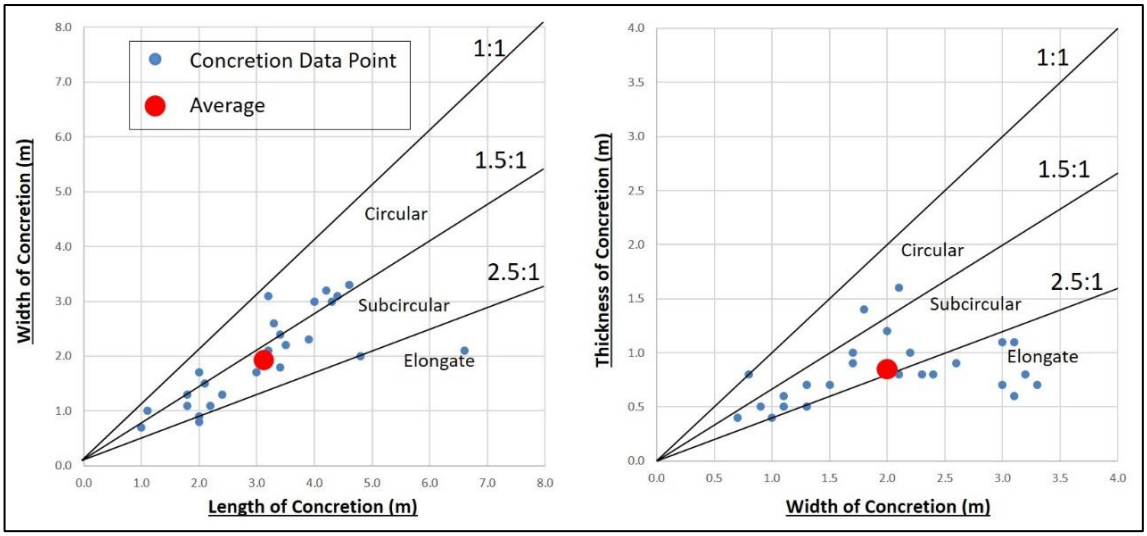

Figure 6.3: Aspect Ratio graph for the twenty-five (25) oblate concretions (blue points) located the within a quarry on Bluegumvale Farm 256 along the road connecting Mount Stewart to Jansenville. The average concretion is represented by the red point and is classified as an subcircular concretion.

A number of additional areas outside of those described in Chapter 5 (Site A to Site G) were also traversed during fieldwork, but none of these exhibited any gypsum mineralisation and therefore did not contribute to the study. Gypsum was only observed in areas where shale of the Whitehill Formation was present and was not identified in any road cuttings, quarries or outcrops associated with the Prince Albert Formation, Collingham Formation or any other stratigraphic sequence.

6.2 Interpretation of Structural Data

Fold orientations appear to play an important role in the study area because gypsum is often located in sub-outcrops of macro-scale fold hinge zones. Part of the aim of this project is to determine whether folding observed at different scales is a product of one event during the Cape Orogeny or multiple events. If the orientation of the folds at different scales is similar, one can assume that the strata were deformed during one event. If, however, it is found that the smaller folds do not have the same orientation characteristics as the major folds, one will probably have to assume that deformation of the strata took place at different times, or that there were major thrust zones in, for example, shale horizons. One possibility for differing orientation of smaller folds in contrast with the major folds is the swelling of shale which occurs during the precipitation of gypsum and other evaporites. Such examples are present in the study area at Site A (**Figure 5.5**). Another cause

of folding, which may not be related to Cape Fold deformation, is that which is brought on by concretionary growth. The carbonate concretions in the Whitehill Formation, for example, have been noted to cause disturbance of the surrounding shale which is likely due to the conical growth of the concretion.

Apart from Fold C, which is asymmetrical, the properties of all macro- and meso-scale folds are identical with regard to shape (cuspate), symmetry (symmetrical) and deformation style (similar). The fold tightness is variable however, all hinge zone folds exhibit a more acute interlimb angle in comparison to their macro-scale counterparts (**Table 5.4** to **Table 5.7**). Tighter interlimb angles result from greater deformation forces and would generally be present in incompetent shale strata. All macro-scale and meso-scale folds have a general west to east strike, as observed at Site F (**Figure 5.43**). Meso-scale folds are therefore of the same generation as macro-scale folds and explains why gypsum target areas are associated with fold hinge zones. Axial planes and fold axes of all folds are fairly similar apart from Fold C, which is the only fold with an axial plane that dips less than 80° and thus is the only asymmetrical fold. The reason for this anomaly is that Fold C is a complex fold which encompasses another smaller-scale fold (Fold B) and would therefore be described as a synclinorium. While axial planes may dip towards the north-northeast and south-southwest, the dip is usually very steep, making this change in direction mostly negligible. Fold axes plunge both to the west-northwest and east-southeast, but again, the plunge is very gentle and almost negligible (**Figure 6.4**).

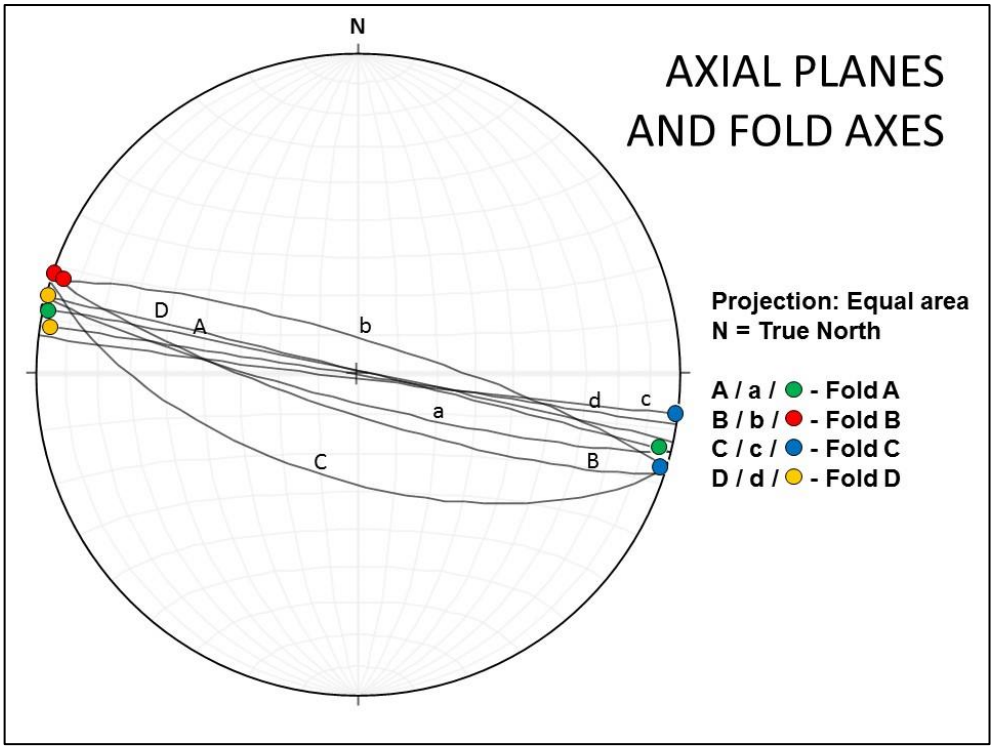

Figure 6.4: Stereoplot showing the axial planes and fold axes of Folds A, B, C and D as well as the average axial planes and fold axes of the folds recorded at a, b, c and d.

There is little difference between axial planes and fold axes of macro-scale folds in comparison with the meso-scale folds located at their hinge zones. This suggests that all folding is a result of deformation by forces acting in the same direction and is likely to be a Cape Fold deformation event causing compression from the south-southwest. It is important to note that at all four areas where the macro-scale fold hinge zones are outcropping (at ‘a’, ‘b’, ‘c’ and ‘d’), the Whitehill Formation is highly weathered and there is also noticeably more gypsum present at the surface as opposed to areas along an exposed fold limb. Meso-scale folds preferentially form in the Whitehill Formation because of local incompetent horizons (thinly bedded shales) buckling and bending between the competent sandstone and siltstone horizons in the overlying Collingham Formation and underlying Prince Albert Formation. Duplication of mesoscale folds results in a larger surface area where gypsum can precipitate and is therefore more suitable as a mining target.

6.3 Interpretation from Analysis of Core

Analysis of the SFT2 borehole core was conducted from above the Collingham Formation-Whitehill Formation contact to below the Whitehill Formation-Prince

Albert Formation and has been represented by a simplified stratigraphic column (**Figure 6.5** to **Figure 6.8**). It is clear from the stratigraphic column that the overlying Collingham Formation and the underlying Prince Albert Formation do not consist of any noticeable pyrite mineralization. Relative pyrite content peaks at approximately 218m below the SFT2 collar position, but is reasonably high over a thickness of some 11m (from 212.5m to 223m). While calcite is visible throughout most the section, there are two noticeable peaks at 210.5m and 226.m with relatively high calcite proportions between these two points. Since relatively high pyrite and calcium overlap at the interval from 212.5m to 223m, it can be assumed these areas would be most suitable for the dissolution of sulphur and calcium ions required for the precipitation of gypsum. The mid to lower shale of the Whitehill Formation would therefore be regarded as the most dominant source of gypsum mineralisation.

The higher carbon and calcium content of the Whitehill Formation, in comparison to the overlying Collingham Formation and underlying Prince Albert, is directly related to the depositional history of the strata. The Whitehill Formation sediments are rich in organic material (Cole and Basson, 1991) and associated calcium-rich material resulted in sediment which would later favour calcite mineralisation. In areas where the shale consists of veins containing both calcite and pyrite, especially when orientated parallel to bedding, the pyrite lenses appear to be surrounded by the calcite (**Figure 5.64** and **Figure 5.66**), possibly suggesting that the calcite formed initially along the walls of the vein and was later infilled by the pyrite. However, there are examples where the pyrite surrounds the calcite in some veins (**Figure 5.72**), suggesting that these gypsum-forming components are more complex, and not subject to any particular mineralisation sequence. Several calcite veins observed in the SFT/2 borehole core rock exhibit a brown discolouration (**Figure 5.67** and **Figure 5.70B**) which is likely due to oxidation of pyrite forming iron oxide, a process associated with the formation of gypsum provided there is sufficient calcium available. Iron oxide is observed directly below the area of high pyrite content within the stratigraphic column (**Figure 6.7**).

While most calcite and pyrite veins remain parallel to bedding (**Figure 5.70**), there are also a number of secondary veins which are randomly orientated and appear to cut across the bedding-orientated veins (**Figure 5.76**). Most, if not all, pyrite

lenses are associated with the bedding-parallel (primary) veins and there is no pyrite observed with the secondary veining. This may suggest that iron and sulphur ions are less abundant than calcium and therefore gypsum formation is limited by the former and not the latter. White powder is observed in the borehole core rock at approximately 228m below the collar position (**Figure 5.80**) and is likely to be gypsum precipitated after the core rock was exposed to the surface. The absence of pyrite in this sample suggests that the processes which convert pyrite to gypsum have already taken place. The presence of calcite veins also suggests that gypsum precipitation is limited by the pyrite, and calcite generally remains in surplus.

Shale observed within the borehole core rock exhibits folding in a number of areas which also contain calcite and pyrite mineralisation (**Figure 5.66**). The deformed nature of the shale, together with sulphur-rich pyrite and calcium-rich carbonates provide three key prerequisites for gypsum formation. The normal and reverse faults, observed at approximately 215.5m below the collar position (**Figure 5.70**) displace both calcite and pyrite mineralisation veins. This indicates that the mineralisation occurred prior to the deformation of the shale. Areas such as this would be susceptible to weathering when exposed at the surface and due to the presence of calcite and pyrite, would be suitable to supply the necessary calcium and sulphate ions required for gypsum formation. The thrust zone observed at the base of Whitehill Formation (**Figure 5.81**) could be a weak area where slip has occurred at the contact between the weaker shale of the Whitehill Formation and the compact more silica-rich shale of the Prince Albert Formation.

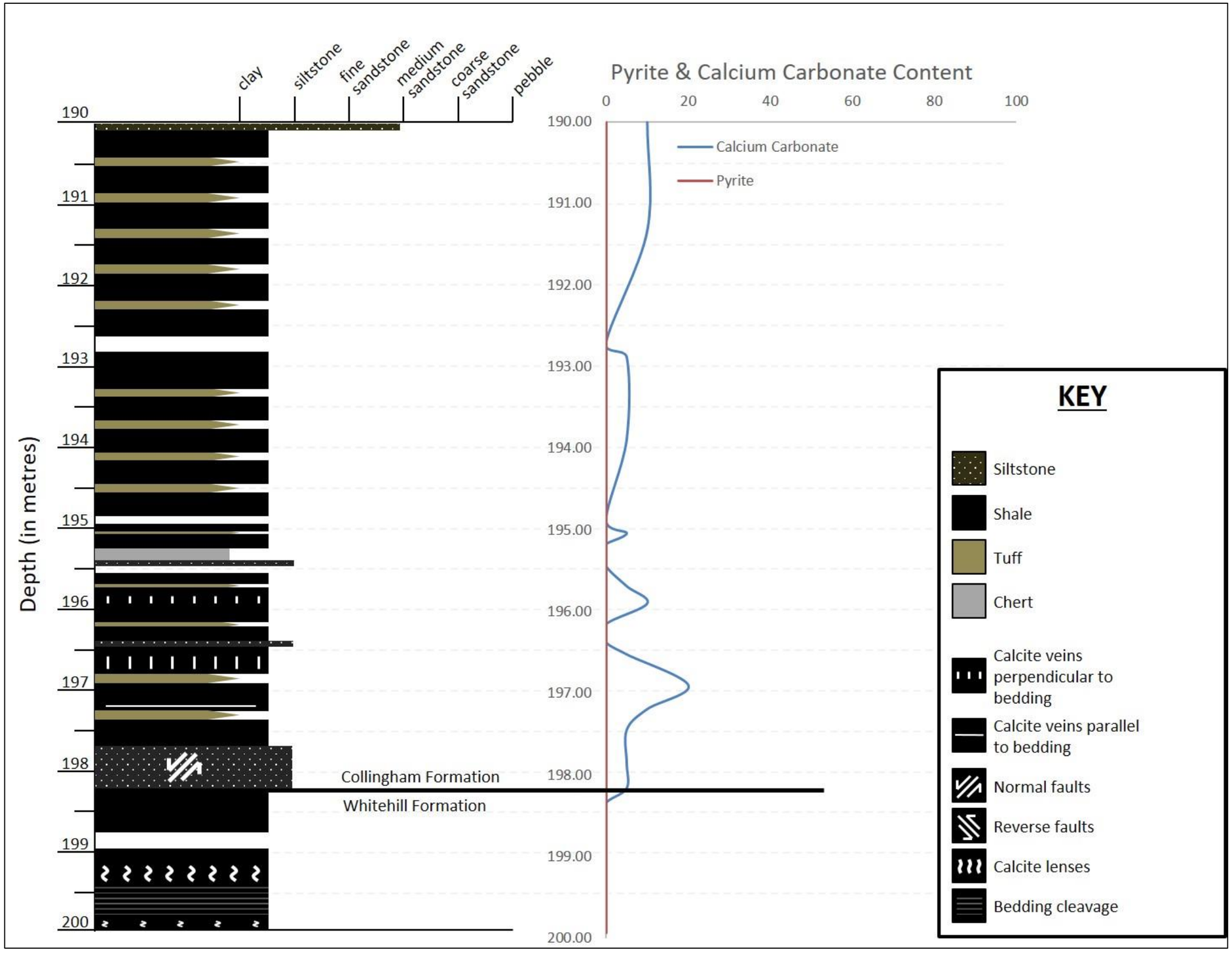

Figure 6.5: Simplified stratigraphic column of the SFT2 borehole core rock – 190m to 200m below the collar position.

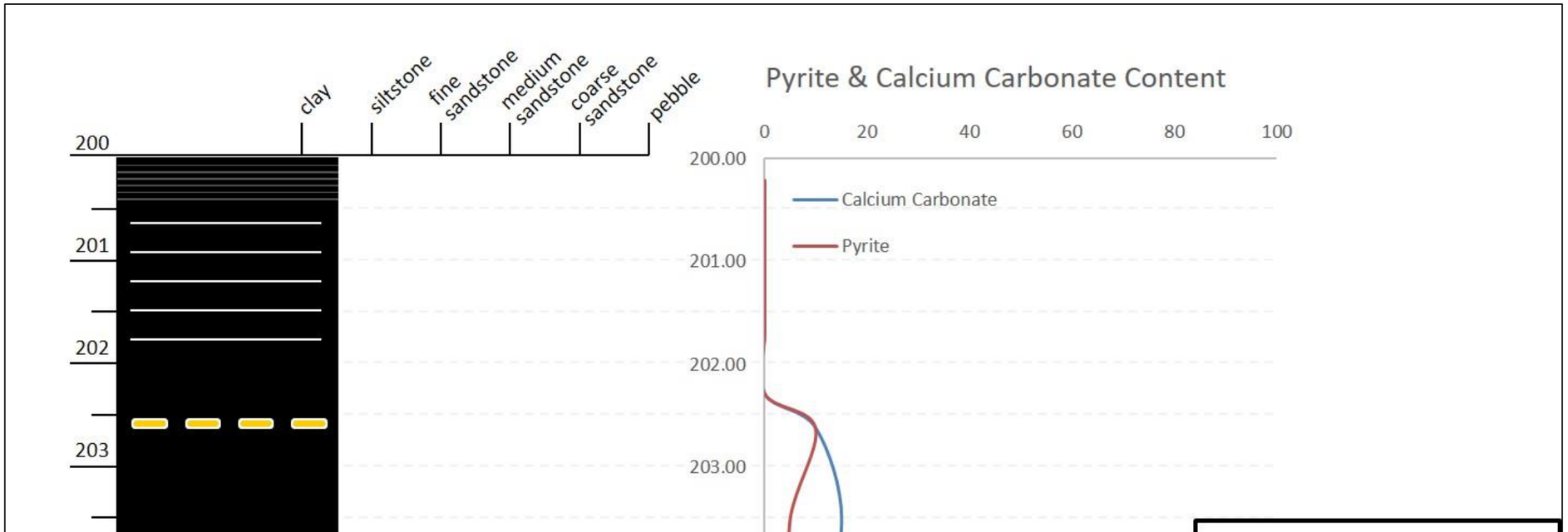

Figure 6.6: Simplified stratigraphic column of the SFT2 borehole core rock – 200m to 210m below the collar position.

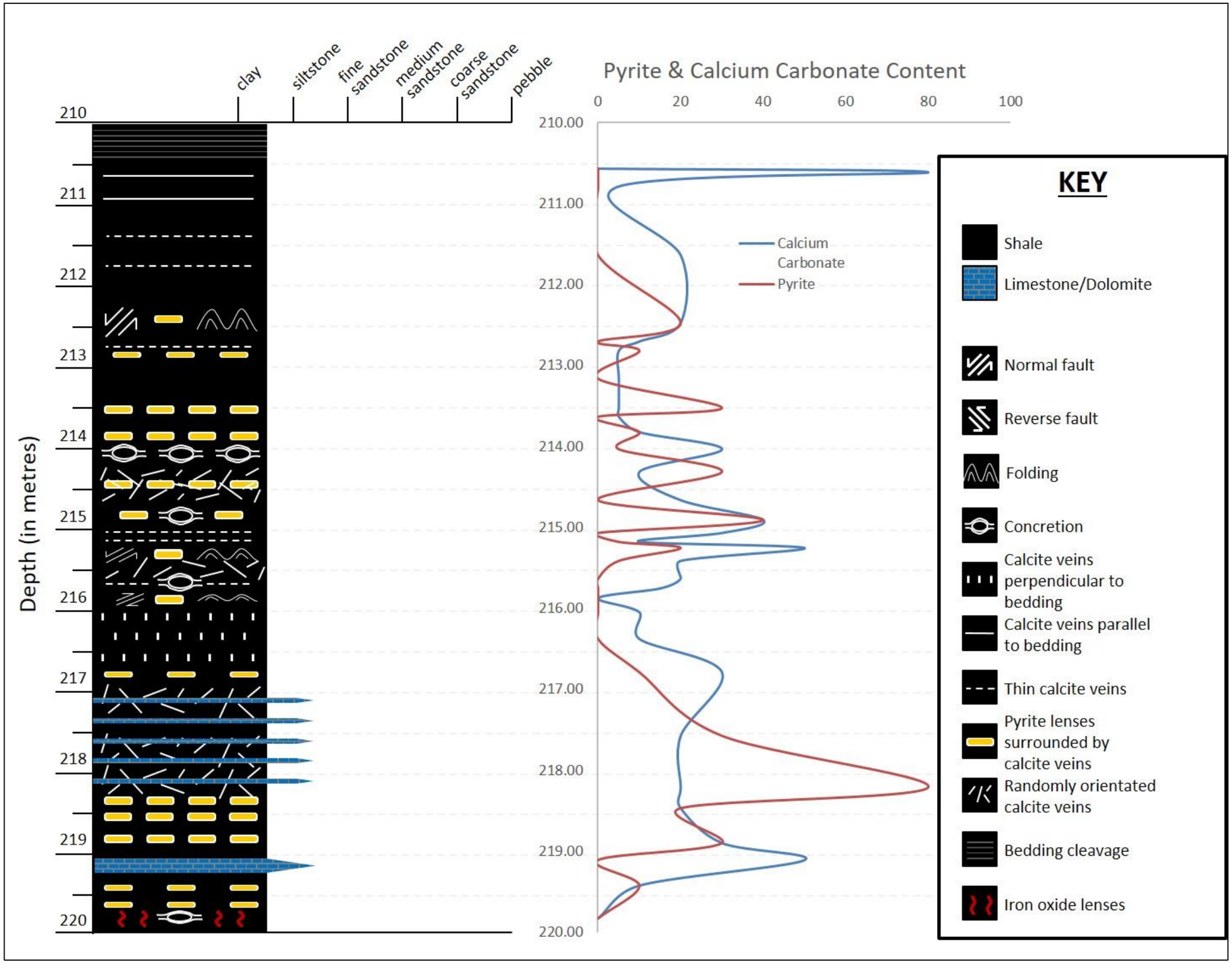

Figure 6.7: Simplified stratigraphic column of the SFT2 borehole core rock – 210m to 220m below the collar position.

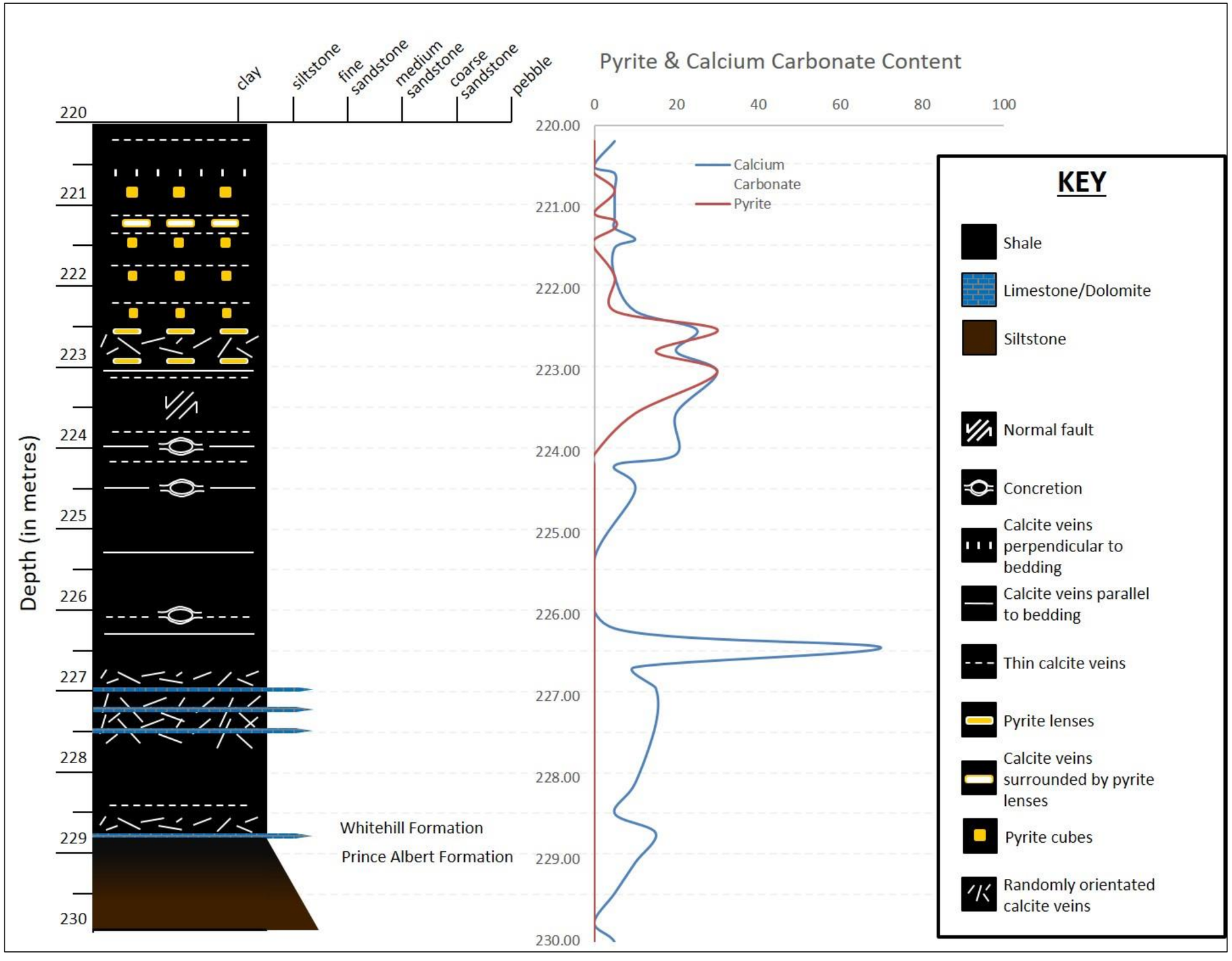

Figure 6.8: Simplified stratigraphic column of the SFT2 borehole core rock – 220m to 230m below the collar position.

The cherty layer observed at 195.15m is likely to correspond to the 'Matjiesfontein chert' horizon as it portrays the characteristics described by Visser (1992) and is located in a similar position within the lower Ecca Group stratigraphy. The limestone or dolomite layer at 219.08m (**Figure 5.74**) could be directly related to carbonate layers observed at Site E (**Figure 5.31**), as both are interbedded in thinly-bedded shale of the Whitehill Formation. Thick pyrite lenses, such as those observed between 216.95m and 219.08m below the borehole collar position (**Figure 5.72**), could be related to the gypsum crusts such as those observed at Site G (**Figure 5.47**). The pyrite-rich area would supply sufficient sulphur ions for gypsum formation and may represent a process where gypsum is formed in areas directly associated with areas of pyrite mineralisation.

There are several examples of nodular concretions within the core rock (**Figure 5.68**, **Figure 5.69**, **Figure 5.75**, **Figure 5.78** and **Figure 5.79**). While most these nodules are relatively small (less than 5cm in diameter), the discolouration of the shale at 223.96m below the collar position potentially exhibits a larger (greater 15cm diameter) concretion. As observed with the concretions in the field, the outer layers exhibit iron-oxide encrustations associated with the oxidation of pyrite (**Figure 5.78**). Evidence of concretions is observed from 214m to 226m below the collar position of the borehole (**Figure 6.7** and **Figure 6.8**), but they are mostly concentrated at 214m to 215.5m. This is within the section of relatively high pyrite and calcite and would suggest that the occurrence of the concretions is directly related to these gypsum-forming minerals. Concretionary growth appears to control the orientation of the calcite and pyrite veins and lenses in several areas (**Figure 5.69**, **Figure 5.75** and **Figure 5.79**). Pyrite and calcite veins usually mineralize within the parallel bedding cleavage of relatively undisturbed shale, but concentric growth of nodules and concretions causes flexing of these veins at various scales. This suggests that concretionary growth took place after the emplacement of the calcite and pyrite mineralization and could in fact be promulgated by the interaction between these two minerals.

Carbon-rich layers in the borehole core rock, such as the one observed between 202.66m and 205.88m below the collar position (**Figure 5.65**), appear to be unweathered with little to no pyrite and calcite present. Layers such as these do not seem to contain concretions or nodule-type structures and their porosity

should therefore be unaffected by swelling or expansion of the shale. This is important when considering the Whitehill Formation for shale gas potential as the strata with less pyrite and calcite could be a more desirable target for natural gas.

6.4 Interpretation from Laboratory Analyses

Monazite, zircon and rutile minerals identified through the EDS could be used to determine the age of the source rocks within the Whitehill Formation. The age dating of the source rocks would not aid the understanding of relatively recent gypsum deposition and was therefore not pursued in this study. The regularity of calcite within the matrix-supported shale observed in Sample SFT2/1 (**Figure 5.84 d**) indicates that the strata of the lower Ecca Group contain sufficient calcium-bearing minerals to form gypsum. Apatite is observed in many the samples examined under the SEM. The synthesis of apatite involves the chemical reaction between phosphate ions and calcium ions, a reaction which is less likely to occur than the reaction between calcium and sulphate ions (to form gypsum). Although the apatite minerals are likely to be of detrital origin, this could suggest that while calcium is abundant throughout the study area, it is in fact sulphide (associated with pyrite) that is the initial limiting factor, or less abundant constituent, in the formation of gypsum. It is also clear from the XRF analyses that sulphur content is the controlling factor regarding gypsum quality. This is likely a result of the availability of pyrite within the host rock which is dissolved into solution.

The manner in which quartz and calcite mineral grains appear to alternate within a vein suggests a calcium- and silica-rich source rock (**Figure 5.85 e**). Goethite identified in thin section sample SFT2/1 (**Figure 5.84 f**) is likely a product of pyrite weathering within the shale. However, no evidence of gypsum was observed in any aspect of the core analysis, suggesting that weathering of pyrite alone is not sufficient for the formation of gypsum. XRF sample KA1925 did not undergo any screening process and should therefore be comparable to sample KA1661. The $CaSO_4 \cdot 2H_2O$ percentage of this sample is far inferior, even though the samples are from a similar location (within a 50m of each other). This suggests that mineable gypsum deposits are not uniform throughout any specific area and are subject to a number of other variables such as deformation, weathering and concretionary growth.

The pyrite cubes surrounded by quartz mineralisation observed in thin section sample SFT2/12 appear to result from deformation of the shale (**Figure 5.86 f**). Deformation of the shale would make it relatively more susceptible to weathering at the surface which, due to the abundance of pyrite, may provide the necessary sulphur proportion required for gypsum formation. Folded calcite veins surrounded by amorphous pyrite, observed in thin section sample SFT2/14 (**Figure 5.87 f**), suggest that pyrite and calcite were precipitated together prior to a particular deformation event. Deformation of the two minerals makes them both more susceptible to weathering at the surface, thus promoting dissolution of calcium from the shale. Muscovite minerals, as identified by the SEM in Sample SFT2/9 (**Figure 5.90 b**), are generally associated with metamorphic alteration from a deformation event, and thus provide further evidence to support the notion that the shale in the project area underwent several deformation processes.

Barite and strontianite identified through EDS (**Figure 5.89 a**) provide evidence of groundwater mineralisation within the shale. These minerals are commonly formed in warm, pressurised groundwater which would also be suitable for the dissolution of calcite and pyrite. Pyrite and calcite which occur interbedded with quartz and clay minerals in the same microscopic view, such as those observed in SFT2/9 (**Figure 5.90 a**), would undergo the same weathering processes. While calcite and clay minerals would dissolve relatively easily, the pyrite and quartz would be more resilient to weathering. It is likely therefore, that a groundwater solution would sooner dissolve the calcite and clay minerals relative to the surrounding the pyrite and the quartz. Areas with greater calcite and clay pores would accommodate more groundwater and can therefore undertake a greater surface area of chemical reactions with the remaining pyrite. The larger mineralisation veins generally consist of greater calcite to quartz ratio in comparison to the smaller veins, as observed in thin section SFT2/9 (**Figure 5.85 d**). The larger veins are likely to fracture when exposed at the surface, such as the example seen in borehole core rock (**Figure 5.71**), and would therefore be susceptible to weathering. When meteoric water passes over these fractures, it dissolves the calcium-carbonate and increases the proportion of calcium ions carried in suspension. This may be the process which provides the necessary calcium ions for the mineralisation of gypsum.

Traces of Manganese (Mn) detected through EDS analysis and observed in several samples is likely associated with the dendritic percolation observed on the surface of the shale in hand sample (**Figure 5.82**). Quartz facets, such as those observed in SFT2/2 (**Figure 5.88 d**) can easily be penetrated by solutions carrying gypsum-forming components. If such facets are filled with gypsum, a bulk sample analysis of this area would exhibit a high silica content and would represent a poor-quality gypsum deposit. It is therefore possible that, even in conditions which are highly favourable for the formation of gypsum, a large silica content would reduce the overall quality of a gypsum deposit which is mined *en masse*. Although the quality of mineable gypsum can be upgraded by over 4% with the use of a screening process (**Table 5.13**), the microscopic textural relationships between silica-rich minerals and gypsum forming minerals would likely result in a bulk sample where the two cannot be easily separated.

Ooliths observed in Sample SFT2/1 (**Figure 5.84 e**) are concentric accretions generally formed from calcite, dolomite or silica. The chemical processes involved in the formation of ooliths at a microscopic scale may be transferable to the processes involved in the formation of the large concretions observed throughout the study area. Quartz and pyrite nodules are also observed under the SEM and therefore suggest that concretions in the Whitehill Formation can occur at various scales (**Figure 5.92 a**). Like the large dolomitic concretions observed in the field, these microscopic nodules exhibit mineralisation around their outer boundary and therefore suggest a concentric growth process (**Figure 5.91 b**). Framboidal pyrite observed under the SEM (**Figure 5.88 b**) is associated with the nucleation and growth of a mineral within a shale host. These nuclei may be associated with the processes which result in the formation of nodules and concretions observed within the Whitehill Formation. The semi-oblate pyrite observed in **Figure 5.88 c**. represents a later stage of nodule formation within the shale. The sample also exhibits folds or waves directly associated with the pyrite nodule and may be a microscopic translation of the folding observed with the mesoscopic concretions located throughout the project area. Deformation associated with folding and concretionary growth, within a pyrite- and calcite-rich shale host, suggest a suitable source of weathered material into which calcium and sulphate ion-

carrying solutions can penetrate and potentially precipitate into gypsum in the presence of water:

$$2FeS_{2\,(s)}\ (\text{pyrite}) + 7O_{2\,(g)} + 2H_2O_{(l)} \rightarrow 2Fe^{2+}_{(aq)}\ 4SO_4^{2-}{}_{(aq)} + 4H^{+}_{(aq)} \quad (1)$$

$$CaCO_{3\,(s)}\ (\text{calcite}) + H^{+}_{(aq)} \rightarrow Ca^{2+}_{(aq)} + HCO_3^{-}{}_{(aq)} \quad (2)$$

$$2SO_4^{2-}{}_{(aq)} + 2Ca^{2+}_{(aq)} + 4H_2O_{(l)} \rightarrow 2CaSO_4 \bullet 2H_2O_{(s)} \quad (3)$$

7. CONCLUSION

Gypsum deposits within the Steytlerville-Jansenville gypsum field were only observed in areas where shale of the Whitehill Formation is present. The mid- to lower-Whitehill Formation is the most likely source of gypsum-forming minerals, namely calcite and pyrite. Chemical reactions between pyrite and calcite within the shale of the Whitehill Formation is supported by the textural characteristics observed during microscopic analysis as well as the presence of by-product iron minerals such as haematite in the field. Gypsum formation is more limited by the availability of pyrite as opposed to calcite, which is in abundance throughout the Whitehill Formation.

Deformation of strata in the study area during the Cape Orogeny produced mostly north-verging folds indicating that stresses were exerted from the south-southwest towards the north-northeast. Structural weakening through folding and faulting of the shale resulted in the strata being doubled up by meso-folds, thus being more susceptible to weathering processes, especially within the hinge zone of the macro-scale folds which would potentially promote the concentration of pyrite mineralisation in these areas. In general, the fieldwork sites located at macro-scale fold hinge zones exhibit a wide variety of fault structures, are highly weathered and play host to a greater abundance of gypsum.

In order to promote the oxidation of pyrite required for the formation of gypsum, surface or near-surface conditions are necessary, where access to water and oxygen activate chemical reactions necessary to produce gypsum. Orthogonal blocks observed throughout the study area indicate that the shale underwent expansion due to pressure release as it became exposed at the surface. This would result in the weathering of the shale, allow for the infiltration of ground and surface water, and provide sufficient porosity for the precipitation of gypsum within the weathered zone. The preferred surface conditions for gypsum formation would be low-lying areas which are surrounded by gently-sloping topography promoting the concentration of aqueous solutions in a calcite- and pyrite-rich area associated with the shale of the Whitehill Formation.

Large dolomitic concretions observed throughout the study area are interpreted to have formed by concentration of nodules and mineralisation nuclei identified in the mid to lower Whitehill Formation. A concretionary growth model is envisaged whereby concentric mineral growth took place after the emplacement of the calcite and pyrite within the shale host and, like the formation of gypsum, could in fact be promulgated by the interaction between these two minerals. The expansion of these irregularly-spaced, subcircular to elongate concretions has resulted in further deformation of the shale, such as folding of the shale observed at various scales, thus promoting adjacent gypsum mineralization.

Mineable gypsum deposits are not uniform throughout any specific area observed in this study and are interpreted to be subject to several variables namely pyrite content, calcite content, tight folds and subsequent deformation, geomorphological controls and nodular or concretionary occurrences. The potential for extensive gypsum reserves within the Steytlerville-Jansenville field remains valid provided the target is located over a predominantly weathered Whitehill Formation outcrop, preferably at an area which has undergone extensive deformation (such as a fold hinge zone) and is favourable for the concentration of ground and surface water within a low-lying area.

8. REFERENCES

Abdel-Wahab, A. and McBride, E.F., 2001. Origin of Giant Calcite-Cemented Concretions, Temple Member, Qasr El Sagha Formation (Eocene), Faiyum Depression, Egypt, *Journal of Sedimentary Research*, vol. 71 (1), pp. 70-81.

Almond, J.E., 2009. Paleontological Impact Assessment: Desktop Study: Proposed gypsum quarry on Portion 1 of East of Gous Kraal No. 257, Cacadu District, Eastern Cape, Cape Town: Natura Viva cc. pp. 5.

Aref, M.A.M., Attia, O.E.A. and Wali, A.M.A., 1997. Facies and depositional environment of the Holocene evaporites in the RasShukeir area, Gulf of Suez, Egypt, *Sedimentary Geology*, v. 110, pp. 123-145.

Arid Zone Trees. 2015, *Introducing Variety 'AZT™' Cloned Quality and Uniformity*, http://www.aridzonetrees.com/-AZT%20Interactive%20Buttons/Variety%20AZT.htm.

Baviaans Tourism, 2012. *Steytlerville Fauna & Flora*, http://www.baviaans.co.za/page/steytlerville_fauna_flora.

Bordy, E.M. and Catuneanu, O., 2002. Sedimentology of the Beaufort-Molteno Karoo fluvial strata in the Tuli Basin, South Africa, *South African Journal of Geology*, vol. 105, pp. 51-66.

Brabers, A.J.M., 1976. Gypsum, *In:* Coetzee, C.B. (Eds.), *Handbook – Geological Survey of South Africa*, Geological Survey of South Africa, pp. 369-372.

Branch, T., Ritter, O., Weckmann, U., Sachsenhofer, R.F. and Schilling F., 2007. The Whitehill Formation - a high conductivity marker horizon in the Karoo Basin, *South African Journal of Geology*, vol. 110, pp. 465-476.

Catuneanu, O., Wopfner, H., Eriksson, P.J., Cairncross, B., Rubidge, B.S., Smith, R.M.H. and Hancox, P.J., 2005. The Karoo basins of south-central Africa, *Journal of African Earth Sciences*, vol. 43, pp. 211-253.

Chermak, J.A. and Schreiber, M.E., 2014. Mineralogy and trace element geochemistry of gas shale in the United States: Environmental Implications, *International Journal of Coal Geology*, vol. 126, pp. 32-44.

Climate-Data.org, 2012. *Climate: Klipplaat*, http://en.climate-data.org/location/763135/.

Cole, D.I. and Basson, W.A., 1991. Whitehill Formation, *In:* Johnson, M.R. (Ed.), *Catalogue of South African Lithostratigraphic Units*, 1st Edition, Belville: SA Geological Survey.

Cole, D. and Van Vuuren, C.J., 1978. Preliminary Report on the Oil Potential of the Whitehill Formation Between Strydenburg (Cape Province) and Hertzogville (Orange Free State), *Report (Geological Survey (South Africa))*, 33 pp.

Craddock, J.P., McKiernan, A.W., de Wit, M.J., 2007. Calcite twin analysis in syntectonic calcite, Cape Fold Belt, South Africa: implications for fold and cleavage formation within a shallow thrust front, *Journal of Structural Geology*, vol. 29, pp. 1100-1113.

Crangle, R.D., 2017. *USGS 2015 Minerals Yearbook: Gypsum [Advance Release]*, Reston, VA: U.S. Geological Survey, 11 pp.

Decker, J. and Marot, J., 2012. Investigation of Hydraulic Fracturing in the Karoo of South Africa, Annexure A, Resource Assessment, *Department of Mineral Resources: South Africa*, 156 pp, http://www.dmr.gov.za/publications/viewdownload/182/854.html.

De Ville Wickens, H., 1996. Die Stratigrafie en Sedimentologie van die Ecca Groep Wes van Sutherland, *Bulletin*, Council for Geoscience, v.107, 49 pp.

De Villiers, J.E. and Wardaugh, T.G., 1962. A sedimentary petrological study of some sandstones, conglomerates and tillites of the Cape and Karoo Systems, *Transactions of the Geological Society of South Africa*, vol. 65, pp. 101-108.

Du Toit, A.L., 1954. *The Geology of South Africa*, 3rd Edition, Edinburgh: Oliver and Boyd, 611 pp.

Eckardt, F.D. and Spiro, B., 1999. The origin of sulphur in gypsum and dissolved sulphate in the Central Namib Desert, Namibia, *Sedimentary Geology*, vol. 123, pp. 255-273.

Farm Chemicals Handbook, 1983. Meister Publishing Company, The University of Wisconsin, Madison, 770 pp.

Flint, S.S., Hodgson, D.M., Sprague, A.R., Brunt, R.L., van der Merwe, W.C., Figueiredo, J., Prélat, A., Box, D., Di Celma, C., Kavanagh, J.P., 2011. Depositional architecture and sequence stratigraphy of the Karoo basin floor to shelf edge succession, Laingsburg depocentre, South Africa. *Marine and Petroleum Geology*, vol. 28, pp. 658-674.

Fockema, R.A.P., Fockema, P.D. and Marais, J.A.H., 1962. Gypsum occurrences in South Africa, *Transactions, Geological Society of South Africa*, vol. 65, no. 2, pp. 1-12.

Foden, W. and Potter, L., 2005. *Chrysocoma ciliata L*, National Assessment: Red List of South African Plants, Webpage: http://redlist.sanbi.org/species.php?species=3214-5.

Geel, C., 2012. *Field Guide: 2nd Shale Gas Workshop February 15-17, 2012*, Nelson Mandela Metropolitan University, Department of Geoscience & AEON, in collaboration with Inkaba yeAfrica, 18 pp.

Geel, C., Schulz, H., Booth, P., de Wit, M. and Horsfield, B., 2013. Shale gas characteristics of Permian black shales in South Africa: results from recent drilling in the Ecca Group (Eastern Cape), *Energy Procedia*, vol. 40, pp. 256-265.

Geology Superstore, 2012. *Geosurveyor 002A Compass Clinometer*, http://www.geologysuperstore.com/index.php/geological-equipment-tools/compass-clinometer/geosurveyor-compasses/geosurveyor-002a-compass-clinometer.html.

Halbich, W., Fitch, F.J. and Miller, J.A., 1983. Dating the Cape orogeny, *Geological Society of South Africa*, vol. 12, pp. 149-167.

Jacana, 2012. *Sweet Thorn: Acacia Karoo*, Germinating and Growing Common African Indigenous Trees, http://www.jacanaent.com/Library/Trees/SweetThorn.htm.

Jacana, 2015. *Kori Bustard*, Lee Ouzman Photographic Library - South African Birds, http://www.jacanaent.com/PhotoLib/Birds/Bustard,%20Kori/!BustardKori.htm.

Johnson, M.R., van Vuuren, C.J., Hegenberger, W.F., Key, R. and Shoko, U., 1996. Stratigraphy of the Karoo Supergroup in southern Africa: an overview, *Journal of African Earth Sciences*, vol. 23 (1), pp. 3-15.

Johnson, M.R. van Vuuren, C.J., Visser, J.N.J., Cole, D.I., Wickens, H.D.V., Christie. A.D.M., Roberts, D.L. and Brandl, G., 2006. Sedimentary Rocks of the Karoo Supergroup, *In:* Johnson, M.R., Anhaeusser, C.R. and Thomas, R.J. (Eds.), *The Geology of South Africa*, Pretoria: Geological Society of South Africa, pp. 461-500.

Kingsley, C.S., 1981. A Composite Submarine Fan-Delta-Fluvial Model for the Ecca and Lower Beaufort Groups of Permian Age in the Eastern Cape Province, South Africa, *Transactions of the Geological Society of South Africa*, v. 84, pp. 27-40.

Kyffhäuser, 2014. *Rhigozum trichotomum Burch*, http://www.kyffhauser.co.za/Plants1/Rhigozum_trichotomum/Image3.htm.

Lash, G.G. and Blood, D. 2004. Geochemical and textural evidence for early (shallow) diagenetic growth of stratigraphically confined carbonate concretions, Upper Devonian Rhinestreet black shale, western New York, *Chemical Geology*, vol. 206, pp. 407-424.

Lokier, S.W., 2012. Development and evolution of subaerial halite crust morphologies in a coastal sabkhas setting, *Journal of Arid Environments*, v. 79, pp. 32-47.

Lurie, J., 2004. *South African Geology for Mining, Metallurgical, Hydrological and Civil Engineering*, Ninth Revised Edition, Johannesburg: Lupon Publishing, 324 pp.

MacRae, C., 1999. *Life Etched In Stone: The Fossils of Southern Africa*, Paris: McCarthy & Rubidge, 305 pp.

McBride, E.F., Picard, M.D. and Milliken, K.L., 2003. Calcite-Cemented Concretions in Cretaceous Sandstone, Wyoming and Utah, U.S.A., *Journal of Sedimentary Research*, vol. 73 (3), pp. 462-483.

Mozley, P.S, 1996. The internal structure of carbonate concretions in mudrocks: a critical evaluation of the conventional concentric model of concretion growth, *Sedimentary Geology*, vol. 103, 85-91.

Nel, H.J., 1962. A petrographic description of the Ecca sediments in the southern Karoo and eastern Orange Free State, *Annual Geological Survey of South* Africa, vol. 1, 91-103.

Nxumalo, V., 2001. *Stratigraphy and Basin Modelling of the Gemsbok Sub-Basin (Karoo Supergroup) of Botswana and Namibia*, MSc Dissertation (unpublished), University of the Witwatersrand, Johannesburg, 182 pp.

Oosterhuis, W.R., 1998. Gypsum, *In:* Wilson, M.G.C. and Anhaeusser, C.R. (Eds.), *The Mineral Resources of South Africa: Handbook*, Silverton: Council for Geoscience, pp. 394-399.

Pirlet, H., Wehrmann, L.M., Brunner, B., Frank, N., Dewanckele, J., Van Rooij, D., Foubert, A., Swennen, R., Naudts, L., Boone, M., Cnudde, V. and Henriet, J.P., 2010. Diagenetic formation of gypsum and dolomite in a cold-water coral mound in the Porcupine Seabight, off Ireland, *Sedimentalogy*, vol. 57, pp. 786-805.

Robertson, H., 2011. *Opuntia aurantiaca (Jointed cactus)*, Biodiversity Explorer, http://www.biodiversityexplorer.org/plants/cactaceae/opuntia_aurantiaca.htm.

Rogers, A.W., Schwarz, E.H.L., Haughton, S.H., 1991. *Geological Map of the Port Elizabeth Area*, Sheet 3324, Geological Survey of South Africa, 1:250 000 Series.

Ryan, P.J., 1967. *Stratigraphic and palaeocurrent analysis of the Ecca Series and lowermost Beaufort Beds in the Karoo Basin of South Africa*, PhD thesis (unpublished), University of Witwatersrand, Johannesburg, 210 pp.

SA Explorer, 2014. *Klipplaat Climate*, http://www.saexplorer.co.za/south-africa/climate/klipplaat_climate.asp.

SA National Biodiversity Institute, 2015. *Nama Karoo Biome*, http://www.plantzafrica.com/vegetation/namakaroo.htm.

Schaetzl, R.J., and Anderson, S., 2005. *Soils: Genesis and Geomorphology*, Cambridge: Cambridge University Press, 817 pp.

Strahler, A. and Strahler, A., 2006. *Introducing Physical Geography*, Fourth Edition, New York: John Wiley & Sons Inc, 728 pp.

The Great Karoo, 2014. *Climate and Vegetation*, http://www.thegreatkaroo.com/index.php?page=climate_and_vegetation.

Theron, A.C., 1967. *The sedimentology of the Koup Subgroup near Laingsburg*, MSc. Thesis (unpublished), University of Stellenbosch.

Theron, J.C., 1973. Sedimentological evidence for the extension of the African Continent southwards during the Late Permian-Early Triassic Times, *Proceeding Paper, Third Gondwana Symposium, Canberra, Australia*, pp. 61-71.

U.S. Geological Survey, 2017. *Mineral Commodity Summaries: Gypsum*, 2 pp, https://minerals.usgs.gov/minerals/pubs/commodity/gypsum/mcs-2017-gypsu.pdf

Visser, J.N.J., 1992. Deposition of the Early to Late Permian Whitehill Formation during a sea-level highstand in a juvenile foreland basin, *South African Journal of Geology*, v. 95 (5/6), pp. 181-193.

Visser, S., 1963. Gips in Die Republiek van Suidafrika, *Geological Survey*, Department of Mines, Pretoria, Handbook 4, 152 pp.

APPENDIX A: GEOLOGICAL LOG OF BOREHOLE SFT2 CORE

Jansenville-Wolwefontein SFT2 Borehole **Geological Log**

Borehole	SF2
Max Depth	
Log Start	192.95
Log End	226.93
Azimuth	
Dip	

Key	
CL - Collingham Formation	Cc - Calcite
WH - Whitehill Formation	Si - Silica
PA - Prince Albert Formation	Fe- Iron
	Qz - Quartz
sst - Sandstone	N1 - Black
mst - Mudstone	N2 - Grayish Black
shl - Shale	N3 - Dark Gray
slst - Siltstone	N4 - Medium Dark Gray
tff - Tuff	N6 - Medium Light Gray
‖ - Parallel to	N7 - Light Gray
NCR - No core recovered	5 Y 8/1 - Yellowish Gray
Si - Silica	10Y5/4 - Moderate Yellowish Brown

Depth (in m)		*Thick (in m)*	*Lithology*	*Colour (Previous)*	*Minerals*	*Structures*	*Weathering*	*Strat*	*Sample*	*Photo*	*HCl rxn / CO3 content*	*Pyrite Content*	*Descriptions & Comments*
From	***To***												
189.95 - Marker Block													
189.95	190.06	0.11	Siltstone	N4-N3				CL	Yes		10	0	Sandy and cherty texture; lighter colour
190.06	192.60	2.54	Shale	(sst) N2	Tuff			CL			10	0	
192.60	192.81	0.21	NCR	(mst/shl)									

192.81	192.95	0.14	Shale	10Y5/4 (tff)				CL			5	0	
192.95 - Marker Block													
192.95	194.83	1.88	Shale	N4-N3 (sst) N2 (mst/shl) 10Y5/4 (tff)	Tuff			CL			5	0	
194.83	194.92	0.09	NCR										
194.92	195.15	0.23	Shale		Tuff			CL			5	0	
195.15 - Marker Block													
195.15	195.19	0.04	Shale	N2 (mst/shl) 10Y5/4 (tff)				CL			0	0	
195.19	195.35	0.16	Chert					CL	Yes	1	0	0	Matjiesfontein' chert horizon
195.35	195.53	0.18	Siltstone					CL	Yes		0	0	Sandy-silty texture
195.53	195.84	0.31	Shale		Tuff		Broken	CL			5	0	
195.84	195.95	0.11	Shale					CL			10	0	Calcite veins 90° to bedding
195.95 - Marker Block													
195.95	196.35	0.40	Shale	N2 (mst/shl) 10Y5/4 (tff)	Tuff			CL			0	0	
196.35	196.39	0.04	Shale				Broken	CL			0	0	
196.39	196.65	0.26	Siltstone		Tuff			CL			5	0	Higher Si content
196.65 - Marker Block													
196.65	197.15	0.50	Shale		Tuff		Broken	CL	Yes		20	0	Calcite veins 90° to bedding
197.15 - Marker Block													
197.15	197.23	0.08	Shale	N4-N3 (sst) N2 (mst/ shl) 10Y5/4 (tff)	Tuff			CL			10	0	
197.23	197.66	0.43	Shale		Tuff			CL			5	0	Calcite vein (9mm) @ 197.47
197.66	198.04	0.38	Siltstone			Faulting - normal fault (horst &		CL		2,3	5	0	

						graben-type features)							
198.04	198.28	0.24	Shale					CL		4,5,6	5	0	Calcite; Higher Si content; Other minerals
198.28	198.40	0.12	Shale		Tuff		Broken	WH			0	0	Carbon-rich
198.40 - Marker Block													
198.40	198.72	0.32	Shale	N1	Tuff		Broken	WH			0	0	Carbon-rich
198.72	198.95	0.23	NCR					WH					
198.95 - Marker Block													
198.95	199.10	0.15	Shale	N1			Broken	WH			0	0	Carbon-rich; Pearly lustre
199.10	199.15	0.05	Shale				Broken	WH			0	0	Carbon-rich
199.15	199.36	0.21	Shale			Slickensides	Broken	WH			0	0	Quartz lenses @ 199.34
199.36	199.65	0.29	Shale				Broken	WH			0	0	Distinct bedding cleavage
199.65 - Marker Block													
199.65	199.83	0.18	Shale	N1 (shl); N6 (slst)		Slickensides	Broken	WH			0	0	Carbon-rich; Pearly lustre; Distinct bedding cleavage
199.83	200.03	0.20	Shale					WH			0	0	Calcite lenses - small
200.03	200.40	0.37	Shale				Broken	WH			0	0	Carbon-rich; Distinct bedding cleavage
200.40 - Marker Block													
200.40	200.66	0.26	Shale	N1			Broken	WH			0	0	
200.66	201.37	0.71	Shale			Slickensides		WH			0	0	Carbon-rich; Pearly lustre
201.37 - Marker Block													
201.37	201.99	0.62	Shale	N1		Slickensides		WH			0	0	Carbon-rich; Pearly lustre
201.99 - Marker Block													
201.99	202.58	0.59	Shale	N1 (shl), N7 (slst)		Slickensides		WH			0	0	
202.58	202.66	0.08	Shale		Cc; Py			WH	Yes		10	10	Carbon-rich; Lenses of mineralization; Calcite veins - randomly orientated
202.66	204.35	1.69	Shale		Cc	Slickensides		WH			15	5	Carbon-rich (higher); Calcite vein @ 203.74

204.35 - Marker Block													
204.35	204.67	0.32	Shale					WH			10	5	Carbon-rich
204.67	204.73	0.06	Shale				Broken	WH			0	0	
204.73	204.92	0.19	NCR				Broken	WH					
204.92	205.32	0.40	Shale			Slickensides		WH			0	0	Calcite veins (few); Pearly lustre
205.32	205.88	0.56	Shale	N1				WH			5	0	Calcite vein (3mm) @ 205.48; Distinct bedding cleavage
205.88	206.37	0.49	Shale		Cc			WH			20	0	Calcite veins - randomly orientated
206.37	206.79	0.42	Shale					WH			20	0	
206.79	207.21	0.42	Shale		Cc			WH			15	0	Calcite vein (8mm) @207.20
207.21	207.85	0.64	Shale					WH			0	0	
207.85 - Marker Block													
207.85	209.21	1.36	Shale					WH			5	0	
209.21	209.43	0.22	Shale		Cc			WH			10	0	Calcite vein (5mm) @ 209.21 &(4mm) ‖ bedding
209.43	210.54	1.11	Shale	N1				WH			10	0	Carbon-rich; Calcite vein (thin) @ 209.72
210.54	210.60	0.06	Shale					WH			0	0	
210.60	210.63	0.03	Shale		Cc			WH			80	0	Calcite veins alternating with shale
210.63	210.95	0.32	Shale					WH			5	0	
210.95 - Marker Block													
210.95	212.33	1.38	Shale					WH			20	0	Calcite veins (thin) @ 211.44 & 211.86
212.33	212.62	0.29	Shale	N1	Cc; Py	Faults - normal fault; Folds - gentle, initiated by fault-related stress		WH			20	20	Pyrite already somewhat oxydised to Fe
212.62	212.79	0.17	Shale					WH			10	0	Calcite vein (2mm) @ 212.78

212.79	212.85	0.06	Shale		Cc; Py			WH			5	10	Calcite & Pyrite lenses ‖ bedding
212.85	213.48	0.63	Shale					WH			5	0	
213.48	213.57	0.09	Shale		Cc; Py			WH		8	5	30	Pyrite lenses surrounded by Calcite
213.57	213.70	0.13	Shale		Cc; Qz	Folds - gentle, monocline		WH		9	5	0	Calcite/Quartz vein (5mm) @ 213.67 - folded
213.70	213.95	0.25	Shale		Cc; Py			WH			10	10	Calcite veins & Pyrite lenses
213.95 - Marker Block													
213.95	214.12	0.17	Shale	N1 (some shale differs between N2 and N3, N4). Slst 5Y 8/1	Cc; Py	Nodules	White weathering	WH	Yes	10,11	30	5	Nodular weathering pattern; Pyrite lense @ 214.10
214.12	214.51	0.39	Shale		Cc; Py			WH			10	30	Calcite veins - swarms; Pyrite lenses (large)
214.51	214.82	0.31	Shale		Cc			WH	Yes		20	0	Calcite veins - randomly orientated
214.82	215.00	0.18	Shale		Cc; Py	Nodule		WH	Yes	12, 13, 14, 15	40	40	Nodule (40mm) @ 214.90 surrounded by Calcite vein & Pyrite lenses (large)
215.00	215.14	0.14	Shale		Cc			WH			30	0	Calcite veins ‖ bedding - evenly distributed
215.14	215.22	0.08	Shale		Cc; Py		Broken; Fe-oxidation	WH			10	5	Calcite (flakes) along cleavage; Pyrite (minor)
215.22	215.29	0.07	Shale		Cc; Py	Faults - normal fault; Folds - gentle, initiated by fault-related stress		WH		16	50	20	Calcite veins; Pyrite lenses; Pearly lustre on cleavage planes
215.29	215.54	0.25	Shale		Cc; Py			WH			20	5	Calcite veins - randomly orientated; Pyrite lenses (small)
215.54	215.73	0.19	Shale		Cc	Nodule		WH			20	0	Nodule (50mm) @ 215.67; Calcite veins (thin) ‖ bedding; Distinct bedding cleavage

215.73	215.78	0.05	Shale		Cc & Fe	Faults - reverse fault, re-activation of normal fault; Folds - gentle, initiated by fault-related stress	Fe-oxidation	WH		17	15	0	Calcite vein - contorted, brown-orange discolouration; Pearly lustre
215.78	215.97	0.19	Shale		Tuff		Broken	WH	Yes		0	0	Distinct cleavage - tuff; Pearly lustre
215.97	216.13	0.16	Shale		Cc			WH		18	10	0	Calcite vein (10mm) 90° to bedding
216.13	216.63	0.50	Shale		Cc			WH			10	0	Calcite veins 90° to bedding - few
216.63	216.95	0.32	Shale		Cc; Py			WH			30	10	Calcite veins - swarms; Pyrite nodules
216.95 - Marker Block													
216.95	218.20	1.25	Shale	N1	Cc; Py	Faults - thrust faults		WH	Yes		20	30	Possible limestone/dolomite layers within thrusts; Calcite veins - swarms; Calcite & Pyrite veins ‖ bedding
218.20	218.22	0.02	Shale		Cc; Py			WH	Yes	19	20	80	
218.22	218.72	0.50	Shale		Cc; Py	Folds - similar, gentle		WH			20	20	Calcite veins - randomly orientated & ‖ bedding; Pyrite ‖ bedding
218.72	219.08	0.36	Shale		Cc; Py	Folds - inclined, open		WH	Yes	20, 21, 22	30	30	Pyrite lenses (thick) surrounded by Calcite veins (thick)
219.08	219.14	0.06	Limestone/ Dolomite		Cc			WH	Yes	23	50	0	Lighter colour; coarser texture; Strong reaction in dil. HCl; Calcite vein - 'younger' (intersects)
219.14	219.71	0.57	Shale		Cc; Py		Fe-oxidation	WH			10	10	Calcite veins ‖ bedding; Pyrite lenses

219.71	219.95	0.24	Shale		Fe; Si	Nodules	Fe-oxidation	WH	Yes		0	0	Distinct bedding cleavage; Unknown mineralization
219.95 - Marker Block													
219.95	220.43	0.48	Shale	N6 shl, N7 slst			Fe-oxidation	WH			5	0	Calcite - minor
220.43	220.56	0.13	Shale					WH			0	0	
220.56	220.61	0.05	Shale					WH			5	0	Calcite veins - minor, in small fractures 90° to bedding
220.61	220.99	0.38	Shale					WH			5	5	Pyrite cubes - minor
220.99	221.15	0.16	Shale					WH			5	0	Calcite veins ‖ bedding - minor
221.15	221.17	0.02	Shale		Py			WH	Yes	24	5	5	Pyrite oxidation; Calcite veins - minor
221.17	221.35	0.18	Shale		Cc; Py			WH			5	5	Calcite veins - small, surrounded by Pyrite
221.35	221.44	0.09	Shale		Cc		Fe-oxidation	WH			10	0	Calcite veins ‖ bedding; Pyrite - small particles, evenly distributed
221.44	221.56	0.12	Shale		Cc		Fe-oxidation	WH			5	0	Calcite veins ‖ bedding; Pyrite - small particles, evenly distributed
221.56	222.14	0.58	Shale					WH			5	5	Calcite veins - minor, ‖ bedding; Pyrite - small particles, evenly distributed
222.14	222.41	0.27	Shale					WH			10	5	Calcite veins - minor, ‖ bedding; Pyrite - small particles, evenly distributed
222.41	222.59	0.18	Shale		Cc; Py			WH			25	30	Calcite veins; Pyrite lenses
222.59	222.95	0.36	Shale		Cc; Py			WH		25, 26	20	15	Calcite veins - swarms; Pyrite lenses (large)
222.95 - Marker Block													
222.95	223.10	0.15	Shale	N6 shl, 5Y 8/1 slst	Cc; Py			WH	Yes		30	30	Calcite veins - swarms, (20mm) vein @ 223.06
223.10	223.96	0.86	Shale		Cc	Faults - normal fault, 90° dip	Fe-oxidation	WH	Yes	27	20	10	Calcite veins - white & brown

223.96	224.11	0.15	Shale		Cc; Fe	Concretion	Fe-oxidation	WH		28	20	0	Concretion - different coloured layering; Calcite veins - thick layers; Iron oxidation weathering causing swelling of strata
224.11	224.23	0.12	Shale		Qz; Fe		Fe-oxidation	PA			5	0	Calcite - brown; Quartz vein (20mm) @ 224.20
224.23	224.72	0.49	Shale		Cc; Fe	Nodules	Fe-oxidation	PA			10	0	Calcite - brown
224.72	225.95	1.23	Shale				Yellow oxidation	PA			0	0	Calcite vein (4mm) @ 225.37
225.95 - Marker Block													
225.95	226.39	0.44	Shale			Nodules	Fe-oxidation; Yellow oxidation (minor)	PA	Yes	29	5	0	Calcite veins - thin, minor; Nodule (18mm) @ 226.20
226.39	226.42	0.03	Shale		Cc			PA			70	0	Calcite vein - thick
226.42	226.87	0.45	Shale	N1 shl, 5Y 8/1 slst	Cc; Fe		Fe-oxidation; Yellow Oxidation	PA		30	10	0	Pyrite oxidation; Folds - small, tight, 90° to bedding; Calcite veins - few, thicker
226.87	226.93	0.06	Shale		Cc			PA		31	15	0	Powdery material - white precipitate; Calcite veins (abundant)
226.93	227.77	0.84	Shale		Cc; Qz	Faults - thrust faults		PA		32	15	0	Calcite & Quartz veins - randomly orientated
227.77	228.37	0.60	Shale		Cc; Qz			PA			10	0	Calcite & Quartz veins - randomly orientated
228.37 - Marker Block													
228.37	228.51	0.14	Shale		Cc; Qz			PA			5	0	Calcite & Quartz veins (thin) - very few

228.51	228.85	0.34	Shale	N1 shl, 5y 8/1 slst	Cc	Faults - thrust faults		PA	Yes	33	15	0	
228.85 - Marker Block													
228.85	229.24	0.39	Shale	N1 shl, 5y 8/1 slst	Cc; Qz			PA			10	0	Calcite & Quartz veins (thin)- randomly orientated
229.24	229.60	0.36	Shale		Cc			PA			5	0	Calcite veins (possibly associated with Quartz veins)
229.60	229.97	0.37	Shale					PA		34, 35	0	0	Distinct bedding cleavage; Mangenese dendrites
229.97	230.08	0.11	Shale		Cc; Qz			PA			5	0	Calcite & Quartz veins (thin)- lenses
230.08	230.80	0.72	Shale		Cc; Qz			PA			5	0	Calcite & Quartz veins (thin)- lenses
230.80 - Marker Block													

APPENDIX B: BOREHOLE SFT2 CORE BOXES

Dry Core

Wet Core

APPENDIX C: STRUCTURAL DATA

Bedding Orientation Readings

BEDDING READINGS						
Reading number	**Azimuth**	**Azimuth (corrected)**	**Dip**	**Scale of Fold (macro- or meso-)**	**Position within macro-fold**	**Fold type**
Bluegumvale 256/RE						
1	59	33	62	meso-scale	fold hinge	syncline
2	216	190	53	meso-scale	fold hinge	syncline
3	202	176	49	meso-scale	fold hinge	syncline
4	39	13	60	meso-scale	fold hinge	syncline
5	318	292	35	meso-scale	fold hinge	syncline
6	316	290	36	meso-scale	fold hinge	syncline
7	203	177	50	meso-scale	fold hinge	syncline
8	201	175	50	meso-scale	fold hinge	syncline
9	32	6	40	meso-scale	fold hinge	syncline
10	36	10	40	meso-scale	fold hinge	syncline
11	209	183	46	meso-scale	fold hinge	syncline
12	31	5	45	meso-scale	fold hinge	syncline
13	202	176	22	meso-scale	fold hinge	syncline
14	212	186	26	meso-scale	fold hinge	syncline
15	223	197	31	meso-scale	fold hinge	syncline
16	213	187	26	meso-scale	fold hinge	syncline
17	207	181	45	meso-scale	fold hinge	syncline
18	221	195	20	meso-scale	fold hinge	syncline
19	220	194	17	meso-scale	fold hinge	syncline
20	220	194	26	meso-scale	fold hinge	syncline
21	217	191	27	meso-scale	fold hinge	syncline
22	218	192	33	meso-scale	fold hinge	syncline
23	217	191	40	meso-scale	fold hinge	syncline
24	215	189	26	meso-scale	fold hinge	syncline
25	215	189	60	meso-scale	fold hinge	syncline
26	192	166	48	meso-scale	fold hinge	syncline
27	215	189	52	meso-scale	fold hinge	syncline
28	215	189	52	meso-scale	fold hinge	syncline
29	201	175	40	meso-scale	fold hinge	syncline
30	205	179	48	meso-scale	fold hinge	syncline
31	196	170	42	meso-scale	fold hinge	syncline
32	219	193	50	meso-scale	fold hinge	syncline
33	184	158	52	meso-scale	fold hinge	syncline
34	213	187	61	meso-scale	fold hinge	syncline
35	219	193	67	meso-scale	fold hinge	syncline
36	217	191	70	meso-scale	fold hinge	syncline

37	219	193	72	meso-scale	fold hinge	syncline
38	215	189	63	meso-scale	fold hinge	syncline
Reading number	**Azimuth**	**Azimuth (corrected)**	**Dip**	**Scale of Fold (macro- or meso-)**	**Position within macro-fold**	**Fold type**
39	211	185	61	meso-scale	fold hinge	syncline
40	228	202	58	meso-scale	fold hinge	syncline
41	224	198	66	meso-scale	fold hinge	syncline
42	198	172	49	meso-scale	fold hinge	syncline
43	221	195	54	meso-scale	fold hinge	syncline
44	194	168	39	meso-scale	fold hinge	syncline
45	35	9	52	meso-scale	fold hinge	syncline
46	44	18	36	meso-scale	fold hinge	syncline
47	35	9	48	meso-scale	fold hinge	syncline
48	31	5	52	meso-scale	fold hinge	syncline
49	53	27	48	meso-scale	fold hinge	syncline
50	57	31	42	meso-scale	fold hinge	syncline
51	41	15	45	meso-scale	fold hinge	syncline
52	27	1	48	meso-scale	fold hinge	syncline
53	40	14	60	meso-scale	fold hinge	syncline
54	29	3	74	meso-scale	fold hinge	syncline
55	23	-3	51	meso-scale	fold hinge	syncline
56	18	-8	41	meso-scale	fold hinge	syncline
57	25	-1	52	meso-scale	fold hinge	syncline
58	41	15	63	meso-scale	fold hinge	syncline
59	13	-13	46	meso-scale	fold hinge	syncline
60	50	24	46	meso-scale	fold hinge	syncline
61	16	-10	55	meso-scale	fold hinge	syncline
62	39	13	57	meso-scale	fold hinge	syncline
63	37	11	53	meso-scale	fold hinge	syncline
64	28	2	56	meso-scale	fold hinge	syncline
65	232	206	5	macro-scale	northern limb	syncline
66	195	169	5	macro-scale	northern limb	syncline
67	224	198	7	macro-scale	northern limb	syncline
68	227	201	6	macro-scale	northern limb	syncline
69	204	178	9	macro-scale	northern limb	syncline
70	220	194	11	macro-scale	northern limb	syncline
71	237	211	12	macro-scale	northern limb	syncline
72	225	199	11	macro-scale	northern limb	syncline
73	209	183	14	macro-scale	northern limb	syncline
74	228	202	12	macro-scale	northern limb	syncline
75	230	204	5	macro-scale	northern limb	syncline
76	240	214	7	macro-scale	northern limb	syncline
77	235	209	6	macro-scale	northern limb	syncline
78	218	192	8	macro-scale	northern limb	syncline
79	241	215	7	macro-scale	northern limb	syncline

80	238	212	9	macro-scale	northern limb	syncline
81	221	195	9	macro-scale	northern limb	syncline
Reading number	**Azimuth**	**Azimuth (corrected)**	**Dip**	**Scale of Fold (macro- or meso-)**	**Position within macro-fold**	**Fold type**
82	212	186	9	macro-scale	northern limb	syncline
83	219	193	4	macro-scale	northern limb	syncline
84	222	196	6	macro-scale	northern limb	syncline
85	220	194	7	macro-scale	northern limb	syncline
86	217	191	5	macro-scale	northern limb	syncline
87	222	196	8	macro-scale	northern limb	syncline
88	220	194	5	macro-scale	northern limb	syncline
89	209	183	6	macro-scale	northern limb	syncline
90	243	217	9	macro-scale	northern limb	syncline
91	226	200	9	macro-scale	northern limb	syncline
92	210	184	6	macro-scale	northern limb	syncline
93	210	184	10	macro-scale	northern limb	syncline
94	190	164	4	macro-scale	northern limb	syncline
95	234	208	6	macro-scale	northern limb	syncline
96	205	179	9	macro-scale	northern limb	syncline
97	231	205	4	macro-scale	northern limb	syncline
98	202	176	5	macro-scale	northern limb	syncline
99	212	186	4	macro-scale	northern limb	syncline
100	209	183	5	macro-scale	northern limb	syncline
101	200	174	4	macro-scale	northern limb	syncline
102	212	186	6	macro-scale	northern limb	syncline
103	197	171	5	macro-scale	northern limb	syncline
104	203	177	3	macro-scale	northern limb	syncline
105	209	183	6	macro-scale	northern limb	syncline
106	213	187	11	macro-scale	northern limb	syncline
107	228	202	6	macro-scale	northern limb	syncline
108	197	171	3	macro-scale	northern limb	syncline
109	209	183	6	macro-scale	northern limb	syncline
110	211	185	4	macro-scale	northern limb	syncline
111	212	186	4	macro-scale	northern limb	syncline
112	213	187	5	macro-scale	northern limb	syncline
113	217	191	6	macro-scale	northern limb	syncline
114	202	176	7	macro-scale	northern limb	syncline
Erasmus Laaghte 13/RE						
Reading number	**Azimuth**	**Azimuth (corrected)**	**Dip**	**Scale of Fold (macro- or meso-)**	**Position within macro-fold**	**Fold type**
115	67	41	61	macro-scale	southern limb	syncline
116	35	9	39	macro-scale	southern limb	syncline
117	348	322	70	macro-scale	southern limb	syncline
118	41	15	65	macro-scale	southern limb	syncline
119	46	20	48	macro-scale	southern limb	syncline

120	55	29	54	macro-scale	southern limb	syncline
Reading number	**Azimuth**	**Azimuth (corrected)**	**Dip**	**Scale of Fold (macro- or meso-)**	**Position within macro-fold**	**Fold type**
121	48	22	59	macro-scale	southern limb	syncline
122	227	201	39	macro-scale	northern limb	syncline
123	217	191	35	macro-scale	northern limb	syncline
124	226	200	39	macro-scale	northern limb	syncline
125	224	198	35	macro-scale	northern limb	syncline
126	222	196	39	macro-scale	northern limb	syncline
127	220	194	36	macro-scale	northern limb	syncline
128	228	202	51	macro-scale	northern limb	syncline
129	226	200	35	macro-scale	northern limb	syncline
130	222	196	40	macro-scale	northern limb	syncline
131	226	200	35	macro-scale	northern limb	syncline
132	244	218	35	macro-scale	northern limb	syncline
133	220	194	36	macro-scale	northern limb	syncline
134	221	195	35	macro-scale	northern limb	syncline
135	226	200	31	macro-scale	northern limb	syncline
136	229	203	35	macro-scale	northern limb	syncline
137	227	201	35	macro-scale	northern limb	syncline
138	212	186	57	macro-scale	northern limb	syncline
139	227	201	42	macro-scale	northern limb	syncline
140	234	208	46	macro-scale	northern limb	syncline
141	248	222	44	macro-scale	northern limb	syncline
142	215	189	44	macro-scale	northern limb	syncline
143	215	189	39	macro-scale	northern limb	syncline
144	217	191	19	macro-scale	northern limb	syncline
145	220	194	48	macro-scale	northern limb	syncline
146	235	209	58	macro-scale	northern limb	syncline
147	236	210	63	macro-scale	northern limb	syncline
148	236	210	59	macro-scale	northern limb	syncline
149	227	201	65	macro-scale	northern limb	syncline
150	224	198	65	macro-scale	northern limb	syncline
151	225	199	45	macro-scale	northern limb	syncline
152	223	197	55	macro-scale	northern limb	syncline
153	219	193	65	macro-scale	northern limb	syncline
154	216	190	60	macro-scale	northern limb	syncline
155	220	194	58	macro-scale	northern limb	syncline
156	219	193	50	macro-scale	northern limb	syncline
157	230	204	60	macro-scale	northern limb	syncline
158	219	193	63	macro-scale	northern limb	syncline
159	217	191	58	macro-scale	northern limb	syncline
160	223	197	44	macro-scale	northern limb	syncline
161	225	199	46	macro-scale	northern limb	syncline
162	217	191	53	macro-scale	northern limb	syncline

163	229	203	59	macro-scale	northern limb	syncline
Reading number	**Azimuth**	**Azimuth (corrected)**	**Dip**	**Scale of Fold (macro- or meso-)**	**Position within macro-fold**	**Fold type**
164	220	194	52	macro-scale	northern limb	syncline
165	235	209	45	macro-scale	northern limb	syncline
166	219	193	60	macro-scale	northern limb	syncline
167	217	191	44	macro-scale	northern limb	syncline
168	223	197	42	macro-scale	northern limb	syncline
169	228	202	55	macro-scale	northern limb	syncline
170	228	202	60	macro-scale	northern limb	syncline
171	220	194	55	macro-scale	northern limb	syncline
172	27	1	55	macro-scale	southern limb	syncline
173	59	33	32	macro-scale	southern limb	syncline
174	40	14	36	macro-scale	southern limb	syncline
175	54	28	31	macro-scale	southern limb	syncline
176	45	19	32	macro-scale	southern limb	syncline
177	42	16	45	macro-scale	southern limb	syncline
178	45	19	60	macro-scale	southern limb	syncline
179	54	28	56	macro-scale	southern limb	syncline
180	48	22	63	macro-scale	southern limb	syncline
181	46	20	61	macro-scale	southern limb	syncline
182	49	23	63	macro-scale	southern limb	syncline
183	48	22	34	macro-scale	southern limb	syncline
184	40	14	52	macro-scale	southern limb	syncline
185	46	20	43	macro-scale	southern limb	syncline
186	40	14	43	macro-scale	southern limb	syncline
187	63	37	63	macro-scale	southern limb	syncline
188	52	26	53	macro-scale	southern limb	syncline
189	48	22	72	macro-scale	southern limb	syncline
190	38	12	60	macro-scale	southern limb	syncline
191	46	20	49	macro-scale	southern limb	syncline
192	43	17	55	macro-scale	southern limb	syncline
193	34	8	53	macro-scale	southern limb	syncline
194	53	27	51	macro-scale	southern limb	syncline
195	44	18	54	macro-scale	southern limb	syncline
196	48	22	60	macro-scale	southern limb	syncline
197	30	4	53	macro-scale	southern limb	syncline
198	222	196	55	meso-scale	fold hinge	syncline
199	230	204	75	meso-scale	fold hinge	syncline
200	226	200	75	meso-scale	fold hinge	syncline
201	239	213	53	meso-scale	fold hinge	syncline
202	245	219	62	meso-scale	fold hinge	syncline
203	216	190	62	meso-scale	fold hinge	syncline
204	208	182	64	meso-scale	fold hinge	syncline
205	222	196	52	meso-scale	fold hinge	syncline

206	226	200	78	meso-scale	fold hinge	syncline
Reading number	**Azimuth**	**Azimuth (corrected)**	**Dip**	**Scale of Fold (macro- or meso-)**	**Position within macro-fold**	**Fold type**
207	220	194	62	meso-scale	fold hinge	syncline
208	22	-4	62	meso-scale	fold hinge	syncline
209	38	12	50	meso-scale	fold hinge	syncline
210	40	14	48	meso-scale	fold hinge	syncline
211	32	6	62	meso-scale	fold hinge	syncline
212	68	42	49	meso-scale	fold hinge	syncline
213	35	9	54	meso-scale	fold hinge	syncline
214	29	3	81	meso-scale	fold hinge	syncline
215	58	32	80	meso-scale	fold hinge	syncline
216	56	30	78	meso-scale	fold hinge	syncline
Erasmus Laaghte 15/RE						
Reading number	**Azimuth**	**Azimuth (corrected)**	**Dip**	**Scale of Fold (macro- or meso-)**	**Position within macro-fold**	**Fold type**
217	41	15	38	macro-scale	southern limb	syncline
218	34	8	54	macro-scale	southern limb	syncline
219	36	10	64	macro-scale	southern limb	syncline
220	41	15	61	macro-scale	southern limb	syncline
221	35	9	60	macro-scale	southern limb	syncline
222	36	10	59	macro-scale	southern limb	syncline
223	36	10	56	macro-scale	southern limb	syncline
224	29	3	66	macro-scale	southern limb	syncline
225	36	10	45	macro-scale	southern limb	syncline
226	50	24	55	macro-scale	southern limb	syncline
227	48	22	58	macro-scale	southern limb	syncline
228	45	19	62	macro-scale	southern limb	syncline
229	47	21	60	macro-scale	southern limb	syncline
230	41	15	45	macro-scale	southern limb	syncline
231	44	18	71	macro-scale	southern limb	syncline
232	45	19	58	macro-scale	southern limb	syncline
233	41	15	65	macro-scale	southern limb	syncline
234	52	26	58	macro-scale	southern limb	syncline
Erasmus Laaghte 13/2 & Minnawill 12/1						
Reading number	**Azimuth**	**Azimuth (corrected)**	**Dip**	**Scale of Fold (macro- or meso-)**	**Position within macro-fold**	**Fold type**
235	29	3	27	macro-scale	southern limb	syncline
236	18	-8	22	macro-scale	southern limb	syncline
237	33	7	29	macro-scale	southern limb	syncline
238	45	19	15	macro-scale	southern limb	syncline
239	52	26	23	macro-scale	southern limb	syncline
240	34	8	20	macro-scale	southern limb	syncline
241	43	17	23	macro-scale	southern limb	syncline

Reading number	Azimuth	Azimuth (corrected)	Dip	Scale of Fold (macro- or meso-)	Position within macro-fold	Fold type
242	32	6	13	macro-scale	southern limb	syncline
243	35	9	13	macro-scale	southern limb	syncline
244	55	29	19	macro-scale	southern limb	syncline
245	36	10	12	macro-scale	southern limb	syncline
246	24	-2	11	macro-scale	southern limb	syncline
247	5	-21	9	macro-scale	southern limb	syncline
248	27	1	15	macro-scale	southern limb	syncline
249	31	5	17	macro-scale	southern limb	syncline
250	33	7	15	macro-scale	southern limb	syncline
251	11	-15	12	macro-scale	southern limb	syncline
252	18	-8	15	macro-scale	southern limb	syncline
253	10	-16	11	macro-scale	southern limb	syncline
254	28	2	13	macro-scale	southern limb	syncline
255	27	1	19	macro-scale	southern limb	syncline
256	6	-20	6	macro-scale	southern limb	syncline
257	26	0	17	macro-scale	southern limb	syncline
258	33	7	22	macro-scale	southern limb	syncline
259	12	-14	14	macro-scale	southern limb	syncline
260	31	5	20	macro-scale	southern limb	syncline
261	25	-1	22	macro-scale	southern limb	syncline
262	35	9	41	macro-scale	southern limb	syncline
263	36	10	28	macro-scale	southern limb	syncline
264	44	18	24	macro-scale	southern limb	syncline
265	20	-6	20	macro-scale	southern limb	syncline
266	46	20	26	macro-scale	southern limb	syncline
267	42	16	27	macro-scale	southern limb	syncline
268	38	12	15	macro-scale	southern limb	syncline
269	47	21	16	macro-scale	southern limb	syncline
270	38	12	24	macro-scale	southern limb	syncline
271	49	23	16	macro-scale	southern limb	syncline
272	49	23	14	macro-scale	southern limb	syncline
273	43	17	24	macro-scale	southern limb	syncline
274	43	17	19	macro-scale	southern limb	syncline
275	33	7	20	macro-scale	southern limb	syncline
276	40	14	19	macro-scale	southern limb	syncline
277	36	10	23	macro-scale	southern limb	syncline
278	12	-14	54	macro-scale	southern limb	syncline
279	32	6	18	macro-scale	southern limb	syncline
280	25	-1	20	macro-scale	southern limb	syncline
281	29	3	35	macro-scale	southern limb	syncline
282	45	19	26	macro-scale	southern limb	syncline
283	29	3	29	macro-scale	southern limb	syncline
284	29	3	25	macro-scale	southern limb	syncline

Junction View 213/2						
Reading number	**Azimuth**	**Azimuth (corrected)**	**Dip**	**Scale of Fold (macro- or meso-)**	**Position within macro-fold**	**Fold type**
285	216	190	16	macro-scale	southern limb	anticline
286	223	197	12	macro-scale	southern limb	anticline
287	220	194	11	macro-scale	southern limb	anticline
288	219	193	11	macro-scale	southern limb	anticline
289	217	191	12	macro-scale	southern limb	anticline
290	235	209	16	macro-scale	southern limb	anticline
291	234	208	17	macro-scale	southern limb	anticline
292	236	210	14	macro-scale	southern limb	anticline
293	237	211	16	macro-scale	southern limb	anticline
294	229	203	20	macro-scale	southern limb	anticline
295	227	201	17	macro-scale	southern limb	anticline
296	227	201	16	macro-scale	southern limb	anticline
297	225	199	15	macro-scale	southern limb	anticline
298	222	196	16	macro-scale	southern limb	anticline
299	230	204	16	macro-scale	southern limb	anticline
300	230	204	10	macro-scale	southern limb	anticline
301	220	194	20	macro-scale	southern limb	anticline
302	220	194	13	macro-scale	southern limb	anticline
303	221	195	18	macro-scale	southern limb	anticline
304	216	190	19	macro-scale	southern limb	anticline
305	212	186	21	macro-scale	southern limb	anticline
306	219	193	17	macro-scale	southern limb	anticline
307	222	196	19	macro-scale	southern limb	anticline
308	240	214	18	macro-scale	southern limb	anticline
309	219	193	20	macro-scale	southern limb	anticline
310	217	191	20	macro-scale	southern limb	anticline
311	220	194	18	macro-scale	southern limb	anticline
312	224	198	17	macro-scale	southern limb	anticline
313	220	194	16	macro-scale	southern limb	anticline
314	222	196	20	macro-scale	southern limb	anticline
315	222	196	19	macro-scale	southern limb	anticline
316	227	201	18	macro-scale	southern limb	anticline
317	225	199	20	macro-scale	southern limb	anticline
318	217	191	17	macro-scale	southern limb	anticline
319	214	188	19	macro-scale	southern limb	anticline
Damplaats 198/RE						
Reading number	**Azimuth**	**Azimuth (corrected)**	**Dip**	**Scale of Fold (macro- or meso-)**	**Position within macro-fold**	**Fold type**
320	20	354	21	meso-scale	fold hinge	anticline
321	13	347	23	meso-scale	fold hinge	anticline

Reading number	Azimuth	Azimuth (corrected)	Dip	Scale of Fold (macro- or meso-)	Position within macro-fold	Fold type
322	22	356	24	meso-scale	fold hinge	anticline
323	11	345	17	meso-scale	fold hinge	anticline
324	352	326	16	meso-scale	fold hinge	anticline
325	21	355	19	meso-scale	fold hinge	anticline
326	13	347	22	meso-scale	fold hinge	anticline
327	10	344	18	meso-scale	fold hinge	anticline
328	21	355	16	meso-scale	fold hinge	anticline
329	19	353	17	meso-scale	fold hinge	anticline
330	19	353	25	meso-scale	fold hinge	anticline
331	12	346	26	meso-scale	fold hinge	anticline
332	10	344	25	meso-scale	fold hinge	anticline
333	15	349	21	meso-scale	fold hinge	anticline
334	22	356	21	meso-scale	fold hinge	anticline
335	218	192	16	meso-scale	fold hinge	anticline
336	202	176	18	meso-scale	fold hinge	anticline
337	222	196	25	meso-scale	fold hinge	anticline
338	224	198	27	meso-scale	fold hinge	anticline
339	217	191	21	meso-scale	fold hinge	anticline
340	223	197	25	meso-scale	fold hinge	anticline
341	218	192	10	meso-scale	fold hinge	anticline
342	173	147	9	meso-scale	fold hinge	anticline
343	220	194	10	meso-scale	fold hinge	anticline
344	214	188	12	meso-scale	fold hinge	anticline
345	52	26	11	macro-scale	northern limb	anticline
346	48	22	12	macro-scale	northern limb	anticline
347	8	-18	15	macro-scale	northern limb	anticline
348	0	-26	14	macro-scale	northern limb	anticline
349	38	12	23	macro-scale	northern limb	anticline
350	15	-11	29	macro-scale	northern limb	anticline
351	56	30	17	macro-scale	northern limb	anticline
352	53	27	16	macro-scale	northern limb	anticline
353	36	10	12	macro-scale	northern limb	anticline
354	57	31	20	macro-scale	northern limb	anticline
Humefield 207/2						
Reading number	**Azimuth**	**Azimuth (corrected)**	**Dip**	**Scale of Fold (macro- or meso-)**	**Position within macro-fold**	**Fold type**
355	265	239	24	meso-scale	fold hinge	anticline
356	266	240	25	meso-scale	fold hinge	anticline
357	265	239	24	meso-scale	fold hinge	anticline
358	260	234	25	meso-scale	fold hinge	anticline
359	255	229	23	meso-scale	fold hinge	anticline
360	108	82	12	meso-scale	fold hinge	anticline

Reading number	Azimuth	Azimuth (corrected)	Dip	Scale of Fold (macro- or meso-)	Position within macro-fold	Fold type
361	116	90	11	meso-scale	fold hinge	anticline
362	109	83	22	meso-scale	fold hinge	anticline
363	115	89	10	meso-scale	fold hinge	anticline
364	108	82	9	meso-scale	fold hinge	anticline
East of Gouskraal 257/1&4						
Reading number	**Azimuth**	**Azimuth (corrected)**	**Dip**	**Scale of Fold (macro- or meso-)**	**Position within macro-fold**	**Fold type**
365	245	219	30	meso-scale	fold hinge	syncline
366	76	50	35	meso-scale	fold hinge	syncline
367	256	230	32	meso-scale	fold hinge	syncline
368	47	21	70	meso-scale	fold hinge	syncline
369	215	189	80	meso-scale	fold hinge	syncline
370	59	33	45	meso-scale	fold hinge	syncline
371	76	50	50	meso-scale	fold hinge	syncline
372	240	214	70	meso-scale	fold hinge	syncline
373	35	9	82	meso-scale	fold hinge	syncline
374	212	186	65	meso-scale	fold hinge	syncline
375	218	192	85	meso-scale	fold hinge	syncline
376	220	194	65	meso-scale	fold hinge	syncline
377	224	198	35	meso-scale	fold hinge	syncline
378	230	204	70	meso-scale	fold hinge	syncline
379	228	202	70	meso-scale	fold hinge	syncline
380	215	189	15	meso-scale	fold hinge	syncline
381	32	6	10	meso-scale	fold hinge	syncline
382	58	32	83	meso-scale	fold hinge	syncline
383	45	19	60	meso-scale	fold hinge	syncline
384	46	20	81	meso-scale	fold hinge	syncline
385	52	26	36	meso-scale	fold hinge	syncline
386	72	46	81	meso-scale	fold hinge	syncline
387	49	23	54	meso-scale	fold hinge	syncline
388	60	34	60	meso-scale	fold hinge	syncline
389	51	25	53	meso-scale	fold hinge	syncline
390	40	14	66	meso-scale	fold hinge	syncline
391	22	-4	70	meso-scale	fold hinge	syncline
392	27	1	86	meso-scale	fold hinge	syncline
393	26	0	46	meso-scale	fold hinge	syncline
394	25	-1	65	meso-scale	fold hinge	syncline
395	29	3	55	meso-scale	fold hinge	syncline
396	26	0	60	meso-scale	fold hinge	syncline
397	15	-11	65	meso-scale	fold hinge	syncline
398	39	13	62	meso-scale	fold hinge	syncline
399	226	200	81	meso-scale	fold hinge	syncline

Reading number	Azimuth	Azimuth (corrected)	Dip	Scale of Fold (macro- or meso-)	Position within macro-fold	Fold type
400	237	211	60	meso-scale	fold hinge	syncline
401	229	203	77	meso-scale	fold hinge	syncline
402	205	179	56	meso-scale	fold hinge	syncline
403	220	194	48	meso-scale	fold hinge	syncline
404	207	181	66	meso-scale	fold hinge	syncline
405	199	173	54	meso-scale	fold hinge	syncline
406	210	184	83	meso-scale	fold hinge	syncline
407	200	174	62	meso-scale	fold hinge	syncline
408	219	193	60	meso-scale	fold hinge	syncline
409	231	205	66	meso-scale	fold hinge	syncline
410	215	189	61	meso-scale	fold hinge	syncline
411	202	176	66	meso-scale	fold hinge	syncline
412	220	194	68	meso-scale	fold hinge	syncline
413	204	178	36	meso-scale	fold hinge	syncline
414	199	173	70	meso-scale	fold hinge	syncline
415	195	169	42	meso-scale	fold hinge	syncline
416	192	166	16	macro-scale	northern limb	syncline
417	225	199	39	macro-scale	northern limb	syncline
418	227	201	38	macro-scale	northern limb	syncline
419	230	204	39	macro-scale	northern limb	syncline
420	236	210	40	macro-scale	northern limb	syncline
421	222	196	52	macro-scale	northern limb	syncline
422	225	199	28	macro-scale	northern limb	syncline
423	225	199	30	macro-scale	northern limb	syncline
424	234	208	31	macro-scale	northern limb	syncline
425	210	184	37	macro-scale	northern limb	syncline
426	237	211	31	macro-scale	northern limb	syncline
427	253	227	13	macro-scale	northern limb	syncline
428	220	194	11	macro-scale	northern limb	syncline
429	197	171	46	macro-scale	northern limb	syncline
430	219	193	22	macro-scale	northern limb	syncline

Joint orientation readings

JOINT READINGS							
Reading number	**Azimuth**	**Azimuth (corrected)**	**Dip**	**Scale of Fold (macro- or meso-)**	**Position within macro-fold**	**Fold Type**	**Joint plane**
Damplaats 198/RE							
1	121	95	89	macro-scale	northern limb	anticline	J1
2	107	81	90	macro-scale	northern limb	anticline	J1
3	211	185	65	macro-scale	northern limb	anticline	J2
4	219	193	58	macro-scale	northern limb	anticline	J2

Reading number	Azimuth	Azimuth (corrected)	Dip	Scale of Fold (macro- or meso-)	Position within macro-fold	Fold Type	Joint plane
5	222	196	57	macro-scale	northern limb	anticline	J2
6	99	73	88	macro-scale	northern limb	anticline	J1
7	216	190	66	macro-scale	northern limb	anticline	J2
8	286	260	81	macro-scale	northern limb	anticline	J1
9	217	191	66	macro-scale	northern limb	anticline	J2
10	104	78	84	macro-scale	northern limb	anticline	J1
Bluegumvale 256/3							
Reading number	**Azimuth**	**Azimuth (corrected)**	**Dip**	**Scale of Fold (macro- or meso-)**	**Position within macro-fold**	**Fold Type**	**Joint plane**
1	13	-13	88	macro-scale	northern limb	syncline	J1
2	278	252	82	macro-scale	northern limb	syncline	J2
3	12	-14	85	macro-scale	northern limb	syncline	J1
4	10	-16	85	macro-scale	northern limb	syncline	J1
5	20	-6	87	macro-scale	northern limb	syncline	J1
6	291	265	87	macro-scale	northern limb	syncline	J2
7	9	-17	86	macro-scale	northern limb	syncline	J1
8	288	262	90	macro-scale	northern limb	syncline	J2
9	12	-14	88	macro-scale	northern limb	syncline	J1
10	281	255	84	macro-scale	northern limb	syncline	J2
11	280	254	83	macro-scale	northern limb	syncline	J2
12	265	239	85	macro-scale	northern limb	syncline	J2
13	5	-21	85	macro-scale	northern limb	syncline	J1
14	0	-26	86	macro-scale	northern limb	syncline	J1
15	296	270	81	macro-scale	northern limb	syncline	J2
16	13	-13	89	macro-scale	northern limb	syncline	J1
17	304	278	78	macro-scale	northern limb	syncline	J2
18	287	261	84	macro-scale	northern limb	syncline	J2
19	283	257	80	macro-scale	northern limb	syncline	J2
20	18	-8	90	macro-scale	northern limb	syncline	J1
21	0	-26	86	macro-scale	northern limb	syncline	J1
22	6	-20	84	macro-scale	northern limb	syncline	J1
23	298	272	81	macro-scale	northern limb	syncline	J2
24	26	0	85	macro-scale	northern limb	syncline	J1
25	308	282	78	macro-scale	northern limb	syncline	J2
26	295	269	80	macro-scale	northern limb	syncline	J2
27	15	-11	82	macro-scale	northern limb	syncline	J1
28	300	274	85	macro-scale	northern limb	syncline	J2
29	12	-14	86	macro-scale	northern limb	syncline	J1
30	109	83	82	macro-scale	northern limb	syncline	J2

APPENDIX D: SEM (EDS) CHEMICAL DATA

Chemical Composition of Minerals Identified in Section 5.5

Chemical Composition (% per element, Oxygen removed)																								
Sample Point	***1***	***2***	***3***	***4***	***5***	***6***	***7***	***8***	***9***	***10***	***11***	***12***	***13***	***14***	***15***	***16***	***17***	***18***	***19***	***20***	***21***	***22***	***23***	***24***
F	-	-	-	-	-	-	-	-	-	5.34	-	-	-	-	-	-	-	-	-	-	-	-	-	-
Na	-	2.1	-	-	0.57	-	-	-	-	-	-	-	-	-	-	-	-	-	-	-	-	-	-	-
Mg	-	-	-	-	-	-	0.53	34.15	-	-	0.9	-	-	2.46	-	8.46	1.98	0.95	-	-	-	-	-	-
Al	1.05	4.56	-	-	1.96	-	-	-	-	-	-	-	-	27.17	-	22.93	27.82	0.48	0.37	-	-	-	-	-
Si	37.03	93.1	0.35	0.51	97.19	-	-	-	-	-	-	100	-	56.09	-	28.85	61.3	0.66	0.36	0.39	100	-	-	0.39
P	-	-	-	-	-	-	-	-	-	39.65	-	-	-	-	-	-	-	-	-	-	-	-	-	-
S	-	-	66.7	66.97	-	31	-	3.58	-	-	-	-	67.95	0.47	-	-	0.45	-	67.23	41.05	-	-	46.54	41.96
Cl	-	-	-	-	-	-	-	-	-	-	-	-	-	-	-	-	0	-	-	-	-	-	-	-
K	-	0.29	-	-	0.29	-	-	-	-	-	-	-	-	6.53	-	-	6.68	-	-	-	-	-	-	-
Ca	0.98	-	-	-	-	2.22	97	55.4	71	53.6	96.78	-	-		96.28	-	-	95.1	0.69	-	-	88.11	-	-
Ti	30.19	-	-	-	-	-	-	-	-	-	-	-	-	0.71	-	0.48	-	-	-	-	-		-	-
Mn	-	-	-	-	-	-	0.93	1.62	-	-	-	0.73	-	-	2.82	-	-	1.24	-	-	-	10.61	-	-
Fe	2.19	-	30.6	31.45	-	-	0.75	4.64	-	-	-	-	32.05	6.57	0.91	38.92	1.59	1.57	31.35	3.13	-	1.29	23.41	1.95
Y	2.27	-	-	-	-	-	-	-	-	-	-	-	-	-	-	-	-	-	-	-	-	-	-	-
Sr	-	-	-	-	-	-	0.6	0.54	28.1	2.52	-	-	-	-	-	-	-	-	-	-	-	-	-	-
Zr	22.55	-	-	-	-	-	-	-	-	-	-	-	-	-	-	-	-	-	-	-	-	-	-	-
Th	3.73	-	-	-	-	-	-	-	-	-	-	-	-	-	-	-	-	-	-	-	-	-	-	-
As	-	-	-	0.85	-	-	-	-	-	-	-	-	-	-	-	-	-	-	-	-	-	-	-	-
Br	-	-	-	0	-	-	-	-	-	-	-	-	-	-	-	-	-	-	-	-	-	-	-	-
Ba	-	-	-	0	-	65.8	-	-	-	-	-	-	-	-	-	-	-	-	-	-	-	-	-	-
Zn	-	-	-	-	-	-	-	-	-	-	-	-	-	-	-	-	-	-	-	55.43	-	-	-	55.71
Cu	-	-	-	-	-	-	-	-	-	-	-	-	-	-	-	-	-	-	-	-	-	-	30.05	-